STUDIES OF CLAY MINERALS

AND

THEIR DECOMPOSITION PRODUCTS

PAUL JOHN MICHAEL

A THESIS SUBMITTED FOR THE DEGREE OF

DOCTOR OF PHILOSOPHY

THE UNIVERSITY OF ASTON IN BIRMINGHAM

DECEMBER 1989

THE UNIVERSITY OF ASTON IN BIRMINGHAM

STUDIES OF CLAY MINERALS AND THEIR DECOMPOSITION PRODUCTS

PAUL JOHN MICHAEL.

A THESIS SUBMITTED FOR THE DEGREE OF DOCTOR OF PHILOSOPHY

DECEMBER 1989

ABSTRACT:

Mössbauer spectroscopy and X-ray diffraction of five coals revealed the presence of pyrite, illite, kaolinite and quartz, together with other minor phases. Analysis of the coal ashes indicated the formation of hematite and an Fe(3+) paramagnetic phase, the latter resulting from the dehydroxylation of the clay minerals during ashing at 700 to 750°C.

By using a combination of several physicochemical methods, different successive stages of dehydroxylation, structural consolidation, and recrystallisation of illite, montmorillonite and hectorite upon thermal treatment to 1300°C were investigated. Dehydroxylation of the clay minerals occurred between 450 and 750°C, the X-ray crystallinity of illite and montmorillonite remaining until 800°C. Hectorite gradually recrystallises to enstatite at temperatures above 700°C. At 900°C the crystalline structure of all three clay minerals had totally collapsed. Solid state reactions occurred above 900°C producing such phases as spinel, hematite, enstatite, cristobalite and mullite. Illite and montmorillonite started to melt between 1200 and 1300°C, producing a silicate glass that contained Fe(3+) and Fe(2+) ions.

Ortho-enstatite, clino-enstatite and proto-enstatite were identified in the thermal products of hectorite, their relative proportions varying with temperature. Proto-enstatite was stabilised with respect to metastable clino-enstatite upon cooling from 1200°C by the presence of exchanged transition metal cations. Solid state Nuclear Magnetic Resonance spectroscopy of thermally treated transition metal exchanged hectorite indicated the levels at which paramagnetic cations could be loaded on to the clay before spectral resolution is significantly diminished.

KEY WORDS:

COAL, CLAY MINERALS, MÖSSBAUER SPECTROSCOPY, ELECTRON SPIN RESONANCE SPECTROSCOPY, SOLID STATE NUCLEAR MAGNETIC RESONANCE SPECTROSCOPY.

DECLARATION

The work described in this thesis was carried out between 1983 and 1986 at the University of Aston in Birmingham. It has been carried out independantly and has not been submitted for any other degree.

PAUL JOHN MICHAEL

TO THE MEMORY OF

MY GRANDMOTHER.

ACKNOWLEDGMENTS

I wish to express my sincere gratitude to Professor W.R. McWhinnie for his advice, encouragement and patience during the course of this work.

I am very grateful for the help and friendship that Nigel Davison has bestowed upon me, and for the friendship of the rest of my colleagues at Aston University. May I also express my thanks to the technical staff of the Chemistry and Geology Departments for their help in running samples, and keeping the various instrumentation in working order.

I am indebted to the Science and Engineering Research Council for the funding of the research project at Aston University.

Finally, I would like to thank my mother and my wife for their help in typing and preparing this thesis.

LIST OF CONTENTS

LIST OF FIGURES

LIST OF TABLES

1. GENERAL INTRODUCTION.

The initial aim of this research project was to investigate the application of Mössbauer Spectroscopy to Coal Processing Technology. Unfortunately, due to the demise of the Solid Fuel Research Group, it was necessary to diverge from this objective and concentrate solely on the inorganic constituents of coal, namely the clay minerals, under the general title: "Studies of Clay Minerals and their Decomposition Products". It is therefore necessary to divide this thesis into two halves: one dealing with the work on minerals within coal, and the other on the thermal decomposition of clay minerals. Wherever possible the two topics are treated together, and the link between the two will be elaborated upon throughout the thesis.

Coal consists of a composite material with organic and inorganic constituents. An apt definition was that given by Francis, W.[1] in 1954: "Coal may be defined as a compact stratified mass of plant debris, which has been modified chemically and physically by natural agencies, interspersed with small amounts of inorganic matter".

It is clearly evident that this definition is somewhat all encompassing and lends itself to many questions concerning:

(1) the parent matter of the coal;

(2) the environment and mode of accumulation of this matter;

(3) The composition of this parent matter, organic and inorganic;

(4) the chemical and physical changes that occurred during diagenesis (biochemical coalification) and metamorphism (geochemical coalification); and

(5) the different types of coal resulting from these processes.

In chapter 2. it is hoped that these questions will be answered, and that the complex nature of coal will be adequately revealed.

Coal covers about 50 per cent of the energy needs of the modern world, but its reserves make up approximately 90 per cent of the total extractable energy reserves. The dynamic growth of demands on the sources of primary energy in the world and the uncertainty concerning the supply of oil and natural gas has led to an ever increasing interest in coal as a potential source of energy. However, this interest tends to be highly dependent on the supply and demand of oil, as was clearly indicated in the early 1970's with the large increase in the price of oil and the present highly erratic market of the 1980's.

The world's reserves of coal (in 10^9 tons) are summarised below (Bouška, V.[2]):

	PROVED	TOTAL ESTIMATE
Anthracite	19	28
Bituminous coal	1058	8093
Lignite and Brown coal	343	2633
TOTAL	1420	10754

Of the total amount of $10,754 \times 10^9$ tons, 13.10 per cent is proved and 5.5 per cent exploitable. Bituminous coal makes up about three quarters of the total amount. With the world production and consumption of coal as they were in 1974, i.e., approximately 3×10^9 tons per year, the total reserves will suffice for 3,600 years, and the proved reserves for 470 years, (Vrtal, V.[3]). The reserves that can be mined and are usable with the present day technology, are estimated for 200 years approximately.

In addition, coal is also used as a raw material for coke, synthetic substances and mineral fertilisers, and its application in the manufacture of heavy chemicals will certainly increase in the future. The importance of coal has recently come to the fore not only as a result of the energy crisis but also of the progressive decline of oil and natural gas reserves. So far coal has been carbonised to produce coke, and the consumption of coal in the chemical industry shows a rising tendency: alkenes (ethene and propene) and aromatics (benzene, toluene, xylene) are being produced. The conversion of coal into liquid fuel is also a permanent theme of specialist treatises, and the possibility of the manufacture of heavy fuel oils, medium to light distillates and even synthetic oil is being considered. For example, the production of petroleum range hydrocarbons by the Sasol processes[4] in South Africa. The gasification of coal for the production of energetic and technological gases awaits its full realisation. It was towards some of these gains that this research project was originally aimed.

The inorganic constituents of coal are of great importance in coal processing and conversion technologies, and will become even more so as the need for coal utilization increases. It has now become necessary to fully understand the different inorganic compounds appearing in coal and their transformation during processing. The typical minerals found within coal consist of: Clays (kaolinite, illite, mixed layer clays), sulphides (pyrite, marcasite, sphalerite, galena), carbonates (calcite, ankerite, siderite, dolomite), quartz, and other minerals in lesser amounts such as rutile, hematite and feldspar.

Several positive effects in coal processing can be associated with the mineral matter in coal. For example, recently several researchers have shown that the mineral matter in coal may play an important role in:

(1)	coking;	(5) - (8)
(2)	coal gasification; and	(9) - (12)
(3)	coal liquefaction.	(13) - (19)

It has been observed that as the total mineral matter content of coal increases, the yields of liquefaction products also increase[14]. The dominant sulphide present in coal is usually pyrite (FeS_2), and it is well known that pyrite, or pyrrhotite ($Fe_{1-x}S$) derived from it during liquefaction, catalyses coal liquefaction; increasing the conversion into liquids and gases, and to liquids soluble in hexane, and decreasing the sulphur content of the products[13]. However, iron sulphides cannot be the only catalytically active

components in the coal, since a number of coals that have a high mineral content but contain very low quantities of pyrite exhibit very good liquefaction behaviour[14].

Of all the minerals in coal, the iron-bearing minerals appear to be the most important, and it is due to the presence of iron in a large percentage of the minerals that has led to the use of the Mössbauer effect as a powerful tool in the characterisation of these minerals. The Mössbauer effect is the name given to the phenomenon of recoilless resonant emission and absorption of γ-rays by nuclei. Of the major elements commonly found in coal, only potassium and iron exhibit Mössbauer effects. Since potassium Mössbauer spectroscopy is experimentally difficult and chemically uninformative with respect to coal, iron Mössbauer spectroscopy is of sole importance as regards the minerals contained in coal. The application of iron Mössbauer spectroscopy to the iron-bearing minerals in coal is explained in greater detail in chapter 4.

The usefulness of iron Mössbauer spectroscopy in coal conversion processes is immediately apparent. It has already been stated that the iron-bearing minerals in coal exhibit the greatest catalytic effects, and it is therefore possible to use Mössbauer spectroscopy not only for the characterisation of these minerals, but also in the study of their transformation during coal conversion. This would give some insight into how these iron-bearing minerals act as catalysts, which coals to utilise in the various processes, and what iron-bearing minerals should be added to the coal before processing to improve its conversion performance.

The application of X-ray diffraction spectroscopy would also provide further useful information about the various mineral phases present during processing, both iron-bearing and non iron-bearing.

Several researchers have shown that the iron-bearing mineral pyrite plays an important role in coal liquefaction[13], [15],[17]-[22], but little work has been done to show whether or not iron-bearing clay minerals also play an important part in coal conversion processes. For some time now it has been thought that clay minerals play a key role as catalysts in the natural formation of petroleum from organic material contained within source rocks[23],[24], and the same may well be the case for clay minerals in coal conversion processes. The original aim was to shed some light on this problem, but due to the demise of the Aston Solid Fuel Research Group this was no longer practical. Therefore, as the majority of coal conversion processes, such as liquefaction and gasification, are carried out under conditions of high temperature and pressure, it was decided to investigate the thermal decomposition of several clay minerals commonly found in coal. This would then give some insight into the sort of phase changes, within the inorganic constituents of coal, that might be taking place during processing.

The clay minerals most frequently found in coal are kaolinite and illite[25]. Much work has already been carried out on the thermal decomposition of kaolinite[26]-[35], mainly due to its use in the pottery and ceramic industries, and it will therefore not be looked into in great detail in this study. Other commonly occurring clay minerals, but to a much

lesser extent than kaolinite and illite, are montmorillonite and a proportion of mixed layer clays. Although ashes resulting from coal conversion processes have been investigated by several workers[5],[6],[36]-[39], using techniques such as Mössbauer and X-ray diffraction spectroscopy, the clay minerals illite and montmorillonite have not been studied in great detail as regards their behaviour during thermal decomposition. It is therefore on these two types of clay mineral that this study is based. Their chemical composition and structure, together with those of other clay mineral types, are fully outlined in chapter 3.

From the viewpoint of catalysis, it is well known that clay minerals act as efficient catalysts for a variety of organic reactions[40]; and historically, clay minerals have been used extensively in the petrochemical industry as catalysts for the high-temperature cracking of large hydrocarbon molecules[41]. Certain transition-metal oxides, such as CrO_3, Mn_2O_3, and Fe_2O_3 supported on alumina, have also been used in catalytic cracking to promote the formation of particularly desirable products[42]. Clay minerals have now largely been superceded by the use of zeolites in hydrocarbon cracking[43],[44], but the idea of combining clay minerals/zeolites and transition-metal oxides as catalysts, has come about in the form of transition-metal ion-exchanged clay minerals and zeolites. Much work is presently being carried out on the catalytic properties of zeolites and ion-exchanged zeolites[43]-[45]; and the catalytic action of natural and ion-exchanged clay minerals in various organic reactions has been cited in the literature by many researchers[40],[41].

One interesting example however, is the use of a copper(2+)-exchanged clay in the detoxification of dioxin[46] —— one of mankind's most toxic chemicals. Usually it takes high temperatures and strong Brønsted acids to produce radicals from dioxin capable of being detoxified chemically. This however can now be done by the simple addition of copper-exchanged clay to a boiling solution of dioxin in hexane (69°C).

In order to fully understand the mechanism of clay catalysis it is necessary to establish, among other things, whether the reactions occur on the internal or external surfaces of the clay and the role played by exchanged ions, and to identify the actual sites of catalysis. As a consequence, the characterisation of the appropriate clay-organic system becomes essential. Many techniques can be used in this chacterisation, such as Infrared spectroscopy, powder X-ray diffraction, and Electron Spin Resonance spectroscopy; but the use of one of the most powerful techniques, Nuclear Magnetic Resonance (NMR) spectroscopy[47], is made difficult by the fact that one is dealing with a solid rather than a liquid and that clay minerals often contain a large proportion of paramagnetic components. The problem of having a solid rather than a liquid is overcome by the use of High-resolution Solid-state (Magic Angle Spinning) — NMR (MAS-NMR) spectroscopy[48]-[54]; but unfortunately, the presence of paramagnetic components within a clay mineral can lead to sideband formation and have a significant broadening effect on its MAS-NMR spectrum; sometimes no signal is obtained at all[52],[55]-[59]. Iron (Fe^{2+},Fe^{3+}), and sometimes manganese (Mn^{2+}), are often present in naturally occurring clay minerals

in quite large proportions; and this problem is aggravated if one is looking at clay-organic systems in which paramagnetic transition-metals have been exchanged onto the clay. With this in mind, the tolerance levels of MAS-NMR towards paramagnetic components exchanged onto a clay mineral have been investigated. Once these levels have been established, it will be possible to ensure that only clay minerals below these levels are used; and hence, that ^{29}Si, ^{27}Al, ^{13}C, and ^{1}H MAS-NMR spectra are obtainable with ease. Towards this end, the thermal decomposition behaviour of hectorite, a clay mineral akin to montmorillonite, has been investigated. Hectorite has the advantage of being structurally very similar to montmorillonite, and having an extremely low iron content when obtained 'pure'. Hence, this clay mineral could be exchanged with various quantities of paramagnetic transition-metals, and their ^{29}Si MAS-NMR spectra observed to give some idea of the maximum exchange levels possible before the effects of broadening lead to the loss of data.

2. COAL — ORIGIN, FORMATION, COMPOSITION AND CLASSIFICATION.

2.1. THE PARENT MATTER OF COAL:

Most coals originate from the peats of low moors which have plant associations of forests or reeds. The parent substances of the organic debris that make up these peats[60] are chiefly the following:

(1) Celluloses; essentially carbohydrates of a cyclic but non-benzenoid structure.

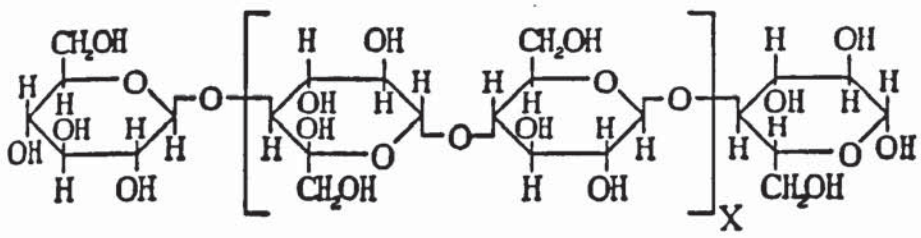

Plant tissues also contain smaller proportions of other carbohydrates, eg. hemi-cellulose, hexoses, pectins and pentosanes (xylane). The composition of wood-tissues can be expressed as an aggregate of cellulose and a 'lignin'-complex $C_{19}H_{18}O_8$ thus:

$$5C_6H_{10}O_5 \cdot C_{19}H_{18}O_8$$

(C = 49.60%, H = 5.74%, O = 44.6%).

Wood (dry and ashless) actually contains:
C = 49.0 - 50.4%, H = 6.0 - 6.5%, O = 43.0% .

(2) Lignins; closely related to celluloses, but having a benzenoid structure. They generally contain: C = 60 - 65%, H = 6.0%, N and S = 1.0%, and O = 30 - 33%.

Lignin contains both -OH and $-OCH_3$ groups, and has an aromatic structure which differs slightly between different plant species:

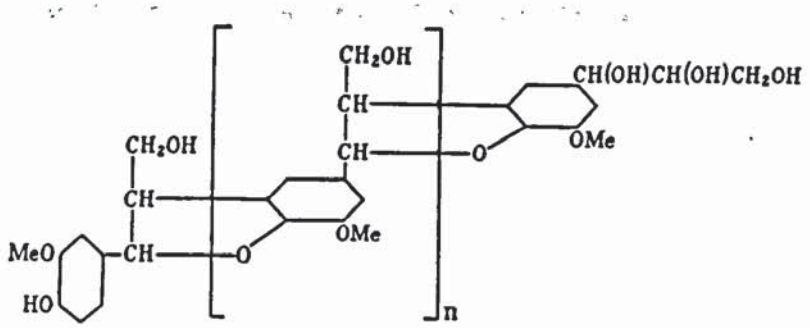

(3) Proteins; large natural polymers composed of carbon, hydrogen, oxygen, nitrogen and sulphur. The elementary composition usually varies between:

	%
C	50.0 - 55.0
H	6.9 - 7.3
N	15.0 - 19.0
O	19.0 - 24.0
S	0.3 - 1.0

(4) Resins, Waxes, Fats, and Gums; compounds of carbon, hydrogen and oxygen only, but of many different chemical types and structures.

TABLE 1., after Francis, W.[1], relates the above constituents to the various parts of the plant bodies constituting the organic debris of peat.

Normally after the plant's death, its organic constituents decompose under the influence of oxygen into gaseous compounds and water. However, in swamps with a high water table and lack of aeration the plant residues are in a reducing environment, which is conducive to the process of peat formation.

TABLE 1. Chemical substances and average elementary composition of plant tissues. (After Francis, W.[1])

Parts of plant body	Chemical substances	Portion of substances (in %)*	Average composition (in %)**		
			C	H	O
wood	saccharides (only cellulose)	45–65	44.4	6.2	49.4
	lignin	20–45	63.2	6.1	30.7
	proteins	12–16	53.5	7.0	22.0
	fats + waxes	0.2–4.0	82.0	14.2	3.8
	resins	0.5–15.0	80.0	10.0	10.0
bark	saccharides	small			
	lignin	20–50	49.0	6.0	45.0
	proteins	absent			
	fats + waxes except suberin	3–15	82.0	14.2	3.8
	suberin	30–40	72.0	10.5	17.5
	resins	absent			
cuticles, spore exines	saccharides (only cellulose)	10–20	44.4	6.2	49.4
	saccharides (except cellulose)	5–15	68.0	9.5	22.5
	lignin	absent			
	proteins	small			
	fats + waxes (except cutin + sporopollenin)	10–40	82.0	14.2	3.8
	cutin + sporopollenin	25–75	72.0	10.5	17.5

* In dry matter.

** S and N (important in some proteins and resins) are not included.

2.2. MODE OF ACCUMULATION OF COAL-FORMING PLANT DEBRIS:

The accumulation of coal-forming debris may be divided into two main types:

(1) In situ material (Autochthonous).

(2) Drift material (Allochthonous).

Since important deposits of coal have been formed almost entirely from land plants, it follows that in situ material grew and accumulated under conditions similar to those existing in peat deposits found today. For the production of what may be termed "Major in situ coalfields", changes in the surface level of the land are necessary, successively repeating the favourable conditions for accumulation. Major in situ coalfields, therefore, generally appear to have been formed either in brackish or fresh water, from massive plant life growing in swamps, or in swamps interspersed with shallow lakes.

Drift material consists mainly of land plants transported by fresh or sea water to an area where conditions are favourable for accumulation.

Most coal measures consist of bands of coal interspersed with inorganic sedimentary rocks, arranged in a sequence that is repeated several times and corresponds to a cyclic process of submergence and sedimentation. Two such sequences are illustrated in FIG. 1., after Hickling, H.G.A.[61].

The sequence illustrated in FIG. 1(a). is characteristic of the deltaic formation of coal, as in the Carboniferous coal measures of England. The coal bands represent the accumulation

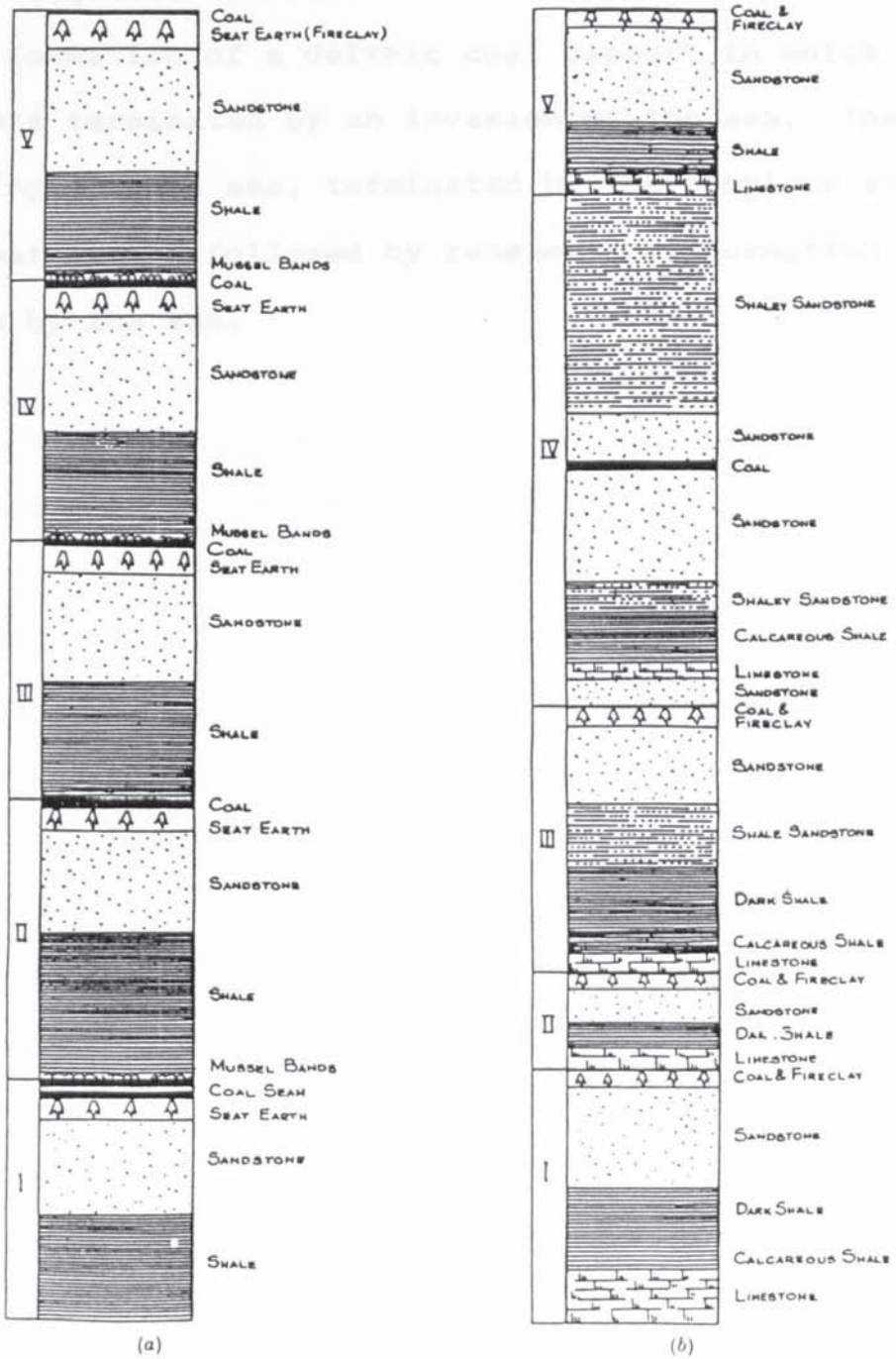

FIG. 1. Sequence of sedimentary deposits in coal formation. (After Hickling, H.G.A.[61])

of plant debris with slight subsidence. A sudden and complete submersion in fresh or sea water, followed by an influx of aquatic life, is superceded by deposits of shale, sandstone and fireclay representing renewed deltaic advancement.

The sequence illustrated in FIG. 1(b). represents the typical formation of a deltaic coal deposit in which plant growth was terminated by an invasion of the sea. The gradual shallowing of this sea, terminated by the complete silting up of the water, was followed by renewed coal formation or further invasion by the sea.

2.3. THE FORMATION OF PEAT:

Humic coal, being the most common type of coal, originated from forest peats, and thus mainly from the wood, bark, leaves and roots of swamp vegetation. During the process of peat formation these constituents are usually almost completely transformed into humic substances, which are characterised by a relatively high oxygen content. These humic substances eventually form vitrinite ——— a maceral (the smallest petrographical unit of coal). Other macerals of coal include: exinite, formed from the chemically resistant and relatively hydrogen-rich plant components; and inertinite, formed from the strong aerobic decomposition of plant residues at the peat surface.

A prerequisite for the formation of peat is stagnant ground-water, in which the plant residues are not decomposed. The peat formation begins at the surface under oxidising conditions, where fungi and aerobic bacteria play an important role. Gradual sinking and covering by younger peat layers produces reducing conditions, and the fungi and aerobic bacteria are replaced by actinomycetae and anaerobic bacteria. The microbial activity decreases with increasing depth. This phase is known generally as biochemical coalification.

The most important chemical process during the formation of peat is undoubtedly the formation of humic acids, which is enhanced by the access of air (eg. by a lowering of the water table and a drying of the peat surface), by higher temperatures (eg. in tropical climates), and by alkaline environments (eg. as a result of the addition of lime). The majority of humic

acids are produced from lignin[62], and a scheme showing this conversion during peatification has been proposed by Manskaya and Kodina[63], FIG. 2.. It is these humic substances which are responsible for the dark colour of peat.

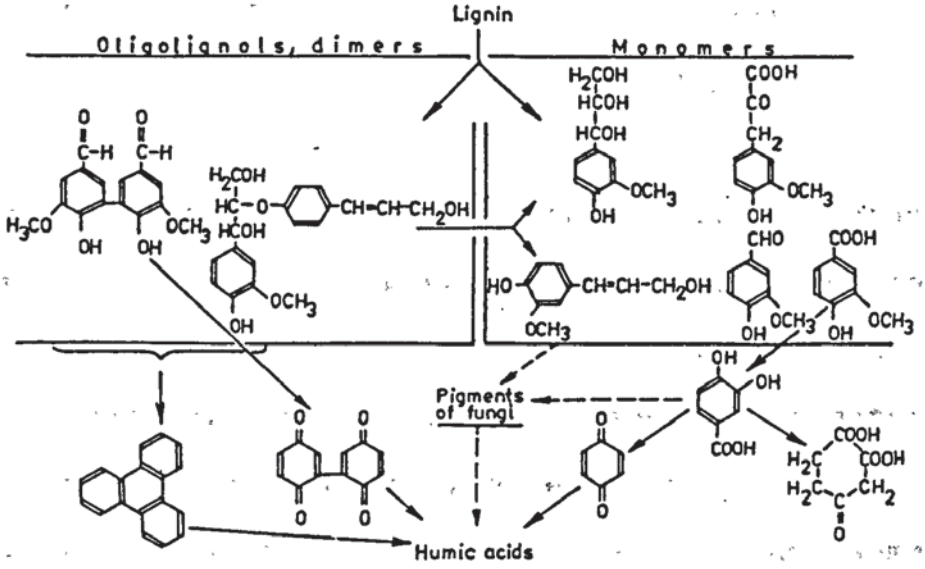

FIG. 2. Scheme showing the alteration of lignin into humic acids in the peat stage. (After Manskaya, S.M. and Kodina, L.A.)[63].

The chemical composition of peat has been given by several researchers:

(1) White, D.[64], gave the composition of humic acid as:
C = 65.31%, H = 3.85%, and O = 30.83%;
and the average composition of 10 peats as:
C = 60.53%, H = 5.56%, and O = 33.81%;
(ash, moisture and sulphur free).

(2) Bone, W.A.[60], gives the usual dry ashless composition of peat as:
C = 50 - 64%, H = 4.7 - 6.8%, O = 28 - 44%, and
N = 0.5 - 2.5%.

(3) Francis, W.[1], gave the composition of several peats from Germany as:

C = 51.13%		58.48%
H = 6.05%	INCREASING MATURITY. →	5.64%
N = 1.83%		2.34%
O = 40.99%		33.54%

The average water content of recent peats is about 90%, and the principal inorganic minerals found in swamps and peat bogs are sulphates (eg. gypsum, epsomite) and sedimentary bog iron ores (hematite, limonite). Extraneous drift material includes abundant clay minerals, especially kaolinite, quartz, muscovite, feldspars, biotite (mostly decayed) and some mafic minerals. Other minerals may be precipitated syngenetically or epigenetically from solutions in the peat or coal, for example: pyrite, marcasite, quartz, calcite, siderite and dolomite.

Relatively little is known about the diagenesis of peats with increasing depth. Undoubtedly the pore volume decreases, the water content decreases, and the density increases with depth of burial. The chemical changes in the anaerobic zone are relatively insignificant; whereas the carbon content (dry, ash-free) in the "peatigenic layer" near the surface may increase from 45 - 60% as a result of the decomposition of cellulose and hemi-cellulose and the concentration of lignin and humic matter, there is only a small increase in carbon content at greater depths[66].

2.4. COALIFICATION — THE COAL SERIES:

The principal changes that occur in the mass of decayed vegetable matter during the transition of peat to mature coals are outlined as follows, after Francis, W.[1]:

(1) Increase in carbon, progressively and uniformly.

(2) Decrease in hydrogen, gradually at first, until the carbon content reaches about 89% and then more rapidly.

(3) Decrease in the proportion of volatile matter evolved on destructive distillation, progressively and uniformly within each series of organic compounds.

(4) Increase in calorific value until the hydrogen has decreased to below 4.5%. This change is related to the change in elementary composition.

(5) Decrease in moisture content, particularly in the inherent or 'hydroscopic' moisture, until anthracitous rank is reached.

(6) Increase in absolute density.

(7) Development of coking properties over a certain range of rank and type.

(8) Decrease in solubility in alkaline solution.

(9) Increase in depth of colour, lustre and reflectivity.

(10) Decrease in reactivity towards oxidising or hydrogenating agents.

The first four changes are the most commonly used to measure the increase in rank of coal.

In the early stages of coalification, ie. in the stages of humic acid formation and peatification, micro-organisms and the oxidation-reduction potential of the environment play the principal role. This biochemical phase is broadly terminated by the formation of peat. Subsequently, lignite, brown coal, bituminous coal and anthracite develop as a result of slow 'inorganic maturing' (geochemical coalification). On the basis of carbon content, coal is divided into ranks. The higher the carbon content, the higher the degree of coalification and the more its chemistry differs from the chemical composition of the primary plant material. TABLE 2, after Hubáček, J.[67], gives the elemental analyses of wood, peat and Czechoslovak coals of different coalification grades.

The principal agents of the geochemical phase controlling coalification are temperature, pressure, volume and time. The end products are solid coaly 'caustobioliths' (brown coal, bituminous coal and anthracite with transitional types to clayey, silty and sandy sediments) and the natural gas escaping from the coal.

The principle of coalification in relation to the thickness of the overburden and the resulting temperature and pressure is presented in TABLE 3, after Bouška, V.[2].

The transition from peat to coal is accompanied by a reduction in volume, which is of importance when studying the concentration of certain elements. The reduction is due partly to the loss of water and the formation of many volatiles (eg. CO_2, CH_4) during the decay of the plant matter, and partly to the weight of overburden. The amount of methane released from bituminous coal and anthracite during the coalification process

has been estimated by Colombo, U.[68] at about 200 l/kg of coal.

TABLE 2. Elemental analyses of wood, peat and Czechoslovak coals of different coalification grades in %. (After Hubáček, J.[67])

	Water (W_t^r)	C^{daf}	O^{daf}	H^{daf}	N^{daf}
Wood	20–60	49–52	43–45	5.9–6.1	0.2
Peat	85–91	56–62	30–36	5.3–6.3	1–3
Lignites (in S. Moravia and S. Bohemia)	40–52	62–69	25–30	5–6.2	1
Earthy brown coals (Sokolov-Cheb coals)	40–50	68–72	19–23	5.6–6.2	0.9–1.2
Brown coals (Sokolov Basin)	35–48	68–75.6	16–23	5.1–6.5	0.8–1.4
Brown coals (North Bohemian Basin)	25–38	69–76.5	14.5–22	5.3–6.4	1–1.5
Brown pitch + bright coals (North Bohemian Basin)	10–20	75–80	11–16	5.5–6.5	1–1.4
Brown coal (Sokolov Basin)	10–20	73–78	11–15	about 7	1
Waxy brown coals (Karlovy Vary and Cheb Basins)	48	73–75	12–15	8–9	0.3–0.5
Subbituminous coals (Rakovník-Slaný and Radnice-Břasy coals)	12–25	73–80	11–19	4.8–5.6	1.3–1.7
Subbituminous coals (Kladno and Plzeň coals)	8–15	80–83	10–14	4.9–5.2	1.3–1.4
Bituminous gas coals (Ostrava and Nýřany coals)	3–10	80–85	7–13	5.3–5.9	1.3–1.7
Bituminous coking coals (Ostrava and Rosice coals)	1–5	82–90	3–11	4.5–5.5	1.4–1.9
Anthracitic coals (lower Ostrava seams)	1–3	86–92	3–8	4–5	1.1–1.5
Anthracite (S. Bohemia and Brandov)	1–3	92–95	1–4	2–3.5	1.1–1.3

Coals of the Rosice-Oslavany and Žacléř-Svatoňovice Basins have more than 3 % S (in volatile matter).

TABLE 3. Scheme of coalification in relation to the thickness of overburden.
(After Bouška, V.[2])

	Depth under the surface (in km)	Temperature (°C)	Hydrostatic pressure (kg/cm²)	Weight of overlying beds (kg/cm²)	Caustobioliths	Volatile matter V^{daf} (in %)
Diagenesis early stage of coalification	0 – 1.0	0 – 30	0 – 100	0 – 270	peat, sapropelite, young brown coal	50 – 80
Coalification	1 – 1.5	30 – 50	100 – 150	270 – 400	brown coal (mainly semi-bright + bright) with a minor amount of hygroscopic water	52
	1.5 – 2.5	50 – 75	150 – 250	400 – 675	subbituminous coal	35
	2.5 – 3.5	75 – 105	250 – 350	675 – 945	bituminous gas coal	36 – 40
	3.5 – 4.5	105 – 135	350 – 450	945 – 1 215	bituminous fat coal	26 – 36
	4.5 – 5.5	135 – 165	450 – 550	1 215 – 1 485	coking coal	18 – 26
	5.5 – 6	165 – 180	550 – 600	1 485 – 1 600	baking + slightly baking coal	13 – 18
	6 – 8	180 – 240	600 – 800	1 600 – 2 160	anthracitic coal	13
	8 – 11	240 – 330	800 – 1 100	2 160 – 2 907	anthracite	1 – 5

The values are not of general validity and are broadly approximate.

2.5. MINERALOGY OF COAL SEAMS:

More than 95% of the inorganic components of coal consist of five minerals: kaolinite, illite, calcite, pyrite (marcasite, melnikowite) and quartz. Greater than 95% of coal ash is formed by Al_2O_3, SiO_2, Fe - oxides and CaO; and the remaining 5% is made up of Mg, Na, K, Ti oxides and chlorides, sulphates and phosphates of common elements.

The first genetic classification of the mineral admixture of coal was proposed by Lessing, R.[69]. He distinquished:

(1) residues of mineral substances contained in the plant material;

(2) detritus washed or blown into the basin during the accumulation of sediments;

(3) salts precipitated from water that was in contact with organic material before or during coal formation;

(4) crystalline substances precipitated from water solutions migrating along fractures and joints of coal during its formation;

(5) products of decomposition or of interactions between the substances mentioned above; organic coal matter may have also taken part in these reactions; and

(6) substances that usually originate in other environments and that were introduced into coal or associated rocks after its development had been completed.

This is a rather intricate classification, and a modern genetic classification (Svoboda, J.V. and Beneš, K.[70]) divides the inorganic substances into: (A) internal ash matter (primary, proper); and (B) external ash matter (secondary, free).

(A) The first group comprises particles present in original plant bodies and trace elements of plants. The total mineral matter in plants is usually less than 2%, but is not evenly distributed:

Woody parts of tree	0.3 - 0.4%
Bark may contain	1 - 10%
Leaves, average	8 - 12%, can be up to 30%.

(B) The external ash matter is divided into, drift, syngenetic, and epigenetic material. The drift material includes such minerals as clays, quartz, muscovite, and feldspars. Syngenetic material includes clayey and siliceous substances, pyrite (marcasite, melnikowite), and carbonates. They were formed during the precipitation of inorganic substances from dissolved salts, products of the decomposition of extraneous minerals, and products of the decay of organic substances such as carbonic acid. The epigenetic minerals originated mainly from the later mineral solutions and from incrustations of fissures and joints in the adjacent rocks. They are as follows: pyrite (marcasite, melnikowite) and other sulphides, chlorides, phosphates, various sulphates, and others.

TABLE 4., after Mackowsky, M.T.[71], reviews the occurrence and genesis of the minerals found in coal; and TABLE 5., after Nelson, J.B.[72], shows the principal groups of minerals to be found in British coals.

TABLE 4. Occurrence and genesis of the minerals in coal. (After Mackowsky, M.T.[71])

Species of mineral	Syngenetic	Epigenetic		
		Primary	Secondary	
			without supply of material	with supply of material
Kaolin and other clayey minerals...	In all banded constituents as clayey impurities, or carbonaceous shaly formations respectively (kaolin worms)	—	—	Transformation into Sericite (ev. lateral secretion)
Pyrites (yellow p., Marcasite, Melnikowite) ...	1. in small concretions in all banded constituents	as impregnation of Fusite or in clefts and fissures (frequently Marcasite)	Pyrites formation from Melnikowite and Marcasite	Pyrites formation by transformation of the radial-structural siderite
	2. as coarse pyrites lumps formed by way of Melnikowite			
Calc-spar	—	as impregnation of Fusite or in clefts and fissures (frequently Marcasite)	—	—
Siderite	as concretions of radial structure			
Ankerite				
Dolomite ...	Dolomite nodules	—	—	—
Zinc blende ...	only quite sporadically	in clefts and fissures	—	—
Copper pyrites ...				
Galena				
Quartz	as small ± naturally rounded crystals in all banded constituents	as impregnation of Fusite or in clefts and fissures	—	—
Haematite ...	—	in clefts and fissures	out of brown ore by H_2O-loss	—

TABLE 5. Mineral species commonly occurring in coals.
(After Nelson, J.B.[72])

Shale Group:	General formula:
Muscovite, hydromuscovite, illite, bravaisite, montmorillonite.	$(K,Na,H_3O,Ca)_2(Al,Mg,Fe,Ti)_4(Al,Si)_8O_{20}(OH,F)_4$.
Kaolin Group:	**Formula:**
Kaolinite, livesite, metahalloysite.	$Al_2(Si_2O_5)(OH)_4$.
Sulphide Group:	**Formula:**
Pyrite, marcasite.	FeS_2.
Carbonate Group:	**General formula:**
Ankerite, ankeritic calcite, ankeritic dolomite, ankeritic chalybite.	$(Ca,Mg,Fe,Mn)CO_3$.
Chloride Group:	**Formula:**
Sylvite, halite.	KCl, NaCl.
Accessory Minerals:	**Approx. formula:**
Quartz	SiO_2.
Feldspar	$(K,Na)_2O.Al_2O_3.6SiO_2$.
Garnet	$3CaO.Al_2O_3.3SiO_2$.
Hornblende	$CaO.3FeO.4SiO_2$.
Gypsum	$CaSO_4.2H_2O$.
Apatite	$9CaO.3P_2O_5.CaF_2$.
Zircon	$ZrSiO_4$.
Epidote	$4CaO.3Al_2O_3.6SiO_2.H_2O$.
Biotite	$K_2O.MgO.Al_2O_3.3SiO_2.H_2O$.
Augite	$CaO.MgO.2SiO_2$.
Prochlorite	$2FeO.2MgO.Al_2O_3.2SiO_2.2H_2O$.
Diaspore	$Al_2O_3.H_2O$.
Lepidocrocite	$Fe_2O_3.H_2O$.
Magnetite	Fe_3O_4.
Kyanite	$Al_2O_3.SiO_2$.
Staurolite	$2FeO.5Al_2O_3.4SiO_2.H_2O$.
Topaz	$Al_2SiO_4(OH,F)_2$.
Haematite	Fe_2O_3.
Penninite	$5MgO.Al_2O_3.3SiO_2.2H_2O$.
Tourmaline	$Na(Mg,Fe,Mn)_3Al_6(BO_3)_3Si_6O_{18}(OH,F)_4$.

3. CLAY MINERALS —— CHEMICAL COMPOSITION AND STRUCTURE.

It is usual to group together under this general heading a number of groups of minerals which share certain characteristic properties. They are soft, easily hydrated, have plastic properties, and exhibit cation-exchange with simple ions and also with many organic ions. Their structures are, with a few minor exceptions, based on composite layers/sheets built from components with tetrahedrally and octahedrally coordinated cations. Chemically, all are hydrous silicates (principally of aluminium or magnesium) which, on heating, lose absorbed and constitutional water, and at high temperatures yield refractory materials. Important differences among the clay minerals, however, lead to their subdivision into several main groups. The most important layered clay mineral groups are: Kandites (Kaolinite Group); Illites (Mica Group); Smectites (Montmorillonite Group); Chlorites; and Vermiculites. These have characteristic basal spacings of approximately 7Å, 10Å, 15Å, 14Å and 14Å respectively (FIG. 3), but of some categories (the kandite mineral halloysite, smectites and vermiculites) the layer separation is variable since swelling may occur through the intercalation of water or organic liquids, and shrinkage may result from dehydration. Chemical composition may vary according to the extent of replacement of Si, Al and Mg by other cations, the nature and quantity of inter-layer cations, and the water content. The clay minerals vary in their dehydration and breakdown characteristics and in their decomposition products, and they also differ in their cation exchange properties according to the nature of their

inter-layer cations and residual surface charges.

FIG. 3. Schematic representation of the structure of the principal clay minerals.
(After Millot, G.[76])

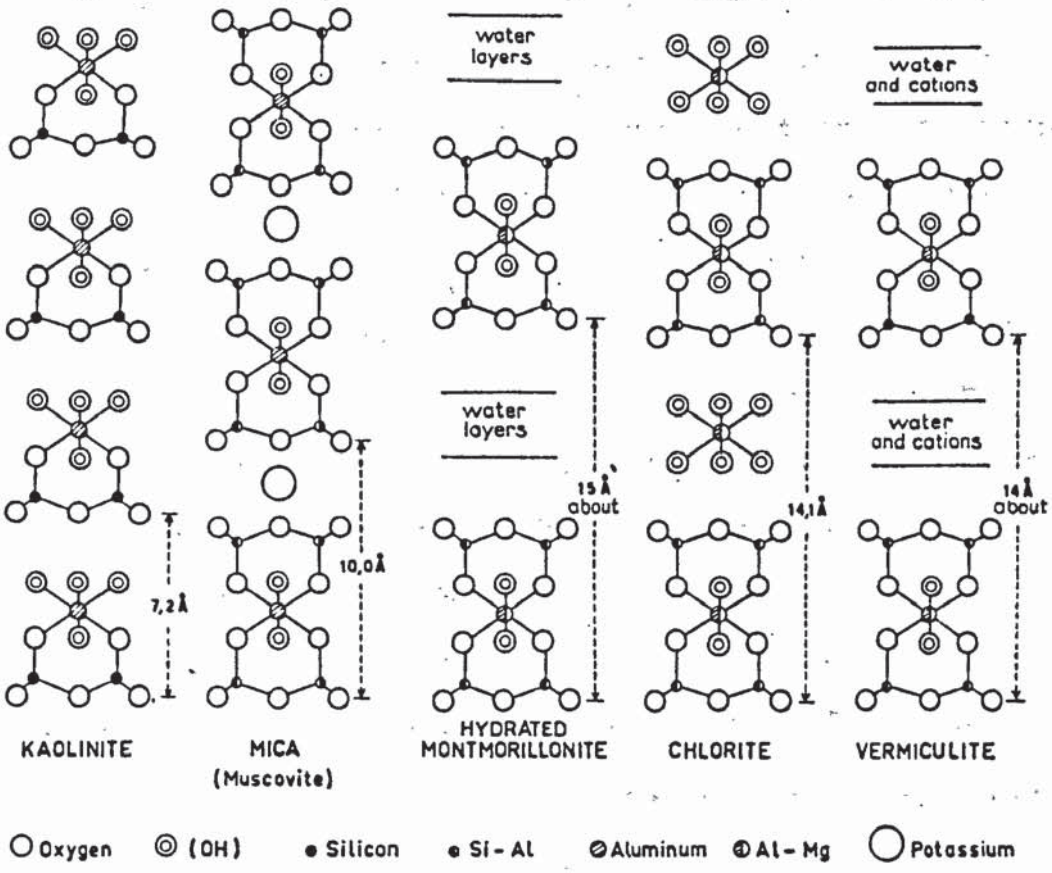

Structurally, the layer silicates or phyllosilicates are essentially made up of layers formed by condensation of sheets of linked $Si(O,OH)_4$ tetrahedra with those of linked $M_{2-3}(OH)_6$ octahedra, where M is either a divalent or trivalent cation. Condensation in a 1:1 proportion gives rise to the two-sheet or dimorphic minerals with a general formula $M_{2-3}Si_2O_5(OH)_4$, of which kaolinite is the best-known example. Similarly, the three-sheet or trimorphic clays are formed by a 2:1 condensation,

the octahedral sheet being sandwiched between two sheets of inward-pointing tetrahedra (the mica-type layer structure) giving a layer formula of $M_{2-3}Si_4O_{10}(OH)_2$. The two hydroxyl ions associated with each octahedral site in a 2:1 type layer silicate give rise to two types of site within the octahedral sheet. These hydroxyl ions may be at opposite (trans, M1) or adjacent (cis, M2) corners of the octahedron. The ratio of cis- to trans- positions is 2:1. Four-sheet or tetramorphic types also occur in which trimorphic units alternate with $M(OH)_{2-3}$ sheets of octahedrally coordinated M^{2+} or M^{3+} ions, exemplified by chlorite. Based on theoretical formulae, these layers are electrically neutral and held together by a combination of hydrogen bonding and Van der Waals forces. A schematic representation of these structures is given in FIG. 3, after Brindley, G.W.[73].

There is scope in these structures for isomorphous replacement, that is, for substitution of Si^{4+} and/or $M^{2+/3+}$ for cations of similar size but different (usually lower) valency. Thus, $3Mg^{2+}$ ions may replace $2Al^{3+}$ ions in the octahedral sheet of a layer silicate and the structure still remain electrically neutral. This is possible because in an electrically neutral layer containing Al^{3+} ions in the octahedral sheet, only two-thirds of the octahedral sites need to be filled to attain neutrality. Minerals of this type are termed dioctahedral (eg. $Al_2(OH)_6$, gibbsite). Hence, there are site vacancies within the octahedral sheet available to accommodate the 3:2 replacement of Mg^{2+} for Al^{3+} ions. Minerals with all the octahedral sites filled are termed trioctahedral (eg. $Mg_3(OH)_6$, brucite). As a result of

isomorphous substitution taking place in the tetrahedral sheet (ie. Al^{3+} for Si^{4+}), which has no site vacancies, or if substitution in the octahedral sheet is only partial, or M^{+} ions are contained in the octahedral sheet of a trioctahedral mineral, the structure of many layer silicates may be negatively charged. This positive charge deficiency may, to some extent, be compensated by internal substitution but for the most part electrical neutrality is maintained by sorption of extraneous cations, which may or may not be exchangeable.

Several excellent texts have been written on the subject of clay mineralogy: Theng, B.G.K.[41]; Brindley, G.W.[73]; Grim, R.E.[74]; Deer, W.A., Howie, R.A., and Zussman, J.[75]; and Millot, G.[76]. Therefore, only a general overview of the main clay mineral groups will be given here.

3.1. THE KANDITES/KAOLINITE GROUP:

The kandites are a group of clay minerals that are characterised by their 1:1 type layer structure. Probably the best-known mineral of this type is kaolinite, which is dioctahedral with the composition $Al_2Si_2O_5(OH)_4$. The structure of kaolinite is shown schematically in FIG. 3, and diagrammatically in FIG. 4, after Grüner[77]. The basal spacing is approximately 7Å and the basal layers are electrically neutral. When the kaolinite layers are separated from each other by sheets of water the mineral is termed halloysite, and the basal spacing increases to approximately 10Å. Isomorphous substitution in kaolinite of (Mg^{2+}, Fe^{2+}, Fe^{3+}) for Al^{3+}, with or without Al^{3+} for Si^{4+}, is almost negligible. This is reflected in the very low cation-exchange capacity (C.E.C.) of kaolinite, which ranges from 3-15 m.eq./100g clay[74].

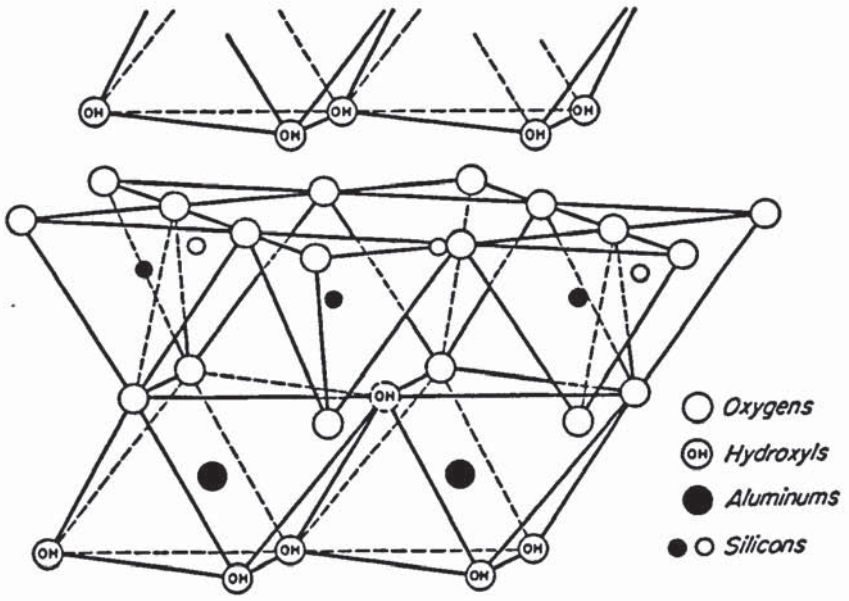

FIG. 4. Diagrammatic sketch of the structure of the kaolinite layer. (After Grüner, J.W.[77])

Other minerals in this group include the triotahedral serpentines, eg. chrysotile, $Mg_3Si_2O_5(OH)_4$. Chamosite may contain Mg^{2+}, Fe^{2+}, Fe^{3+}, and Al^{3+} in the octahedral sheet.

3.2. THE ILLITES/MICA GROUP:

Clay minerals of this group are characterised by a 2:1 type layer structure, FIG 3. The basal layers are usually charged, and neutrality is achieved by positive ions that are strongly bonded between the basal layers. The basal spacing is approximately 10Å. If the bonds are of a weaker type, the mineral belongs to the smectite group. The Illites/Mica group can be divided into several sub-groups or divisions on the grounds of their chemical composition.

(1) Micas: In micas, around one-quarter of the silicon atoms in the tetrahedral sheets are replaced by aluminium, resulting in a charge dificit in these sheets. The octahedral sheet contains varied cations which determine the diversity of micas. Potassium ions generally establish charge neutrality, which occur between the basal layers and strengthen their bonding. Dioctahedral micas include: muscovite, $KAl_2(AlSi_3)O_{10}(OH)_2$; and paragonite; $NaAl_2(AlSi_3)O_{10}(OH)_2$. Trioctahedral micas include: phlogopite, $Mg_3(AlSi_3)O_{10}(OH)_2$; and biotite, $(Mg,Fe^{2+})_3(AlSi_3)O_{10}(OH)_2$. Iron can substitute in the octahedral sheet as Fe^{2+} or Fe^{3+}, and occasionally as Fe^{3+} in the tetrahedral sheet. The structure of muscovite is shown diagrammatically in FIG 5, after Grim, R.E.[74].

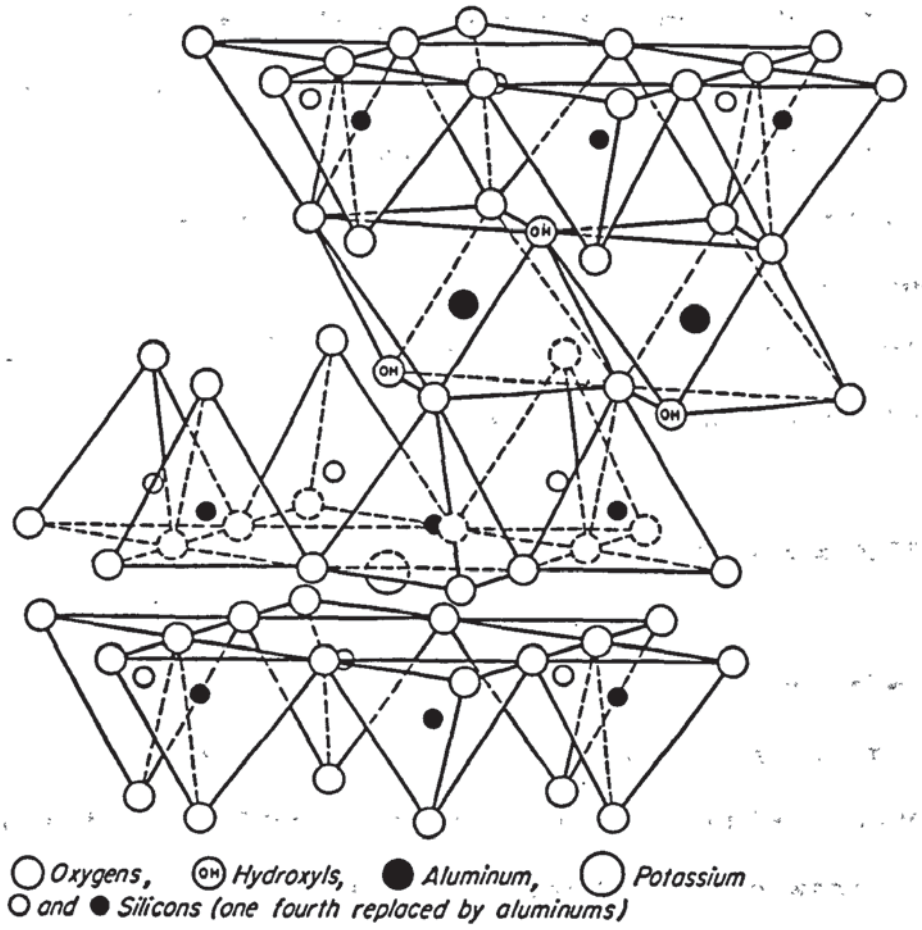

FIG. 5. Diagrammatic sketch of the structure of muscovite. (After Grim, R.E.[74])

(2) Pyrophyllite and Talc: In these two minerals there is no substitution of aluminium for silicon in the tetrahedral sheets. Therefore, the base is neutral and there is no need for alkali ions between the layers. This explains the ease with which talc layers slip past each other. Pyrophyllite is dioctahedral, $Al_2Si_4O_{10}(OH)_2$; while talc is trioctahedral, $Mg_3Si_4O_{10}(OH)_2$.

(3) Illites: Illites are the most common clay minerals in nature. They resemble micas in many respects, apart from the aluminium for silicon substitution in the tetrahedral sheets which is much less pronounced. This results in a proportionate diminution of alkali ions between the layers. A partial replacement of aluminium in the octahedral sheets by Mg^{2+}, Fe^{2+}, and Fe^{3+} ions is frequently found. The basic formula for illites is as follows:

$$K_xAl_2(Si_{4-x}Al_x)O_{10}(OH)_2;\quad 0.5<x<0.75.$$

Besides potassium, calcium and sodium, the hydroxonium ion (H_3O^+) also appears in inter-layer positions. When hydroxonium ions replace some of the potassium ions, the bases are more weakly bound and may expand. Illites have a C.E.C. of between 10-40 m.eq./100g clay[74].

(4) Glauconite: The structural formula of glauconite is close to that of illite, but containing a higher proportion of Fe^{3+} in the octahedral sheet. Basic formula:

$$K_x(Fe^{3+},Al^{3+},Fe^{2+},Mg^{2+})_2(Si_{4-x}Al_x)O_{10}(OH)_2;\ 0.5<x<1.$$

3.3 THE SMECTITES/MONTMORILLONITE GROUP:

Montmorillonites are minerals close in structure (2:1 type) and chemical composition to the mica group, but the bonds between the layers are considerably weaker. Due to these weak bonds water in varying amounts can enter between the layers. Depending on the content of water, the basal spacing may vary between 10 and 20 Å, but frequently found to be around 14 Å. The name montmorillonite (after Montmorillon, Vienne, France) was originally applied to a clay mineral with composition similar to that of pyrophyllite except for the presence of excess water, $Al_2Si_4O_{10}(OH)_2 \cdot nH_2O$ (inter-layer). Chemical variation of this basic formula yields a group of clay minerals which are related by a common structure and by similarity of chemical and physical properties. One member of this group is itself called montmorillonite and has the formula:

$$Na^{+}_{0.33}(Al^{3+}_{1.67}Mg^{2+}_{0.33})Si_4O_{10}(OH)_2 \cdot nH_2O.$$

The structure of montmorillonite is shown diagrammatically in FIG. 6, after Hofmann, U.et al.[78]; Marshall, C.E.[79]; and Hendricks, S.B.[80].

Smectite is an alternative term for this type of clay mineral, which contains the following principal members: montmorillonite, beidellite, nontronite, saponite, and hectorite. The latter two are trioctahedral smectites which are based on the formula and structure of talc rather than pyrophyllite.

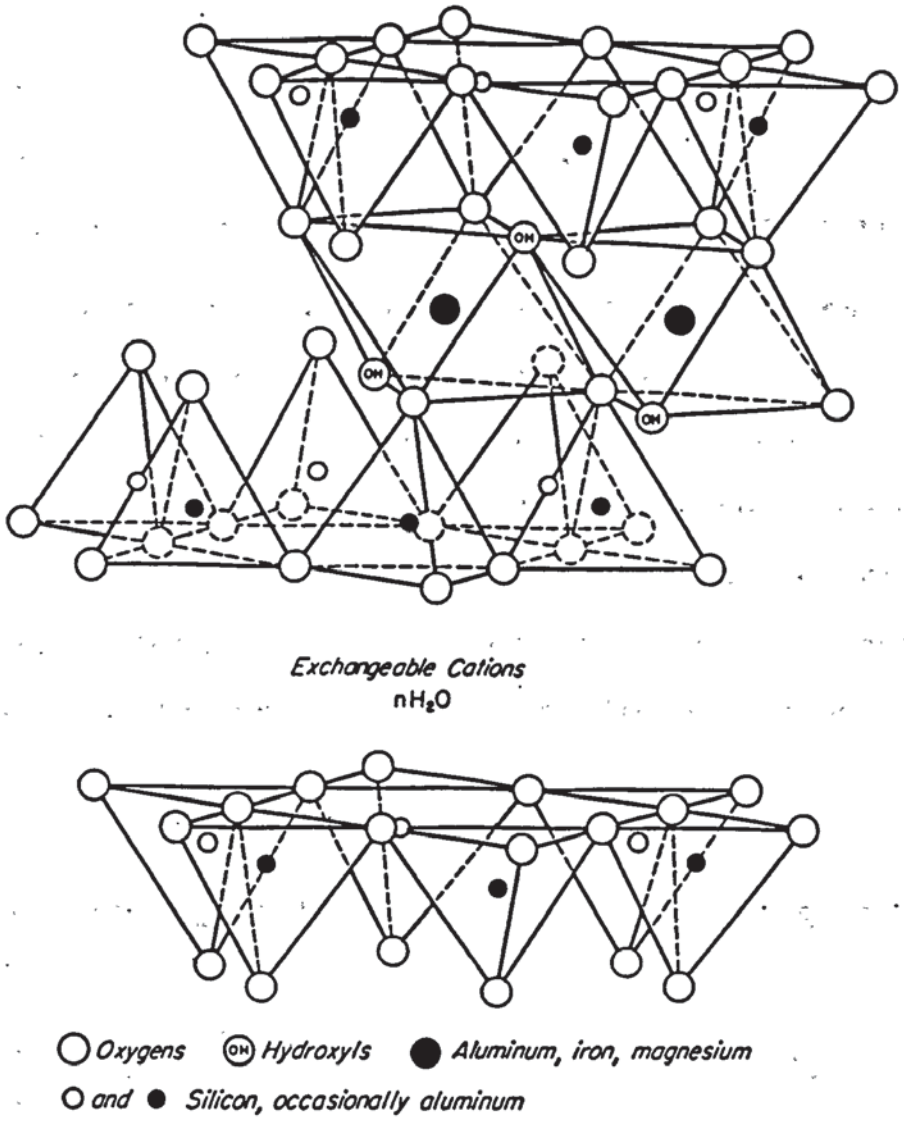

FIG. 6. Diagrammatic sketch of the structure of montmorillonite. (After Hofmann, U.[78])

The chemical formulae of all smectites are similar to those of either pyrophyllite or talc in which substitutions in octahedral or tetrahedral sites by ions of lower valency are accompanied by the addition of an equivalent number of inter-layer cations, usually sodium or calcium, to achieve charge neutrality. The average extent of such substitution requires about 0.33 additional monovalent cations (or their equivalent) per formula unit, and these ions are in general exchangeable (C.E.C. = 80-150 m.eq./100g clay[74]). The smectites are subdivided according to the substitutions

involved[81], montmorillonite and hectorite having substitution almost entirely in the octahedral sheet, while in beidellite and saponite it takes place principally in the tetrahedral sheets. Nevertheless, combinations of both types of substitution can occur, and there appears to be a continuous solid solution series between the principal members of the dioctahedral minerals; montmorillonite-beidellite-nontronite. Likewise, there is a similar series between the trioctahedral minerals, hectorite-saponite; but there does not appear to be a solid solution series between the di- and trioctahedral members[75].

(1) Dioctahedral 'montmorillonite-beidellite-nontronite' series:

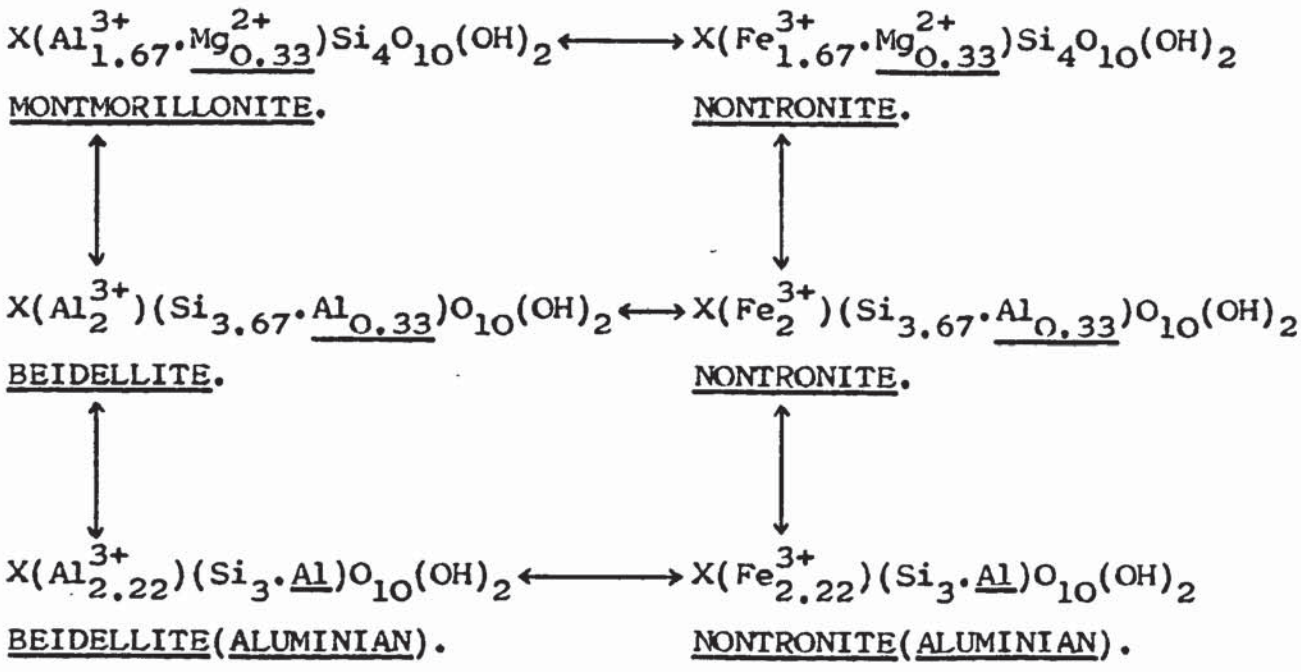

$X = (\frac{1}{2}Ca^{2+}, Na^{+})_{0.33}\cdot(nH_2O)$.

—— = Site of charge deficiency.

(2) Trioctahedral 'hectorite-saponite' series:

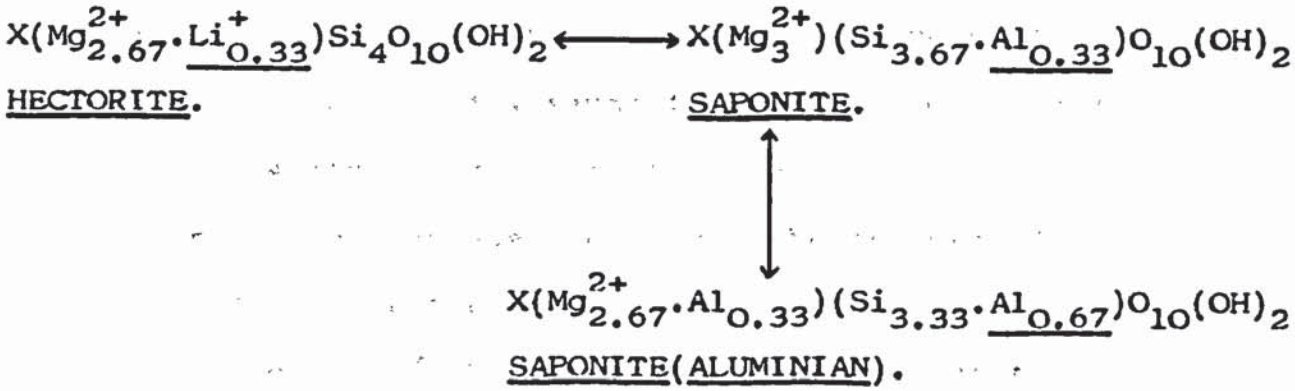

$X = (\frac{1}{2}Ca^{2+}, Na^{+})_{0.33}\cdot(nH_2O)$.

—— = Site of charge deficiency.

3.4 THE CHLORITE GROUP:

The structure of chlorite consists of layers of 2:1 trioctahedral mica sheets, separated by octahedral sheets with a brucite structure (2:1:1 type layer silicate). Dioctahedral chlorites are known, but the trioctahedral chlorites are by far the most common. The basal spacing is approximately 14 Å, but in contrast to the smectites, it stays constant (C.E.C. = 10-40 m.eq./100g clay[74]).

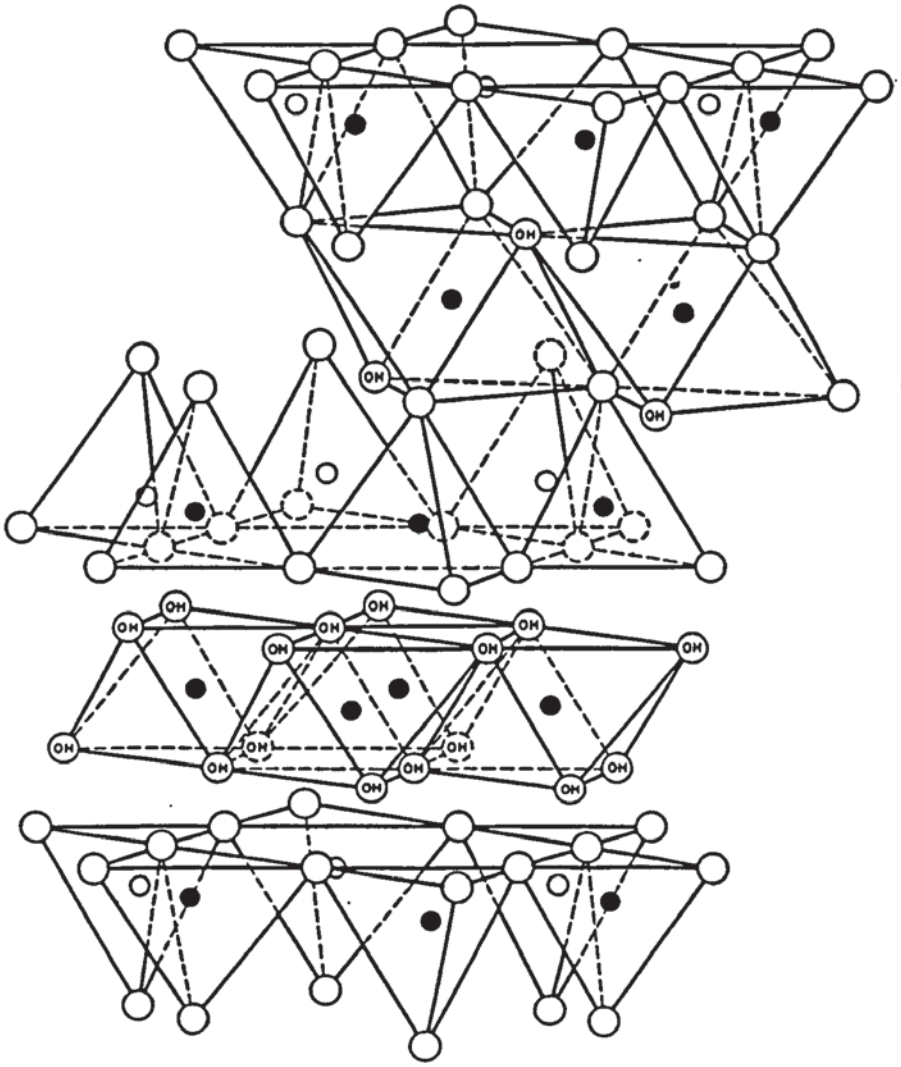

FIG. 7. Diagrammatic sketch of the structure of chlorite. (After McMurchy, R.C.[82])

The general formula for the chlorite group is:

$$(Mg,Fe,Al)_6\ (Al,Si)_4O_{10}(OH)_8.$$

Substitutions in the tetrahedral and octahedral micaceous sheets, as well as in the brucitic sheet, are extremely varied. Chlorites often have a high iron content. The structure of chlorite is shown schematically in FIG. 3, and diagrammatically in FIG. 7, after McMurchy[82].

3.5 THE VERMICULITE GROUP:

Vermiculite could well be regarded as a trioctahedral member of the smectite group. Its structure consists of 2:1 type layers separated by water molecules, FIG. 3. The basal layers are not neutral, and are balanced by inter-layer cations, most commonly magnesium and sometimes calcium. The basal spacing is approximately 14 Å, although it is not fixed (C.E.C. = 100-150 m.eq./100g clay[74]). The structural formula is:

$$(Mg,Ca)_{x/2}(Mg,Fe)_3(Si_{4-x}.Al_x)O_{10}(OH)_2.$$

3.6 THE MIXED-LAYER CLAY MINERALS:

Clay minerals also appear in nature as mixed-layer clays consisting of interstratified layers of different minerals. There are three types of mixed-layer structure:

(1) regular layers of different types alternating according to a specific law;
(2) irregular layers randomly interstratified; and
(3) layers segrated within one crystallite into zones of regular and irregular.

The majority of mixed-layer clays consist of combinations of the four following minerals: illite, montmorillonite, vermiculite and chlorite. One quite common mixed-layer clay consists of a combination of illite and montmorillonite layers.

4. EXPERIMENTAL TECHNIQUES.

4.1. SAMPLE PREPARATION AND STORAGE:

4.1.1. COAL SAMPLES:

Several coal samples were supplied by the British Gas Corporation (B.G.C.), details of which are given in TABLE 6. Each sample was mixed as thoroughly as possible by hand, except for sample BGC3 which had to first be broken into small pieces (0.5-1cm average diameter). It can be assumed that after this mixing each sub-sample was fairly representative of the sample as a whole. However, it is very doubtful if the original sample is representative of the coal seam that it originated from. In Chapter 2. it was pointed out that the majority of coals differ in both organic and inorganic constituents from the bottom to the top of a coal seam. Changes laterally are also common. Thus, any results obtained from the samples must be regarded as characteristic of the sample alone, and at most of the coal seam in the immediate vicinity of the sample location.

Sub-samples of all of the coals were taken and further crushed by hand, using a pestle and mortar, to $\leq$3mm size pieces. These samples were then crushed to a fine powder ($<$100 mesh; 0.150mm) in a temer, equipped with a tungsten carbide drum, for 30 seconds. The powdered samples were stored under nitrogen in a desiccator containing anhydrous calcium chloride. These conditions of storage were necessary because of the reactivity of finely divided coal and the

TABLE 6. Details of coal samples.

COAL.	DETAILS.
BGC3	Supplied by British Gas Corporation in one solid piece (640g). Markham Main Coal.
BGC7	Supplied by British Gas Corporation. Sample already crushed to a powder (ca. 20g). Markham Coal.
LEÃOI	Supplied by British Gas Corporation. South American Coal. DRUM 9; ca. 35% ash. (27/7/82). Approximately 2kg of coal chips (0.5 - 1cm average diameter) supplied in sealed plastic bag. Maceral analysis: Vitrinite, V = 60%. Exinite, E = 6%. Inertinite, I = 34%.
SANTA CATARINA .... SEAM.	Supplied by British Gas Corporation. South American Coal. DRUM 8; BARRO BRANCO. ca. 35% ash. (22/7/83). Approximately 2kg of coal chips. Maceral analysis: Vitrinite, V = 57%. Exinite, E = 7%. Inertinite, I = 36%.
RIO GRANDE	Supplied by British Gas Corporation. South American Coal. DRUM 2; IRUI MINE. ca. 2kg of coal chips. Maceral analysis: Vitrinite, V = 61%. Exinite, E = 5%. Inertinite, I = 34%.

minerals contained therein, towards a humid oxygen containing atmosphere, ie. coal weathering[6],[83],[84]. Typical weathering products such as hematite, magnetite and various iron sulphates can be recognised relatively easily using Mössbauer spectroscopy; an example spectrum of weathered coal refuse is shown in FIG. 14(a), after Huggins, F.E. and Huffman, G.P.[6].

Portions of the samples were taken, for various analyses, with minimal exposure of the original sample to the atmosphere. The sample jar was thoroughly shaken after each removal of sample material in order to improve the representative nature of the results obtained from any one set of samples. This effectively eliminates any minor heterogeneous variations within the sample.

4.1.2. CLAY MINERAL SAMPLES:

None of the three clay minerals investigated in this study needed any special storage requirements. The montmorillonite and illite clay minerals were supplied in a crushed and dried form. Only the original hectorite sample, which was supplied as a solid lump straight from the mine, needed drying and crushing. All were stored in ordinary screw top jars.

Illite:

The origin of this sample is unknown, and the only information available is that it is 85% pure and referred to as Illite #36. The sample, light grey in colour, had been pre-washed, dried and crushed. The main impurity is quartz.

Montmorillonite:

The sample was supplied by Steetley Minerals Ltd., and termed BERKBOND 1 (Woburn Fullers Earth); DATE: 21.11.84. The sample, light brown-yellow in colour, had been pre-crushed and dried. It consisted of calcium-montmorillonite. The main impurities are quartz and iron/aluminium oxy-hydroxides.

The full address of Steetley Minerals is given below:

Steetley Minerals Ltd.,
Woburn Road,
Woburn Sands,
Milton Keynes,
MK17 8TU.

Hectorite:

The sample was supplied by N.L. Industries in the form of a solid lump of clay obtained straight from the mine in California. Apart from iron oxy-hydroxide staining the sample was pure white in colour with a waxy texture. The sample was initially cleaned of any visible iron impurities on the surface (brown staining), and then hand picked and scraped like wax into flakes, carefully avoiding any iron staining and hard calcitic portions. A very pure sample was obtained in this way. The clay was dried at 110-120°C for 24 hr. in order to remove any adsorbed water, and placed in a desiccator containing anhydrous calcium chloride to cool. The dried clay was then crushed in a temer to a fine white powder ready for use (<100 mesh).

A further sample of hectorite supplied by N.L. Industries was unfortunately already in a pre-crushed and dried form, and

according to the analysis sheet sent with the sample only of the order of 50% pure. The sample was off-white in colour and contained impurities of calcite, iron oxy-hydroxides and some quartz. Various pretreatments and separations were tried, such as density settling in water (15g clay dispersed in 300ml H_2O, 48 hr. settling time, 15cm high column) followed by selective chemical removal of carbonates[85] and iron oxy-hydroxides[86]. After several attempts it was found to be impossible to obtain the same level of purity, especially as regards to the iron content, as in the original sample and it was decided not to proceed with the utilisation of this second clay sample. It should be stressed here that if any further sample of pure hectorite is required it should be obtained in the form of a solid lump taken straight from the mine, and hand picked in the way previously described.

The full address of N.L. Industries is given below:

N.L. Chemicals/N.L. Industries, Inc.,
31763, Mountain View Road,
Newberry Springs,
California (92365),
United States of America.

4.2. IRON-57 MÖSSBAUER SPECTROSCOPY:

Mössbauer spectra were obtained using a constant acceleration Mössbauer spectrometer of standard design, as shown diagrammatically in FIG. 8(a).

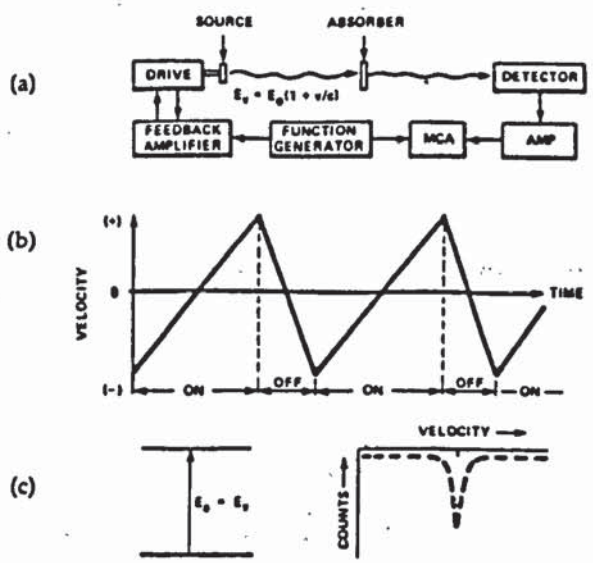

FIG. 8. Schematic representation of a Mössbauer experiment. (After Huggins, F.E. and Huffman, G.P.[6])

The δ-rays were detected using a gas filled proportional counter, counts being recorded on 512 channels of an Inotech 5200 multichannel analyser (MCA). A calibration spectrum of iron foil was run either before or just after the collection of the sample spectrum; isomer shifts were measured relative to metallic iron at room temperature.

The source consisted of 25mCi of ^{57}Co in a Pd matrix of relatively high recoil-free fraction (Amersham International). The source was vibrated in the constant acceleration driving mode by an electromechanical drive unit, so that the source

velocity was a linear function in time as shown in FIG. 8(b). The Doppler-shifted energy of γ-rays emitted when the source is moving at velocity (V) is:

$$E_v = E_o (1 + V/c),$$

where c is the speed of light and E_o is the energy of the γ-ray emitted from a stationary source. The γ-rays passing through the absorber were detected, the signal amplified, and fed to the multichannel analyser, where each channel stored the total number of γ-rays transmitted by the absorber at a particular source velocity, ie. E_v.

The absorbers studied were all powdered samples, mounted in either card or perspex holders. The dimensions of the holders were 5cm by 5cm square with a circular hole of 2.5cm diameter cut in the middle. The card holders gave a sample thickness of approximately 0.3mm - 0.5mm, whereas the perspex holders were of either 1.5mm or 2.5mm in thickness. One side of the holder was covered with selotape and the hole hand packed with the sample before sealing the other side. The sample holder chosen, and hence sample thickness, was solely dependent on the iron content of the sample. Hence, the iron content of coal being relatively low (typically 1-2wt%, of which ^{57}Fe only represents 2.19%), a relatively thick powder sample was consequently required with total areal density of coal of about 0.4-1.0g/cm^2, yielding an areal density of iron in the optimum range, 5-20mg/cm^2 of iron[5],[6]. Fortunately the organic components of coal are essentially transparent to 14.4keV γ-rays, and hence one can use these thicknesses of coal without any significant deterioration in the spectral resolution. The clay samples generally had a higher iron

content and such thick samples were seldom required.

The spectra were recorded at room temperature and were computer fitted (ICL 1904S; HARRIS H800) to Lorentzians using the Gaussian non-linear regression method[87]. It was often necessary to constrain the line-widths and intensities of the spectral 'peaks' during the initial fitting procedure in order to obtain convergence, and for the fit to be acceptable in terms of the χ^2 criterion[36],[83],[88]. (See chapter 6 for full details of the use of the χ^2 criterion).

4.2.1. PHYSICAL DESCRIPTION:

The Mössbauer effect is the name given to the phenomenon of recoilless resonant emission and absorption of γ-rays by nuclei, that was first demonstrated by Mössbauer in 1957. For iron, only the nuclide of mass 57 exhibits a Mössbauer effect. The most convenient method of generating the necessary ^{57}Fe γ-rays is to use the radioactive decay of ^{57}Co as shown in FIG. 9.

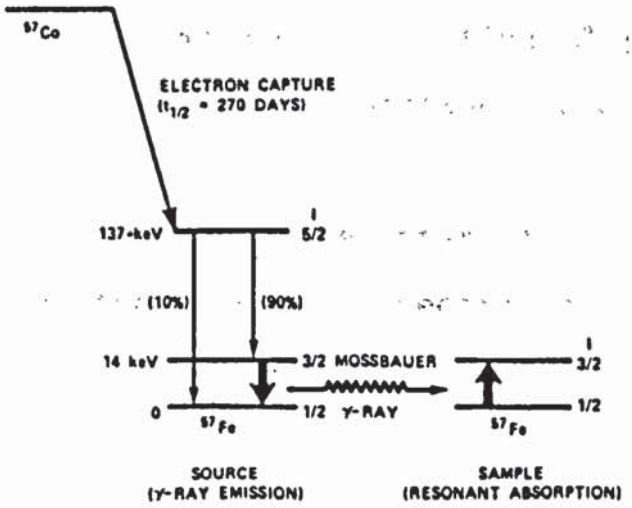

FIG. 9. Nuclear energy levels involved in the generation and resonant absorption of ^{57}Fe Mössbauer γ-rays. The symbol I denotes the nuclear spin quantum number. (After Huggins, F.E. and Huffman, G.P.[6])

^{57}Co decays by electron capture to an excited nuclear state of ^{57}Fe, which subsequently decays to its ground state by successive emission of a 123keV γ-ray and a 14.4keV γ-ray; the 14.4keV γ-ray is the one used in ^{57}Fe Mössbauer spectroscopy. When such a γ-ray interacts with a second ^{57}Fe nucleus in its ground state, this nucleus can be excited to the 14.4keV level, provided the energy of the incident γ-ray precisely matches the energy difference between the ground and excited states of the absorbing nucleus. This process is the resonant emission and absorption criterion.

Hyperfine interactions between the nuclei and the electrons in solids cause the nuclear energy levels to shift and split in several ways. The three principal types of interaction between electrons and nuclei in solids are the electrostatic, quadrupole, and magnetic hyperfine interactions. These give rise to three Mössbauer parameters respectively:

(1) Isomer shift (δ);

(2) Quadrupole splitting (Δ); and

(3) Magnetic hyperfine field (H).

The effects of these three interactions on the nuclear energy levels and the Mössbauer spectra for ^{57}Fe nuclei are shown in FIG. 10.

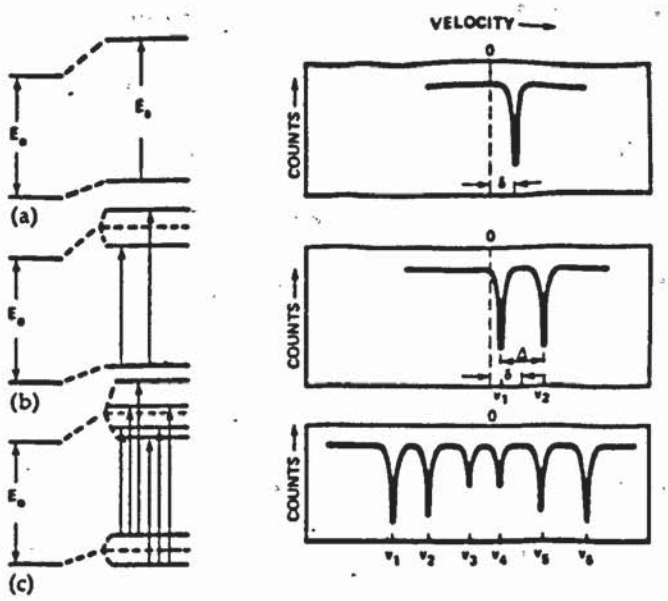

FIG. 10. Schematic illustration of the shifts and splittings in the nuclear levels and resulting Mössbauer spectra caused by interactions between the nucleus and the electrons: (a) isomer shift, (b) quadrupole splitting, (c) magnetic hyperfine splitting. (After Huggins, F.E. and Huffman, G.P.[6])

(a) represents ^{57}Fe nuclei in a cubic, nonmagnetic environment.

(b) represents a less than cubic environment, an electric field gradient (EFG) interacts with the quadrupole moment of the ^{57}Fe excited state; for nonmagnetic absorbers, this causes the single peak to split into two.

$$\delta = (V_1 + V_2)/2.$$

$$\Delta = V_2 - V_1.$$

(c) represents a magnetically ordered absorber, a large internal magnetic field interacts with the nuclear magnetic moment, giving rise to six symmetrical absorption peaks.

$$\delta = (V_1 + V_2 + V_5 + V_6)/4.$$

$$\Delta = ((V_6 - V_5) - (V_2 - V_1))/4.$$

$$H = 30.98(V_6 - V_1).$$

In order to sweep the energies of the emitted γ-rays through the various transition energies of the ^{57}Fe nuclei in the absorber, the source is vibrated back and forth over a small velocity range, typically of the order of ±1cm/s. This motion causes the γ-ray energy to be varied due to the Doppler effect.

The above is rather a simplified description of the Mössbauer effect, and it would be inappropriate here to go into greater detail. Much more complete descriptions of the theory, practice, and applications of Mössbauer spectroscopy can be found in the books by Bancroft, G.M.[88]; Wertheim, G.K.[89]; Greenwood, N.N. and Gibb, T.C.[90]; and Gibb, T.C.[91].

4.2.2. MÖSSBAUER ANALYSIS OF IRON-BEARING MINERALS IN COAL:

More than fifty different minerals have been found in coal; however, most have been found in trace amounts only. For example, Stach, E. et al.[92] lists 45 different minerals, of which only 13 contribute more than 5% to the mineral matter in some coals. TABLE 7 lists all common and many rare minerals in coal and classifies them according to their iron content[6]. This table shows that iron-bearing minerals constitute approximately half of the minerals known to occur in coal at the present time. Mössbauer data for these minerals will be discussed according to the groups shown in TABLE 7. Of the common minerals in coal, only quartz and kaolinite are essentially iron free.

TABLE 7. Partial list of minerals found in coal, classified according to their iron content.
(After Huggins, F.E. and Huffman, G.P.[6])

Iron in mineral is:	Essential (>5%)		Minor (1 to 5%)		Absent (<1%)	
Occurrence of the mineral in coal is:	Common*	Rare*	Common	Rare	Common	Rare
Sulfides	Pyrite	Marcasite Chalcopyrite Arsenopyrite Pyrrhotite Melnikovite		Sphalerite		Galena
Clays/silicates		Chlorite Biotite, etc.	Illite	Montmorillonite Muscovite, etc.	Kaolinite	Feldspars Zircon, etc.
Carbonates	Siderite Ankerite		Calcite	Dolomite		
Oxides/hydroxides		Hematite Magnetite Goethite Lepidocrocite Limonite			Quartz	Rutile Diaspore
Sulfates		Szomolnokite Rozenite Melanterite Roemerite Coquimbite Jarosite etc.				Gypsum Barite, etc.
Others		Humboldtine, etc.				Apatite Halite, etc.

* Common—usually >5%; rare—usually <5% of total mineral matter.

4.2.2.1. SULPHIDES:

Two iron-bearing sulphides are of importance; the first is pyrite, and the second is marcasite. Pyrite and marcasite can be identified readily by X-ray diffraction, but because pyrite is usually dominant in any particular coal, the two dimorphs usually are considered collectively as pyrite.

Pyrite:

Pyrite is the most common sulphide mineral in coal and is usually the dominant iron-bearing phase in their Mössbauer spectra. Huffman, G.P. and Huggins, F.E.[5] detected pyrite in all 40 coals they investigated and found it to be the major iron-bearing mineral in 70% of the samples. Typical Mössbauer spectra of pyrite rich coals are shown in FIG. 11. The Mössbauer parameters obtained from pyrite in various coals and from pure samples are listed in TABLE 8,[6].

Marcasite:

Marcasite has been recognised in some coals by optical microscopy techniques; however, it is always subordinate to pyrite and, given the similarity of Mössbauer parameters of marcasite and pyrite (TABLE 8), it is not surprising that no Mössbauer study has found unequivocable evidence for marcasite in coal.

TABLE 8. Mössbauer parameters[a] for iron-bearing sulphides and pyrite-rich coals. (After Huggins, F.E.[6])

Mineral and formula.	%Fe	δ	Δ	Reference.
Pyrite, FeS_2.	100	0.31	0.62	(6)
	100	0.25	0.62	(93)
	100	0.33	0.61	(94)
	100	0.28	0.61	(95)
Marcasite, FeS_2.	100	0.29	0.50	(94)
	100	0.25	0.50	(95)
	100	0.26	0.51	(96)

Coal seam and state.	$\%Fe^{b}_{pyr}$	δ_{pyr}	Δ_{pyr}	Reference.
Rosebud, Mont. (Sbb).	99	0.32	0.62	(6)
Herrin No. 6, Ill.	99	0.30	0.62	(6)
Redstone, W. Va.	97	0.31	0.60	(97)
Pittsburgh, W. Va.	92	0.31	0.60	(97)
Pittsburgh, Pa.	87	0.29	0.59	(6)
Average of 31 coals.	-	0.303	0.614	(5)

[a] All parameters measured at room temperature; isomer shifts (δ) relative to metallic iron; (δ) and (Δ) in mm/s.
[b] $\%Fe_{pyr}$: percentage of total iron in the coal as pyrite.

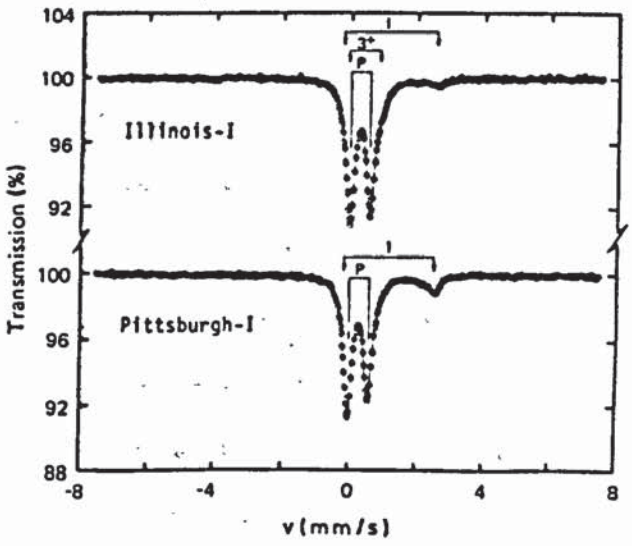

FIG. 11. Mössbauer spectra of two coals of relatively high pyrite content. The arrows labelled P, I, and 3^+ indicate the peaks contributed by pyrite, illite and ferric sulphate. (After Huffman, G.P.[5])

4.2.2.2. CLAY MINERALS:

Clay minerals are generally the predominant inorganic constituents associated with coal, often comprising as much as 50% of the total mineral matter. The most commonly occurring clays in coal are usually kaolinite, montmorillonite, illite and mixed-layer illite/montmorillonite. In general the clay minerals appearing in coal show slightly different Mössbauer parameters than pure clays[98]. A coal rich in clay is shown in FIG. 12 (about 10% mineral matter), after Montano, P.A.[16].

The appearance of two peaks at higher velocity is not due to the presence of two sites in the clay or to two different clay minerals, it is produced by szomolnokite ($FeSO_4.H_2O$). By treating the sample with HCl, the sulphate is washed away and the spectrum due to the clay (possibly illite) can clearly be seen, FIG. 13, after Montano, P.A.[98]. Treating the coal with HNO_3 dissolves the pyrite iron and the spectrum of the clay minerals can be detected more clearly.

The Mössbauer analysis of clay minerals is outlined in greater detail in section 4.2.3..

4.2.2.3. CARBONATES:

The major carbonates in coal are calcite ($CaCO_3$), siderite ($FeCO_3$), ankerite ($Ca(Fe,Mg,Mn)(CaCO_3)_2$), and dolomite ($CaMg(CO_3)_2$). From these carbonates only siderite and ankerite are of importance to the Mössbauer spectroscopist.

The presence of siderite or ankerite has been observed in several coals[16]. The electronic ground state of $FeCO_3$ is an orbital doublet. Siderite is magnetically ordered at low temperatures (T = 38K) with a very distinctive Mössbauer

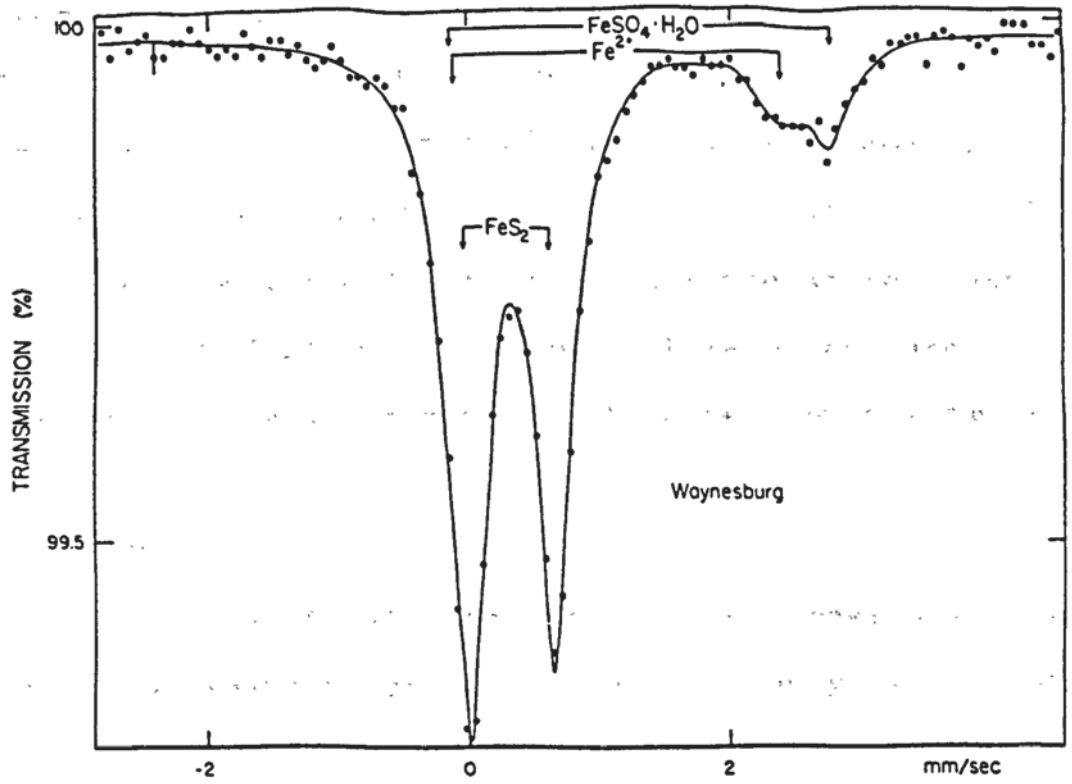

FIG. 12. Mössbauer spectrum of a Waynesburg coal at room temperature. Pyrite, szomolnokite, and illite are present. (After Montano, P.A.[16])

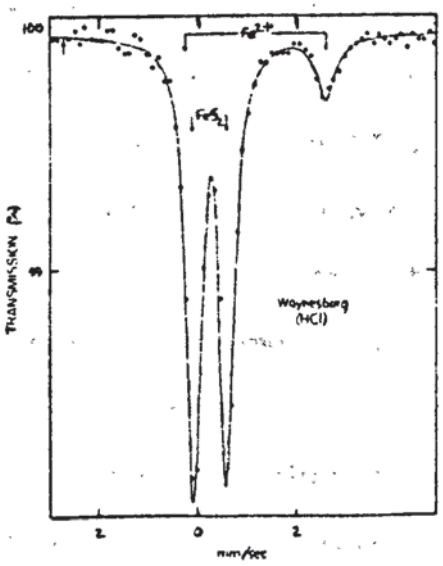

FIG. 13. Waynesburg coal after treatment with HCl (RT). (After Montano, P.A.[98])

spectrum (Q.S. = 2.06mm/s, magnetic hyperfine field +184 KOe, and I.S. = 1.36mm/s). The Mössbauer parameters at room temperature are Q.S. = 1.798mm/s and I.S. = 1.24mm/s. Ankerite also appears in some coals, and it is difficult to distinguish between ankerite and siderite at room temperature (Ankerite: I.S./Q.S. = 1.50/1.20mm/s. However, low-temperature measurements allow a clear distinction between the two minerals.

4.2.2.4. SULPHATES:

The presence of sulphates in coal is almost always an indication of weathering; and in general, only very fresh coal will be free of iron sulphates. The following iron sulphate minerals are associated with coals: szomolnokite ($FeSO_4.H_2O$), rozenite ($FeSO_4.4H_2O$), melanterite ($FeSO_4.7H_2O$), coquimbite ($Fe_2(SO_4)_3.9H_2O$), kornelite ($Fe_2(SO_4)_3.7H_2O$), roemerite ($FeSO_4.Fe_2(SO_4)_3.12H_2O$), and jarosite $(Na,K)Fe_3(SO_4)_2(OH)_6$. Melanterite dehydrates to rozenite and rozenite dehydrates to szomolnokite. Mössbauer data for the iron sulphates is given in TABLE 9; and the Mössbauer spectrum of a Waynesburg coal containing szomolnokite is shown in FIG. 12.

The identification of jarosite and szomolnokite by Mössbauer spectroscopy is fairly straightforward, even though the Mössbauer parameters of szomolnokite are similar to those of the ferrous clay component of coal; refer FIG. 12. However, the presence of coquimbite and other ferric sulphates can only be inferred on the basis of the asymmetry of the pyrite absorption peaks, FIG. 14(b), after Huggins, F.E. and Huffman, G.P.[6].

TABLE 9. Mössbauer data for iron sulphates and sulphate-bearing coals. (After Huggins and Huffman[6])

Mineral, formula.	%Fe	δ	Δ	Reference.
Melanterite, $FeSO_4.7H_2O$.	100	1.31	3.20	(99)
Rozenite, $FeSO_4.4H_2O$.	100	1.23	3.17	(99)
Szomolnokite, $FeSO_4.H_2O$.	100	1.26	2.71	(5)
Roemerite, $FeSO_4.Fe_2(SO_4)_3.14H_2O$.	26	1.27	3.27	(6)
	27	0.53	0.25	
	47	0.38	0.37	
Coquimbite, $Fe_2(SO_4)_3.9H_2O$.	32	0.51	0.00	(6)
	68	0.43	0.26	
Kornelite, $Fe_2(SO_4)_3.7H_2O$.	100	0.44	0.15	(6)
Jarosite, $XFe_3(SO_4)_2(OH)_6$.				
$X = K^+$	100	0.40	1.15	(100)
$X = Na^+$	100	0.40	1.10	

Coal seam, state, phase.	$\%Fe_{coal}$	δ	Δ	Reference.
Lignite, unknown, Jarosite.	71	0.37	1.15	(5)
Pittsnurgh (refuse), Pa., Jarosite.	39	0.36	1.14	(5)
Herrin No. 6, Ill., Jarosite.	21	0.38	1.10	(6)
Pocahontas No. 4, W. Va., Szomolnokite.	55	1.25	2.71	(97)
Pittsburgh, W. Va., Szomolnokite.	8	1.27	2.71	(97)
Davis, Ill.,				(6)
Szomolnokite,	14	1.27	2.71	
Coquimbite.	6	0.55	-	
Herrin No. 6, Ill., Coquimbite.	>12	-	-	(6)

TABLE 10. Mössbauer data for oxides and oxyhydroxides and coals containing such phases. (After Huggins[6])

Mineral, formula.	%Fe	δ	Δ	H(kG)	Reference.
Hematite, α-Fe_2O_3.	100	0.37	-0.10	515	(90).
Magnetite, Fe_3O_4.	67	0.67	0.0	463	(91).
	33	0.31	0.0	498	
Goethite, α-FeOOH.	100	0.37	0.25	0-390[a]	(92).
Lepidocrocite, γ-FeOOH.	100	0.39	0.55	0	(90).
Coal, location.	**%Fe**	**δ**	**Δ**	**H(kG)**	**Reference.**
Pittsburgh, Pa.					
α-Fe_2O_3.....	10	0.39	-0.08	514	
	14	0.66	0.00	461	(6).
Fe_3O_4.....	7	0.27	0.00	491	
Sewell, W. Va.					
Fe_3O_4.....	19	0.65	0.00	453	(6).
	9	0.30	0.00	491	

[a]Goethite at room temperature may be antiferromagnetic (H=390) or superparamagnetic (0< H< 390kG) depending on grain size.

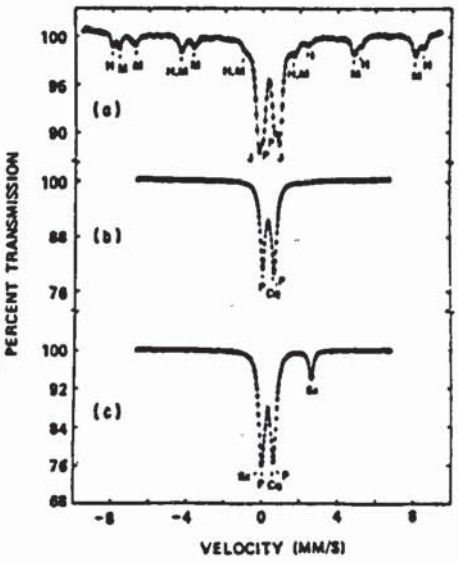

FIG. 14. Mössbauer spectra of coal refuse (a) (Pittsburgh seam, Pa) and of low-temperature ashes (Herrin No. 6 seam (b) and Davis seam, Ill (c)). The arrows labelled H, M, J, P, I, Cq and Sz indicate peaks due to hematite, magnetite, jarosite, pyrite, illite, coquimbite, and szomolnokite, respectively. (After Huggins, F.E. and Huffman, G.P.[6])

4.2.2.5. OXIDES AND OXYHYDROXIDES:

Iron-bearing oxides and oxyhydroxides are not common in fresh, unweathered coals, and their presence will usually be indicative of weathering and oxidation processes. The oxides, magnetite and hematite, are easy to recognise in Mössbauer spectra because they give rise to six-peak magnetically split spectra. The most intense peaks of these spectra are well removed from the peaks for pyrite, siderite, and iron-bearing clays, and identification of very small amounts of these oxides is straightforward. FIG. 14(a) shows the spectrum of coal refuse from Pittsburgh seam, Pennsylvania. Both hematite and magnetite are present. TABLE 10, lists the Mössbauer parameters for iron oxides and oxyhydroxides.

As the iron oxyhydroxide phases have parameters very similar to pyrite at room temperature, except in the case of magnetically ordered goethite, low temperature spectra may be useful since all these phases will become magnetically ordered.

4.2.2.6. SUMMARY:

Several researchers have produced work on the Mössbauer analysis of iron-bearing minerals in coal: Lefelhocz, J.F. et al.[95]; Huggins, F.E. and Huffman, G.P.[6]; Montano, P.A.[16], [98]; Huffman, G.P. and Huggins, F.E.[5]; and Smith, G.V. et al.[37]. A study of British Columbia coals by Taneja, S.P. and Jones, C.H.W.[36] provides some interesting work which is well worth consulting during the interpretation of the Mössbauer spectra of coals. TABLE 11, taken from this study, summarises the Mössbauer literature data for some of the most common iron-bearing phases in coal.

TABLE 11. Mössbauer literature data for some iron-bearing phases in coal.

Mineral.	Temp. (K)	δ^* (mm s^{-1})	Δ (mm s^{-1})	Hi (k Oe)	Reference.
Pyrite.	RT	0.25-0.32	0.61-0.62	-	(6),(20),(90), (93),(103),(104).
	78	0.36(1)	0.64(1)	-	(93).
	4.2	0.43(1)	0.66(1)	-	(93).
Marcasite.	RT	0.25-0.29	0.50-0.56	-	(6),(90).
Siderite	RT	1.21-1.24	1.78-1.81	-	(6),(90).
($FeCO_3$).	80	1.361	2.043	-	(90).
Ankerite.	RT	1.20	1.50	-	(6).
Illite Fe^{2+}.	RT	1.01-1.31	2.50-2.68	-	(5),(83),(105).
	78	1.47(6)	2.56(6)	-	(105).
	4.2	1.47(6)	2.61(6)	-	(105).
Chlorite Fe^{2+}.	RT	1.13	2.52-2.67	-	(6).
Montmorillonite Fe^{2+}.	RT	1.13	2.87	-	(6).
Clay mineral, Fe^{3+}.	RT	0.31-0.37	0.54-0.70	-	(5).
Jarosite.	RT	0.36-0.43	1.00-1.24	-	(6),(90).
	4.2	-	-	470-480	(90).
Szomolnokite $FeSO_4.H_2O$.	RT	1.26	2.71	-	(6),(105).
Rozenite $FeSO_4.4H_2O$.	RT	1.32	3.17	-	(16).
Melanerite	RT	1.261	3.217	-	(90).
$FeSO_4.7H_2O$.	5	1.391	3.384	-	(90).
Hematite	RT	0.38	0.12	515	(10),(90).
(α-Fe_2O_3).		0.363	-0.18	508	
Maghemite	RT	0.32-0.41	~0	496-505	(10).
(γ-Fe_2O_3).					
Magnetite	RT	A 0.61-0.67	0	450-463	(6),(10),(90).
(Fe_3O_4).		B 0.27-0.36	0	491-500	

* δ, isomer shift relative to iron metal.

(After Taneja, S.P. and Jones, C.H.W.[36])

The ^{57}Fe Mössbauer parameters for various iron-bearing phases listed in TABLE 11 and elsewhere in section 4.2, together with example spectra, have been employed to elucidate the iron-bearing phases present in the coals, coal ashes and clay minerals investigated in this thesis. Assignment of the various phases have therefore been made on the basis of the finger printing technique together with some empirical assignments as indicated in chapter 6.

When computer-fitting minor phases in multi-component Mössbauer spectra great care must be taken as it is often possible to fit the spectral lines in more than one position. Different mineral phases may therefore be assigned to the same spectrum. This topic has been dealt with in depth by Karl, R.E. and Zuckerman, J.J.[83], and the reader is directed to this work.

4.2.3. MÖSSBAUER ANALYSIS OF CLAY MINERALS:

Comprehensive studies of Mössbauer spectroscopy applied to clay and related minerals have been presented by Ericsson, T. et al.[106], and Goodman, B.A.[107]. The Mössbauer analysis of clay minerals is best illustrated by citing as an example the work of Ericsson, the results of which are presented in TABLE 12, and the spectra in FIG. 15.

The Mössbauer parameters of some of the clay minerals relevant to this work are discussed below, with reference to Ericsson's results.

Kaolinite:

The peak at approximately 2.3mm/s indicates that this sample of kaolinite contains Fe^{2+}, FIG. 15. Assuming that the f-factors (the recoil-free fractions) for the different iron sites are the same, the amount of Fe^{2+} is approximately 8% of the total iron content. Bowen, L.H. et al.[108], found that variations in f-factors in and between different micas were small; hence one can assume that the same is true for clay minerals, if all the iron is found in structural positions. The I.S. (Isomer shift)/Q.S. (Quadrupole splitting) for Fe^{3+}, 0.36/0.51 mm/s, indicates that the ferric iron is in octahedral

TABLE 12. Mössbauer parameters of the samples studied. The chemical shift (CS) is given relative to metallic iron at room temperature. ΔEq is the quadrupole splitting and W is the full half-width. I is the relative intensity of the Mössbauer pattern. Constrained values are given in brackets. Figures in brackets are standard deviations, according to the fitting program. (After Ericsson, T. et al.[106])

	Fe^{3+}				Fe^{2+}			
Sample	*I*	CS	ΔEq	*W*	*I*	CS	ΔEq	*W*
(*a*) Kaolinite	0.92 (1)	0.36 (1)	0.51 (1)	0.59 (1)	0.08 (1)	0.89 (4)	2.84 (9)	0.51 (1)
(*b*) Mont. no. 11	0.53 (1)	0.32 (8)	0.30 (3)	0.63 (4)				
	0.47 (1)	0.22 (2)	0.33 (2)	0.35 (10)				
(*c*) Mont. no. 21	1	0.35 (1)	0.57 (1)	0.57 (1)				
(*d*) Mont. no. 25	0.92 (1)	0.31 (1)	0.63 (1)	0.73 (2)	0.08 (1)	1.32 (2)	2.39 (3)	0.26 (4)
(*e*) UD 78-	0.71 (2)	0.35 (1)	0.53 (1)	0.50 (1)	0.20 (1)	1.12 (2)	2.58 (4)	(0.50 (1))
beidellite	0.09 (1)	0.36 (4)	1.05 (6)	(0 50 (1))				
(*f*) Black Hills bentonite	0.87 (1)	0.33 (1)	0.66 (1)	0.69 (1)	0.13 (1)	1.21 (4)	2.46 (8)	(0.69 (1))
(*g*) Umiat	0.37 (10)	0.33 (1)	0.52 (2)	0.44 (5)				
bentonite	0.63 (10)	0.35 (1)	0.86 (10)	0.84 (3)				
(*h*) Coalgate bentonite	1	0.37 (1)	0.46 (1)	0.47 (1)				
(*i*) Muscovite					1	1.15 (1)	3.05 (1)	0.37 (1)
(*j*) Illite 35	0.51 (2)	0.33 (1)	0.54 (1)	0.40 (1)	0.06 (2)	1.03 (5)	2.42 (2)	(0.40 (1))
	0.13 (2)	0.40 (2)	0.97 (4)	(0.40 (1))	0.31 (2)	1.13 (1)	2.74 (2)	(0.40 (1))
(*k*) Illite 36	0.62 (1)	0.32 (1)	0.58 (1)	0.32 (1)	0.15 (1)	1.18 (1)	2.88 (1)	(0.32 (1))
	0.23 (1)	0.41 (1)	1.07 (3)	(0.32 (1))				
(*l*) Mn mica	0.64 (15)	0.37 (1)	0.70 (2)	0.57 (6)				
	0.36 (15)	0.34 (2)	1.14 (32)	1.14 (10)				
(*m*) Transvaal	0.52 (3)	0.38 (1)	0.71 (1)	0.50 (1)	0.03 (2)	0.99 (5)	2.5 (2)	(0.50 (1))
vermiculite	0.34 (2)	0.40 (1)	1.23 (1)	(0.50 (1))	0.10 (2)	0.99 (51)	2.85 (5)	(0.50 (1))
(*n*) Hectorite	1	0.36 (1)	0.77 (2)	0.48 (3)				
(*o*) Bjärnå	0.09 (1)	0.57 (1)	0.71 (2)	0.40 (2)	0.41 (2)	1.08 (1)	2.24 (1)	0.36 (1)
biotite					0.50 (3)	1.11 (1)	2.58 (1)	0.27 (1)
(*p*) Greenland	0.06 (1)	0.48 (3)	0.46 (7)	0.34 (1)	0.62 (1)	1.12 (1)	2.56 (1)	(0.34 (1))
biotite	0.04 (1)	0.60 (6)	0.71 (12)	(0.34 (1))	0.27 (1)	1.10 (1)	2.09 (1)	(0.34 (1))
(*q*) Görledsjokk chlorite	0.30 (1)	0.38 (1)	0.61 (2)	0.58 (3)	0.70 (1)	1.13 (1)	2.64 (3)	0.32 (1)
(*r*) Chlorite 090352						1.14 (1)	2.63 (4)	0.31 (1)
(*s*) Chlorite 67/8	0.10 (1)	0.39 (1)	0.56 (2)	0.32 (2)	0.90 (1)	1.14 (1)	2.62 (1)	0.30 (1)

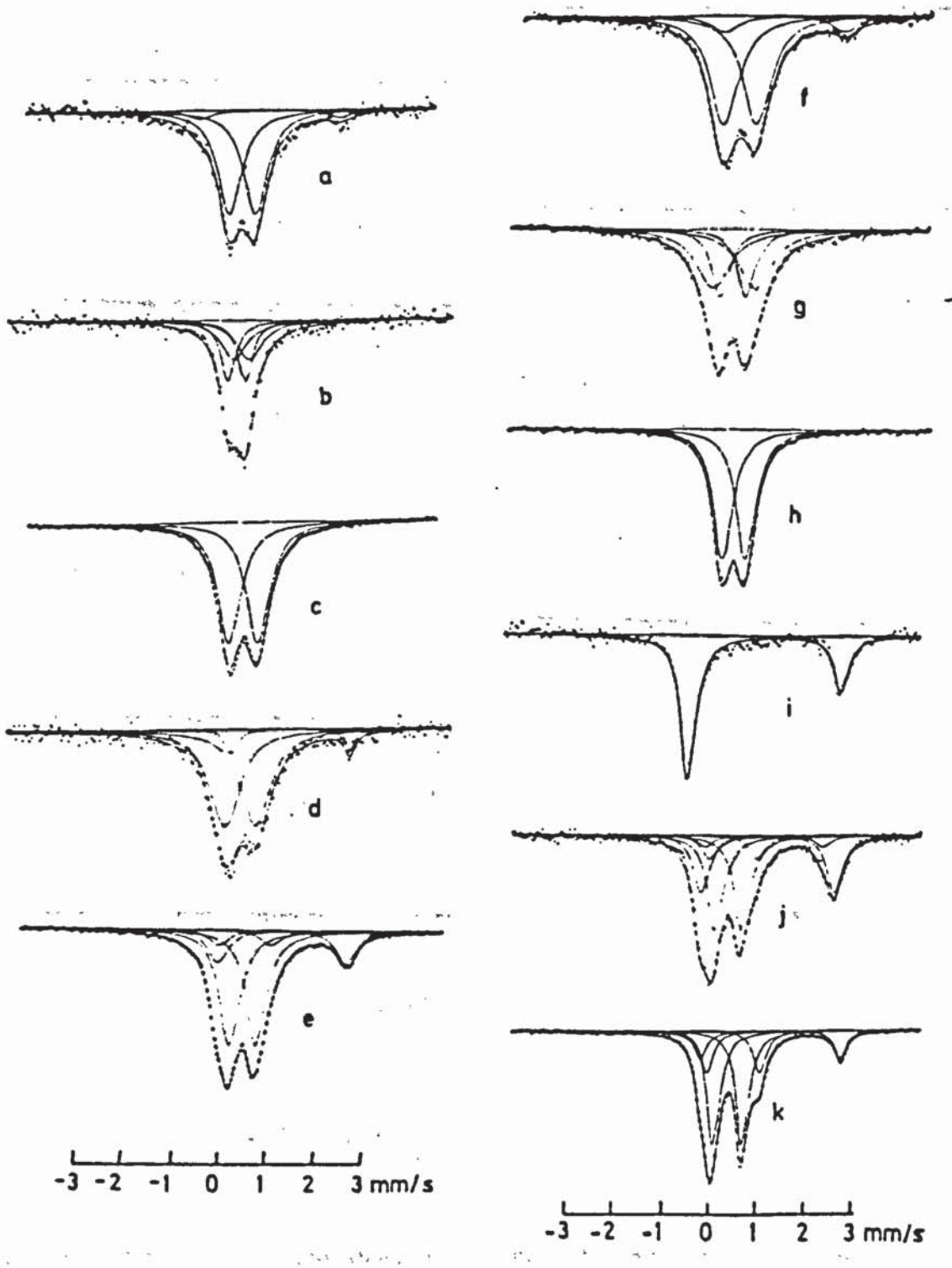

FIG. 15. Mössbauer spectra of samples studied. (a) Kaolinite, (b) Montmorillonite 11, (c) Montmorillonite 21, (d) Montmorillonite 25, (e) UD 78-beidellite, (f) Black Hills bentonite, (g) Na Umiat bentonite, (h) Coalgate bentonite, (i) Muscovite, (j) Illite 35, (k) Illite 36. (After Ericsson, T.et al.[106])

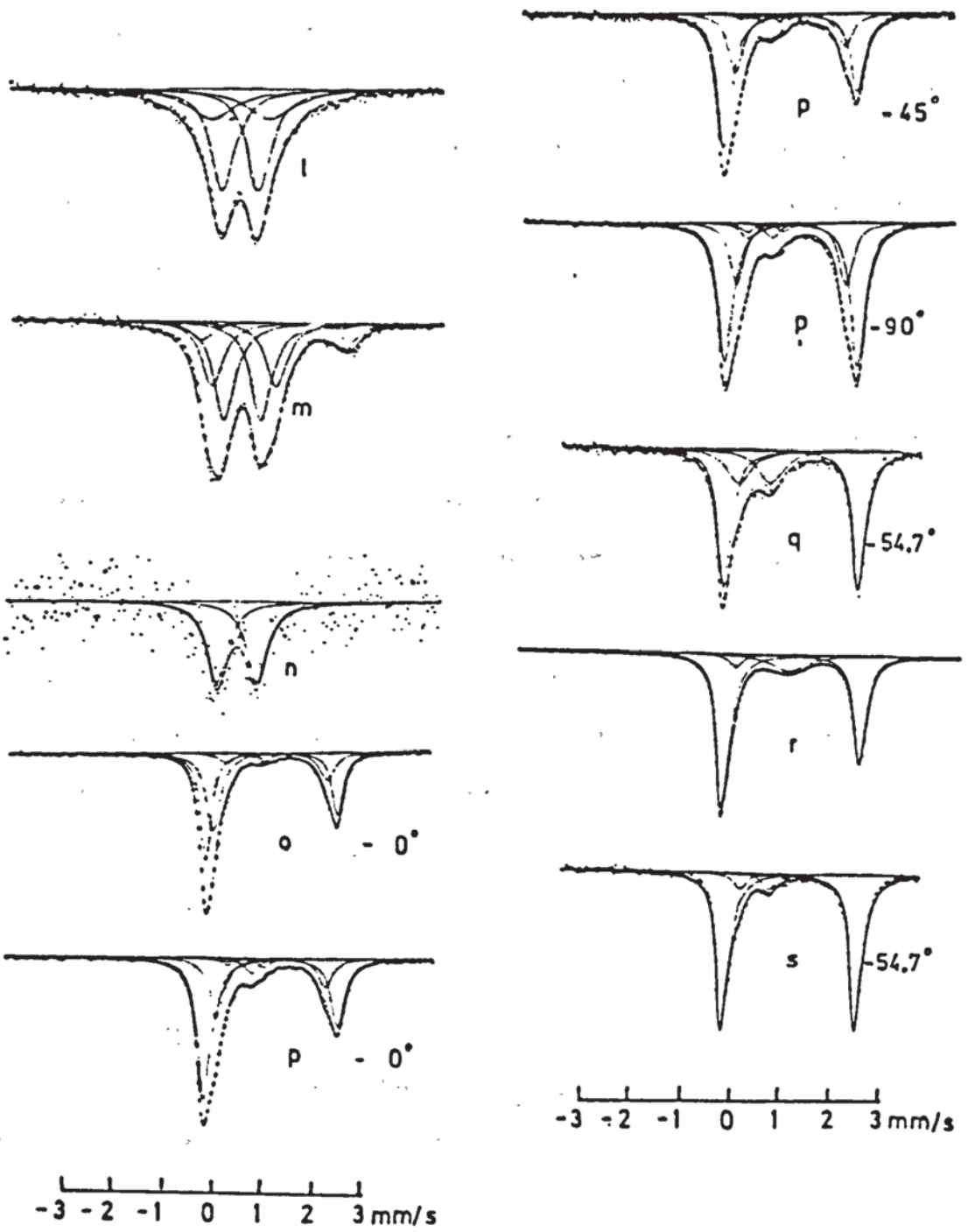

FIG. 15 (cont.). Mössbauer spectra of samples studied. (l) Mn mica Ultevis, (m) Transvaal vermiculite, (n) Hectorite 34, (o) Bjärnå biotite, (p) Greenland biotite, (q) Görledsjokk chlorite, (r) Chlorite 090352, (s) Chlorite 67/8. The angles denoted are between the γ-ray and the normal of the absorber plane. (After Ericsson, T. et al.[106])

coordination. (For Fe^{3+} in tetrahedral coordination, the I.S. is considerably smaller.)

Malden, P.J. and Meads, R.E.[109] showed that iron may appear substitutionally for aluminium in kaolinite. They found I.S./Q.S. of 0.39(4)/0.50(5) mm/s in reasonable agreement with the values given above.

Jefferson, D.A. et al.[110], studied several kaolinites, of which two came from South Carolina. They found I.S./Q.S. of 0.36/0.52 mm/s and 0.35/0.55 mm/s respectively. In the first mentioned sample, there was approximately 10% of ferrous iron, but it is not quite clear whether it was in substitutional positions.

However, Malden and Meads also detected a small fraction of ferrous iron in a magnetically cleaned sample and the studies of that sample at different stages in the cleaning process actually indicated that the ferrous iron was within the kaolinite structure.

Montmorillonite:

A sample of montmorillonite (No. 11) is fitted with two Fe^{3+} doublets. For one of these, I.S. = 0.22 mm/s, I (intensity) = 0.47, which indicates that about 50% of iron is in tetrahedral coordination. For both doublets, Q.S. is small, approximately 0.3mm/s, which indicates small distortions for both the tetrahedral and the octahedral sites.

In Montmorillonite (No. 21), only ferric iron is found but in montmorillonite (No. 25) there is also approximately 8% of ferrous iron. For Fe^{3+} Q.S. is 0.57 mm/s for No. 21, and 0.63 mm/s for No. 25. The ferrous iron in No. 25 resulted in I.S./Q.S. of 1.32/2.39 mm/s.

Illites:

The analysis of the Mössbauer spectra of illites 35 and 36 indicate that they contain mostly ferric iron. In illite 35, the peak at approximately 2.5mm/s is asymmetrical, which reveals that Fe^{2+} appears both in cis and trans positions, although preferentially in the former. Illite 36 contains comparatively less Fe^{2+} and the asymmetry is much less pronounced. The ferrous iron seems to prefer the cis site.

The interpretation of the signals from ferric iron is complicated by impurities such as pyrite and limonite. These both give parameters which coincide with the Fe^{3+} doublet, I.S./Q.S. of 0.32/0.58 mm/s. However, studies of acid treated illite have made it plausible to assume that ferric iron occupies two different positions in the illite structure in these samples, and the I.S./Q.S. are about 0.32/0.58 mm/s for the cis position and 0.41/1.07 mm/s for the trans position.

Hectorite:

The sample of hectorite from California was quite deficient in iron (0.03% Fe_2O_3), resulting in a poor spectrum even with a large absorber areal density. For this reason, it was not possible to resolve the broad doublet, but the values, I.S./Q.S. of 0.36/0.77 mm/s, indicates that the iron is in the ferric state and in octahedral coordination.

4.3. ELECTRON SPIN RESONANCE SPECTROSCOPY:

Electron spin resonance (E.S.R.) spectra were recorded on a Japan Electron Optics Limited (JEOL) PE-1X type spectrometer operating in the X-band microwave region (approximately 9.5GHz) with a modulation frequency of 100 kHz. Monochromatic microwaves were obtained from a Klystron oscillator and fed to the sample cavity via wave-guides. Automatic frequency control allows the Klystron frequency to be locked to the resonant frequency at the sample cavity. The sample cavity is a high (Q) cylindrical reflection cavity operating in the TE_{011} mode [111]. Large magnetic pole pieces on either side of the cavity provide a uniform magnetic field that can be varied in a linear fashion by a scanning system connected to the power supply. The microwaves emerging from the sample cavity are detected by a semiconducting crystal detector which acts as a microwave rectifier, and the resulting absorption curve is plotted out graphically as the first derivative.

The samples consisted of finely powdered solids which were mounted inside the cavity in standard quartz tubes. Samples giving a low signal intensity were packed directly into the tube, whereas those with a high signal intensity could be placed in a standard glass melting point tube which was then inserted into the quartz tube. A sample height of approximately 4mm was required. It was necessary to use a pure quartz tube free from any traces of paramagnetic transition metals as these often give quite strong interfering e.s.r. signals. Glass melting point tubes do in fact give a

relatively strong signal at approximately 1600 GAUSS together with other minor signals, but these are usually swamped by the high intensity signals of the sample.

Sample spectra were compared with that of a standard sample run under identical operating conditions. The standard sample consists of a manganese (II) salt contained in a matrix of magnesium oxide. The e.s.r. parameters of this standard are known, and from these the parameters of the unknown sample spectrum can be calculated as is shown in section 4.3.1.

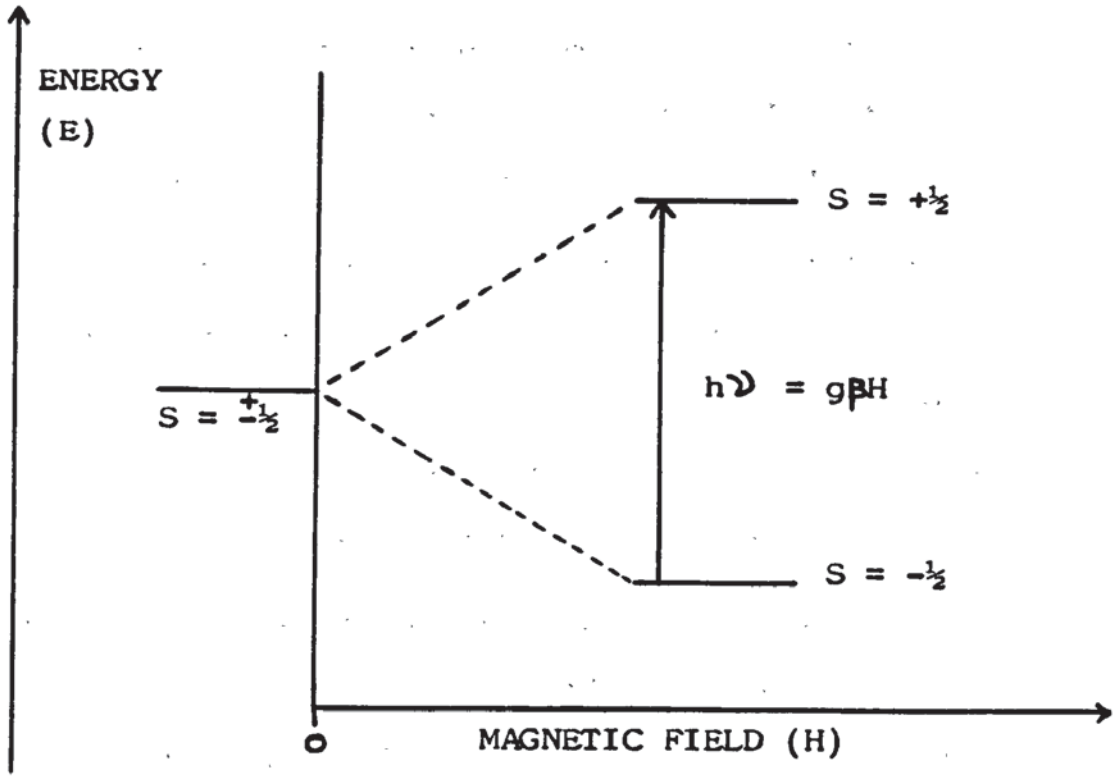

FIG. 16. Removal of electron spin degeneracy of a single electron by an applied magnetic field.

4.3.1. PHYSICAL DESCRIPTION:

The fundamental principle of E.S.R. spectroscopy is that an electron has a spin together with an associated magnetic moment. Electron spin resonance can thus be observed when molecules or ions that contain one or more unpaired electrons are placed in a magnetic field. When an electron is present in a molecule with an S ground state (i.e. L = 0), an applied magnetic field (H) will lift the spin degeneracy ($\pm\frac{1}{2}$) by causing the magnetic moment to align either parallel or antiparallel to the applied field, FIG. 16.

The energy difference between these levels is equal to $g\beta H$, where g is the gyromagnetic ratio, β is the Bohr magneton and H is the strength of the magnetic field. At thermal equilibrium the lower energy state is slightly more populated than the upper state, so when electromagnetic radiation of frequency (ν) is applied at the appropriate magnetic field strength (H), a net absorption occurs as upward absorptive transitions are more numerous than radiative downward transitions. The frequency of radiation required lies within the microwave region, and by sweeping the frequency at a static magnetic field strength it is possible to obtain absorption spectra. In practice the microwave frequency is fixed and the magnetic field is swept so that resonance is observed at a certain field strength. The equation relating frequency to the applied magnetic field is:

$$h\nu = g\beta H \text{ , (h = Plank's constant).}$$

From this equation it can be seen that under resonant conditions all terms are known except g, thus giving a value to the gyromagnetic ratio. This value is often termed the 'g-value' or 'g-factor', which for a free electron has the value g = 2.0023. The g-value of a free electron will vary according to the electronic environment it finds itself in, thus the detailed structural information available from e.s.r. is vast. With some anisotropic molecules and crystals it is sometimes possible to obtain up to three different observable g-values depending upon which axis the magnetic field is applied.

Electron spin resonance is also susceptible to interactions between the nuclear magnetic moment and the electronic spin state leading to hyperfine splitting of the already magnetically split energy levels. A good example of this is shown by Fremy's salt, potassium nitrosyl disulphate. Here the magnetically split energy levels of the unpaired electron of a ^{14}N nucleus are further split by the hyperfine interaction of its nuclear magnetic moment (I=1), FIG. 17. This leads to three possible orientations (i.e. 2I+1) of the ^{14}N nucleus in the presence of a magnetic field. The selection rules state that $\Delta M_s = \pm 1$ and that $\Delta M_I = 0$ so that three absorptions are observed.

One of the chief advantages of e.s.r. spectroscopy is its high sensitivity to extremely small concentrations of paramagnetic species. It is possible to detect spin concentrations as low as 10^{11} spins per litre. However, the technique is somewhat limited when studying ferromagnetic and antiferromagnetic systems since high paramagnetic spin

concentrations can lead to the interaction of paramagnetic centres and the loss of information.

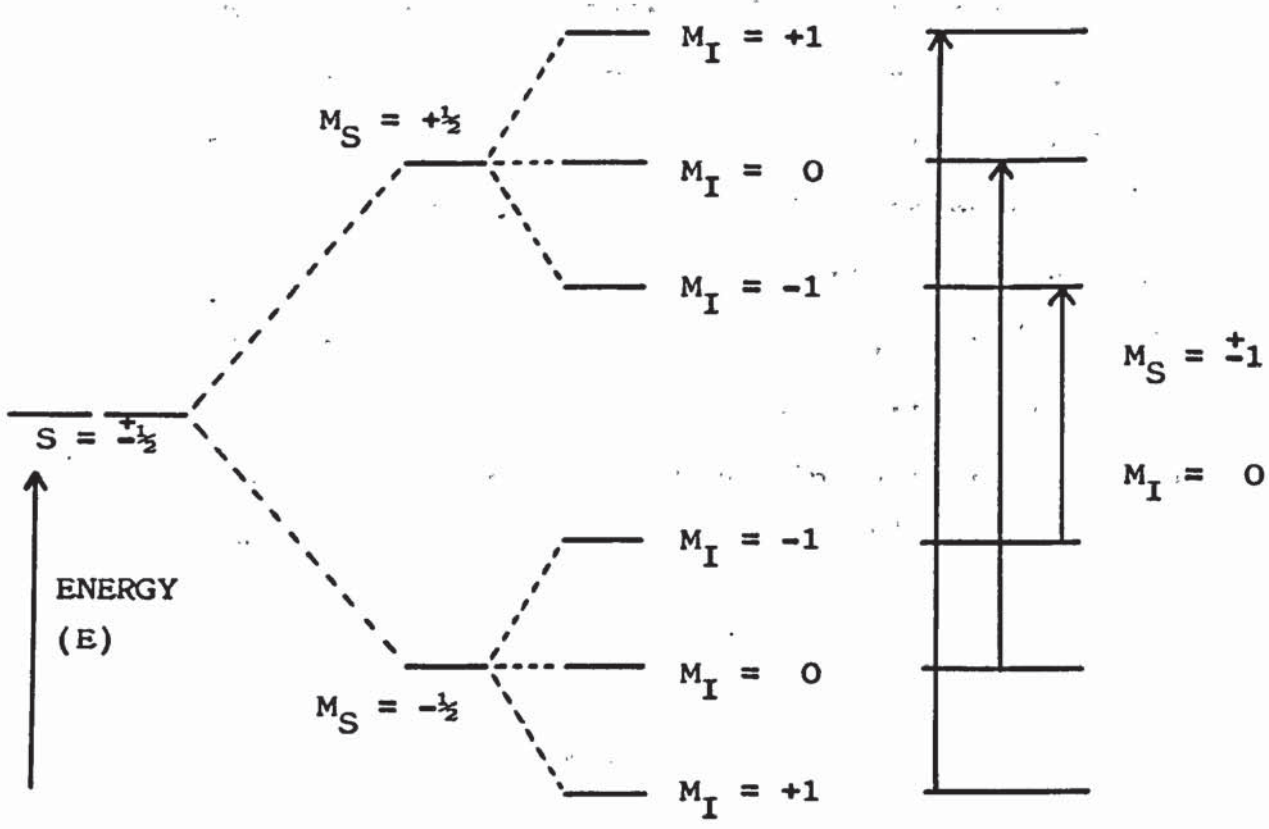

FIG. 17. Hyperfine splitting due to the ^{14}N nucleus of Fremy's salt.

Several general texts on e.s.r. spectroscopy have been produced, but most concentrate on the mathematical and theoretical aspects, such as that by Atherton, N.M.[112]. However, a short text by McLauchlan, K.A.[113] outlines the basic theory of magnetic resonance, and the recent text by Wertz, J.E. and Bolton, J.R.[111] outlines the elementary theory and practical applications of e.s.r..

The measurement of g-values:

The g-values of paramagnetic molecules or ions are calculated by comparison with the known parameters of a standard sample, namely a manganese (II) salt contained in a magnesium oxide matrix. ^{55}Mn (I=5/2) gives an e.s.r. spectrum of six sharp lines, the fourth line from the low magnetic field side being used as a field reference marker and the spacing between the third and fourth lines giving a field calibration. As is shown in FIG. 18., $g(Mn^{2+}) = 1.981$ and the separation between the third and fourth lines is 86.9 GAUSS, ΔH represents the distance in Gauss between the measured sample spectrum and the fourth (Mn^{2+}) line.

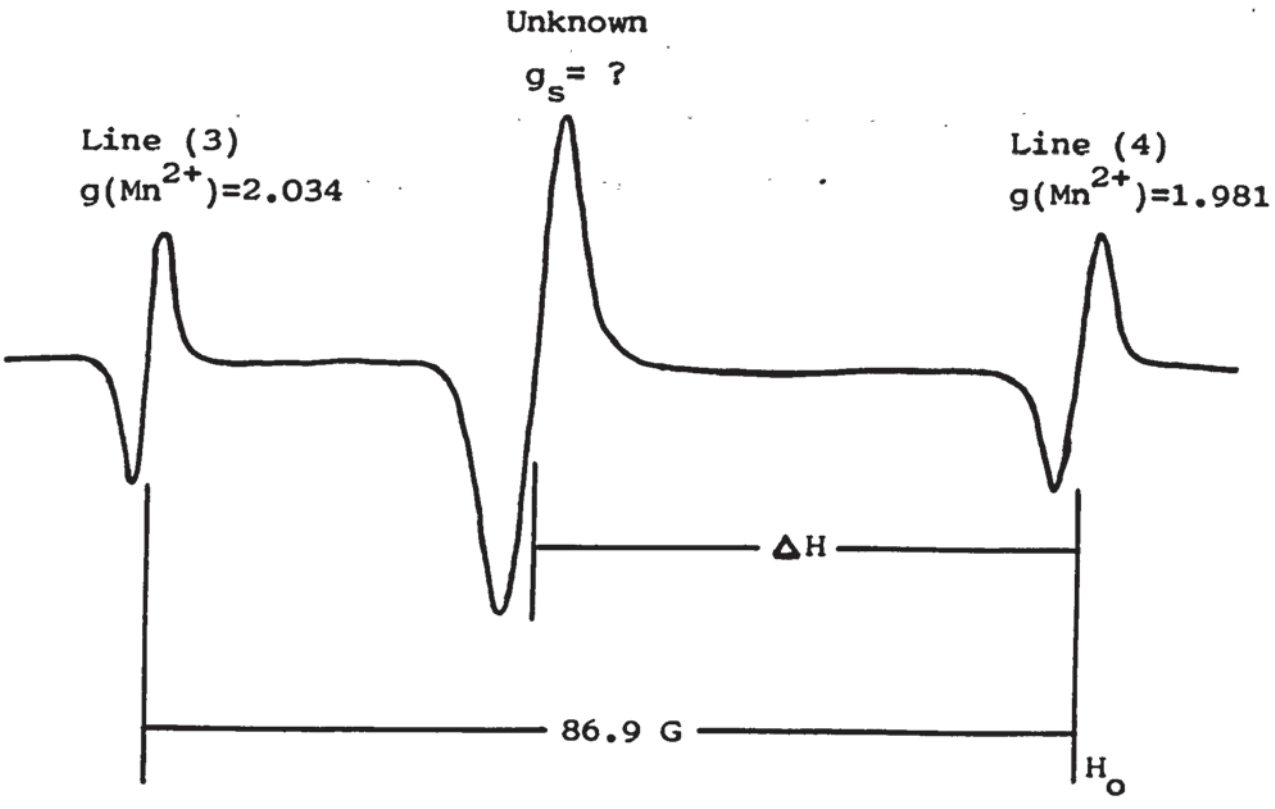

FIG. 18. Schematic representation of e.s.r. spectral calibration.

Now:

$$h\nu = g(Mn^{2+})\beta H_o \text{ , for standard.}$$

$$h\nu = g_s\beta(H_o - \Delta H) \text{ , for sample.}$$

Therefore:

$$g_s = \frac{h\nu/\beta}{h\nu/g(Mn^{2+})\beta - \Delta H} \text{ ,}$$

where:

g_s is the g-value of the unknown sample.

$g(Mn^{2+})$ is the g-value of standard (line 4).

h is Plank's constant.

ν is the microwave frequency.

β is the Bohr magneton.

ΔH is the difference in Gauss between the sample signal and line 4 of the standard.

4.3.2. E.S.R. ANALYSIS OF CLAY MINERALS:

The application of e.s.r. spectroscopy to coal technology was initially pursued in the early stages of this research project, mainly with the aim of detecting paramagnetic metal ions within the inorganic constituents of coal, but unfortunately the initial results were poor and together with the demise of the Solid Fuel Research Group at Aston the topic was pursued no further. The initial results gave spectra with extremely large spectral line widths, probably due to the presence of iron oxide species within the coal. However, several researchers have looked at the application of e.s.r. to coal with varying degrees of success[114-116]. The natural progression from this line of research was to the application of e.s.r. spectroscopy to clay minerals and their thermal decomposition products, mainly looking at the behaviour of iron, and then to the thermal behaviour of various other transition metal ions that had been exchanged onto natural hectorite.

Electron spin resonance spectroscopy has proven to be a powerful tool in studies of clay mineral chemistry. Structurally, e.s.r. is useful in the detection of isomorphous substitutions of paramagnetic elements, in the study of defect centres, and is invaluable in the elucidation of the orientations, dynamics and reactions of a variety of intercalated paramagnetic species, both organic and inorganic. The high ion exchange capacities of a variety of clay minerals and the ability of transition metal ions and complexes to exchange onto these clays has led to a vast wealth of

research papers on this subject. Several review articles on the application of e.s.r. spectroscopy to clay minerals have been produced[117-119], and fairly recent texts by Pinnavaia, T.J.[120] and McWhinnie, W.R.[121] are worth consulting. The e.s.r. study of transition metal ions is adequately covered in the treatise of Abragam, A. and Bleaney, B.[122]. No particular examples of the application of e.s.r. spectroscopy to clay minerals will be given here due to the vast amount of literature already available.

The various e.s.r. spectra presented in chapter 6, together with their respective g-values for the natural clay mineral samples, thermally treated clays and ion-exchanged clays, have been interpreted on the basis of the finger printing technique and on an empirical basis with reference to the literature data on clay minerals.

4.4. SILICON-29 MAS-NMR SPECTROSCOPY:

Solid state N.M.R. spectra of natural and thermally treated hectorite together with some selected samples of thermally treated ion-exchanged hectorite were run at the University of Durham on a BRUCKER CXP200 spectrometer operating at 4.7 tesla. Solid powder samples were used and spun at the 'magic angle' of 54.74°. Spectra were measured relative to tetra-methyl silane (T.M.S.).

4.4.1. PHYSICAL DESCRIPTION:

Nuclear magnetic resonance spectroscopy is very similar in some respects to e.s.r. spectroscopy. As for the electron, some nuclei possess the property of 'spin' and hence have magnetic moments which may give rise to a set of energy levels in an applied magnetic field. Nuclei with odd mass numbers possess spin, I, of n/2 where n is an integer, for example: ^{1}H (I=½), ^{19}F (I=½), ^{23}Na (I=3/2), ^{27}Al (I=5/2), ^{29}Si (I=½) and ^{31}P (I=½). Nuclei with even mass numbers but odd atomic charge numbers also possess spin but the values of I are integral, e.g. ^{2}D (I=1), ^{14}N (I=1). If both mass and charge numbers are even, then I=0 and the nucleus is non-magnetic, e.g. ^{12}C, ^{16}O. As with e.s.r. spectroscopy resonant transitions between the magnetically split nuclear energy levels can be brought about by the application of electromagnetic radiation of the appropriate frequency. With N.M.R. spectroscopy these resonant frequencies are located in the radiofrequency range. In the study of liquids by

N.M.R. spectroscopy, dipolar and quadrupolar interactions are averaged to zero by molecular tumbling, thus giving rise to sharp lines; but with solids this is not the case. However, theory fortunately tells us that this can also be achieved in the solid state by rapidly spinning the sample at 54.74° (54).

The theory and applications of Solid State N.M.R. are outlined in greater detail by Fyfe, C.A.(54) and in a general text by McWhinnie, W.R.(121).

4.4.2. SILICON-29 MAS-NMR ANALYSIS OF CLAY MINERALS:

Silicon-29 MAS-NMR is a powerful tool in the interpretation of the structure of silicates and aluminosilicates. The SiO_4 tetrahedron is one of the basic building blocks of silicates and aluminosilicates, and it is possible to observe separate signals for the ^{29}Si nucleus (4.7% natural abundance) depending on the environment given by the four atoms attached to the oxygens at the corners of the SiO_4 tetrahedron in the second coordination sphere. These different environments are termed Q^0 through to Q^4, where for example Q^2 represents an SiO_4 unit where two of the oxygens are bonded to a further silicon atom. Further to this it is possible to distinguish between silicon and aluminium atoms. For example, a $Q^4(Al)$ corresponding to the environment $SiO_4(Al,3Si)$ will give a different signal to a $Q^4(2Al)$ environment. However, warning should be given that some overlap of the chemical shift ranges of ^{29}Si environments in silicates and aluminosilicates may occur. These applications are reviewed by Fyfe, C.A.(54) and McWhinnie, W.R.(121), the latter having tabulated as a useful

review the typical ^{29}Si chemical shifts for different environments as observed in the literature. It is with reference to the literature data for ^{29}Si that the chemical shifts of the various N.M.R. spectra shown in chapter 6 have been interpreted.

Some work has been done on the application of ^{29}Si and ^{27}Al solid state N.M.R. to characterising minerals in coals. This has mainly been applied to low temperature ashes and fly ash, the aim being mainly in the interpretation of clay mineral types present in the coal and the aluminosilicate phases resulting after coal processing[123].

4.5. OTHER TECHNIQUES:

4.5.1. X-RAY DIFFRACTION:

Finely powdered samples were packed into standard aluminium X.R.D. slides and analysed on either a JEOL X-ray diffractometer employing Cu Kα radiation (30kV/30mA) with a typical scan speed of 2° 2θ/min, or a Phillips X-ray diffractometer employing Co Kα radiation (40kV/40mA) and an iron filter with a typical scan speed of 1° 2θ/min. The d-spacings of the various minerals present were calculated, from the 2θ values of the peaks on the diffractograms, using standard Cu Kα and Co Kα 2θ charts[73].

4.5.2. X-RAY FLUORESCENCE:

Major element analyses of the natural clay minerals under investigation were obtained by the fusion of the dry powdered specimens (15%) with a borax flux (85%) at 1100°C to form glass discs, which were subsequently analysed on a Phillips PW1400 sequential X-ray spectrometer using a Rhodium anode. With this machine five analysing crystals cover the wavelength range of the spectrometer, with the secondary radiation being detected using either a scintillation or gas flow detector. Amplified pulses are fed into a DEC computer system where comparison with a set of internationally accepted silicate standards gives the parts per million (ppm) of elements present.

4.5.3. ATOMIC ABSORPTION SPECTROPHOTOMETRY:

The elemental concentrations of various cations in solution were measured on a Perkin Elmer Model 460 atomic absorption spectrophotometer. Absorbance was electronically converted directly into ppm after initial calibration of the instrument using B.D.H. AA-standards.

4.5.4. DIFFUSE REFLECTANCE ULTRA VIOLET SPECTROSCOPY:

Several solid state U.V. spectra were obtained for powdered hectorite samples. The spectra were run over a wavelength range of 250 - 700nm on a Pye Unicam SP 800B U.V. spectrometer with an SP 890 diffuse reflectance attachment. Powdered magnesium oxide (MgO) does not absorb radiation in the wavelength range of 250 - 700nm and was therefore used as a reference.

4.5.5. SCANNING ELECTRON MICROSCOPY:

Several clay mineral samples were investigated using a Steroscan 5150 scanning electron microscope; vacuum $<3 \times 10^{-5}$ torr, EHT = 8 - 20kV. The instrumentation was equipped with an energy dispersive X-ray analyser (EDAX - System 500) providing an elemental analysis for elements with atomic numbers greater than ten. Software was available for converting these results from elemental composition into percent oxide composition. Samples consisted of a few grains of the dried clay mineral mounted on aluminium S.E.M. stubs using double sided adhesive.

This was then sprayed with a conductive solution (DCMC - Anti-static spray No. 865) to prevent charge build up on the sample during analysis.

4.5.6. THERMAL TREATMENT OF CLAY MINERALS:

Clay mineral samples were thermally treated in a Carbolite Muffle furnace under oxidising conditions. Powdered samples of up to a few grams were placed in glazed porcelain crucibles, heated to the required temperature (Max. = 1,300°C), and left to stand for 3 hrs.. The samples were then removed and placed in a desiccator to cool before recrushing. Transition metal ion-exchanged hectorite samples were initially heated in a platinum crucible, but it was found that diffusion of the metal into the crucible occurred at high temperatures, thus contaminating subsequent samples. Porcelain crucibles were hence used for all thermal treatments and disposed of after use. Samples were usually run in duplicate.

4.5.7. CATION EXCHANGE OF CLAY MINERALS:

Samples of hectorite were exchanged with various transition metal cations. Various solution concentrations of the metal in the chloride form were made up in distilled water, typically 0.1, 0.075, 0.05, 0.025 and 0.01 molar. 5g samples of hectorite were shaken with 50ml of solution for three days. At low metal ion concentrations it was sometimes required to double the volume of solution in order to stop gelation occurring. After shaking, the supernatant was

separated from the ion-exchanged clay using centrifugation (approx. 3,000 rpm). The pH of the supernatant was measured using a Corning model 12 pH meter before being filtered (Whatman 541 filter paper) and set aside for analysis by atomic absorption spectrophotometry. The clay was washed five times with 20ml aliquots of distilled water, the mixture being centrifuged and the supernatant discarded after each washing. The washed clay was then shaken for three days with a further 200ml of distilled water, centrifuged off, and dried at 120°C for 24 hrs. before crushing by hand with a pestle and mortar.

4.5.8. PROXIMATE AND ULTIMATE ANALYSIS OF COAL:

The proximate and ultimate analyses of coal are defined by ASTM D121 (American Standard Test Method) as follows:

Proximate analysis: "..... the determination by prescribed methods of moisture, volatile matter, fixed carbon (by difference) and ash."

Ultimate analysis: "..... the determination of carbon and hydrogen in the material, as found in the gaseous products of its complete combustion; the determination of sulphur, nitrogen and ash in the material as a whole and the estimation of oxygen by difference."

The majority of coal samples used in this study were subjected to these determinations. The various techniques of analysis are described fully by Montgomery, W.J.[124].

4.5.9. CHEMICALS AND REAGENTS:

All chemicals and reagents were of 'A.R. grade', or if not obtainable 'General purpose reagents' were used. Aqueous chemical solutions were made up with singularly distilled water.

5. EXPERIMENTAL RESULTS AND DISCUSSION FOR COAL.

5.1. PROXIMATE AND ULTIMATE ANALYSIS:

5.1.1. PROXIMATE ANALYSIS:

The proximate analysis results for the five coals investigated are given in TABLE 13.

TABLE 13. Proximate analysis results for coal samples.

PROXIMATE ANALYSIS.	BGC3	BGC7	LEÃOI	RIO	SANTA
	WT % OF COAL.				
MOISTURE.	5.0	-	7.1	9.3	1.5
ASH.	7.8	17.5	32.1	35.3	31.4
VOLATILE MATTER.	-	-	27.0	23.7	24.5
FIXED CARBON.	-	-	33.8	31.7	42.6

The moisture results are the average of three determinations, and the ash results are the average of five determinations.

5.1.2. ULTIMATE ANALYSIS:

The ultimate analysis results for the five coals investigated are given in TABLE 14. The carbon, hydrogen, nitrogen and sulphur results for each coal are the average determinations of five sub-samples, each sub-sample being analysed twice. The ash results are the same as for proximate

analysis, and all analysis percentages have been adjusted to their moisture free coal equivalents.

TABLE 14. Ultimate analysis results for coal samples.

ULTIMATE ANALYSIS.	BGC3	BGC7*	LEÃOI	RIO	SANTA
	WT % OF mf COAL.				
CARBON.	78.8	64.5	49.8	45.0	54.8
HYDROGEN.	4.5	4.2	3.7	3.2	3.5
NITROGEN.	1.1	0.6	0.2	0.4	0.7
SULPHUR.	3.1	2.1	2.6	2.0	2.8
ASH.	8.2	17.5	34.5	38.9	31.9
OXYGEN.	4.3	-	9.2	10.5	6.3

mf = moisture free.
* = figures for BGC7 are in WT % of coal.

The dry, ash free (daf) results for carbon, hydrogen, nitrogen, sulphur and oxygen (by difference) for the five coals are given in TABLE 15.

TABLE 15. Dry, ash free results for coal samples.

ELEMENT.	BGC3	BGC7*	LEÃOI	RIO	SANTA
	WT % OF daf COAL.				
CARBON.	85.8	78.2	76.0	73.6	80.5
HYDROGEN.	4.9	5.1	5.6	5.2	5.1
NITROGEN.	1.2	0.7	0.3	0.7	1.0
SULPHUR.	3.4	2.5	4.0	3.3	4.1
OXYGEN.	4.7	-	14.1	17.2	9.3

daf = dry, ash free.
* = figures for BGC7 are in WT % of ash free coal.

On comparison of these results with TABLE 2, Section 2.4, the coals may be assigned ranks:

BGC3	Bituminous coking coal.
BGC7	Subbituminous coal.
LEÃOI	Brown/subbituminous coal.
RIO	Brown/subbituminous coal.
SANTA	Subbituminous/bituminous coal.

The mineral matter contents of the coals, calculated by the Parr formula[125], are given below:

	WT % mf COAL.
BGC3	10.6
BGC7	20.1
LEÃOI	38.7
RIO	43.1
SANTA	36.0

5.2. X-RAY DIFFRACTION DATA:

5.2.1. COAL SAMPLES:

The X-ray diffraction traces of the five powdered coals revealed the presence of four mineral phases: quartz, illite, kaolinite and pyrite. Coal BGC3 showed no apparent trace for illite or pyrite, and coal BGC7 showed no apparent trace for pyrite. No attempt has been made to quantify the proportions of these minerals in each coal. Manvers coke, $2D_3$, a coal that had been coked at 500°C under 20 atmospheres of deuterium and spiked with 5% W/W pyrite (FeS_2), was also investigated and found to contain pyrrhotite ($Fe_{1-x}S$).

5.2.2. COAL ASH SAMPLES:

The X-ray diffraction traces of the ashed coals all showed strong signals for quartz and relatively moderate signals for hematite (Fe_2O_3). Apart from coal ash BGC3 all the ashed coals gave other relatively weak signals that could not clearly be assigned to any particular mineral phase. These signals appear to have characteristic d-spacings similar to those observed for illite, kaolinite and their dehydroxylation products.

5.3. MÖSSBAUER SPECTROSCOPY DATA:

5.3.1. COAL SAMPLES:

5.3.1.1. MARKHAM MAIN COAL, BGC3:

The Mössbauer spectrum of BGC3 consists of a single quadrupole doublet, FIG. 19. The parameters of this doublet are as follows:

Isomer shift	= 0.31 ($\pm$0.01) mm/s.
Quadrupole splitting	= 0.60 ($\pm$0.01) mm/s.
Half-Width	= 0.35 ($\pm$0.01) mm/s.

These parameters indicate the presence of pyrite, possibly with some contribution from Fe^{3+}(clay mineral), most probably illite.

FIG. 19. Mössbauer Spectrum of Markham Main Coal, BGC3.

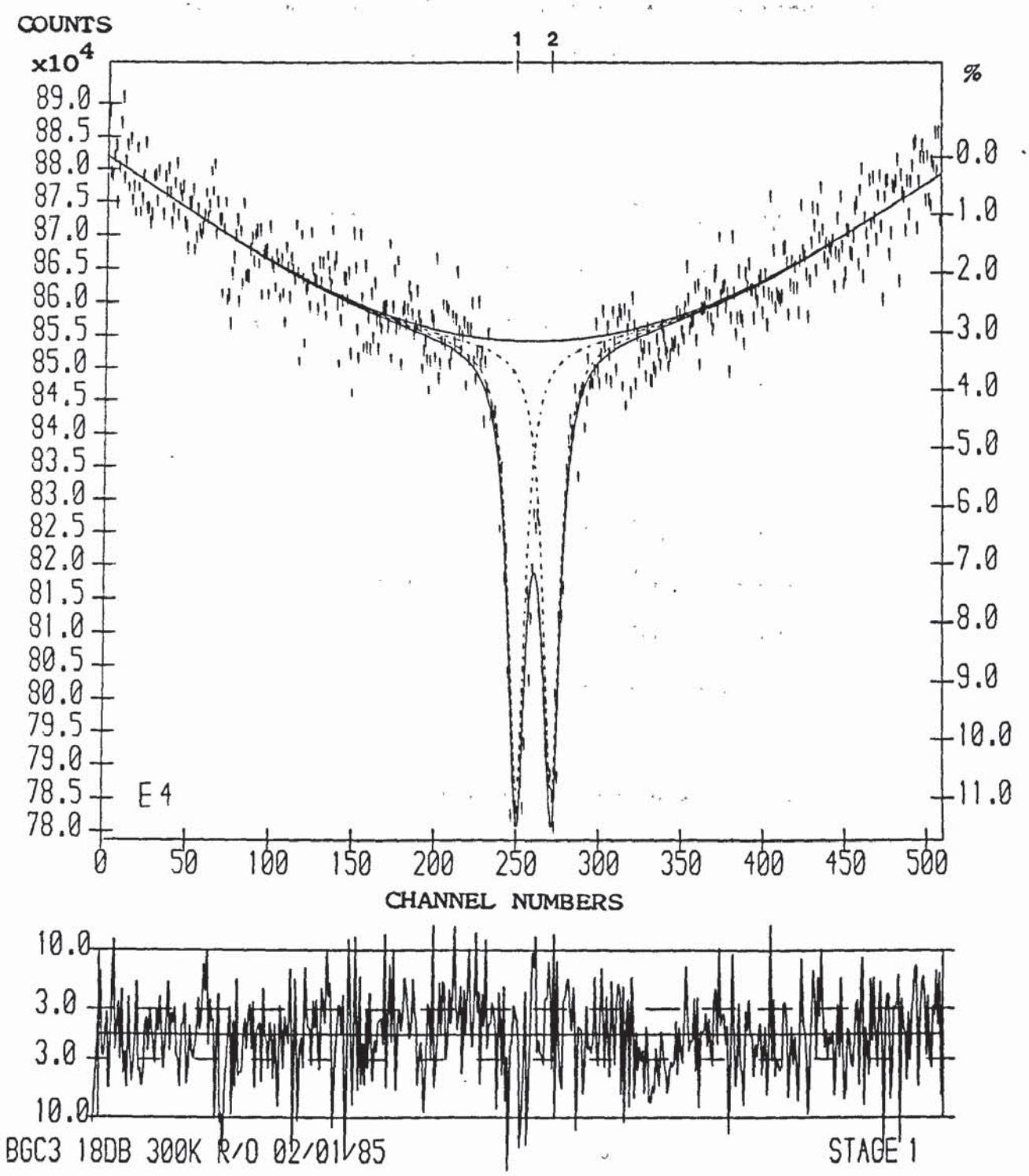

5.3.1.2. MARKHAM COAL, BGC7:

The Mössbauer spectrum of BGC7 consists of two quadrupole doublets, spectrum lines (1)+(3) and (2)+(4) respectively, FIG. 20. The parameters for these doublets are as follows:

Lines (1)+(3):

Isomer shift = 0.24 ($\pm$0.05) mm/s.

Quadrupole splitting = 0.66 ($\pm$0.10) mm/s.

Half-Width = 0.49 ($\pm$0.12) mm/s.

Relative intensity = 59062 ($\pm$10153).

Lines (2)+(4):

Isomer shift = 1.21 ($\pm$0.02) mm/s.

Quadrupole splitting = 1.66 ($\pm$0.04) mm/s.

Half-Width = 0.38 ($\pm$0.05) mm/s.

Relative intensity = 90417 ($\pm$11314).

These parameters indicate the presence of pyrite $\pm$ Fe^{3+} (clay mineral) probably illite, and siderite/ankerite respectively.

FIG. 20. Mössbauer Spectrum of Markham Coal, BGC7.

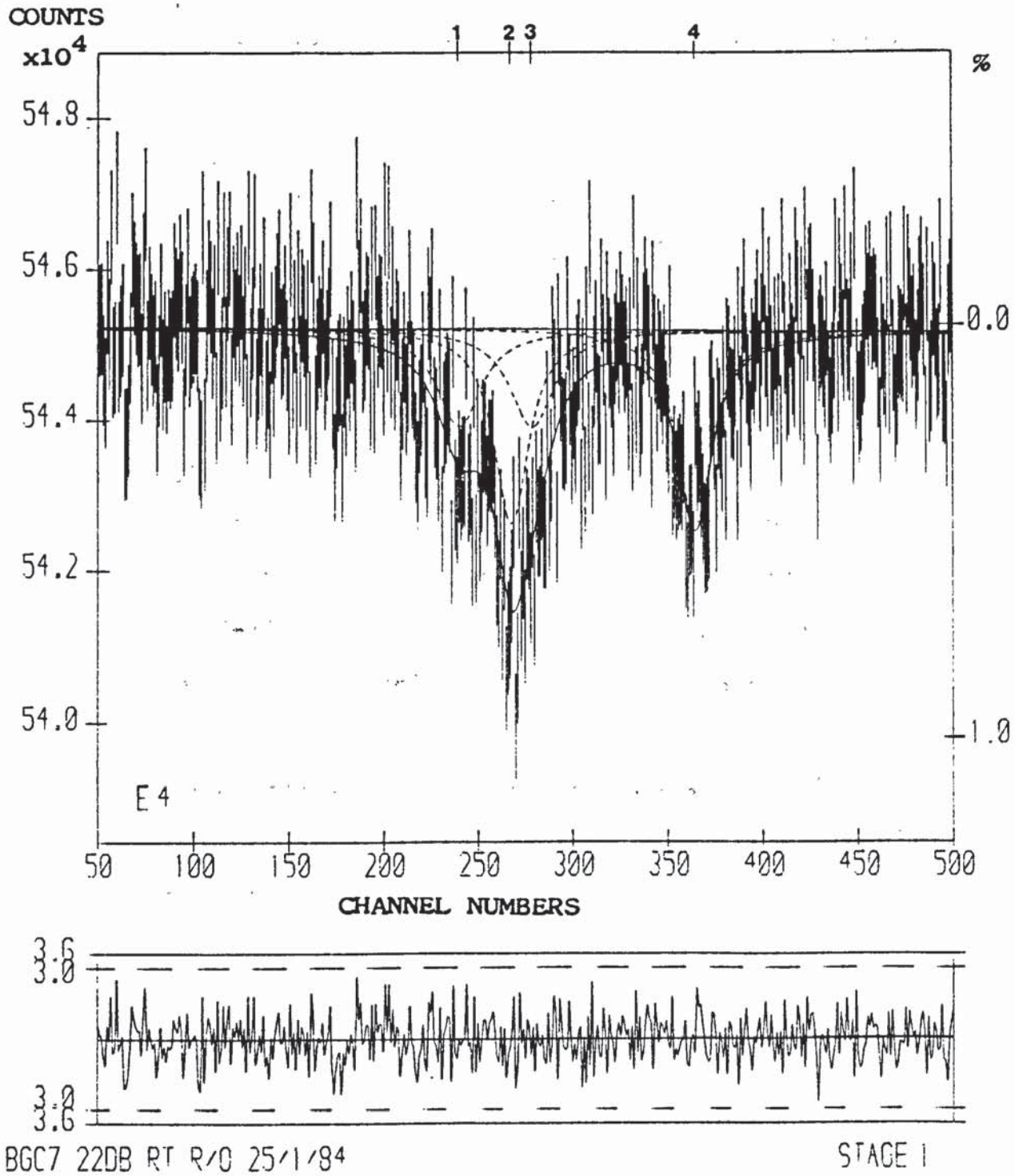

5.3.1.3. LEÃOI COAL:

The Mössbauer spectrum of Leãoi consists of two quadrupole doublets, spectrum lines (1)+(3) and (2)+(4) respectively, FIG. 21. The parameters for these doublets are as follows:

Lines (1)+(3):

Isomer shift	= 0.31 ($\pm$0.01) mm/s.
Quadrupole splitting	= 0.66 ($\pm$0.01) mm/s.
Half-Width	= 0.35 ($\pm$0.01) mm/s.
Relative intensity	= 332926 ($\pm$4911).

Lines (2)+(4):

Isomer shift	= 1.25 ($\pm$0.01) mm/s.
Quadrupole splitting	= 1.98 ($\pm$0.02) mm/s.
Half-Width	= 0.51 ($\pm$0.02) mm/s.
Relative intensity	= 219347 ($\pm$8616).

These parameters indicate the presence of Fe^{3+}(clay mineral) most probably illite $\pm$ pyrite, and illite (Fe^{2+})/ siderite respectively.

FIG. 21. Mössbauer Spectrum of Leãoi Coal.

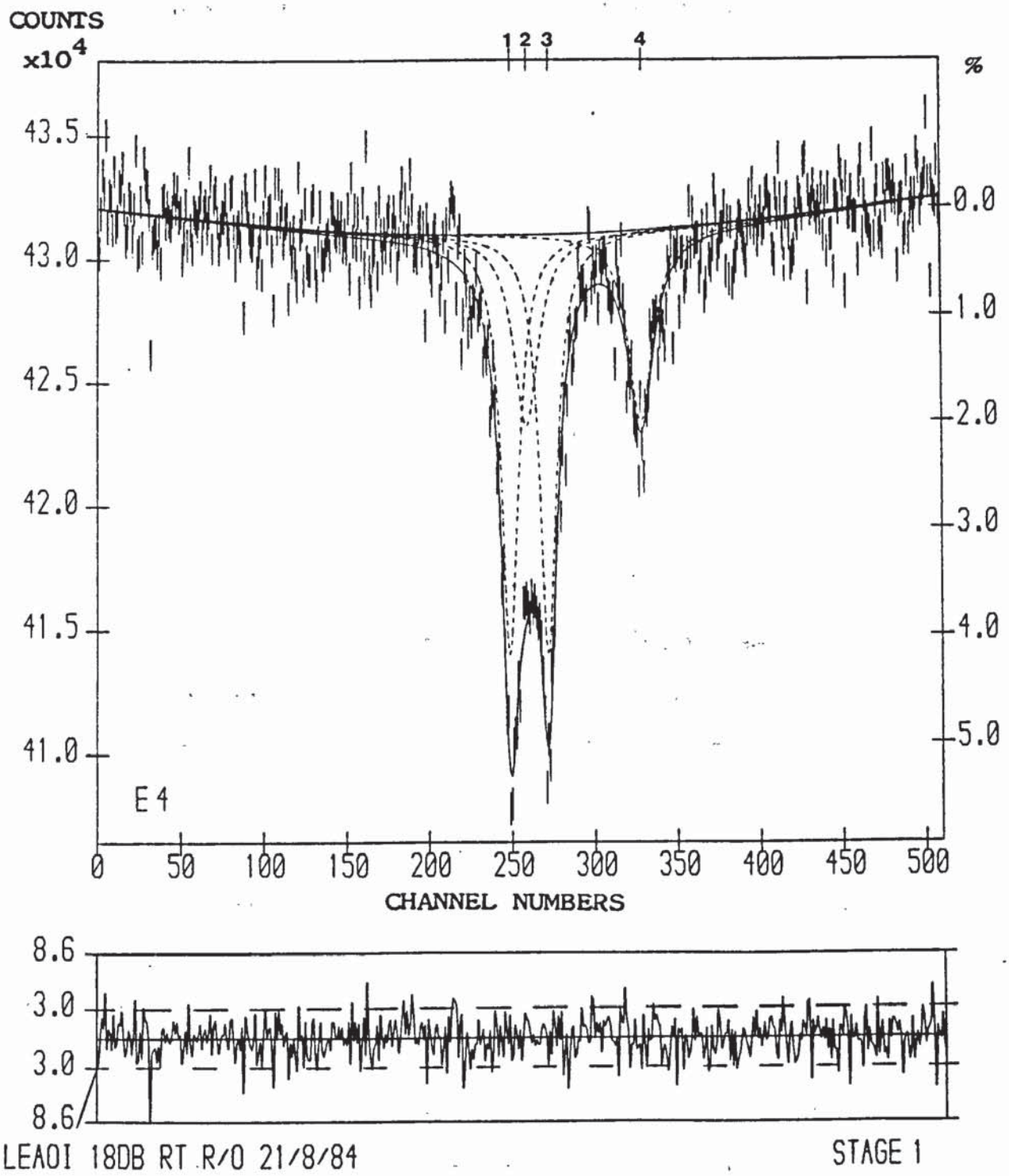

5.3.1.4. RIO GRANDE COAL:

The Mössbauer spectrum of Rio Grande consists of two quadrupole doublets, spectrum lines (1)+(4) and (2)+(3) respectively, FIG. 22. The parameters for these doublets are as follows:

Lines (1)+(4):

Isomer shift	= 1.28 ($\pm$0.04) mm/s.
Quadrupole splitting	= 3.25 ($\pm$0.08) mm/s.
Half-Width	= 0.28 ($\pm$0.09) mm/s.
Relative intensity	= 21401 ($\pm$5706).

Lines (2)+(3):

Isomer shift	= 0.32 ($\pm$0.01) mm/s.
Quadrupole splitting	= 0.63 ($\pm$0.02) mm/s.
Half-Width	= 0.39 ($\pm$0.02) mm/s.
Relative intensity	= 145805 ($\pm$5333).

These parameters indicate the presence of melanerite ($FeSO_4.7H_2O$)/rozenite ($FeSO_4.4H_2O$), and pyrite/Fe^{3+}(clay mineral) probably illite, respectively. The fitting and assignment of quadrupole doublet (1)+(4) is rather tentative due to the narrow half-width and relatively small peak height as compared to the base line scatter. χ^2 is not significantly decreased by the computer fitting of this doublet.

FIG. 22. Mössbauer Spectrum of Rio Grande Coal.

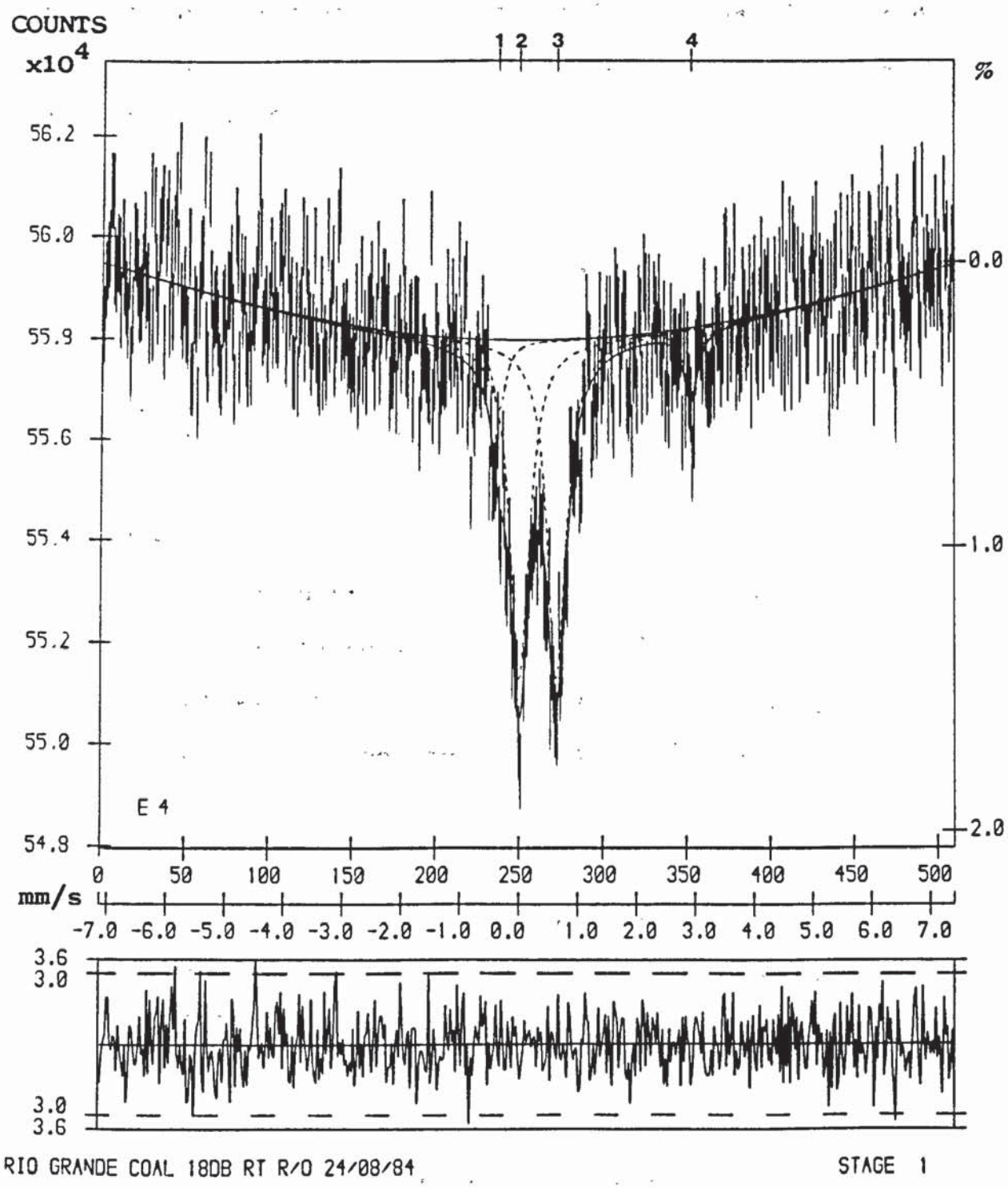

5.3.1.5. SANTA CATARINA SEAM COAL:

The Mössbauer spectrum of Santa Catarina Seam consists of three quadrupole doublets, spectrum lines (1)+(5), (3)+(4) and (2)+(6) respectively, FIG. 23. The parameters for these doublets are as follows:

Lines (1)+(5):

Isomer shift	= 0.38 ($\pm$0.05) mm/s.
Quadrupole splitting	= 1.15 ($\pm$0.10) mm/s.
Half-Width	= 0.40 ($\pm$0.10) mm/s.
Relative intensity	= 55360 ($\pm$17212).

Lines (3)+(4):

Isomer shift	= 0.31 ($\pm$0.01) mm/s.
Quadrupole splitting	= 0.58 ($\pm$0.01) mm/s.
Half-Width	= 0.30 ($\pm$0.01) mm/s.
Relative intensity	= 305031 ($\pm$14627).

Lines (2)+(6):

Isomer shift	= 1.25 ($\pm$0.14) mm/s.
Quadrupole splitting	= 2.50 ($\pm$0.28) mm/s.
Half-Width	= 0.54 ($\pm$0.21) mm/s.
Relative intensity	= 39519 ($\pm$12934).

These parameters indicate the presence of jarosite; pyrite/Fe^{3+}(clay mineral) probably illite; and illite (Fe^{2+}) respectively.

FIG. 23. Mössbauer Spectrum of Santa Catarina Seam Coal.

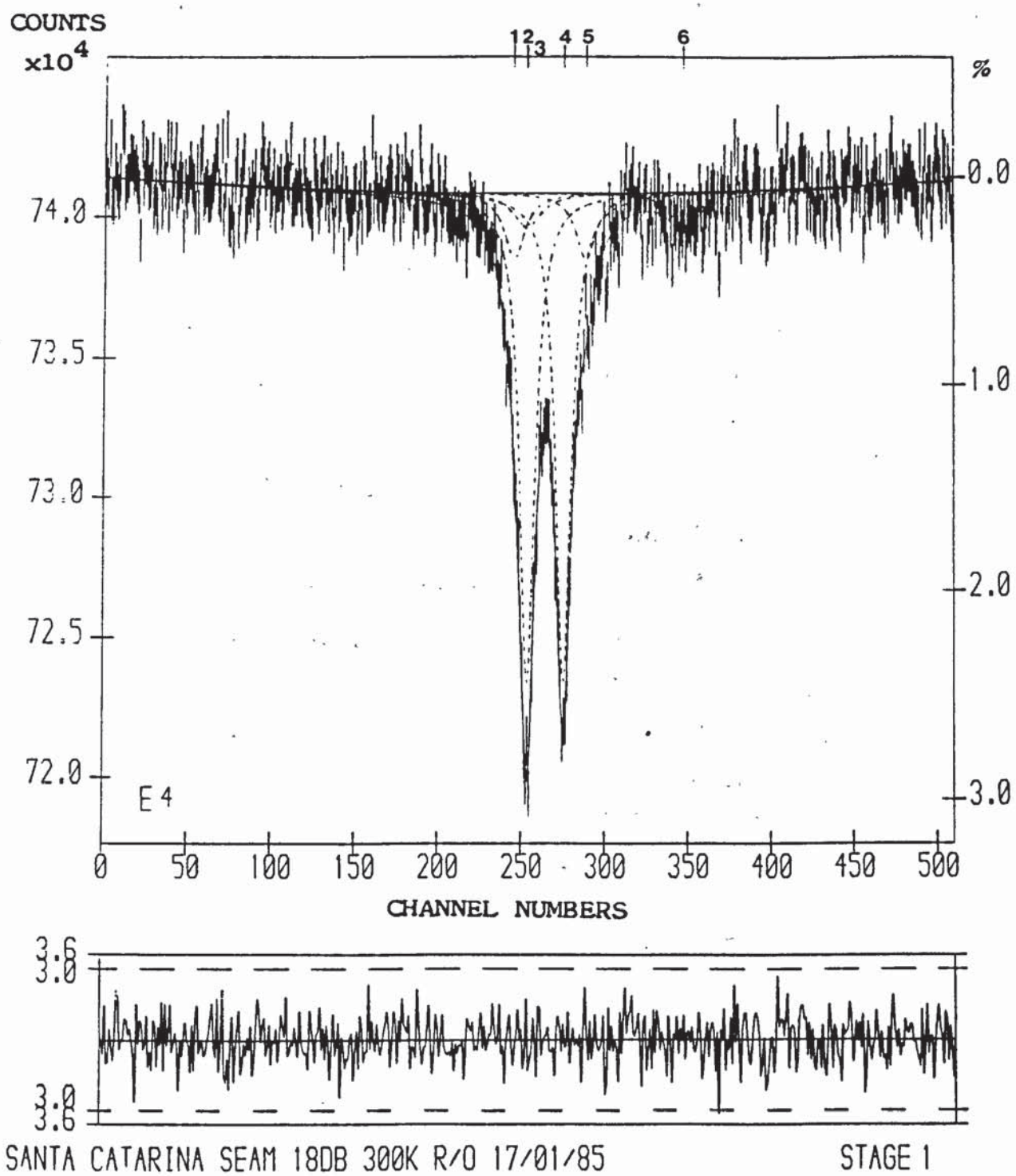

5.3.1.6. COKE, $2D_3$:

The Mössbauer spectrum of Coke $2D_3$ consists of a quadrupole doublet and a six peak magnetic hyperfine spectrum. The parameters are as follows:

Quadrupole Doublet:

Isomer shift	= 0.30 ($\pm$0.03) mm/s.
Quadrupole splitting	= 0.67 ($\pm$0.06) mm/s.
Half-Width	= 0.36 ($\pm$0.05) mm/s.
Relative intensity	= 70059 ($\pm$10258).

Magnetic Hyperfine Spectrum:

Isomer shift	= 0.66 ($\pm$0.02) mm/s.
Quadrupole splitting	= 0.01 ($\pm$0.02) mm/s.
Magnetic hyperfine field	= 273 ($\pm$1) kG.
	= 27.3 ($\pm$0.1) T.
Half-Widths	= 1.08 ($\pm$0.05) mm/s.
	0.79 ($\pm$0.04) mm/s.
	0.71 ($\pm$0.06) mm/s.
Relative intensities	= 431150 ($\pm$24489).
	301635 ($\pm$19355).
	232623 ($\pm$22210).

These parameters indicate the presence of pyrite and pyrrhotite respectively[5],[6].

5.3.2. COAL ASH SAMPLES:

5.3.2.1. COAL ASH BGC3:

The Mössbauer spectrum of coal ash BGC3 consists of a quadrupole doublet (lines (4)+(5)) and a six peak magnetic hyperfine spectrum (lines (1)-(3) and (6)-(8)), FIG. 24. The parameters are as follows:

Quadrupole Doublet:

Isomer shift	= 0.30 ($\pm$0.03) mm/s.
Quadrupole splitting	= 0.83 ($\pm$0.05) mm/s.
Half-Width	= 0.55 ($\pm$0.06) mm/s.
Relative intensity	= 85920 ($\pm$6693).

Magnetic Hyperfine Spectrum:

Isomer shift	= 0.38 ($\pm$0.03) mm/s.
Quadrupole splitting	= -0.17 ($\pm$0.03) mm/s.
Magnetic hyperfine field	= 539 ($\pm$2) kG.
	= 53.9 ($\pm$0.2) T.
Half-Widths	= 0.71 ($\pm$0.10) mm/s.
	0.50 ($\pm$0.08) mm/s.
	0.43 ($\pm$0.11) mm/s.
Relative intensities	= 96573 ($\pm$12942).
	54696 ($\pm$ 7482).
	36217 ($\pm$ 7946).

These parameters indicate the presence of an Fe^{3+} paramagnetic phase[6],[36], and hematite (α-Fe_2O_3) respectively.

FIG. 24. Mössbauer Spectrum of BGC3 Coal ash.

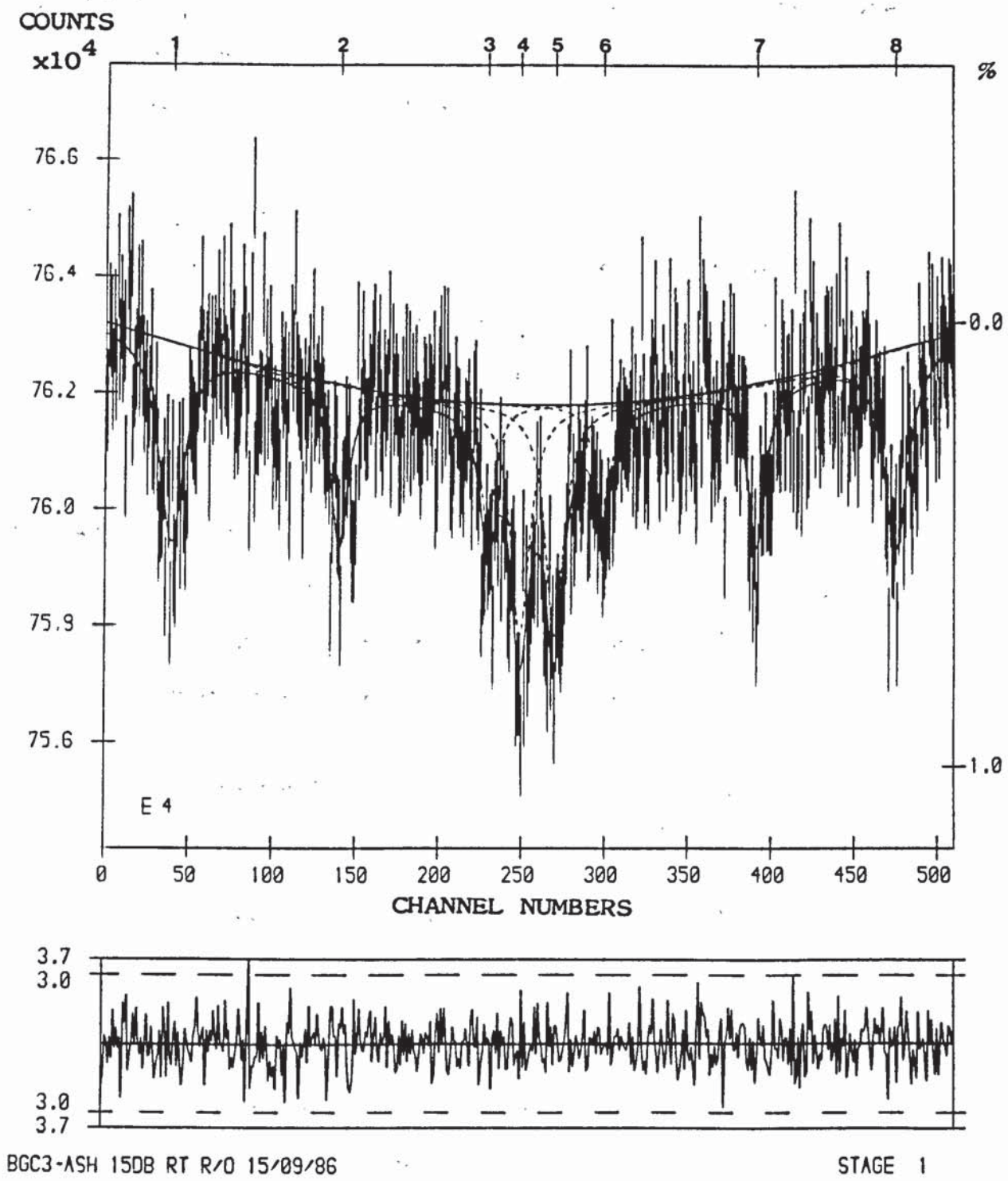

5.3.2.2. COAL ASH BGC7:

The Mössbauer spectrum of coal ash BGC7 consists of a quadrupole doublet (lines (4)+(5)) and a six peak magnetic hyperfine spectrum (lines (1)-(3) and (6)-(8)), FIG. 25. The parameters are as follows:

Quadrupole Doublet:

Isomer shift	= 0.38 ($\pm$0.07) mm/s.
Quadrupole splitting	= 1.25 ($\pm$0.14) mm/s.
Half-Width	= 0.72 ($\pm$0.16) mm/s.
Relative intensity	= 36171 ($\pm$6785).

Magnetic Hyperfine Spectrum:

Isomer shift	= 0.38 ($\pm$0.07) mm/s.
Quadrupole splitting	= -0.14 ($\pm$0.07) mm/s.
Magnetic hyperfine field	= 547 ($\pm$4) kG.
	= 54.7 ($\pm$0.4) T.
Half-Widths	= 1.19 ($\pm$0.26) mm/s.
	1.00 ($\pm$0.18) mm/s.
	0.40 ($\pm$0.10) mm/s.
Relative intensities	= 71488 ($\pm$19447).
	55268 ($\pm$ 9747).
	25626 ($\pm$ 5870).

These parameters indicate the presence of an Fe^{3+} paramagnetic phase, and hematite (α-Fe_2O_3) respectively. There is also the hint of another six peak magnetic hyperfine spectrum contained within the overall spectrum, as indicated by the upward arrows in FIG. 25, but it cannot be resolved

because of the very small percentage absorption. This component may correspond to the phase magnesioferrite ($Mg_xFe_{3-x}O_4$, $x<1$)[6],[36]. Its approximate parameters calculated from the spectrum are given below:

Isomer shift	= 0.38 mm/s.
Quadrupole splitting	= 0.00 mm/s.
Magnetic hyperfine field	= 464 kG.
	= 46.4 T.

FIG. 25. Mössbauer Spectrum of BGC7 Coal ash.

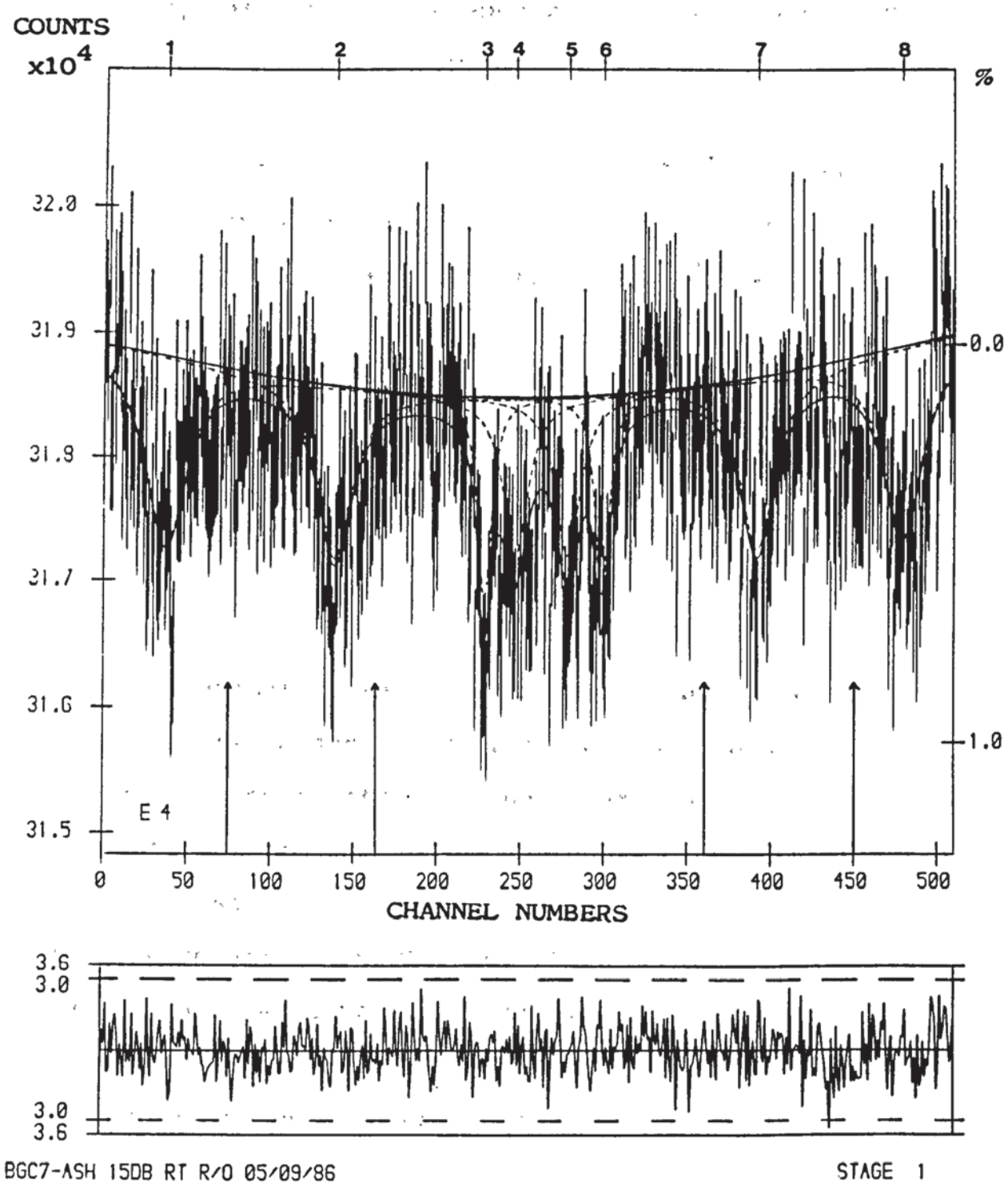

5.3.2.3. COAL ASH LEÃOI:

The Mössbauer spectrum of coal ash Leãoi consists of a six peak magnetic hyperfine spectrum (lines (1)-(6)), FIG. 26. The parameters are as follows:

Isomer shift	= 0.37 ($\pm$0.03) mm/s.
Quadrupole splitting	= -0.11 ($\pm$0.03) mm/s.
Magnetic hyperfine field	= 539 ($\pm$2) kG.
	= 53.9 ($\pm$0.2) T.
Half-Widths	= 0.73 ($\pm$0.10) mm/s.
	0.39 ($\pm$0.06) mm/s.
	0.74 ($\pm$0.20) mm/s.
Relative intensities	= 70130 ($\pm$9655).
	35717 ($\pm$4590).
	31466 ($\pm$8151).

These parameters indicate the presence of hematite. Lines (3) and (4) are rather broader, higher in intensity than expected, and the spectrum fit not that good; this would tend to indicate the presence of a quadrupole doublet with a small percentage absorption between lines (3) and (4), as indicated by the upward arrows in FIG. 26. This would be indicative of an Fe^{3+} paramagnetic phase. There may also be a slight hint within the spectrum of the presence of magnesioferrite, but this is by no means as clear as for coal ash BGC7.

FIG. 26. Mössbauer Spectrum of Leãoi Coal ash.

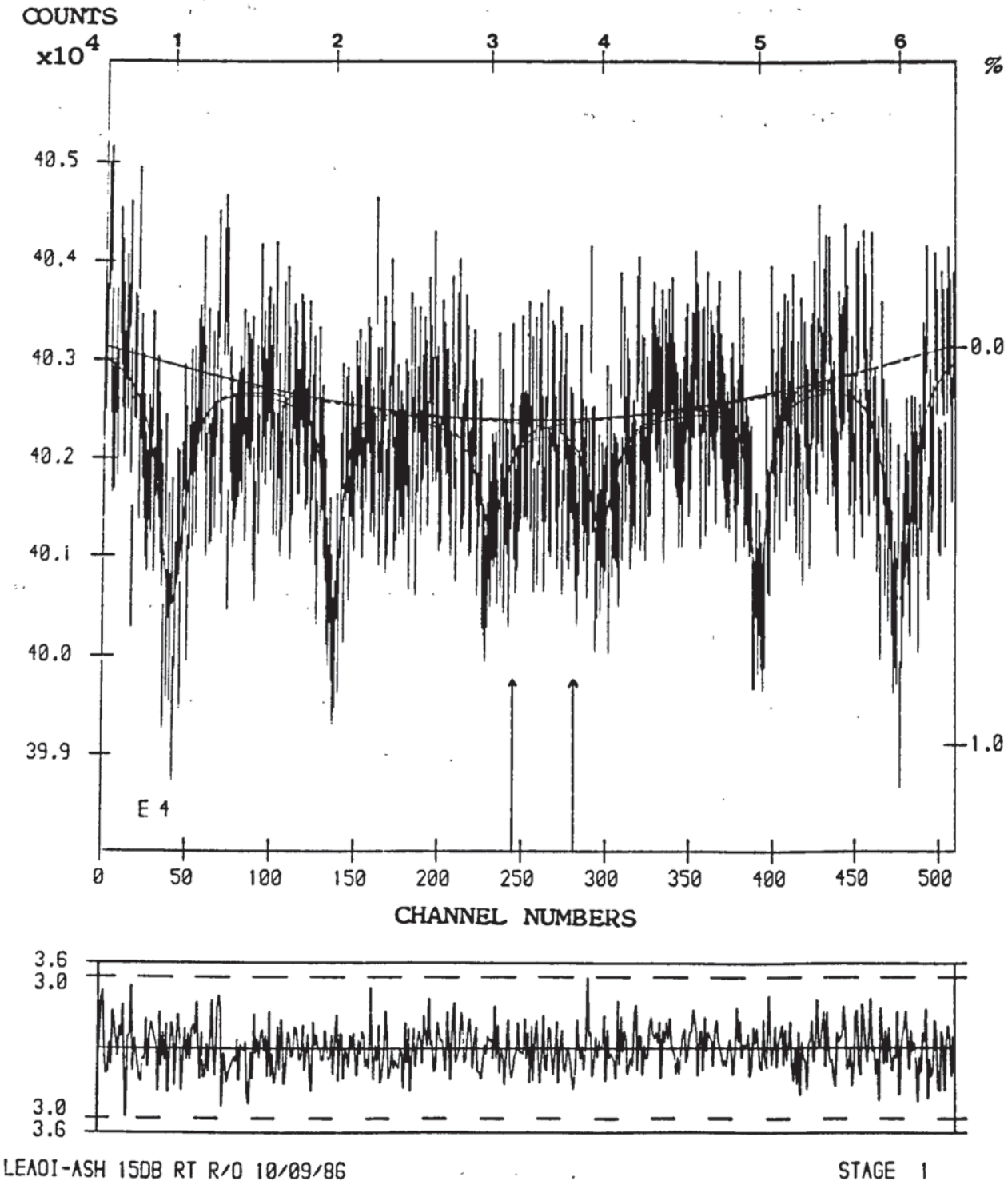

5.3.2.4. COAL ASH RIO GRANDE:

The Mössbauer spectrum of coal ash Rio Grande is rather poor in quality, but clearly consists of a very broad quadrupole doublet (lines (4)+(5)) and a six peak magnetic hyperfine spectrum (lines (1)-(3) and (6)-(8)), FIG. 27. The parameters are as follows:

Quadrupole Doublet:

Isomer shift	= 0.32 ($\pm$0.07) mm/s.
Quadrupole splitting	= 1.23 ($\pm$0.14) mm/s.
Half-Width	= 1.02 ($\pm$0.18) mm/s.
Relative intensity	= 84239 ($\pm$11655).

Magnetic Hyperfine Spectrum:

Isomer shift	= 0.33 ($\pm$0.03) mm/s.
Quadrupole splitting	= -0.09 ($\pm$0.03) mm/s.
Magnetic hyperfine field	= 540 ($\pm$2) kG.
	= 54.0 ($\pm$0.2) T.
Half-Widths	= 0.46 ($\pm$0.09) mm/s.
	0.20 ($\pm$0.06) mm/s.
	0.16 ($\pm$0.06) mm/s.
Relative intensities	= 41956 ($\pm$7299).
	14474 ($\pm$3528).
	11841 ($\pm$4246).

These parameters indicate the presence of an Fe^{3+} paramagnetic phase, and hematite (α-Fe_2O_3) respectively.

FIG. 27. Mössbauer Spectrum of Rio Grande Coal ash.

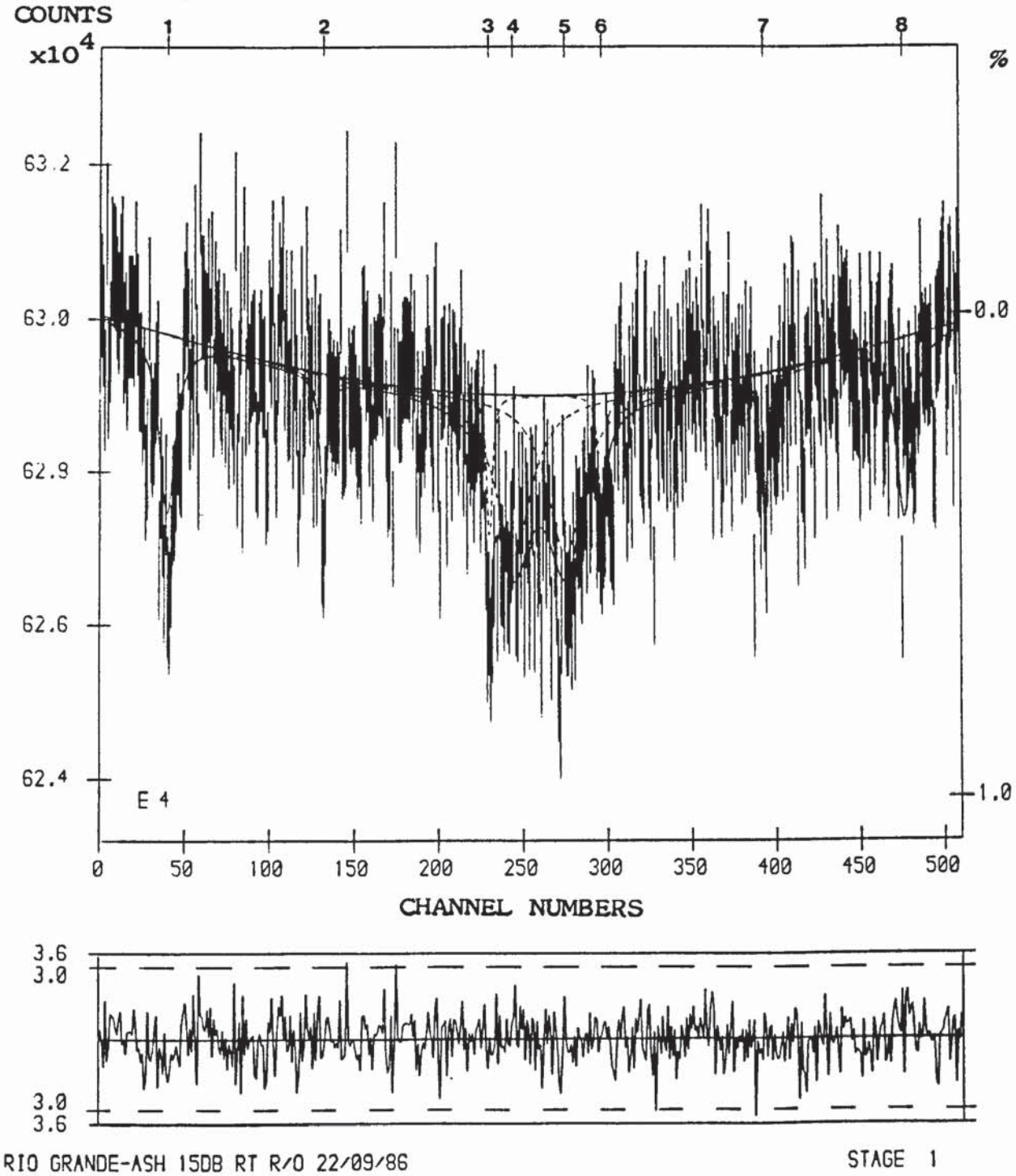

5.3.2.5. COAL ASH SANTA CATARINA SEAM:

The Mössbauer spectrum of coal ash Santa Catarina Seam consists of a six peak magnetic hyperfine spectrum (lines (1)-(6)), FIG. 28. The parameters are as follows:

Isomer shift	= 0.36 ($\pm$0.02) mm/s.
Quadrupole splitting	= -0.12 ($\pm$0.02) mm/s.
Magnetic hyperfine field	= 548 ($\pm$1) kG.
	= 54.8 ($\pm$0.1) T.
Half-Widths	= 0.67 ($\pm$0.05) mm/s.
	0.46 ($\pm$0.03) mm/s.
	0.52 ($\pm$0.05) mm/s.
Relative intensities	= 142873 ($\pm$9565).
	90252 ($\pm$5152).
	75887 ($\pm$6431).

These parameters indicate the presence of hematite. The spectrum quality is very good and the intensities of lines (1) and (2)/(5) and (6) exhibit the 3:2/2:3 ratio expected for hematite[88]. Lines (3) and (4) are slightly broader and higher in intensity than would be expected for the typical intensity ratio (3:2:1) of the magnetic hyperfine spectrum of hematite. Combined with the poor spectrum fit between these lines, this would indicate the presence of a small percentage absorption quadrupole doublet, probably due to the presence of an Fe^{3+} paramagnetic phase.

FIG. 28. Mössbauer Spectrum of Santa Catarina Seam Coal ash.

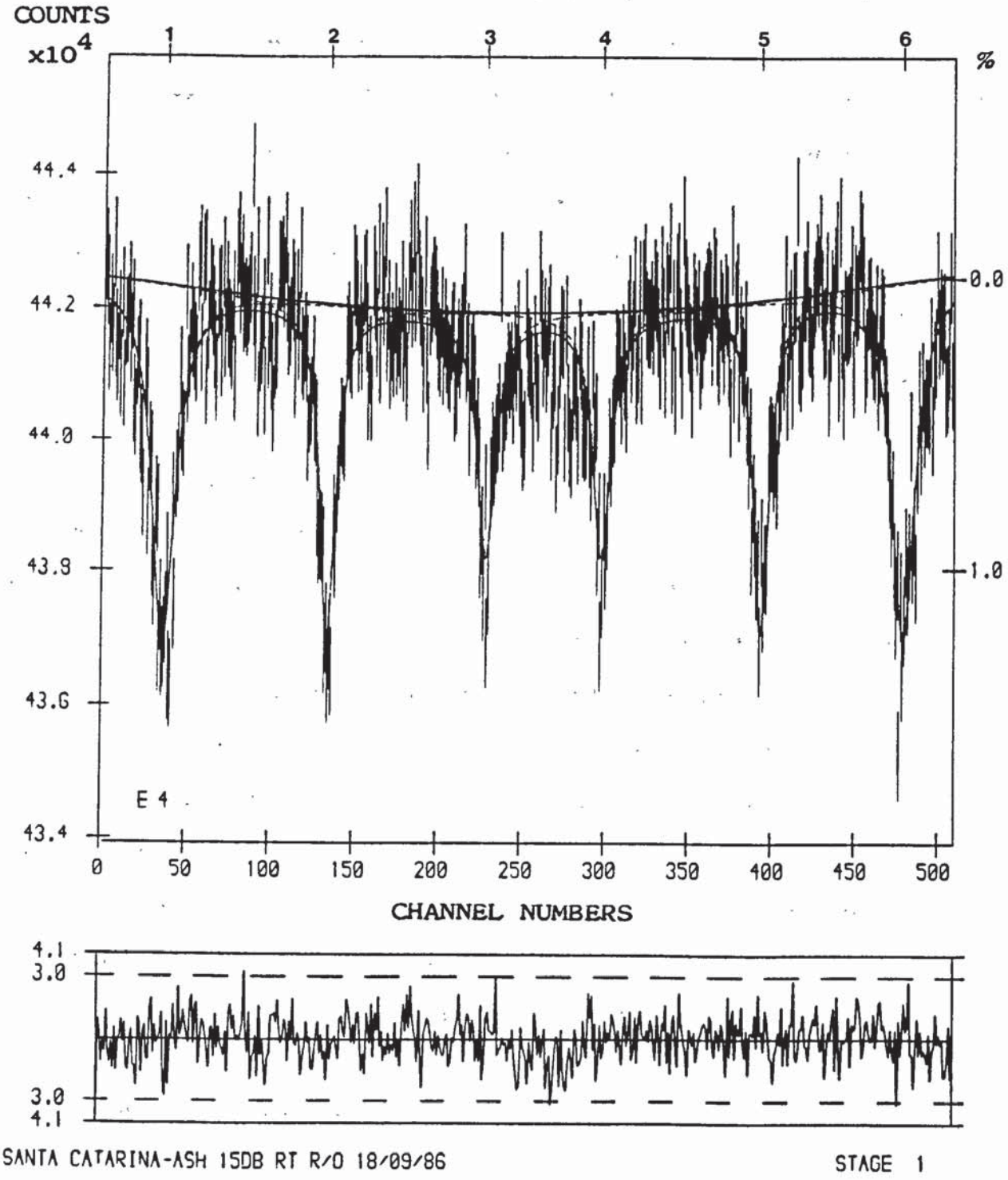

5.4. DISCUSSION:

The proximate and ultimate analysis results reveal that all the five coals are of approximately sub-bituminous coal rank, and contain between 10 - 40 WT% mineral matter on a moisture free basis. The mineral matter was found to consist of quartz, illite, kaolinite and pyrite; all of the coal samples containing these four minerals except for BGC3 (no apparent illite or pyrite) and BGC7 (no apparent pyrite). The ashed coal samples all showed the presence of quartz and hematite (Fe_2O_3), the latter probably resulting from the oxidation of pyrite (FeS_2) on ashing[6],[11]. These mineral phases were identified by X-ray diffraction, and it is somewhat surprising that pyrite was not observed in the coal samples BGC3 and BGC7, and only gave a very weak signal in the traces of the other three coals. This tends to contradict the relatively high sulphur content of all the coals (TABLE 15), and the presence of hematite in the ashed samples. The absence of a strong pyrite signal may be due to the pyrite being present in small quantities with respect to the other mineral phases, and to the dilution effect of the organic material if the pyrite is in the form of relatively large crystals or aggregates. Identification of these minerals within the natural coal samples could, however, be greatly improved by the use of Low Temperature Ashing[126].

The low temperature asher utilises an RF-electromagnetic field to induce discharge in a stream of oxygen, yielding an oxygen plasma. The organic matter of the coal is oxidised, without the need for an external heat source, and the actual

ashing temperature does not exceed 150°C. Most of the mineral phases normally found within coal show less than 1% weight change during ashing and exhibit no discernible structural changes[125]. Mössbauer spectroscopic analysis indicates some conversion of pyrite into ferric species[97], and partial oxidation of Fe^{2+} in clay minerals to Fe^{3+} [6]. Nevertheless, the mineral matter of coal remains relatively unchanged, yielding an ash that can be directly analysed by X-ray diffraction and is in an ideal form for Mössbauer spectroscopy, Scanning Electron Microscopy and Electron Spin Resonance work.

The X-ray diffraction traces of the coal ash samples also gave relatively weak signals with d-spacings similar to those observed for illite, kaolinite and their dehydroxylation products. These unassigned signals are probably due to the relic silicate structures remaining after the dehydroxylation of the clay minerals present within the coal. The dehydroxylation of clay minerals generally occurs at 550-650°C and the remaining structure does not collapse until 850-950°C [74],[127]. Since the coal samples were ashed at 700-750°C, this would explain why the unassigned signals observed in the traces had d-spacings similar to those of the parent clay minerals.

Mössbauer spectroscopy is an extremely powerful technique for characterising iron-bearing mineral phases, but unfortunately when observing low mineral and iron-content coals, it becomes all but impossible to fit any more than the most prominent peaks to the spectrum. This can be seen from the various spectra shown in the experimental section, 5.3.1. It is even possible to assign more than one mineral to

some of the doublets, their low relative intensity and/or the possibility of unresolvable overlapping doublets giving rise to relatively broad peaks. This results in an inherent uncertainty in the precise spectral positions of the peaks. Leãoi coal, for example, gave a Mössbauer spectrum consisting of two quadrupole doublets, FIG. 21. Spectral lines (2)+(4) have a Half-Width (Full peak width at half maximum height) of 0.51 mm/s as compared to that of the higher relative intensity doublet (lines (1)+(3)) of 0.35 mm/s. The broadness of lines (2)+(4) indicated the possibility of an unresolved overlapping doublet, leading to the dual assignment of this doublet, TABLE 16. Low temperature ashing would go a long way in solving this problem by primarily concentrating up the mineral phases present in the coal samples. This can be partly seen by the improvement of the spectra quality for the coal ash samples, section 5.3.2. The iron-bearing mineral phases assigned to the five coal samples from their Mössbauer spectra, together with the 'iron-free' phases identified by X-ray diffraction, are given in TABLE 16.

On comparison with the X-ray diffraction results, TABLE 16 clearly shows the usefulness of Mössbauer spectroscopy in identifying iron-bearing mineral phases that would otherwise have been missed by X-ray diffraction, particularly if the coal samples have not been subjected to low temperature ashing before analysis. Evidence for the presence of pyrite in all of the coal samples, in particular for BGC3 and BGC7, is further provided by its observed presence within their Mössbauer spectra. Indirect evidence is again provided by the presence of hematite in the Mössbauer spectra of all the ashed

TABLE 16. Mineral phases present within the coal samples.

MINERAL.	BGC3	BGC7	LEÃOI	RIO	SANTA
PYRITE.	X	X	X	X	X
ILLITE (Fe^{3+}).	X	X	X	X	X
ILLITE (Fe^{2+}).			X		X
SIDERITE.		X	X		
ANKERITE.		X			
MELANERITE.				X	
ROZENITE.				X	
JAROSITE.					X
KAOLINITE.*	X	X	X	X	X
QUARTZ.*	X	X	X	X	X

* = 'Iron-free' mineral phases as identified by x-ray diffraction.

} = Joint assignment to a single quadrupole doublet.

coals. Likewise, the apparent absence of illite in coal BGC3, as indicated by its X-ray diffraction data, is contradicted and disproved. The Mössbauer spectrum of coal BGC3 indicates the possible presence of a clay mineral (Fe^{3+}, illite), which is finally proved by the presence of signals within the X-ray diffraction trace and Mössbauer spectrum of the coal ash indicative of the dehydroxylation products of an iron-bearing clay mineral (illite).

The Mössbauer spectra of the five coal ashes clearly show the presence of hematite (α-Fe_2O_3) and an Fe^{3+} paramagnetic phase. Coal ash BGC7, and possibly Leãoi, also show the presence of magnesioferrite ($Mg_xFe_{3-x}O_4$, $x<1$). Hematite would have mainly been produced from the oxidation of pyrite (FeS_2), although part could have arisen from the decomposition and oxidation of siderite[6],[36]. As siderite was not observed in any of the X-ray diffraction traces of the natural coal samples, and was only found to be present at relatively low percentage absorption in the Mössbauer spectra of BGC7 and Leãoi, it was concluded that most of the hematite arose from the oxidation of pyrite. Magnesioferrite arises from the decomposition of ankerite and magnesium rich siderite[6],[36], which explains its presence in the Mössbauer spectrum of coal ash BGC7. The Mössbauer spectrum of the natural coal (BGC7) showed the presence of siderite and/or ankerite, whereas that of Leãoi gave a spectrum more typical of siderite. This could explain why Leãoi only gave a very weak Mössbauer signal for magnesioferrite. The Fe^{3+} paramagnetic phase observed in all the Mössbauer spectra of the ashed coals probably represents Fe^{3+} contained within the relic silicate structure resulting

from the dehydroxylation of the clay minerals. Huggins, F.E. and Huffman, G.P.[6] found that the Fe^{3+} paramagnetic phase consists of at least two components; one exhibiting a relatively large quadrupole splitting ($\Delta \simeq 1.50$ mm/s) with broad spectral peaks (Half-Width $\simeq 0.90$ mm/s), probably corresponding to Fe^{3+} in a glass, and the other having a smaller quadrupole splitting ($\Delta \simeq 0.85$ mm/s) with spectrum peak widths typical of Fe^{3+} crystalline phases (Half-Width $\simeq$ 0.60 mm/s). It was not possible to resolve these two components within the Mössbauer spectra presented here, but the fitted quadrupole doublets of coal ashes BGC7 and Rio Grande gave parameters typical of a combination of the two unresolved components, section 5.3.2. The transformations of iron-bearing minerals during ashing (ASTM D3174) can be summarised as follows[6]:

Pyrite, FeS_2 ⟶ α-Fe_2O_3.

Siderite, $FeCO_3$ ⟶ α-Fe_2O_3.

Ankerite, $(Ca,Fe,Mg)CO_3$ ⟶ $Mg_xFe_{3-x}O_4$, and other phases.

Fe^{2+}/Fe^{3+}, clay minerals ⟶ Fe^{3+} phases (silicates, glass, oxides).

The Mössbauer spectrum of the coke sample ($2D_3$) indicates the presence of pyrrhotite ($Fe_{1-x}S$) together with pyrite (FeS_2), whereas the X-ray diffraction data only indicate the presence of pyrrhotite. This could be due to the fact that only small quantities of pyrite remain after coking, or that the pyrrhotite particles contain a central core of unreacted

pyrite. As indicated in the introduction, pyrite plays an important catalytic role in coal processing, and the addition of pyrite to a coal before coking improves the yield of coking products and produces pyrrhotite as a result. In coking and liquefaction processes under hydrogen, H_2S is believed to be formed at the surface of pyrite particles, thus producing pyrrhotite[104]. Sulphur then diffuses to the particle surface from the central core of pyrite until the particle is of all the same composition. A high partial pressure of H_2S will in fact turn the pyrrhotite ($Fe_{1-x}S$) back into pyrite (FeS_2), and a very low partial pressure will result in troilite (FeS). A study of cokes by Huggins, F.E. and Huffman, G.P.[6] using Mössbauer spectroscopy, detected the presence of both troilite and pyrrhotite in coke residues. Once H_2S is formed it is free to migrate through the coke.

There is some debate as to whether H_2S or pyrrhotite/pyrite is the catalysing agent during processing[21],[128], but it is most probable that both pyrrhotite and H_2S are beneficial to coal conversion. A review article by Rebick, C.[129], establishes that H_2S is an affective hydrogen transfer catalyst for reactions of the type:

$$R\cdot + R'H \longrightarrow RH + R'\cdot$$

The catalysis occurs by replacing this slow hydrogen transfer step with two faster steps:

$$R\cdot + H_2S \longrightarrow RH + HS\cdot$$

$$HS\cdot + R'H \longrightarrow H_2S + R'\cdot$$

A similar mechanism by Ogawa, T. et al.[128], but also employing pyrrhotite, has been put forward on his studies of the hydrocracking of diphenylmethane. It is believed that the sulphur atom of a H_2S molecule 'sits-over' an iron-deficient site of pyrrhotite weakening the SH bonds during the reformation of pyrite; the loosely bonded hydrogen atoms are then available for transfer onto organic radicals and unsaturated species. The transfer of the two hydrogens may not be simultaneous and the second may not even occur in some circumstances, the SH thus formed possibly being reduced directly to H_2S.

It was hoped to further investigate these mineral phase changes, and their catalytic properties during coal processing, by spiking a low mineral matter or acid demineralised coal with various naturally occuring iron-bearing mineral phases. This work would have been concentrated around the effects caused by the clay minerals illite and montmorillonite upon the coking of coal. The organic phases thus produced would have been analysed for any significant changes in their composition and quantity caused by the addition of these mineral phases. Changes within the mineral phases themselves would have been investigated by X-ray diffraction and Mössbauer spectroscopy. The use of oxygen plasma equipment for the production of low temperature ashes was also being looked into. Unfortunately, this was brought to a disappointing conclusion by the closure of the Solid Fuel Research Group at Aston.

6. EXPERIMENTAL RESULTS AND DISCUSSIONS FOR CLAY MINERALS.

It is intended within this chapter to elucidate the thermochemistry of illite, montmorillonite and hectorite between 20°C and 1300°C. Techniques such as ^{57}Fe Mössbauer spectroscopy, electron spin resonance spectroscopy, X-ray diffraction, thermo-gravimetric analysis and, to a lesser extent ^{29}Si MAS-NMR spectroscopy, have been used analytically on the basis of the finger printing technique to achieve this aim.

6.1. METHODOLOGY:

6.1.1. ^{57}Fe MÖSSBAUER SPECTROSCOPY:

The basic theory and experimental procedures of ^{57}Fe Mössbauer spectroscopy with respect to clay minerals are outlined in chapter 4. However, it is intended here to elaborate upon the general fitting procedures and interpretation of the various spectra obtained.

The raw spectral data for a sample is obtained in numerical form with respect to signal intensity per channel number. These data points can be plotted out and roughly fitted with a spectral line by identifying the main absorption peaks in the raw data and specifying their approximate position, intensity and half-width within the fitting program[87]. Such an initial assignment and spectral plot is shown in FIG. 29, for natural illite. The computer program will attempt to fit the spectrum and given parameters to Lorentzians by adjusting

FIG. 29. Initial assignment of absorption lines and spectral plot to the Mössbauer data for natural illite.

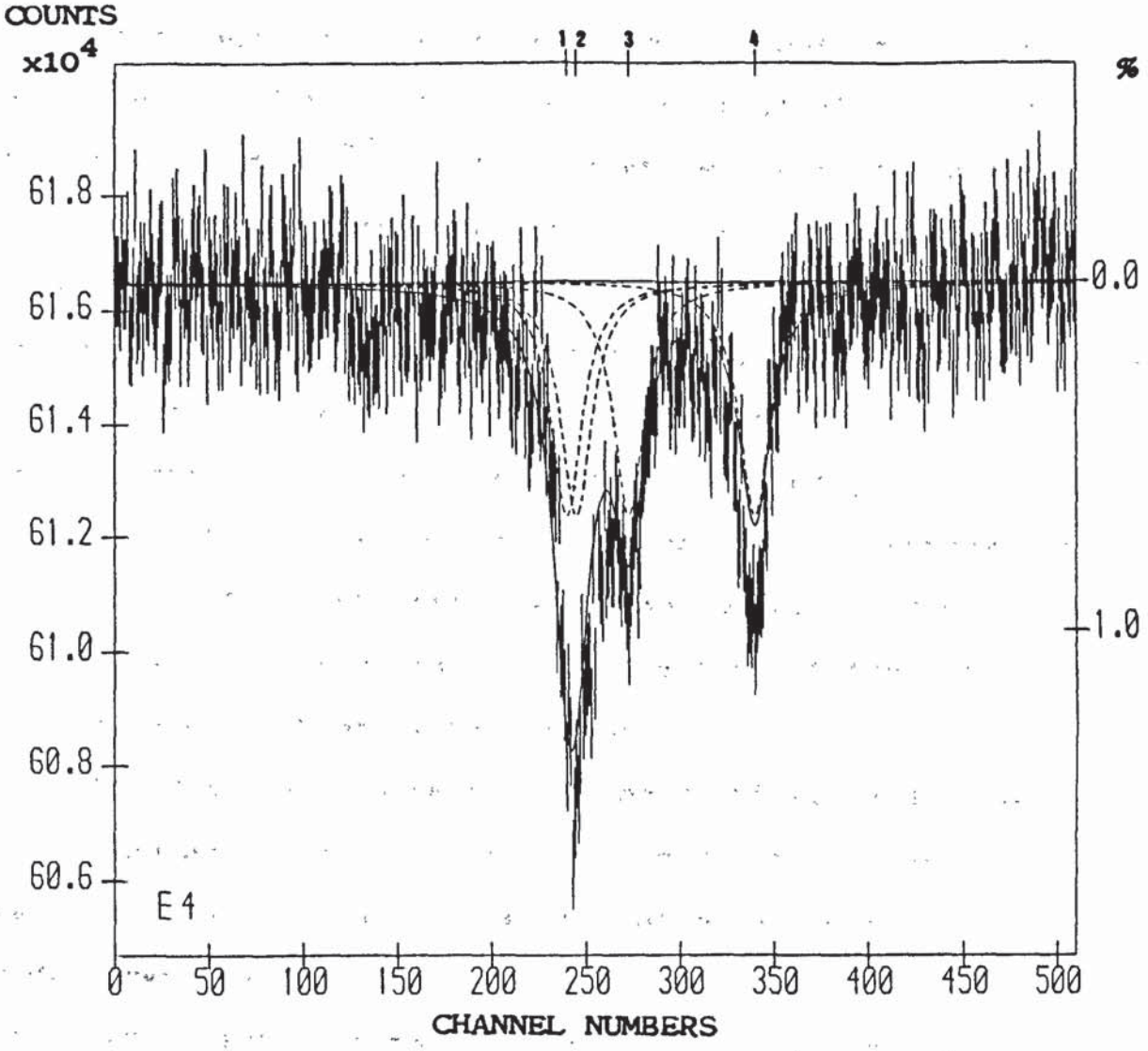

ILLITE 18DB RT R/O 29/8/84 STAGE 0

the spectral line to allow for base line drift and the maximum coincidence of data points with the spectral line. In order to do so the program will change the position, intensity and half-width of the approximated absorption peaks. Computer adjustments are made on a step by step basis (iterations), using the Gaussian non-linear regression method[87], until the 'best spectral fit' is obtained. The spectral fit is then said to have converged[87]. It is often necessary to constrain the line-widths and intensities of an absorption doublet to be equal during the initial fitting procedure in order to obtain convergence[88]. In subsequent computer fittings with refined parameters it is often possible to remove some or all of these constraints in spectra consisting of only one or two absorption doublets. FIG. 30 shows the computer fitted spectrum for natural illite which consists of two absorption doublets where the half-widths are constrained in pairs but the intensities of the outer doublet peaks are not.

The Mössbauer parameters (isomer shift, quadrupole splitting and magnetic hyperfine field) are measured with respect to a calibration spectrum of metallic iron which is run under identical operating conditions and gives rise to the calibration scale in mm/s shown in FIG. 30. The 0.0 mm/s mark on this scale represents the centre of the metallic iron spectrum. The line plot at the bottom of FIG. 30 represents the residual deviation (in standard deviation units) versus channel number, giving a visual representation of the deviation of each data point from the fitted spectrum. For a good spectral line fit the majority of the data points should lie between the two horizontal dashed lines.

The χ^2 criterion is a way of expressing the degree to which a spectrum is said to have the 'best spectral fit' and the computer fitting program operates so as to minimise χ^2. χ^2 itself can be defined as the sum of the squared deviation from the best fit divided by the variance at a single count[88]. The computer program carries out iterations on the spectral data until the values of χ^2 obtained by successive iterations differ by less than 10^{-6}. This is the basis on which a spectral fit is said to have converged.

For a fit to be statistically acceptable it is required that the value of χ^2 be between the 1% and 99% points of the χ^2 distribution; that is, between $(v + 2.2 - 3.3\sqrt{v})$ and $(v + 2.2 + 3.3\sqrt{v})$, where v, the number of degrees of freedom, is the number of channels used in fitting a spectrum minus the number of adjustable parameters in the fitted curve. A typical spectral fit with 490 degrees of freedom should therefore have a χ^2 value between 419 and 565. However, to obtain statistically acceptable χ^2 values, the spectrometer must be working perfectly[88], otherwise very large χ^2 values may be obtained.

When computer fitting a given spectrum such as that shown in FIG. 30, it may be possible to fit the spectrum with further quadrupole doublets. However, if the additional fitting does not significantly reduce the value of χ^2 the fitting can be said to be invalid. The spectrum of the natural illite shown in FIG. 30 has been further fitted with three and then four quadrupole doublets, FIGS. 31 and 32 respectively. χ^2 values for the two, three and four quadrupole doublet fits are: 557 (with 497 degrees of freedom), 503 (with 494 degrees of

FIG. 30. Four line spectral fit to the Mössbauer data for natural illite.

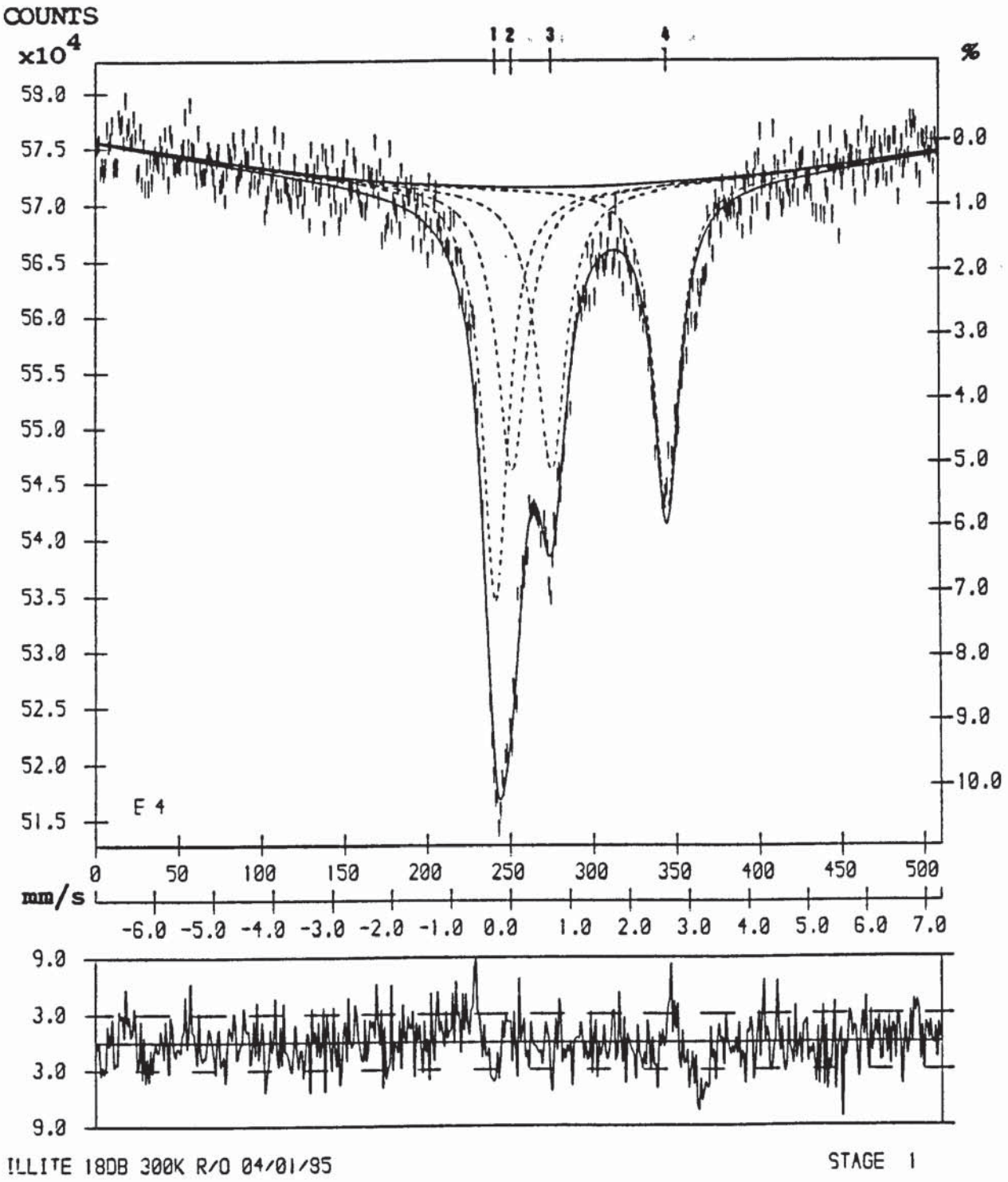

FIG. 31. Six line spectral fit to the Mössbauer data for natural illite.

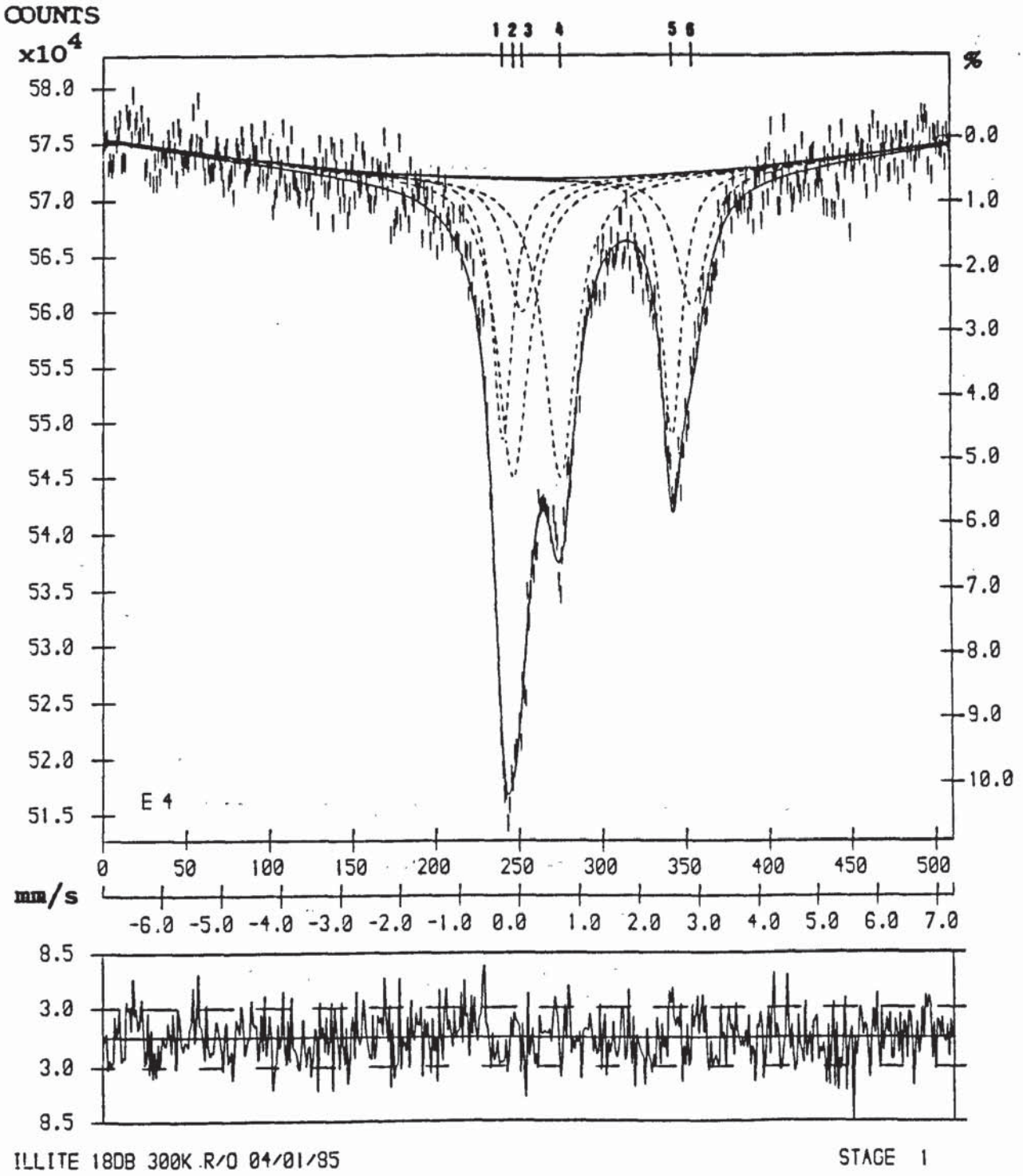

FIG. 32. Eight line spectral fit to the Mössbauer data for natural illite.

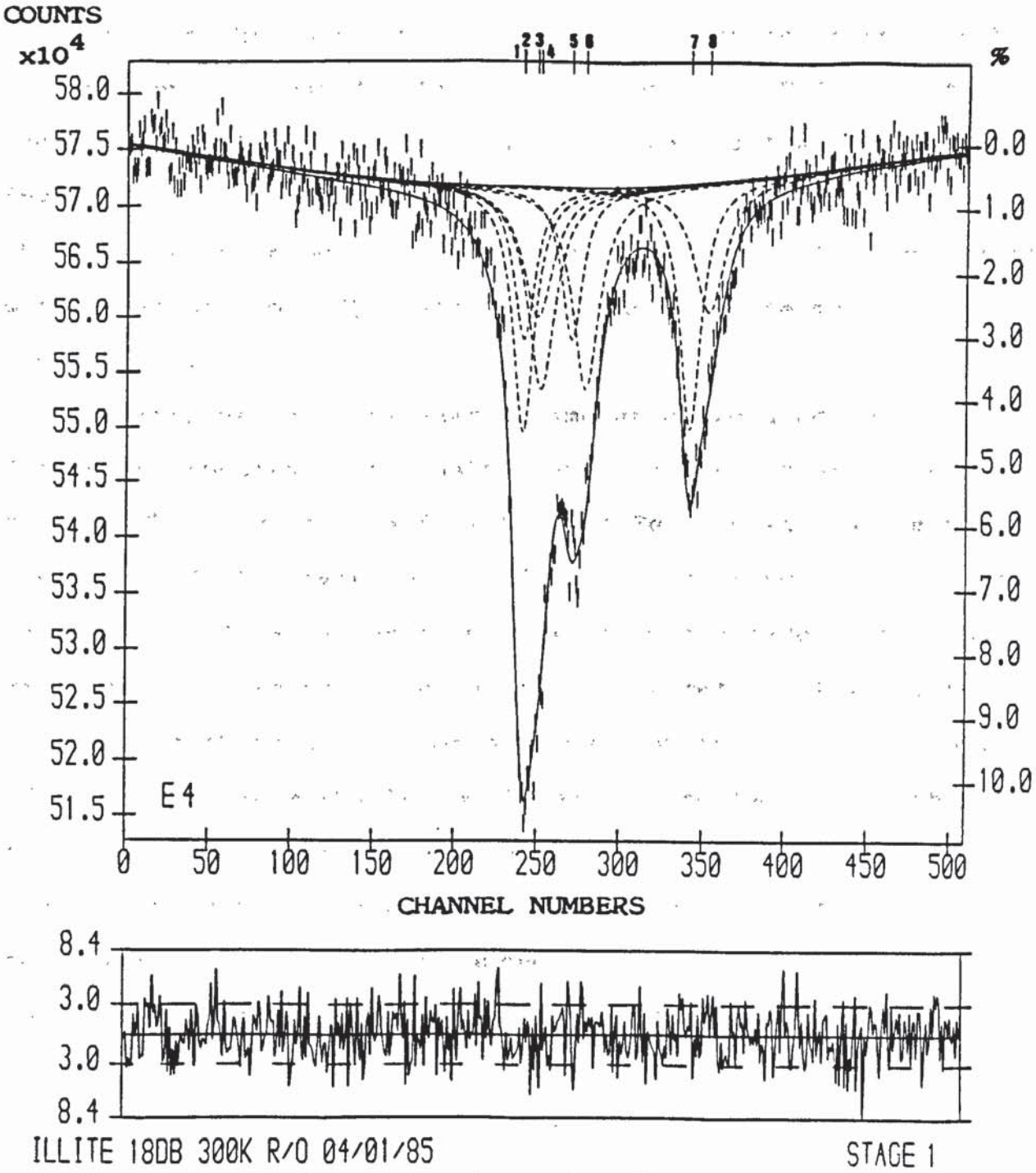

freedom) and 497 (with 490 degrees of freedom) respectively. These figures would tend to indicate that the two doublet fit (FIG. 30) is statistically acceptable in terms of the χ^2 value. However, there is a significant decrease in χ^2 (> 50)[88] for the three doublet spectrum (FIG. 31) indicating that this is the more appropriate fit. Although it is possible to computer fit four doublets to the spectrum (FIG. 32), the reduction in χ^2 is insignificant, indicating that this fit is invalid. It is upon this basis that the various spectra in this chapter have been produced, the most simple fit consistent with a satisfactory χ^2 value being taken as the most appropriate.

Another useful Mössbauer parameter often used in the fitting of spectra is the half-width (full-width at half-height), $\Gamma_{\frac{1}{2}}$. Typical half-widths for Fe^{2+} in silicate minerals invariably fall between 0.28 and 0.35 mm/s using a ^{57}Co in Pd source[88]. If an absorption peak is much broader than 0.35 mm/s and/or if there is any hint of assymmetry, it is quite likely that there are two or more overlapping lines present. If χ^2 decreases markedly (> 50) on fitting two lines, then this is evidence for the existence of appreciable amounts of iron in two sites. However, it should be noted that non-Lorentzian line shapes caused by poorly prepared sources, very thick absorbers, or the strong overlap of a number of non-resolvable Lorentzians can lead to the erroneous fitting of several lines to what appears to be a broad or slightly assymmetrical absorption peak. This is often the case where a large number of very similar iron-sites occur within a mineral phase giving rise to a broad, non-Lorentzian absorption

peak to which it is possible to computer fit a large number of spectral lines. In such a case, unless there is a significant decrease in χ^2, it is artificial to carry on fitting more than one or two spectral lines.

Further examples of the fitting procedure and a more detailed explanation of the factors involved can be found in the work by Bancroft, G.M.[88].

The various Mössbauer spectra presented in this chapter have been interpreted on the basis of the finger printing technique. Spectra are directly compared with those previously reported in the literature or semi-empirically with the typical ranges of isomer shift(δ) and quadrupole splitting(Δ) observed for Fe^{II} and Fe^{III} in fully characterised compounds and mineral phases. In principle, every mineral and every different iron site in the mineral yields a characteristic Mössbauer spectrum. The parameters δ and Δ for a component of a given spectrum are sensitive to the oxidation state, electronic configuration, co-ordination number and site symmetry of the iron atom involved. With these factors in mind, Maddock, A.G.[65] and Bancroft, G.M.[88] have produced bar charts of δ and Δ as a function of oxidation state and co-ordination number, FIG. 33. These charts can be used to great effect in the interpretation of spectra where an assemblage of unknown iron-containing mineral phases are present within a sample. Another useful observation by Bancroft, G.M. et al.[152], to use alongside these two charts, is that for six co-ordinate Fe^{2+} species δ and Δ decrease with increasing distortion from octahedral symmetry, whereas for six co-ordinate Fe^{3+} species δ decreases

and Δ increases with increasing distortion of the nearby atoms from octahedral symmetry.

(A)

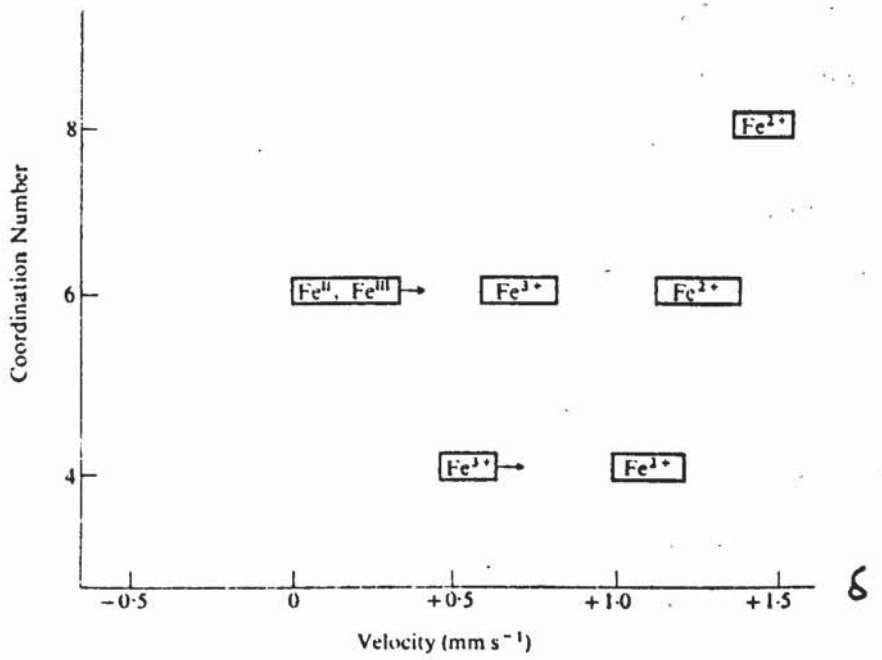

(B)

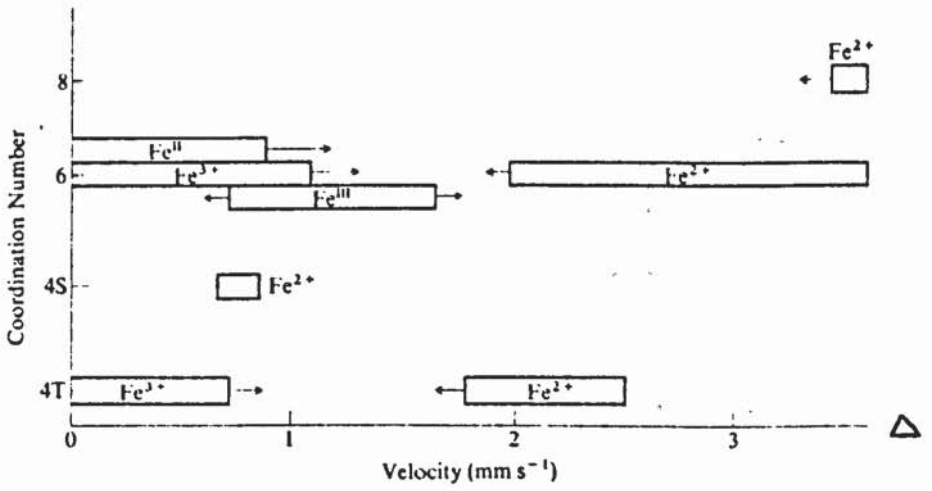

FIG. 33. Ranges of ^{57}Fe Mössbauer Isomer shifts (A) and Quadrupole splittings (B) plotted versus coordination number for 'ionic' high spin and low spin compounds and minerals. Arrows indicate that values outside the boxed areas have been observed. (Velocities, δ quoted w.r.t. sodium nitroprusside; w.r.t. metallic iron deduct 0.257 mm/s.)
(After Bancroft, G.M.[88]).

6.1.2. ELECTRON SPIN RESONANCE SPECTROSCOPY:

The basic theory and experimental procedures of Electron spin resonance spectroscopy are outlined in chapter 4. The various e.s.r. spectra presented in this chapter have been interpreted on the basis of the finger printing technique. Spectra are directly compared with those reported in the literature or semi-empirically with the typical g-values, hyperfine splitting constants (A) and line widths observed in fully characterised compounds and mineral phases.

An investigation of several shales by Inazumi, A.; Isobe, T. and Tarutani, T.[134] resulted in the presentation of typical e.s.r. resonances observed for shales and clay minerals. A schematic representation of the resonance types observed in illite are shown in FIG. 34, and their interpretations are summarised below:

Type A: This type of resonance ($g \approx 2$) is divided into two groups on the basis of its line shape; one gives six sharp lines (type A-1) and the other shows six relatively broader lines (type A-2).

Type A-1: This resonance pattern has been interpreted as being due to Mn^{2+} randomly distributed in calcite.

Type A-2: This resonance pattern has been interpreted as being due to Mn^{2+} randomly distributed in clay minerals.

Type B: This broad resonance centred on $g \approx 2.0$ has been interpreted as due to Fe^{3+} ions, probably contained within the clay mineral structure.

FIG. 34. Schematic representation of the resonance types observed in natural illite. (After Inazumi, et al.)[134]

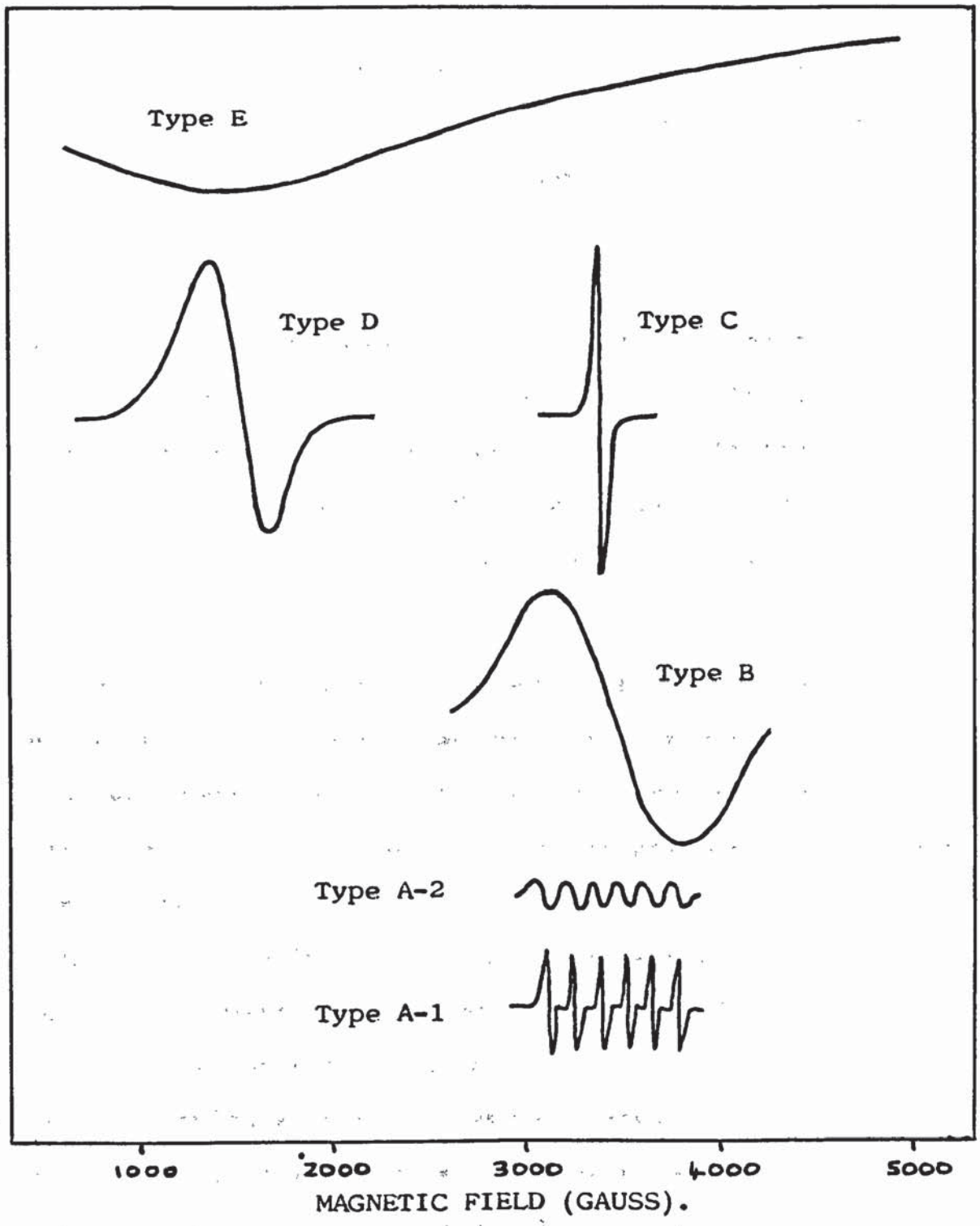

Type C: This very sharp and relatively intense resonance pattern centred on g = 2 is thought to represent the presence of organic free radicals in carbonaceous materials present within the clay.

Type D: This relatively broad resonance centred on $g \approx 4$ has been interpreted as Fe^{3+} ions occupying sites of orthorhombic symmetry with high distortion parameters within the clay mineral structure.

Type E: This pattern shows a remarkably inclined resonance producing a general signal drift across a spectrum, upon which the other resonance types are superimposed. It has been interpreted as the presence of trace amounts of iron oxide phases present within the clay mineral, possibly hematite.

Comparison of the e.s.r. spectra of the natural clay minerals and their thermal decomposition products with the work shown above, and that of other researchers presented in the literature, has led to the interpretation of these spectra within chapter 6.

As previously indicated the parameters of an e.s.r. signal are g-value, hyperfine coupling constant and line-width. The area under the absorption curve is proportional to the number of unpaired spins within the sample. However, the g-value may be anisotropic, in which case the line from a single crystal changes its position as the crystal is rotated in the magnetic field. In polycrystalline samples the spectra of randomly orientated crystallites are averaged to give three principal

g-values: g_x, g_y and g_z. The hyperfine coupling is due to the interaction between an unpaired electron spin (s) and the nuclear spin of nearby nuclei. A nuclear spin of I gives rise to 2I + 1 lines of equal intensity; the patterns due to more than one nucleus are obtained by simple superposition.

Spectra may be further complicated by the phenomenon of zero field splitting, whereby any spin $S > \frac{1}{2}$ gives rise to different energy levels even in the absence of a magnetic field. The resulting spectrum, for a single crystal, contains 2S fine structure lines which are often averaged to zero for a polycrystalline sample. As an example, Mn (II), with five unpaired electrons, has five fine structure lines. One of these lines is not orientation dependant and is therefore easily observed in polycrystalline samples; this line is split into six by hyperfine coupling to the manganese nucleus (^{55}Mn; $I = 5/2$). However, the six line Mn (II) spectrum can be further complicated by zero field splitting, resulting in extra doublets between the hyperfine lines, caused by the electronic and nuclear spins flipping together, something which is normally forbidden. These hyperfine lines may also be further split into two (second-order splitting). The immediate environment of Mn (II) and the size of the zero field splitting determine which of these spectra is observed. Mn (II) doped into calcite can show both these features and is exemplified in chapter 6.

6.1.3. THERMO-GRAVIMETRIC ANALYSIS AND X-RAY DIFFRACTION:

The thermal treatment of the clay minerals is outlined in chapter 4. However, thermo-gravimetric analysis of the clay minerals was carried out by heating individual, weighed samples (in duplicate) to a given temperature and then reweighing after cooling in a desiccator. Therefore, each data point on a graph of weight loss against temperature arises from a fresh sample.

The experimental procedure for the analysis of the clay minerals by X-ray diffraction is outlined in chapter 4. The resulting d-spacings of a sample, as obtained from its diffractogram, were compared with those presented in the literature for typical clay minerals and other mineral phases. A comprehensive list of d-spacings by value, mineral type and elemental content is presented in the "Inorganic index to the powder diffraction file"[149]. Mineral phases were assigned to the diffractograms by reference to these works.

6.1.4. SILICON-29 MAS-NMR SPECTROSCOPY:

Brief theoretical details and the application of ^{29}Si MAS-NMR to clay minerals are given in chapter 4. Samples of thermally treated hectorite and ion-exchanged hectorite were run by Dr. P. Gillespie at the University of Durham on a BRUCKER CXP200 spectrometer. Solid powder samples were used and spun at the 'magic angle' of 54.74^{o}. Spectra were measured relative to tetra-methyl silane (T.M.S.) and chemical shifts stated in parts per million (ppm).

The clay mineral hectorite was chosen for this study due to its low Fe_2O_3 and Al_2O_3 content (TABLE 17). This is because Fe^{3+} ions, being paramagnetic, have a significant broadening effect on the solid-state MAS-NMR spectra of minerals. The advantage of having a low Al_2O_3 content within the silicate phase is that it eliminates resonances due to Si-O-Al groupings. Spectra therefore only contain resonances due to Si-O-Si groupings. The interpretations of the various spectra are therefore greatly simplified and restricted to Q^{o} through to Q^{4} environments. The chemical shift ranges for these environments are shown in FIG. 35.

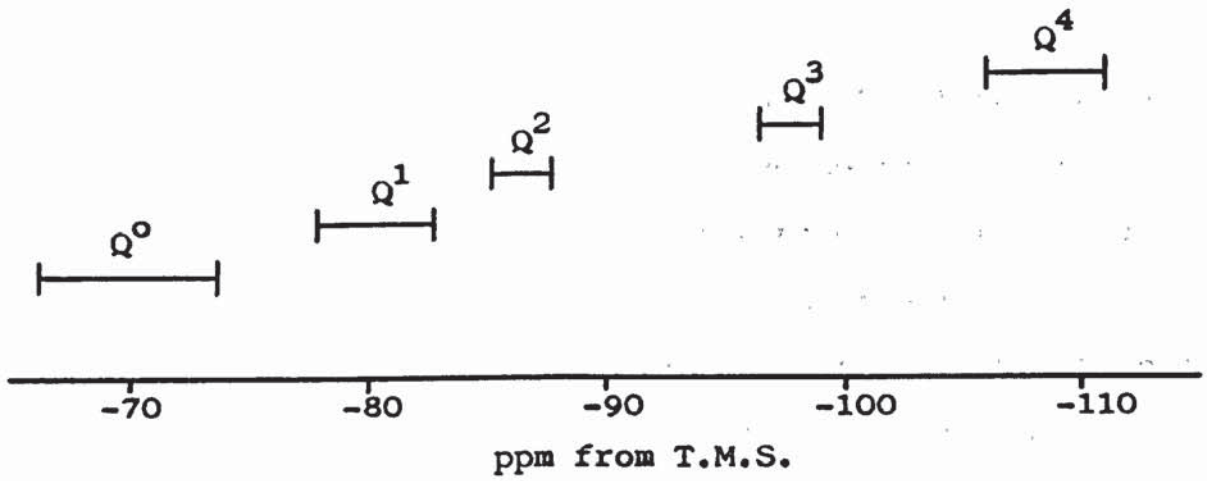

FIG. 35. Ranges of ^{29}Si chemical shifts for silicate structural units in solid silicates. (After Fyfe, C.A.[54]).

6.2. THE THERMAL TREATMENT OF ILLITE:

The chemical composition of the natural illite sample, as given by X-ray fluorescence analysis and corrected for H_2O content, is detailed in TABLE 17. The results are in close agreement with those of other natural illite samples cited in the literature[74],[75]. The weight percent of SiO_2, however, is slightly higher than expected, probably due to the inclusion of quartz impurity within the sample.

Portions of the natural illite were heated at various temperatures up to a maximum of 1300°C. The thermal products were investigated in 100°C steps from a starting point of 400°C; ILL1A400 to ILL1A1300. The percent weight loss and change in morphology of the clay upon heating are outlined in TABLE 18, and a graphical representation of the weight loss is shown in FIG. 36.

It can be seen that the percent weight loss increases gradually until about 400°C, representing the loss of absorbed interstitial water[130], whereupon it increases rapidly to about 650/700°C, representing the temperature range over which dehydroxylation is occurring[74],[127]. The graph levels out at about 700°C, the weight loss increasing by only 0.6% up to 1300°C. This slight increase probably represents the loss of residual hydroxyl ions[130].

TABLE 17. Chemical composition of the natural clay minerals.

%	ILLITE.[a]	MONTMORILLONITE.[b]	HEC1A.[a]	HEC2A.[a]
Fe_2O_3	5.20	10.76	0.18	0.48
MnO	0.04	0.00	0.00	0.01
TiO_2	0.89	0.33	0.04	0.03
CaO	0.96	1.90	0.42	25.43
K_2O	5.74	0.39	0.04	0.29
P_2O_5	0.13	0.10	0.01	0.02
SiO_2	60.11	53.10	60.78	27.23
Al_2O_3	18.45	12.70	0.15	1.26
MgO	2.35	2.20	28.50	11.19
Na_2O	0.07	0.12	1.96	1.00
SO_3	0.02	0.05	0.02	0.11
Li_2O†	-	-	1.22	1.22
H_2O+*	4.50	3.40	4.70	-
H_2O-*	1.55	14.95	3.20	2.90
H_2O+/CO_2	-	-	-	30.05
TOTAL.	100.01%	100.00%	101.22%	101.22%

HEC1A. = Hectorite sample 1A.

HEC2A. = Hectorite sample 2A.

a = Average result of two samples.

b = Average result of four samples.

† = Li_2O not analysed. Literature value for Li_2O content of hectorite = 1.22%[74].

* H_2O- = Absorbed H_2O (400°C).
H_2O+ = Structural H_2O (1100°C).

TABLE 18. Weight loss and change in morphology of illite upon heating.

TEMP., °C.	% WT. LOSS.*	MORPHOLOGY.
20	-	Light grey powder.
100	1.35	Light grey powder.
200	1.04	Light grey powder.
300	1.45	Light grey powder.
400	1.56	Light grey-brown powder.
500	2.77	Light grey-brown powder.
600	4.61	Light grey-brown powder.
700	5.74	Light grey-brown powder.
800	5.61	Light brown powder.
900	5.86	Light brown, compact but soft briquette. Powdered easily.
1000	5.90	Light brown, firm but brittle, porous briquette. Powdered easily.
1100	6.05	Dark brown, hard but brittle, porous briquette. Slight glassy texture - sintering. Very hard to crush.
1200	6.20	Dark green-grey, very hard but brittle, porous briquette. Highly vesicular texture - large scale sintering. Powdered easily to a grey powder.
1300	6.30	Dark brown, very hard but brittle, solid briquette. Highly vesicular. Glassy texture to surface - high degree of sintering or melting. Powdered easily to a light brown powder.

* = Average result of two samples.

FIG. 36. Graph of the weight loss of illite with respect to temperature.

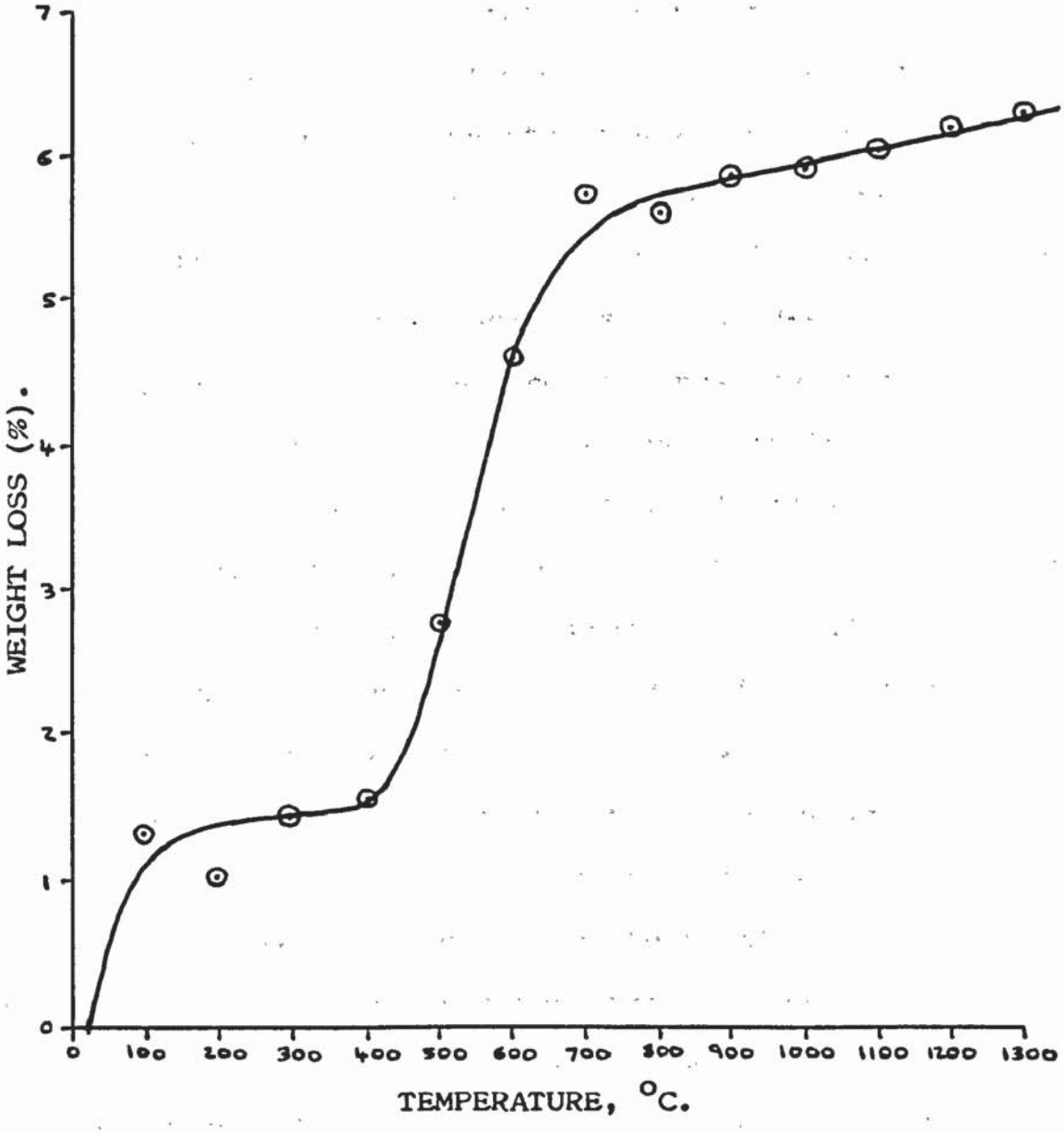

6.2.1. X-RAY DIFFRACTION DATA:

The X-ray diffraction trace of the natural illite sample revealed the characteristic trace expected for illite[73] together with a relatively strong trace for ∝-quartz[131], indicating the presence of quartz impurity within the sample. Investigation of the basal spacing of the clay gave a relatively strong signal representative of illite, d-spacing = 10.05 Å, and two relatively weaker signals, d-spacing = 13.10 Å and 7.25 Å, probably representing the presence of mixed layer illite-montmorillonite and chlorite respectively.

The X-ray diffraction traces of the thermal products showed no appreciable change from 400 to 800°C, other than a drift of the 060 line for illite from 1.50 to 1.52 Å. This indicates that the X-ray crystallinity of illite is not lost as a result of dehydroxylation[130]. Between 800 and 900°C a rapid consolidation of the illite structure occurred, representing a collapse of the crystalline lattice. This resulted in a drastic reduction in the relative intensity of the trace for illite, all but the three strongest peaks being lost at 900°C. There also appears to be a slight hint of the formation of spinel ($MgAl_2O_4$) at this temperature, which would tend to indicate the onset of reactions taking place within the relic octahedral sheets of the illite lattice[130].
At 1000°C illite was no longer represented within the X-ray diffraction trace, being replaced by the increasing presence of spinel and the appearance of hematite (Fe_2O_3) within the trace.

The relatively strong trace of the quartz impurity remained unchanged until 1100°C, whereupon it decreased greatly in intensity. This was accompanied by a further increase in the intensity of the trace for spinel and the continuing presence of hematite. As no new silicate phases were present within the X-ray diffraction trace, it would appear that the reduction in the quartz trace represents the onset of melting to an amorphous, glassy phase[130]. At 1200°C the trace for quartz had completely disappeared and been replaced by the presence of mullite ($3Al_2O_3.2SiO_2$). The intensity of the spinel trace again increased slightly, whereas that of hematite had decreased almost to nothing. These changes are representative of the further melting of quartz, its assimilation with alkali oxides (K_2O) and SiO_2 from the relic illite lattice, the further formation of spinel and its partial reaction with the silicate liquid to form mullite. The reduction in the intensity of hematite is probably due to its dissolution in the silicate liquid and the isomorphous substitution of Fe^{3+} for Al^{3+} in mullite[130]. At 1300°C the X-ray diffraction trace was practically free of any mineral traces, indicating an almost completely amorphous product, typical of glass. The very weak trace that was present indicated the presence of mullite. It would appear from this that at 1300°C the thermal products had all melted, and that the spinel present at 1200°C had dissolved in the silicate melt, reacted to form mullite, and had then started to dissolve in the liquid[130].

6.2.2. MÖSSBAUER SPECTROSCOPY DATA:

The Mössbauer spectra for the natural illite sample and its thermal decomposition products are shown in FIGS. 37 to 47. The interpretation of each individual spectrum together with the Mössbauer parameters are given in the following sub-sections.

6.2.2.1. NATURAL ILLITE:

The Mössbauer spectrum of the natural illite sample consists of two quadrupole doublets, spectrum lines (1)+(4), and (2)+(3) respectively, FIG. 37. The parameters are as follows:

Lines (1)+(4):

Isomer shift	= 1.21 ($\pm$0.01) mm/s.
Quadrupole splitting	= 2.88 ($\pm$0.01) mm/s.
Half-Width	= 0.52 ($\pm$0.01) mm/s.
Relative intensities	= 1096422 ($\pm$17043).
	869703 ($\pm$ 9445).

Lines (2)+(3):

Isomer shift	= 0.38 ($\pm$0.01) mm/s.
Quadrupole splitting	= 0.67 ($\pm$0.01) mm/s.
Half-Width	= 0.60 ($\pm$0.01) mm/s.
Relative intensity	= 863736 ($\pm$11770).

These parameters indicate the presence of Fe^{2+} and Fe^{3+} respectively, in cis-octahedral coordination of the hydroxyl ions. The isomer shift and quadrupole splitting of lines (2)+(3) are slightly higher than expected for pure cis-coordination, possibly indicating some contribution from Fe^{3+} in trans-coordination[106]. The half-width is also higher than expected, providing further evidence for this unresolved overlapping doublet. Spectrum line (4) is slightly asymmetrical in shape, lower in relative intensity than line (1), and the half-width relatively broad, indicating the presence of another unresolved quadrupole doublet. An attempt to computer fit this doublet (FIG. 31) reduced the half-width of lines (1)+(4) to 0.39 mm/s, lowered the relative intensity of line (1), and gave the following parameters for the new doublet:

Isomer shift	= 1.48 ($\pm$0.02) mm/s.
Quadrupole splitting	= 2.84 ($\pm$0.04) mm/s.
Half-Width	= 0.62 ($\pm$0.03) mm/s.

These parameters would tend to indicate the presence of a combination of szomolnokite ($FeSO_4.H_2O$), rozenite ($FeSO_4.4H_2O$) and melanerite ($FeSO_4.7H_2O$). The Mössbauer spectrum of a sample of this illite that had been treated with 0.5M acetic acid showed no trace of the above doublet, thus providing further evidence for its assignment as hydrated ferrous sulphates.

6.2.2.2. ILL1A400:

The Mössbauer spectrum of ILL1A400 consists of two quadrupole doublets, spectrum lines (1)+(4) and (2)+(3) respectively, FIG. 38. The parameters are as follows:

Lines (1)+(4):

Isomer shift	= 1.18 ($\pm$0.04) mm/s.
Quadrupole splitting	= 2.90 ($\pm$0.08) mm/s.
Half-Width	= 0.69 ($\pm$0.04) mm/s.
Relative intensity	= 191203 ($\pm$10986).

Lines (2)+(3):

Isomer shift	= 0.30 ($\pm$0.02) mm/s.
Quadrupole splitting	= 1.10 ($\pm$0.03) mm/s.
Half-Width	= 0.91 ($\pm$0.02) mm/s.
Relative intensity	= 737709 ($\pm$10325).

These parameters indicate the presence of Fe^{2+} in cis-coordination and Fe^{3+} in cis- or trans-coordination within the octahedral layer, respectively. There is a drop in the intensity of the Fe^{2+} doublet relative to that of Fe^{3+} when compared to that observed for natural illite, FIG. 37. This would indicate the onset of oxidation of Fe^{2+} to Fe^{3+} within the clay structure. The spectral lines are all relatively broad, particularly for the Fe^{3+} doublet. Removal of the adsorbed water by heating to 400^{o}C is unlikely to have affected the structural iron, but the onset of dehydroxylation would create a range of environments with similar Mössbauer

parameters[132]. These unresolved doublets would explain the broad spectral lines and the relatively poor spectrum fit, FIG. 38. The unusually high quadrupole splitting for the Fe^{3+} doublet is indicative of the increase in distortion from octahedral symmetry of the Fe^{3+} sites upon dehydroxylation[152]. This also results in a decrease of the isomer shift from 0.38 mm/s for natural illite to 0.030 mm/s for ILL1A400. However, similar changes in the parameters for the Fe^{2+} sites are not observed.

6.2.2.3. ILL1A500:

The Mössbauer spectrum of ILL1A500 consists of two quadrupole doublets, spectrum lines (1)+(4) and (2)+(3) respectively, FIG. 39. The parameters are as follows:

Lines (1)+(4):

Isomer shift	= 0.36 ($\pm$0.02) mm/s.
Quadrupole splitting	= 1.53 ($\pm$0.03) mm/s.
Half-Width	= 0.71 ($\pm$0.02) mm/s.
Relative intensity	= 1346122 ($\pm$149423).

Lines (2)+(3):

Isomer shift	= 0.36 ($\pm$0.01) mm/s.
Quadrupole splitting	= 0.95 ($\pm$0.02) mm/s.
Half-Width	= 0.59 ($\pm$0.02) mm/s.
Relative intensity	= 1458037 ($\pm$140157).

The half-widths of the two fitted quadrupole doublets are relatively broad, especially for lines (1)+(4), indicating that a two doublet fit does not entirely represent the true situation[133]. The parameters for the higher relative intensity lines (2)+(3) would tend to indicate the presence of a combination of the remaining fully hydroxylated Fe^{3+} sites and the distorted octahedral Fe^{3+} sites resulting from the partial dehydroxylation of cis- and trans-octahedrally coordinated Fe^{3+} ions[132]. The parameters for lines (1)+(4) with a quadrupole splitting = 1.53 mm/s, could well represent the highly distorted fully dehydroxylated Fe^{3+} octahedral sites.

The continuing presence but greatly reduced signal for Fe^{2+} within the clay at 500°C is indicated by the slight deviation of the fitted spectrum from the plotted data at approximately 2.25 mm/s.

6.2.2.4. ILL1A600:

The Mössbauer spectrum of ILL1A600 consists of two quadrupole doublets, spectrum lines (1)+(4) and (2)+(3) respectively, FIG. 40. The parameters are as follows:

Lines (1)+(4):

Isomer shift	= 0.32 ($\pm$0.03) mm/s.
Quadrupole splitting	= 1.73 ($\pm$0.06) mm/s.
Half-Width	= 0.66 ($\pm$0.05) mm/s.
Relative intensity	= 267713 ($\pm$47675).

Lines (2)+(3):

Isomer shift	= 0.37 ($\pm$0.02) mm/s.
Quadrupole splitting	= 1.11 ($\pm$0.04) mm/s.
Half-Width	= 0.54 ($\pm$0.04) mm/s.
Relative intensity	= 232871 ($\pm$43098).

The observed Mössbauer spectrum and doublet parameters for ILL1A600 are very similar to those observed for ILL1A500. The interpretations for ILL1A500 can therefore be applied to ILL1A600. An increase in the quadrupole splitting values of lines (1)+(4) and (2)+(3), with respect to ILL1A500, indicates the increasing contribution to the doublets of fully dehydroxylated Fe^{3+} sites and partially dehydroxylated Fe^{3+} sites respectively. The presence of Fe^{2+} within the spectrum is not indicated at this temperature (600°C).

6.2.2.5. ILL1A700:

The Mössbauer spectrum of ILL1A700 consists of two quadrupole doublets, spectrum lines (1)+(4) and (2)+(3) respectively (FIG. 41). The parameters are as follows:

Lines (1)+(4):

Isomer shift	= 0.34 ($\pm$0.02) mm/s.
Quadrupole splitting	= 1.76 ($\pm$0.05) mm/s.
Half-Width	= 0.68 ($\pm$0.03) mm/s.
Relative intensity	= 519555 ($\pm$66509).

Lines (2)+(3):

Isomer shift	= 0.36 ($\pm$0.01) mm/s.
Quadrupole splitting	= 1.14 ($\pm$0.02) mm/s.
Half-Width	= 0.50 ($\pm$0.02) mm/s.
Relative intensity	= 525366 ($\pm$58769).

The Mössbauer spectrum and doublet parameters are very similar to those observed for ILL1A500 and ILL1A600. The interpretation of ILL1A700 is therefore considered to be similar.

6.2.2.6. ILL1A800:

The Mössbauer spectrum of ILL1A800 consists of a single quadrupole doublet, FIG. 42. The parameters are as follows:

Isomer shift	= 0.37 ($\pm$0.01) mm/s.
Quadrupole splitting	= 1.42 ($\pm$0.02) mm/s.
Half-Width	= 0.79 ($\pm$0.03) mm/s.

These parameters are representative of a range of similar distorted Fe^{3+} octahedral environments within the relic illite lattice, resulting from the almost complete dehydroxylation of the natural clay. A decrease in the quadrupole splitting value from that observed for lines (1)+(4) of ILL1A700 might well be due to: (a) the unresolvable contribution of a minor doublet representing residual partially dehydroxylated Fe^{3+} sites, and/or (b) the onset of the irreversible breakdown and restructuring of the silicate lattice producing less distorted octahedral Fe^{3+} sites.

6.2.2.7. ILL1A900:

The Mössbauer spectrum of ILL1A900 consists of two quadrupole doublets, spectrum lines (1)+(4) and (2)+(3) respectively, FIG. 43. The parameters are as follows:

Lines (1)+(4):

Isomer shift	= 0.33 ($\pm$0.01) mm/s.
Quadrupole splitting	= 1.36 ($\pm$0.02) mm/s.
Half-Width	= 0.75 ($\pm$0.02) mm/s.
Relative intensity	= 726704 ($\pm$45569).

Lines (2)+(3):

Isomer shift	= 0.28 ($\pm$0.01) mm/s.
Quadrupole splitting	= 0.78 ($\pm$0.02) mm/s.
Half-Width	= 0.43 ($\pm$0.03) mm/s.
Relative intensity	= 289783 ($\pm$39496).

The parameters for the relatively broad lines (1)+(4) are similar to those observed for the single doublet fit for ILL1A800, indicating a range of similar Fe^{3+} environments as outlined in section 6.2.2.6.. The parameters for lines (2)+(3), however, appear to represent a new paramagnetic Fe^{3+} crystalline phase[6], resulting from the partial collapse and recrystallisation of components within the relic illite lattice. There is also a slight hint of the presence of a magnetic hyperfine sextet within the spectrum (upwards pointing arrows in FIG. 43), indicating the onset of formation of a ferromagnetic phase, probably α-Fe_2O_3.

6.2.2.8. ILL1A1000:

The Mössbauer spectrum of ILL1A1000 consists of a quadrupole doublet (lines (4)+(5)) and a six peak magnetic hyperfine spectrum (lines (1)-(3) and (6)-(8)), FIG. 44. The parameters are as follows:

Quadrupole Doublet:

Isomer shift	= 0.27 ($\pm$0.01) mm/s.
Quadrupole splitting	= 0.88 ($\pm$0.02) mm/s.
Half-Width	= 0.60 ($\pm$0.02) mm/s.
Relative intensity	= 400842 ($\pm$7871).

Magnetic Hyperfine Spectrum:

Isomer shift	= 0.42 ($\pm$0.06) mm/s.
Quadrupole splitting	= -0.08 ($\pm$0.06) mm/s.
Magnetic hyperfine field	= 513 ($\pm$4) kG.
	= 51.3 ($\pm$0.4) T.
Half-Widths	= 0.73 ($\pm$0.19) mm/s.
	0.70 ($\pm$0.17) mm/s.
	0.31 ($\pm$0.14) mm/s.
Relative intensities	= 55583 ($\pm$14448).
	50764 ($\pm$10393).
	17326 ($\pm$ 6958).

The parameters for the quadrupole doublet are similar to those observed for lines (2)+(3) in the spectrum for ILL1A900. This doublet is indicative of an Fe^{3+} paramagnetic phase resulting from the total collapse and partial recrystallisation of the relic illite lattice. The parameters for the magnetic hyperfine spectrum indicate the presence of hematite, α-Fe_2O_3.

6.2.2.9. ILL1A1100:

The Mössbauer spectrum of ILL1A1100 consists of a quadrupole doublet (lines (4)+(5)) and a six peak magnetic hyperfine spectrum (lines (1)-(3) and (6)-(8)), FIG. 45. The parameters are as follows:

Quadrupole Doublet:

Isomer shift	= 0.33 ($\pm$0.01) mm/s.
Quadrupole splitting	= 0.83 ($\pm$0.02) mm/s.
Half-Width	= 0.54 ($\pm$0.01) mm/s.
Relative intensity	= 319403 ($\pm$5956).

Magnetic Hyperfine Spectrum:

Isomer shift	= 0.40 ($\pm$0.05) mm/s.
Quadrupole splitting	= -0.15 ($\pm$0.05) mm/s.
Magnetic hyperfine field	= 516 ($\pm$3) kG.
	= 51.6 ($\pm$0.3) T.
Half-Widths	= 0.71 ($\pm$0.14) mm/s.
	0.66 ($\pm$0.12) mm/s.
	0.34 ($\pm$0.08) mm/s.
Relative intensities	= 56664 ($\pm$10532).
	49791 ($\pm$ 7931).
	28527 ($\pm$ 5872).

The parameters for the quadrupole doublet are similar to those observed for the doublet in the spectrum for ILL1A1000. The doublet is representative of an Fe^{3+} paramagnetic phase. As for ILL1A1000, the presence at 1100°C of hematite, α-Fe_2O_3, is again clearly indicated by the parameters for the magnetic hyperfine spectrum.

6.2.2.10. ILL1Al200:

The Mössbauer spectrum of ILL1Al200 consists of two quadrupole doublets, spectrum lines (1)+(4) and (2)+(3) respectively, FIG. 46. The parameters are as follows:

Lines (1)+(4):

Isomer shift	= 0.83 ($\pm$0.12) mm/s.
Quadrupole splitting	= 2.15 ($\pm$0.25) mm/s.
Half-Width	= 0.68 ($\pm$0.29) mm/s.
Relative intensity	= 21004 ($\pm$7651).

Lines (2)+(3):

Isomer shift	= 0.32 ($\pm$0.01) mm/s.
Quadrupole splitting	= 0.77 ($\pm$0.03) mm/s.
Half-Width	= 0.55 ($\pm$0.03) mm/s.
Relative intensity	= 151942 ($\pm$5112).

The parameters for lines (1)+(4) appear to represent an Fe^{2+} phase, probably Fe^{2+} in a silicate glass[10],[132]. However, the relative intensity of the doublet is rather small, producing some doubt in the accuracy of the parameters as indicated by their standard deviations. The parameters for lines (2)+(3), although similar to those for the quadrupole doublet in the spectrum for ILL1Al100, may well represent Fe^{3+} contained within mullite ($3Al_2O_3.2SiO_2$)[10],[130]. No trace for hematite, α-Fe_2O_3, is apparent within the spectrum.

6.2.2.11. ILL1A1300:

The Mössbauer spectrum of ILL1A1300 consists of two quadrupole doublets, spectrum lines (1)+(4) and (2)+(3) respectively, FIG. 47. The parameters are as follows:

Lines (1)+(4):

Isomer shift	= 0.85 ($\pm$0.01) mm/s.
Quadrupole splitting	= 2.59 ($\pm$0.02) mm/s.
Half-Width	= 0.67 ($\pm$0.02) mm/s.
Relative intensity	= 330614 ($\pm$10438).

Lines (2)+(3):

Isomer shift	= 0.41 ($\pm$0.01) mm/s.
Quadrupole splitting	= 1.13 ($\pm$0.01) mm/s.
Half-Width	= 0.77 ($\pm$0.01) mm/s.
Relative intensity	= 1094080 ($\pm$8986).

The parameters for lines (1)+(4) and (2)+(3) appear to represent Fe^{2+} and Fe^{3+}, respectively, contained within a silicate glass[6],[10],[132]. However, due to the relatively broad half-widths of both doublets, it is highly likely that these doublets represent a range of environments with similar parameters[10]. Again, there is no apparent trace for hematite within the spectrum.

FIG. 37. Mössbauer spectrum of the natural illite sample.

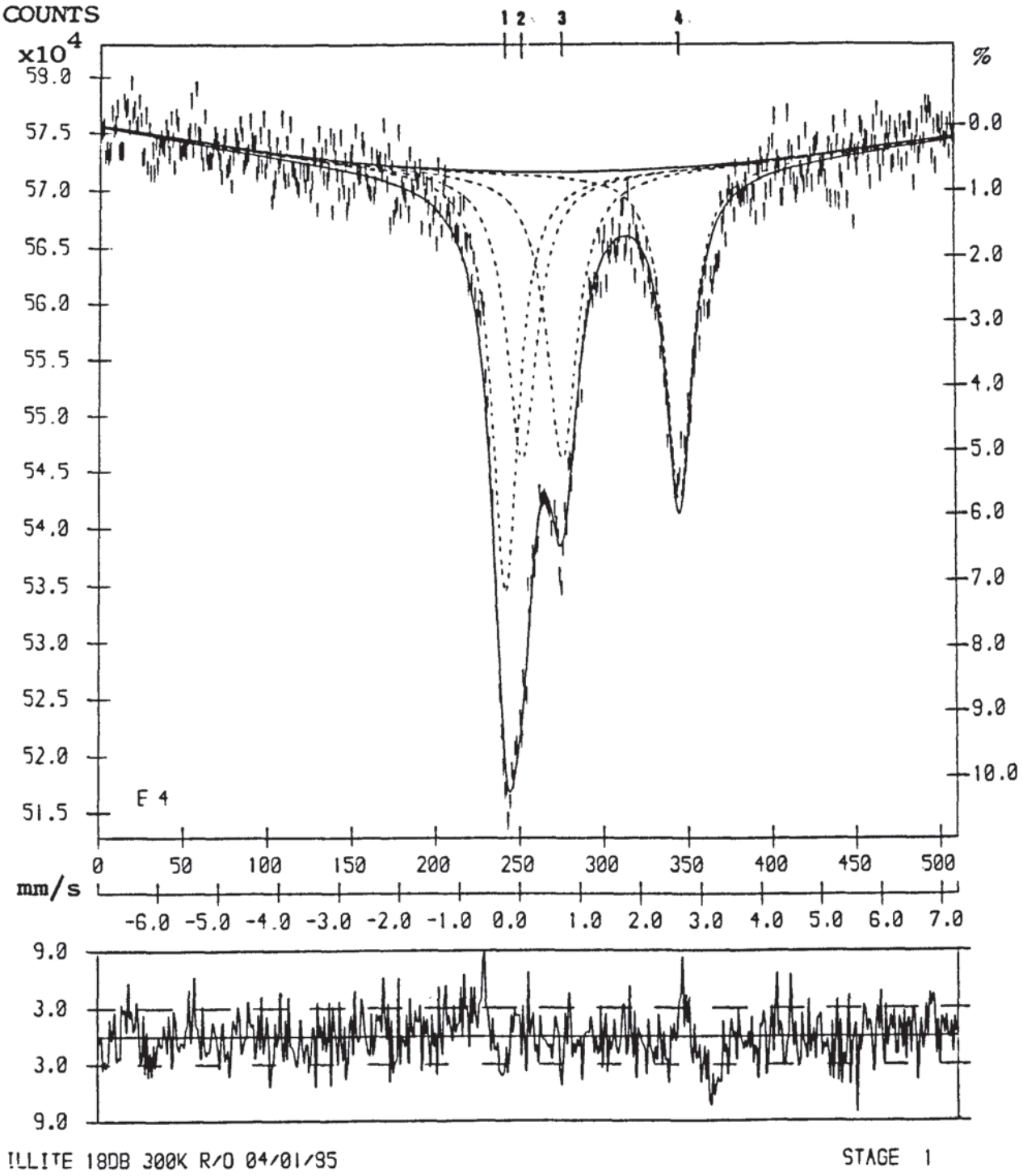

FIG. 38. Mössbauer spectrum of ILL1A400.

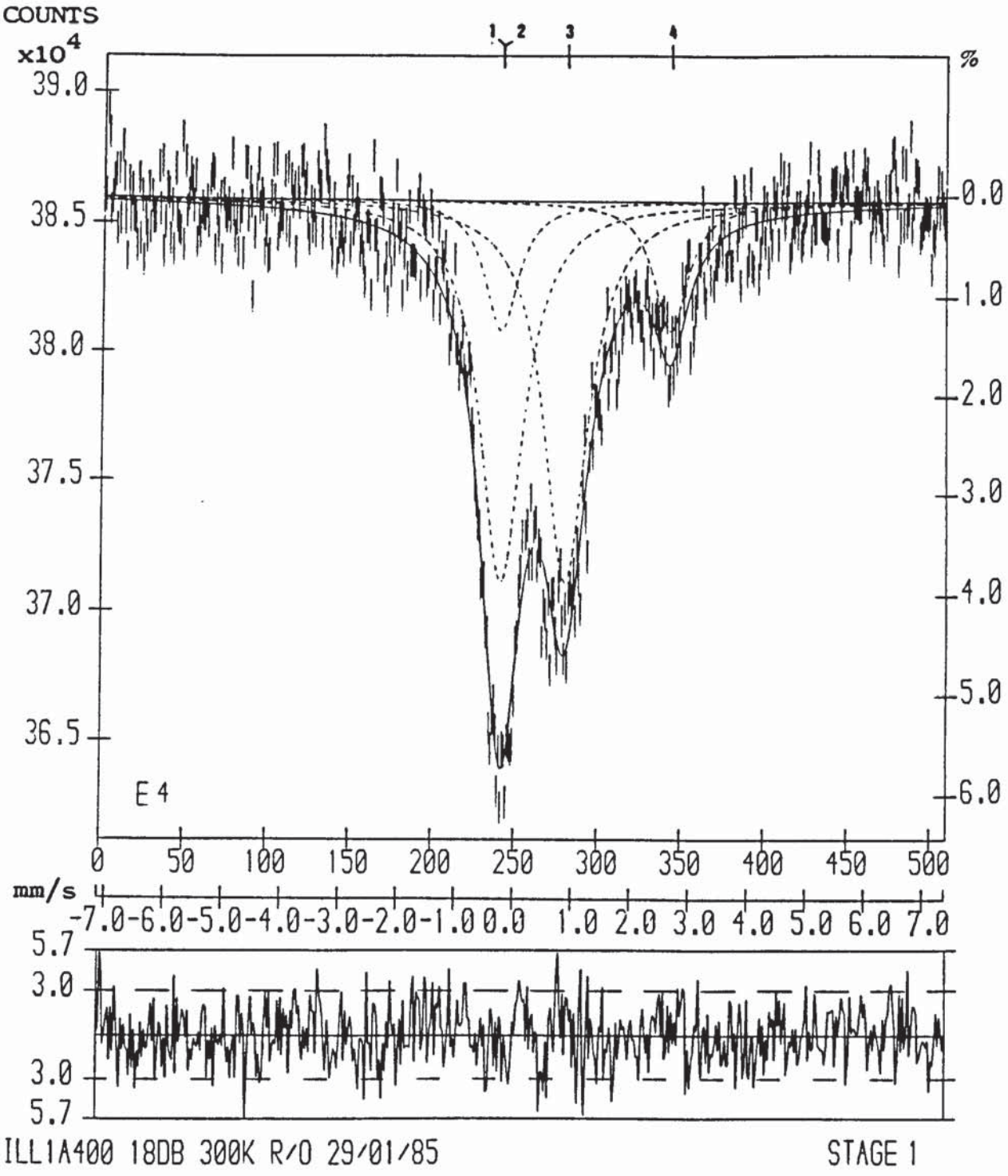

FIG. 39. Mössbauer spectrum of ILL1A500.

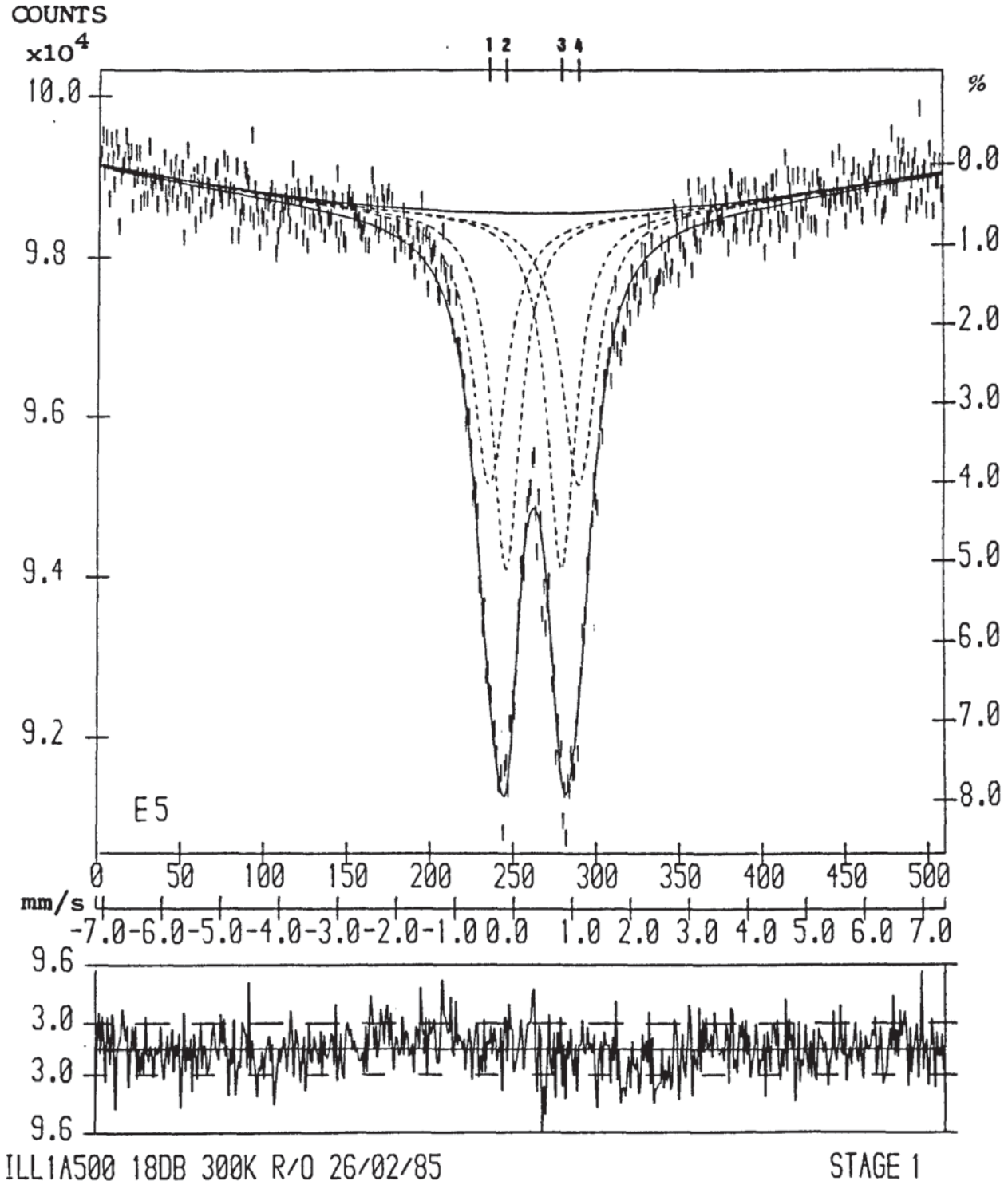

FIG. 40. Mössbauer spectrum of ILL1A600.

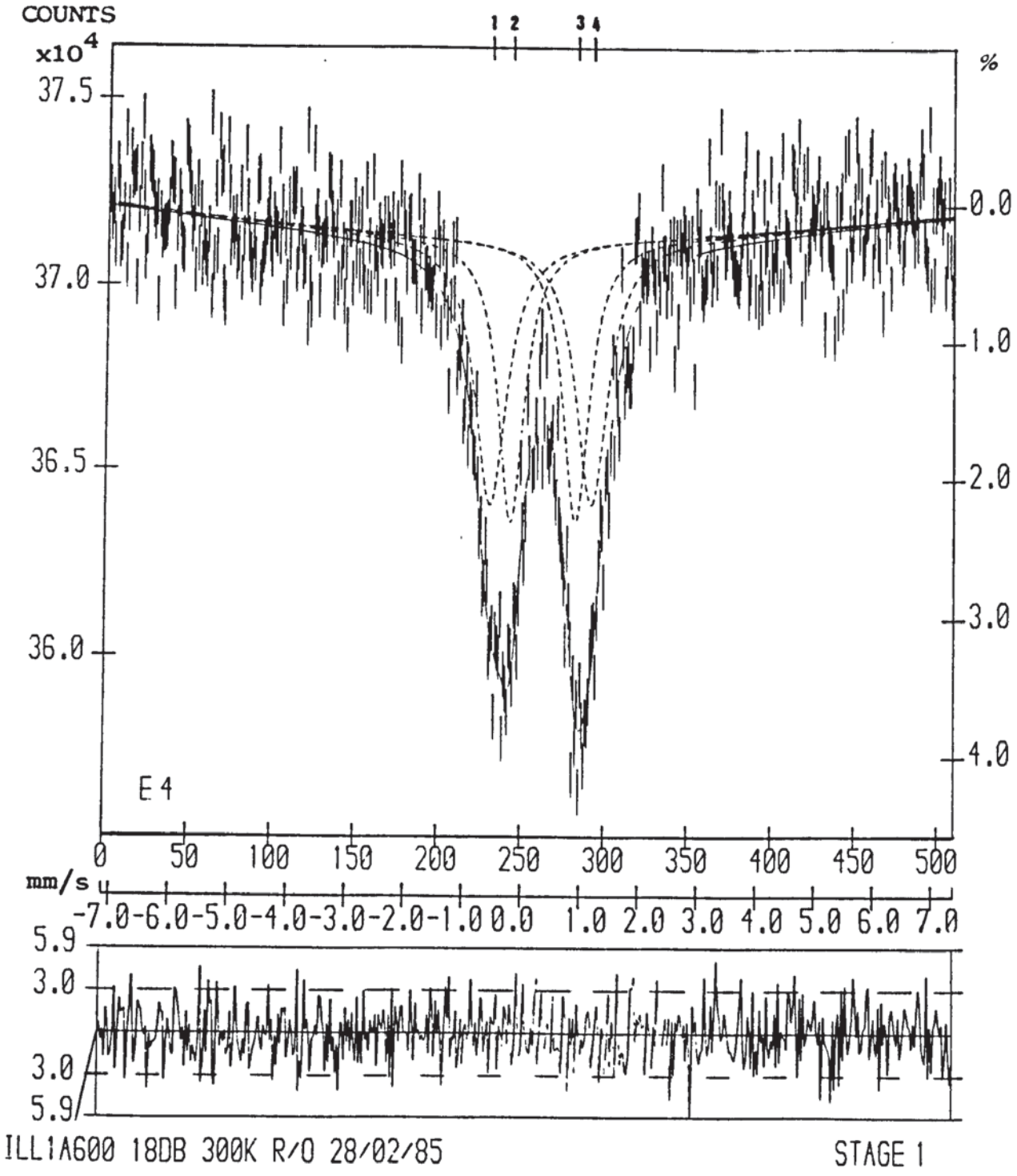

FIG. 41. Mössbauer spectrum of ILL1A700.

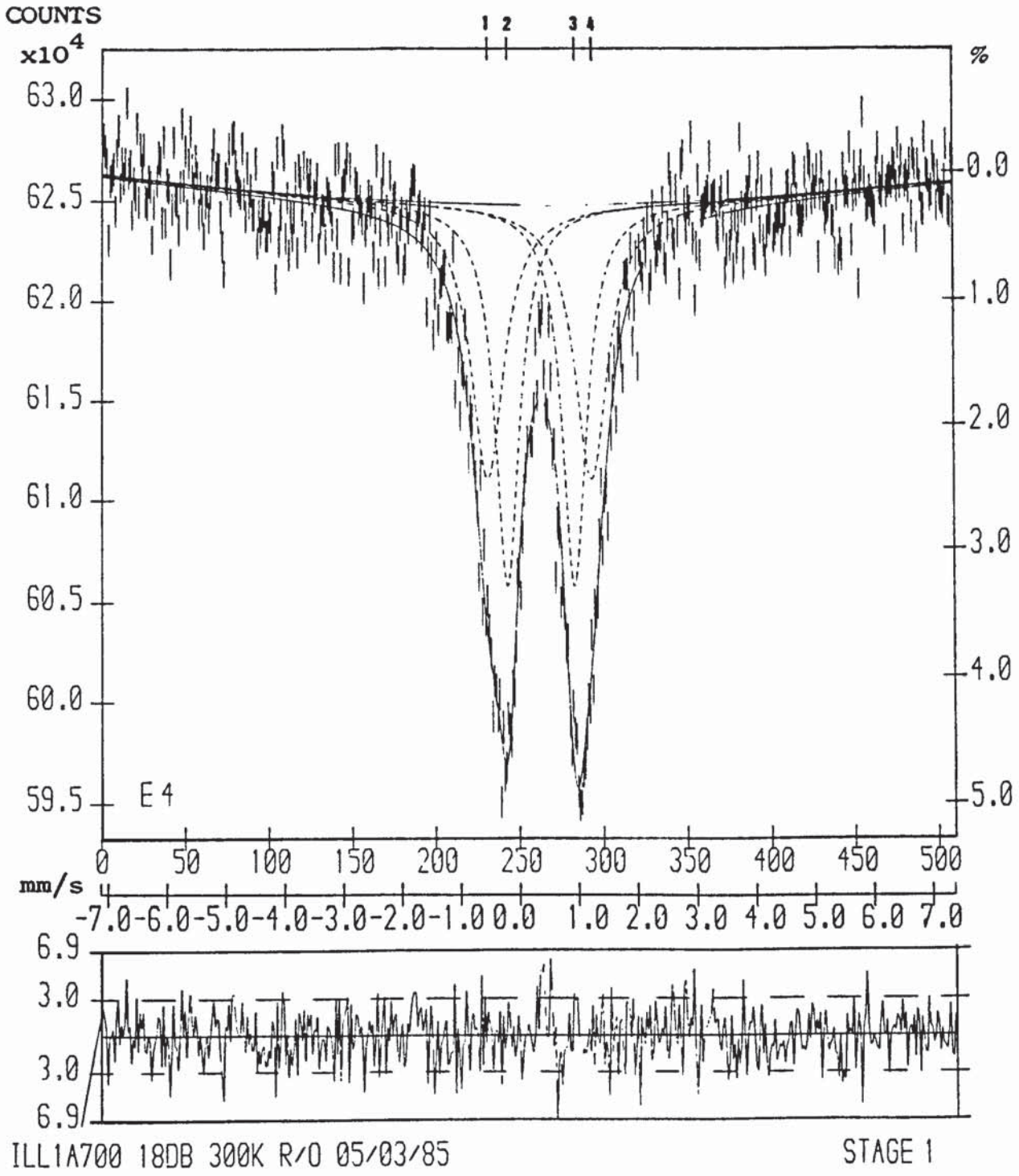

FIG. 42. Mössbauer spectrum of ILL1A800.

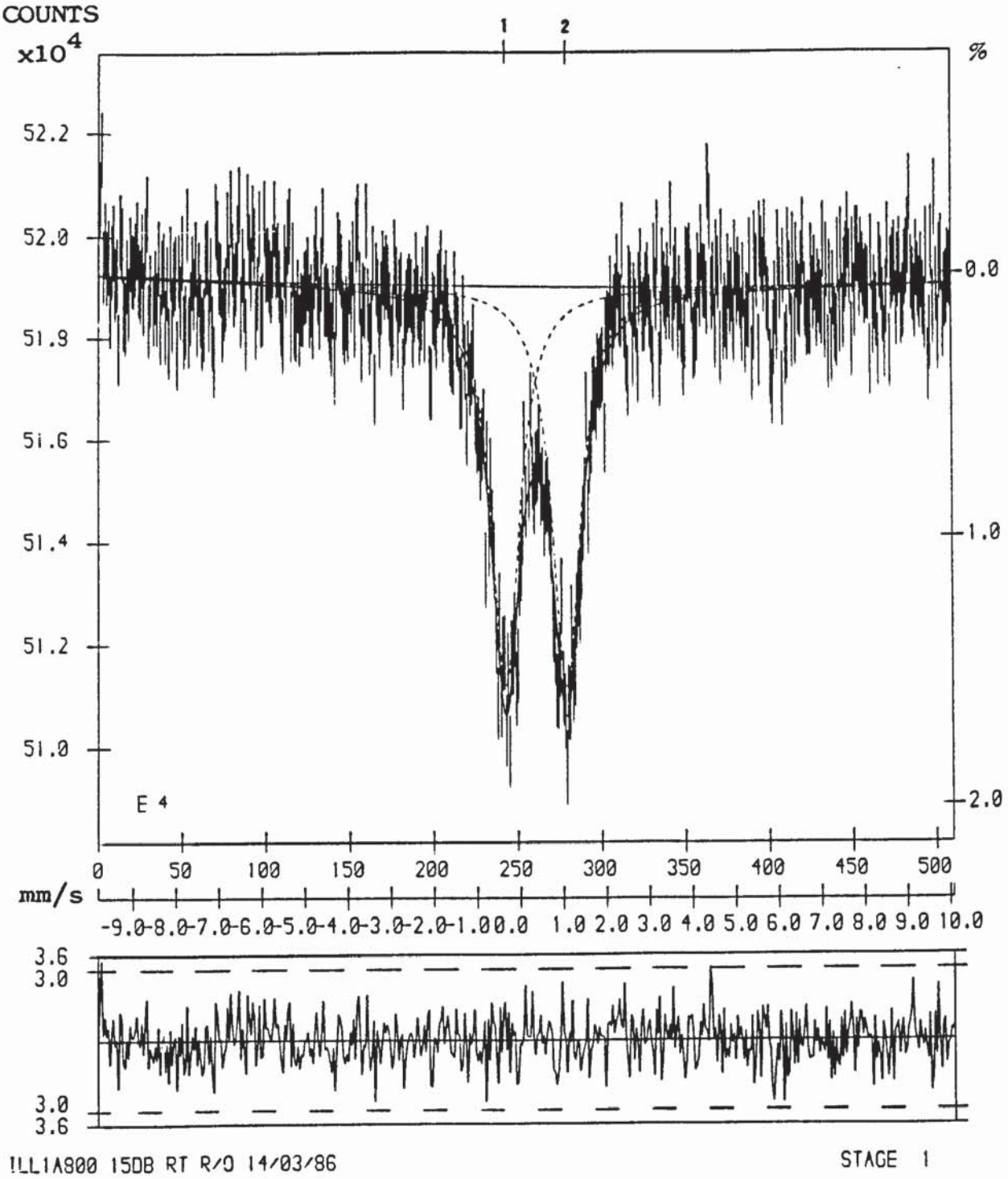

FIG. 43. Mössbauer spectrum of ILL1A900.

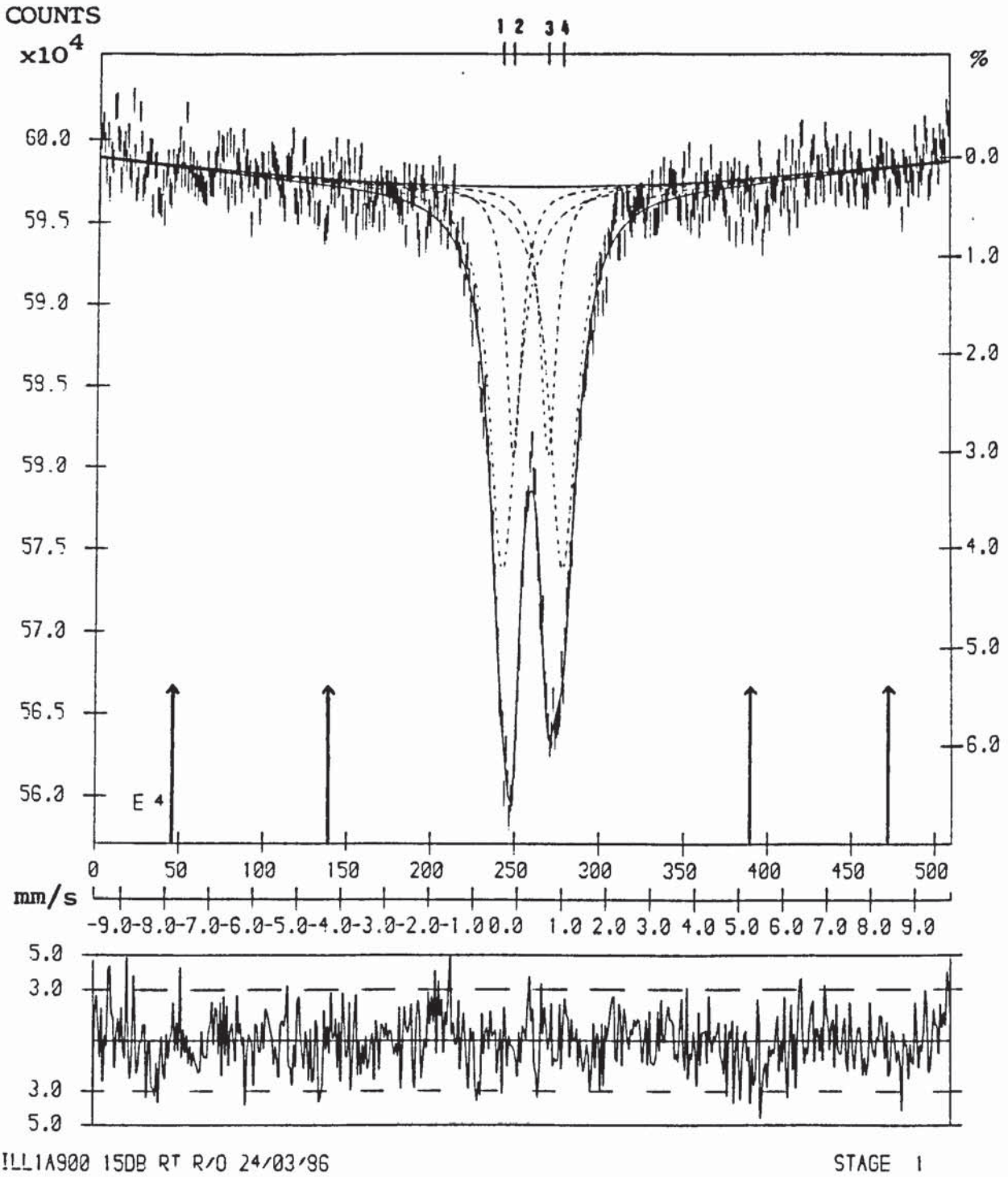

FIG. 44. Mössbauer spectrum of ILL1A1000.

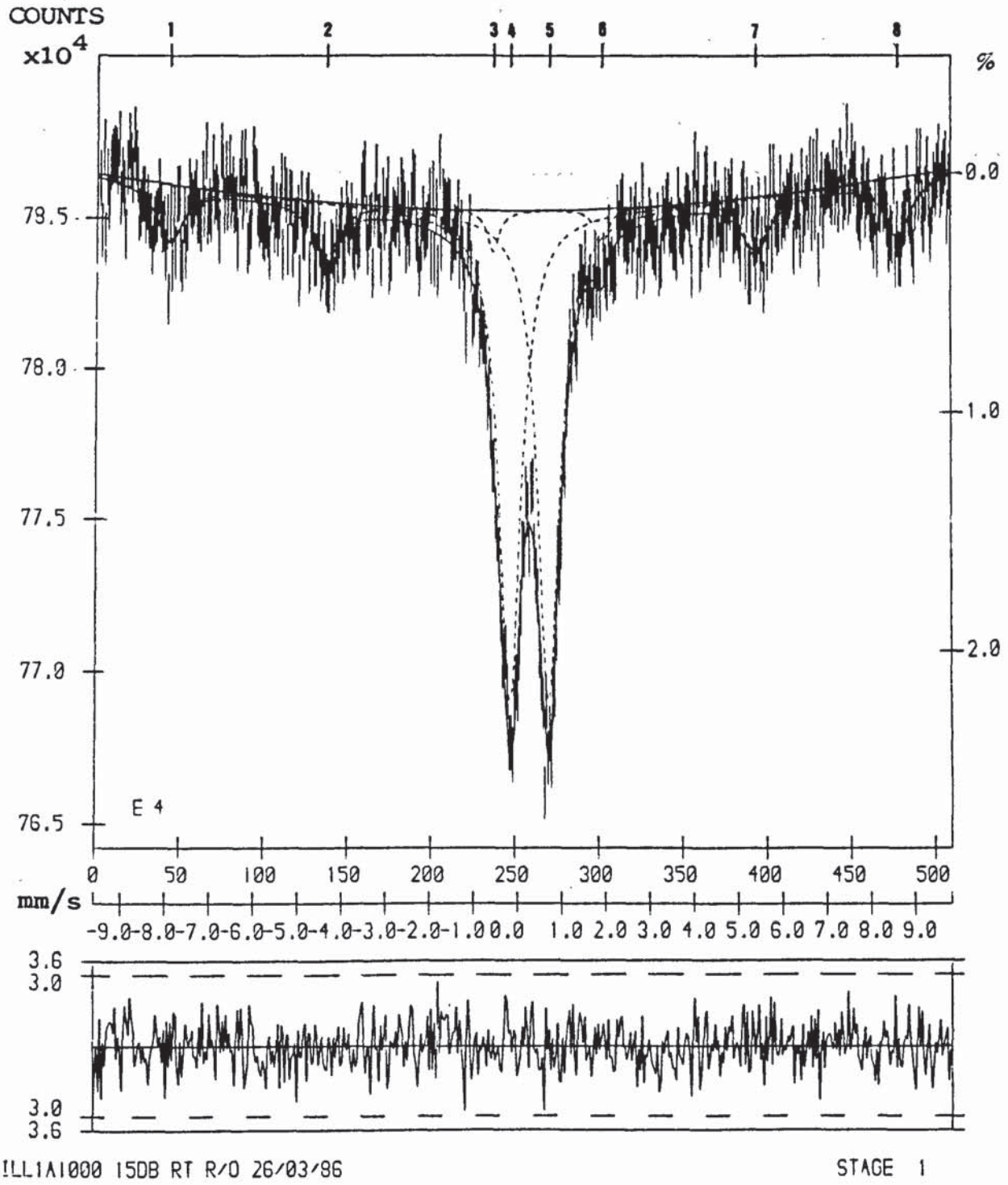

FIG. 45. Mössbauer spectrum of ILL1A1100.

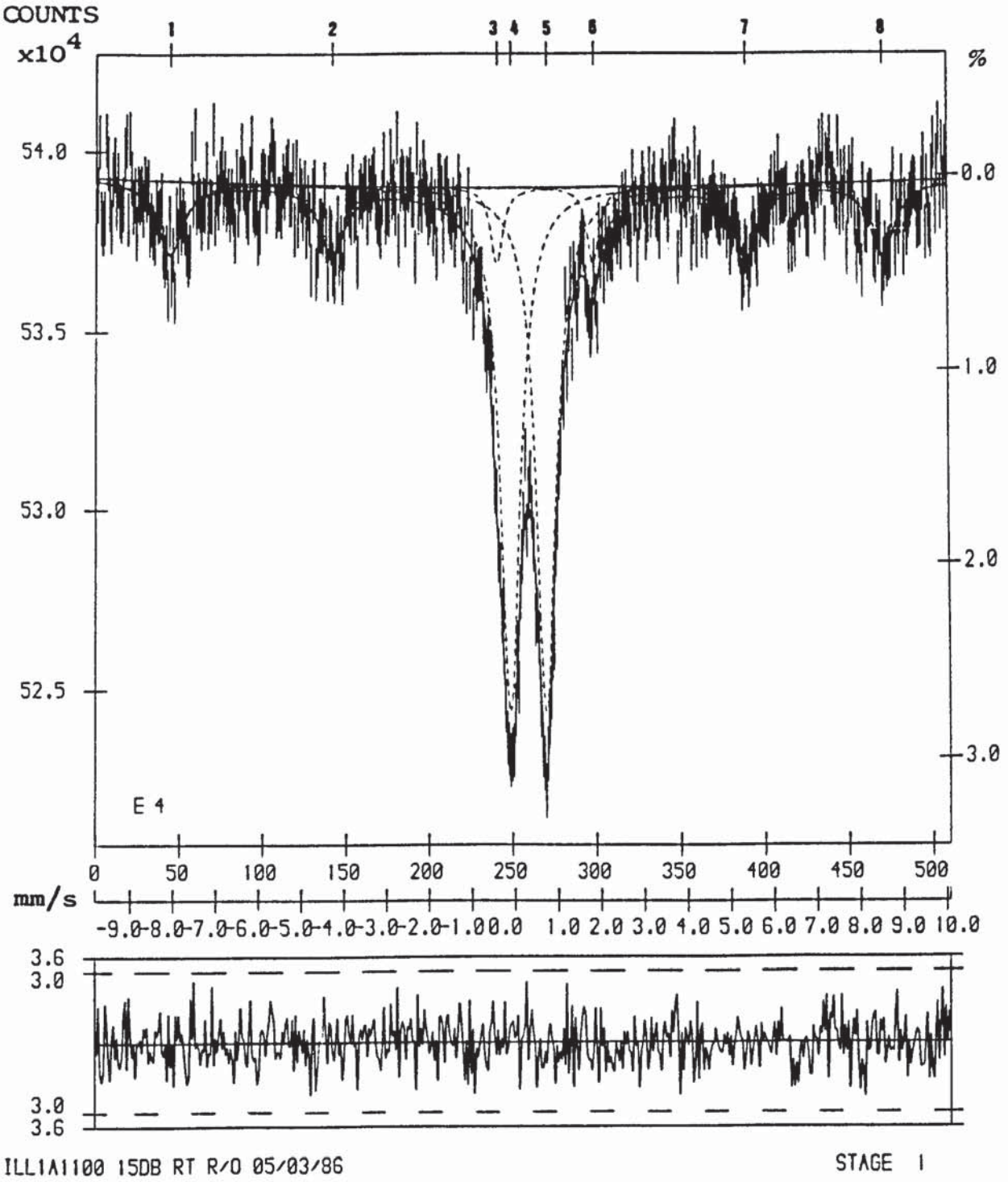

FIG. 46. Mössbauer spectrum of ILL1A1200.

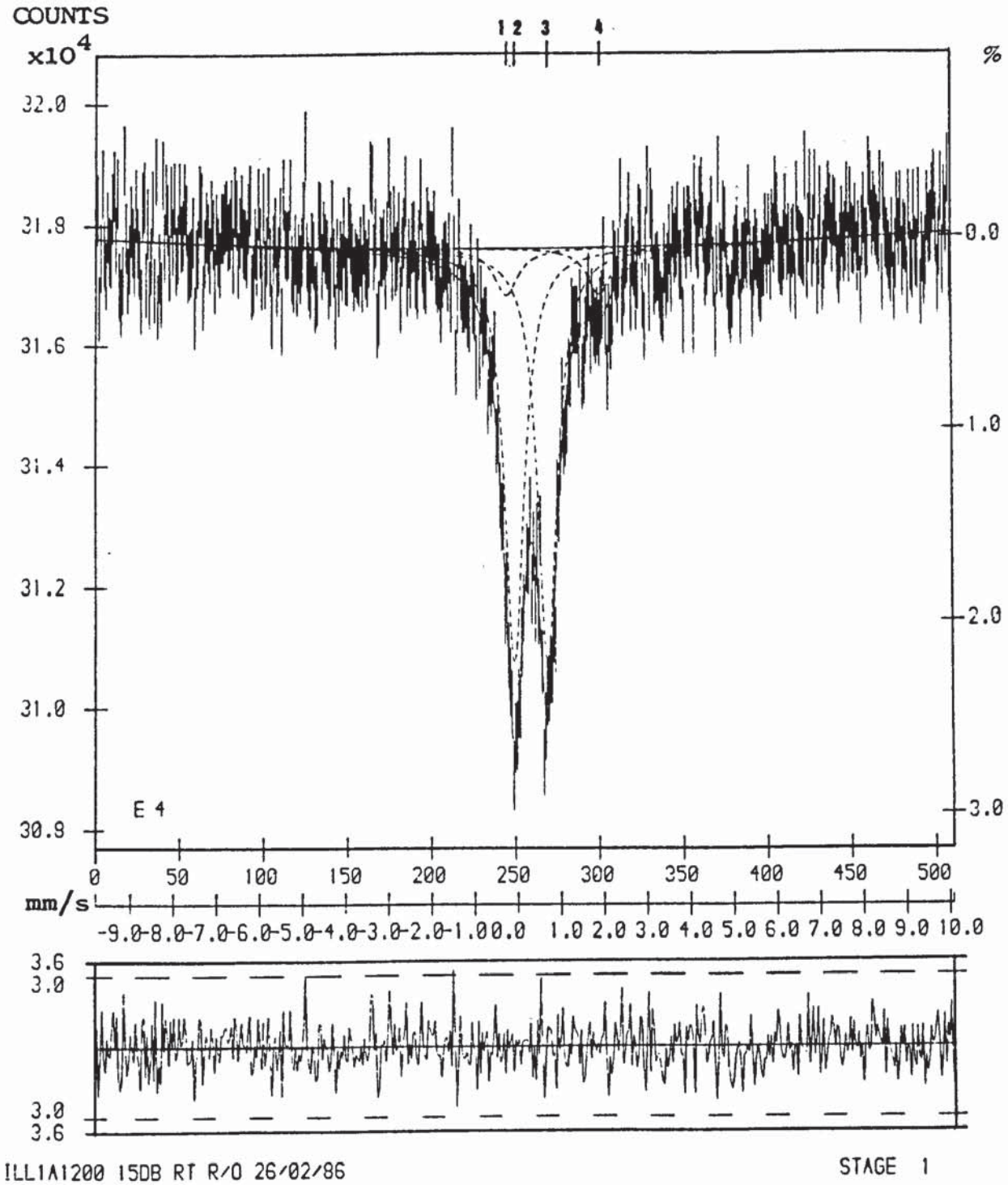

FIG. 47. Mössbauer spectrum of ILL1A1300.

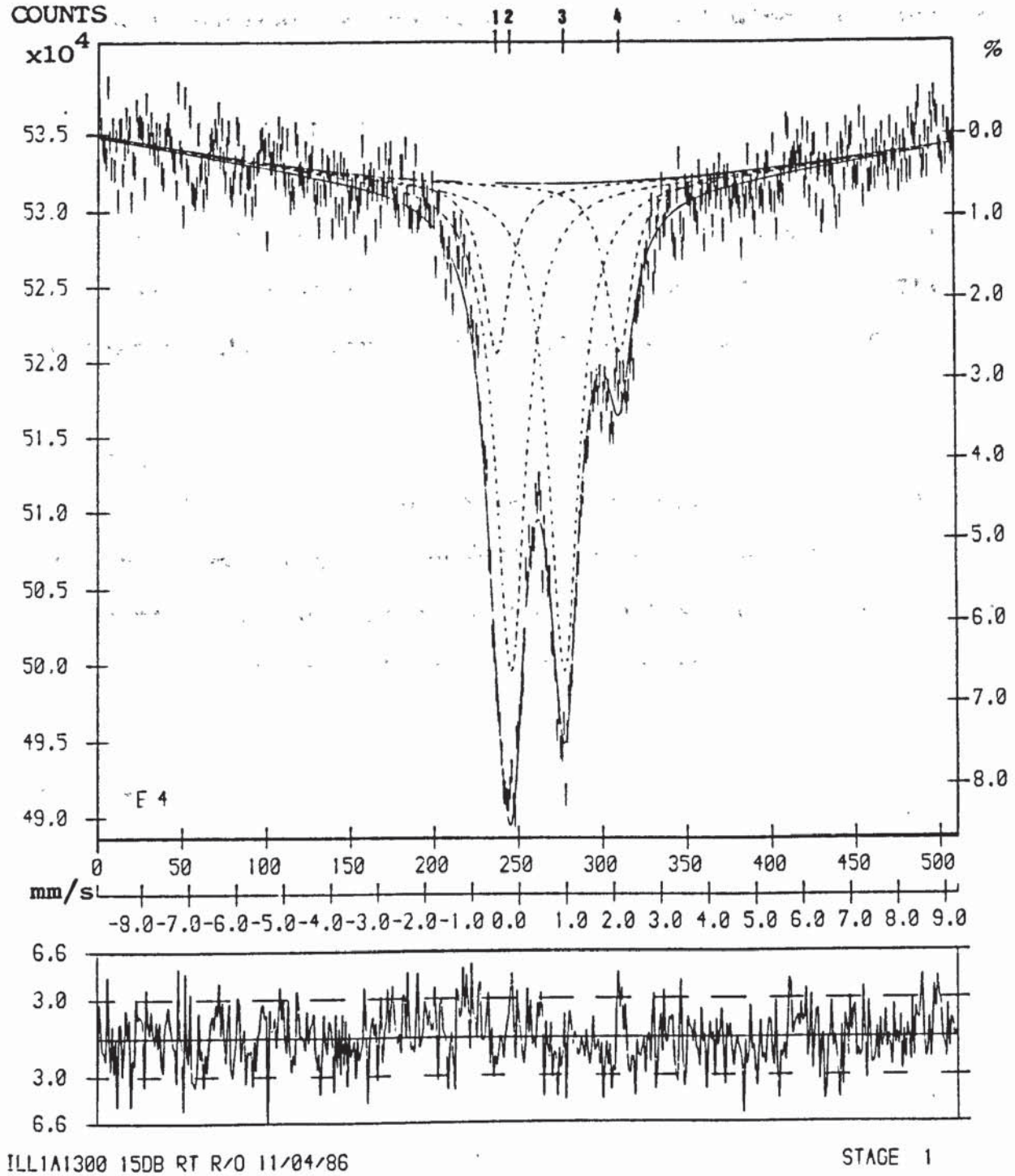

6.2.3. ELECTRON SPIN RESONANCE DATA:

The E.S.R. spectra for the natural illite sample and its thermal decomposition products are shown in FIGS. 48 to 56. The interpretation of each individual spectrum together with the E.S.R. parameters are given in the following sub-sections.

6.2.3.1. NATURAL ILLITE:

The E.S.R. spectrum of the natural illite sample consists of a combination of six resonance patterns, FIG. 48. The g-values of the different types of resonance are as follows:

Type A-1:

$g \approx 2.0$; Hyperfine Splitting Constant, $A \approx 81$ G. This pattern shows six sharp hyperfine lines (line width ≈ 28 G) representing trace amounts of Mn^{2+} randomly distributed within a small quantity of calcite ($CaCO_3$) impurity.

Type A-2:

$g \approx 2.0$; $A \approx 94$ G. This pattern shows six relatively broad hyperfine lines (line width ≈ 47 G) representing trace amounts of Mn^{2+} randomly distributed within the illite structure.

Type B:

$g \approx 2.0$. This pattern shows a very broad resonance (line width $\approx$ 650 G) and may be attributed to Fe^{3+} ions, probably contained within the illite structure.

Type C:

$g = 2.010 (\pm 0.004)$. This pattern shows a very sharp and relatively intense resonance (line width $\approx$ 16 G) attributed to the presence of organic free radicals in carbonaceous material. These were probably produced by decomposition of organic impurities within the clay during diagenesis.

Type D:

$g = 4.15 (\pm 0.05)$. This pattern shows a relatively broad resonance (line width $\approx$ 225 G) resulting from Fe^{3+} ions occupying sites of orthorhombic symmetry with high distortion parameters within the clay mineral structure.

Type E:

This pattern shows a general signal drift across the whole spectrum, upon which the other resonance types are superimposed. This would indicate the presence of trace amounts of iron oxide impurities within the clay, possibly hematite.

FIG. 48. E.S.R. spectrum of the natural illite sample (2500 $\pm$ 2500 G).

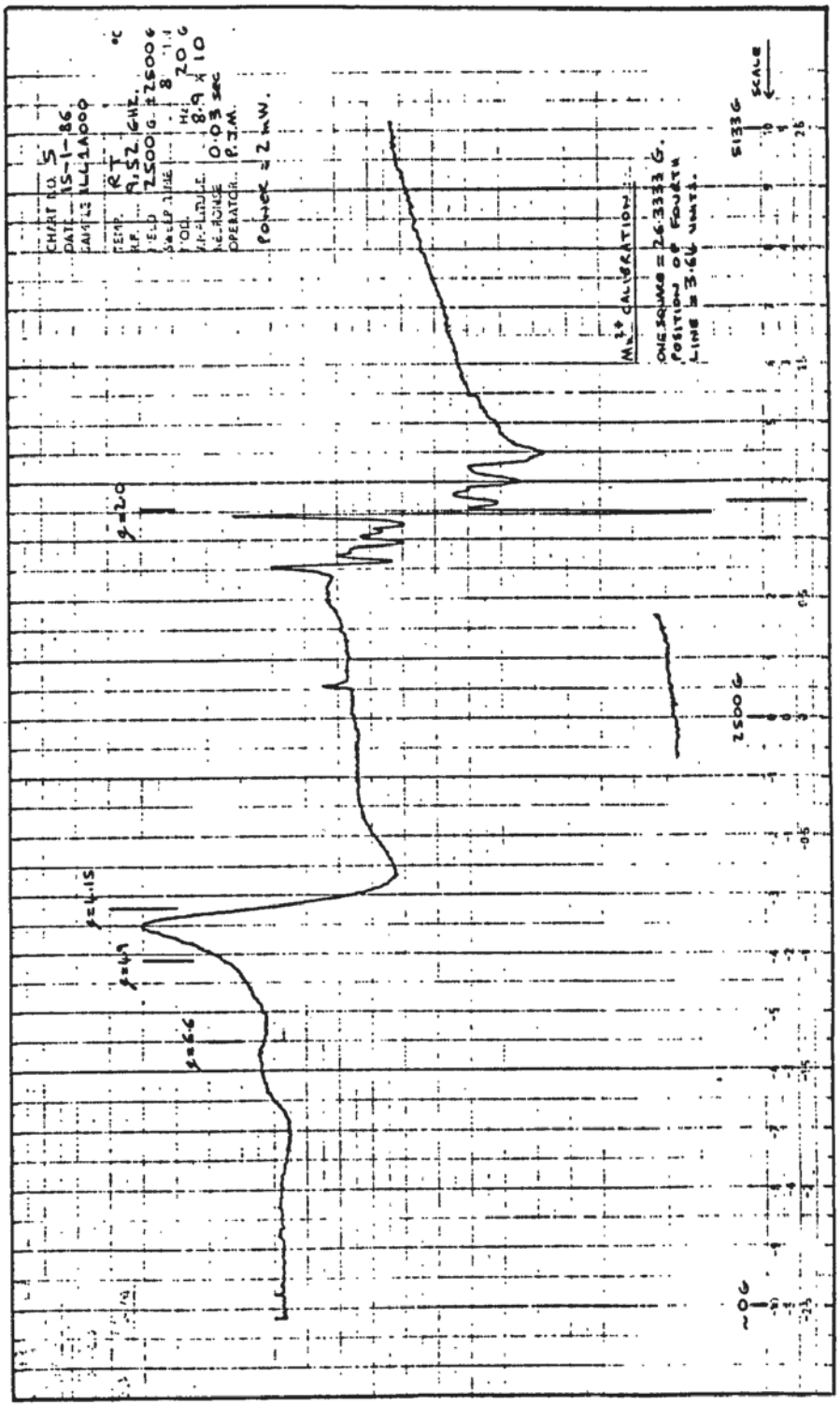

FIG. 49. E.S.R. spectrum of the natural illite sample (3500 ± 500 G).

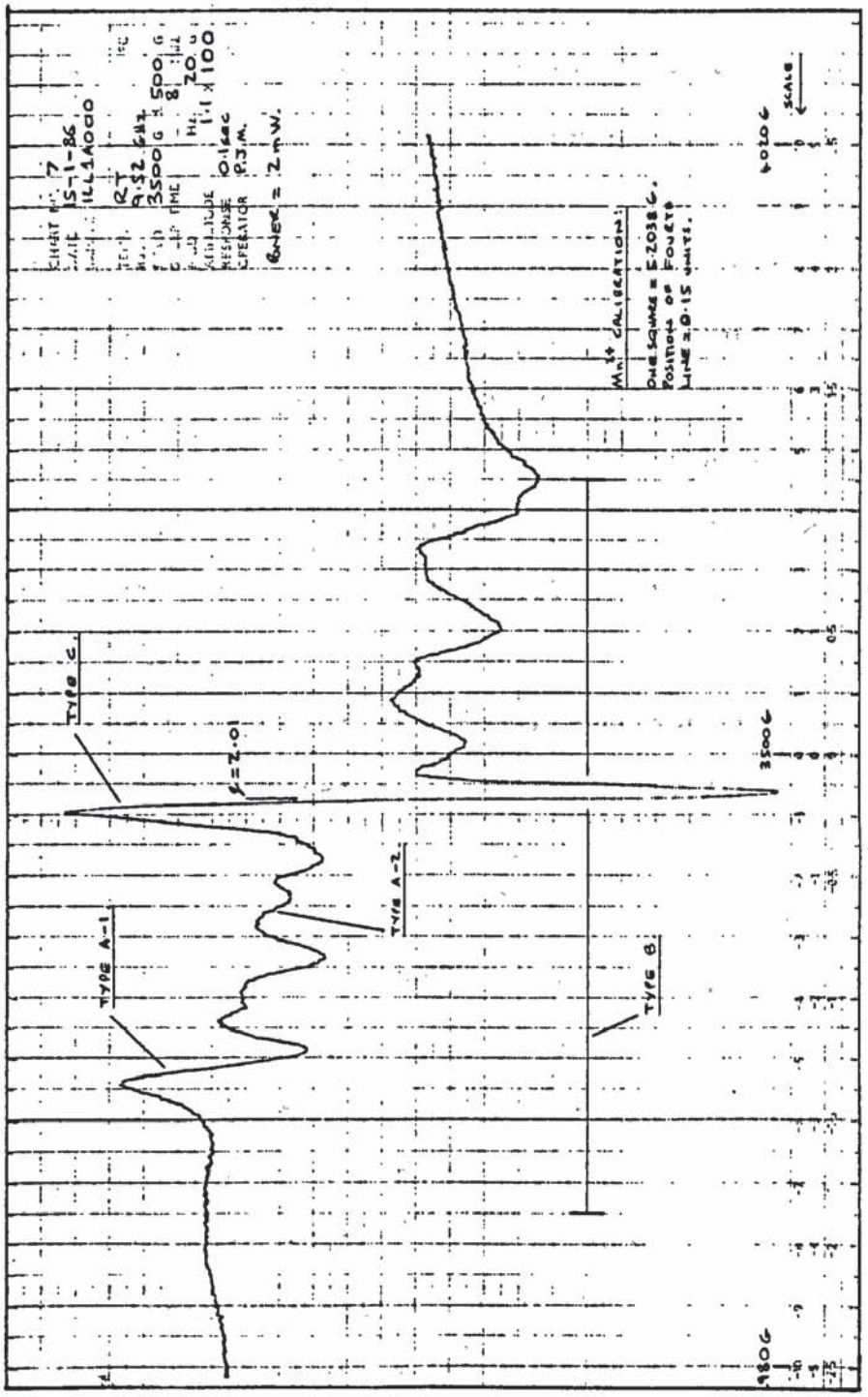

The above interpretation of the E.S.R. spectrum of natural illite is based mainly on the E.S.R. investigation of several shales by Inazumi, A.; Isobe, T. and Tarutani, T.[134]. The results presented here correspond very closely to those presented by them for illite containing shales. Resonance types A-1, A-2, B and C are shown in greater detail in a spectrum run over a narrower magnetic field range, FIG. 49. A schematic representation of the different resonance types is shown in FIG. 34.

Apart from the main resonance types indicated above, there also appears to be a relatively weak resonance at $g \approx 4.9$ and another at $g \approx 6.6$. The $g \approx 4.9$ resonance has been attributed to Fe^{3+} ions in 'partial' orthorhombic symmetry[117],[121],[135], and the $g \approx 6.6$ resonance is probably due to Fe^{3+} ions in an axially distorted environment [121],[136],[137].

Many interpretations of the above resonance types have been reported in the literature, particularly for the $g \approx 4$ (type D) region. Hall, P.L.[117]; Meads, R.E. and Malden, P.J.[135]; and Jones, J.P.E., et al.[138], indicated for kaolinite the presence of at least two Fe^{3+} substitutional sites, whose resonances partially overlap. One gave an isotropic resonance at $g = 4.2$, similar to that observed for the natural illite described here, requiring $\lambda = E/D = 1/3$ and $D \geqslant 0.8\ cm^{-1}$, indicating the presence of Fe^{3+} ions occupying sites of complete orthorhombic symmetry[121],[134]. The crystal field parameters, E and D, describe respectively the rhombic and axial distortion of the Fe^{3+} sites[135]. The other gave an anisotropic three line resonance corresponding to g-values:

$g_z = 4.9$, $g_x = 3.7$ and $g_y = 3.5$; the latter two frequently being unresolved in powder spectra[117]. This would correlate with g = 4.9 for the natural illite sample, and indicate the presence of Fe^{3+} ions occupying sites of 'partial' orthorhombic symmetry having $\lambda = 0.22$ (± 0.01) and $D = 0.45$ (± 0.02) cm^{-1}. The complex spectrum in the g = 4 region has also been related to degrees of crystallinity[135],[138] in that Fe^{3+} may be present both in layers with stacking disorder and in sites of high crystallinity with ordered stacking. Smectites, micas and vermiculites also show complex resonances in the $g \approx 4$ region, which can be interpreted in terms of two non-equivalent octahedrally disposed Fe^{3+} ions, perhaps indicating a distinction between cis- and trans- $FeO_4(OH)_2$ arrangements within these triple layer clay minerals[121].

The broad type B resonance at $g \approx 2.0$ can be attributed to transitions within the super-exchange multiplet resulting from the coupling of two S = 5/2 ions in adjacent cation sites, i.e. Fe-O-Fe pairs, either in the clay lattice or in an impurity phase[117],[121],[135]. Meads, R.E. and Malden, P.J.[135] observed this resonance in kaolinite and attributed it to the iron-rich micas present as impurities. However, some kaolinite samples still showed this resonance after magnetic separation, indicating Fe^{3+} in structural positions and possibly relating to tetrahedrally or octahedrally coordinated sites within illite[134]. The sharp type C resonance at g = 2.010 has been attributed here to organic free radicals, however, lattice defect centres can give a similar resonance [117],[135].

The type A resonances have been attributed here to Mn^{2+} contained within calcite impurity (A-1) and structurally within the natural illite sample (A-2). However, Meads, R.E. and Malden, P.J.[135] observed a similar resonance to type A-2, splitting constant A = 90-100 G, attributable to an impurity phase[117]. Similarly, Mg^{2+}-hectorite doped with Mn^{2+} has been observed to give a line width for the hyperfine sextet of 28.6 G[120], which could provide an alternative explanation for the type A-1 resonance.

6.2.3.2. ILL1A400:

The E.S.R. spectrum of ILL1A400 is shown in FIG. 50. The spectrum is similar to that of the natural illite except for a change in the relative intensities and line widths of some of the resonances. The interpretations of the resonances are, however, the same.

Type A:

The relative intensities of the two types of resonance, A-1 and A-2, are somewhat reduced with respect to the type B resonance.

Type A-1:

$g \approx 2.0$; $A \approx 86$ G; line width ≈ 29 G.

Type A-2:

$g \approx 2.0$; $A \approx 94$ G; line width ≈ 47 G.

Type B:

$g \approx 2.0$. The relative intensity of this broad resonance (line width ≈ 850 G) has increased somewhat from that observed for the natural illite. This, along with the slight increase in line width, is probably indicative of the increase in the number and type of Fe^{3+} sites within the illite due to the oxidation of Fe^{2+} ions[139].

Type C:

$g = 2.012\ (\pm 0.004)$; line width $\approx$ 16 G. The relative intensity of this resonance has reduced with respect to type A and B resonances. This may be explained by the partial oxidation of organic material present within the illite sample or the partial removal of lattice defect centres due to the oxidation of Fe^{2+} ions[117].

Type D:

$g = 4.17\ (\pm 0.05)$; line width $\approx$ 340 G. The slight increase in relative intensity and line width of this type of resonance is again probably due to the oxidation of Fe^{2+} ions within the illite lattice[117],[139],[140]. The apparent increase in relative intensity of the $g \approx 5.0$ resonance with respect to this resonance is indicative of some of the original Fe^{2+} ions occupying different environmental sites to those occupied by Fe^{3+} ions. The resonance observed at $g \approx 6.6$ for the natural illite sample is also present in ILL1A400. This resonance also appears to have increased in intensity slightly.

Type E:

It is not possible to identify positively the presence of this resonance within the spectrum.

6.2.3.3. ILL1A500:

The E.S.R. spectrum of ILL1A500 is dominated by a very broad resonance centred on g = 2.35 ($\pm$0.05), line width $\approx$ 1340 G, FIG. 51. Other resonances occur at g = 4.21 ($\pm$0.05), g $\approx$ 5.0 and g $\approx$ 6.6. A relatively weak six line hyperfine signal centred on g $\approx$ 2.0, A $\approx$ 86 G is present, together with a slightly more intense isotropic signal centred on g = 1.998 ($\pm$0.004), line width $\approx$ 20 G.

The very broad g = 2.35 resonance can be related to the type B resonance of ILL1A400. However, the increase in relative intensity and shift in g-value are probably related to the continuing oxidation of Fe^{2+} ions and the onset of dehydroxylation producing a range of distorted octahedrally coordinated Fe^{3+} sites. The other resonances can be directly related to those observed for ILL1A400 and the natural illite sample.

6.2.3.4. ILL1A600:

The E.S.R. spectrum of ILL1A600 is shown in FIG. 52. The spectrum consists of two relatively sharp and intense isotropic resonances centred on g = 4.25 ($\pm$0.01), line width $\approx$105 G and g = 1.99 ($\pm$0.01), line width $\approx$ 160 G. Other resonances include a relatively weak resonance at g $\approx$ 6.6, a broad resonance (line width $\approx$ 1000 G) g = 2.35 ($\pm$0.05) and a weak six line hyperfine signal centred on g $\approx$ 2.0, A $\approx$ 84 G.

The strong isotropic g = 4.25 resonance and the loss of the already weakened g $\approx$ 5.0 resonance observed in ILL1A500 may be directly attributed to a change in the local symmetry of Fe^{3+} ions from octahedral to more highly distorted six-coordinate configurations as the result of dehydroxylation of the $FeO_4(OH)_2$ environmental sites. The relatively strong isotropic resonance at g = 1.99 could also be interpreted in the same way, perhaps even, the relatively weakened signal with respect to ILL1A500 at g = 2.35 representing an intermediate stage in the local symmetry of Fe^{3+} ions before complete dehydroxylation.

Castner, T., et al.[137], investigating Fe^{3+} contained within glasses, indicated that if an Fe^{3+} ion is at the centre of a regular tetrahedron surrounded by four negative charges, then D = 0 and E = 0 and an intense absorption at g = 2.0 is expected. However, if one of the four negative charges is not equal to the other three, then D $\neq$ 0 and E = 0 and an intense absorption at around g = 6.0 is expected. If only two of the four charges are equal, then D = 0 and E $\neq$ 0 which gives an intense absorption at g = 4.28. Although no direct evidence

is available here, it could be possible that the g = 1.99 and g = 4.25 resonances for ILL1A600 result from Fe^{3+} ions in regular and distorted tetrahedral sites respectively. An increase in intensity of the g = 4.2 resonance for kaolinite, upon dehydroxylation of the $FeO_2(OH)_4$ octahedral sites, has been interpreted to a change in the local symmetry of Fe^{3+} from distorted octahedral to distorted tetrahedral configurations[121],[140]. However, it is unlikely that $FeO_4(OH)_2$ octahedral sites in 2:1 phyllosilicates can give rise to a large proportion of tetrahedral configurations upon dehydroxylation.

The weak six line hyperfine resonance at $g \approx 2.0$ can be attributed to the type A-1 resonance observed in the natural illite sample. However, its reduction in relative intensity here and in ILL1A500 cannot clearly be explained, particularly as this resonance is attributed to Mn^{2+} ions present within calcite impurity. Perhaps a considerable proportion of the Mn^{2+} resonance observed in the natural illite sample and ILL1A400 is in fact intimately associated with the clay mineral, either as an exchange ion within the interlayers or as a structural component. Dehydration of the clay mineral would remove the Mn^{2+} resonance for exchanged ions, whereas dehydroxylation would remove the resonance due to structural Mn^{2+}. These would both produce a modified Mn^{2+} environment such that no electron spin resonance spectrum could be obtained.

6.2.3.5. ILL1A700:

The E.S.R. spectrum of ILL1A700 is shown in FIG. 53. The spectrum consists of three relatively intense resonances centred on: g = 4.25 ($\pm$0.01), line width $\approx$ 94 G; g = 2.02 ($\pm$0.02), line width $\approx$ 370 G and g = 1.98 ($\pm$0.01), line width $\approx$ 130 G. Other resonances include a relatively broad and very weak resonance at g $\approx$ 6.6, and a very much weakened resonance corresponding to the g = 2.35 resonance observed in ILL1A600. There are no apparent resonances indicating the presence of Mn^{2+} ions.

The observed resonances can be interpreted in the same way as those for ILL1A600. Changes include the appearance of a relatively broad and intense resonance at g = 2.02 and very much weakened g = 2.35 and g $\approx$ 6.6 resonances. These changes are representative of further dehydroxylation of the clay and slight structural changes within the relic octahedral lattice. The g = 2.02 resonance can be attributed to exchange interactions between clusters of fully dehydroxylated Fe^{3+} ions. This may tentatively indicate the presence of two former Fe^{3+} sites within the clay structure, one of which undergoes dehydroxylation at a lower temperature than the other, i.e. one between 500-700^{o}C (g = 4.25 and 1.98) and 600-800^{o}C (resulting in g = 2.02). Alternatively, Fe^{3+} ions may be migrating within the relic illite structure producing Fe^{3+} clusters above 600^{o}C.

6.2.3.6. ILL1A800:

The E.S.R. spectrum of ILL1A800 is shown in FIG. 54. The spectrum consists of an intense resonance centred on g = 2.01 ($\pm$0.01), line width $\approx$ 380 G; and a relatively small resonance centred on g = 4.25 ($\pm$0.02), line width $\approx$ 80 G. These resonances can be interpreted in the same way as those for ILL1A700. Changes include the apparent loss of the relatively intense resonance centred on g = 1.98 and an increase in intensity of the g = 2.01 resonance with respect to that at g = 4.25. These changes are indicative of structural changes taking place within the relic octahedral lattice or of an increase in Fe-O-Fe pair interactions caused by the migration of Fe^{3+} ions.

6.2.3.7. ILL1A900:

The E.S.R. spectrum of ILL1A900 is identical in all respects to that of ILL1A800. Resonances occur at g = 2.01 ($\pm$0.01), line width $\approx$ 400 G and g = 4.25 ($\pm$0.02), line width $\approx$ 80 G.

6.2.3.8. ILL1A1000:

The E.S.R. spectrum of ILL1A1000 is very similar to that of ILL1A900 and ILL1A800, except for an increase in the relative intensity of the g = 1.98 resonance with respect to the g = 4.25 resonance, FIG. 55. The g = 1.98 ($\pm$0.01) resonance, line width $\approx$ 320 G, is slightly assymetrical in shape. This probably indicates the presence of two overlapping resonances at g $\approx$ 2. The decrease in line width with respect to ILL1A900 may indicate the breakdown of the relic illite lattice and the formation of new crystalline phases containing Fe^{3+} ions.

6.2.3.9. ILL1A1100:

The E.S.R. spectrum of ILL1A1100 is identical to that of ILL1A1000. Resonances occur at g = 1.98 ($\pm$0.01), line width $\approx$ 300 G, and g = 4.21 ($\pm$0.02).

6.2.3.10. ILL1A1200:

The E.S.R. spectrum of ILL1A1200 consists of a very broad resonance centred on g = 2.03 ($\pm$0.02), line width $\approx$ 1000 G, and a relatively sharp resonance centred on g = 4.15 ($\pm$0.02), line width $\approx$ 94 G. The spectrum is shown in FIG. 56, and is typical of an Fe^{3+} containing glass[137]. The Fe^{3+} ions occupying a range of environmental sites within the glass, together with Fe-O-Fe pair interactions result in the very broad resonance at g = 2.03. The g = 4.15 resonance is representative of Fe^{3+} ions in a distorted tetrahedral environment[136],[137].

6.2.3.11. ILL1A1300:

The E.S.R. spectrum of ILL1A1300 is identical to that of ILL1A1200. Resonances occur at g = 2.04 ($\pm$0.02), line width $\approx$ 1100 G; and g = 4.07 ($\pm$0.02), line width $\approx$ 95 G.

FIG. 50. E.S.R. spectrum of ILL1A400.

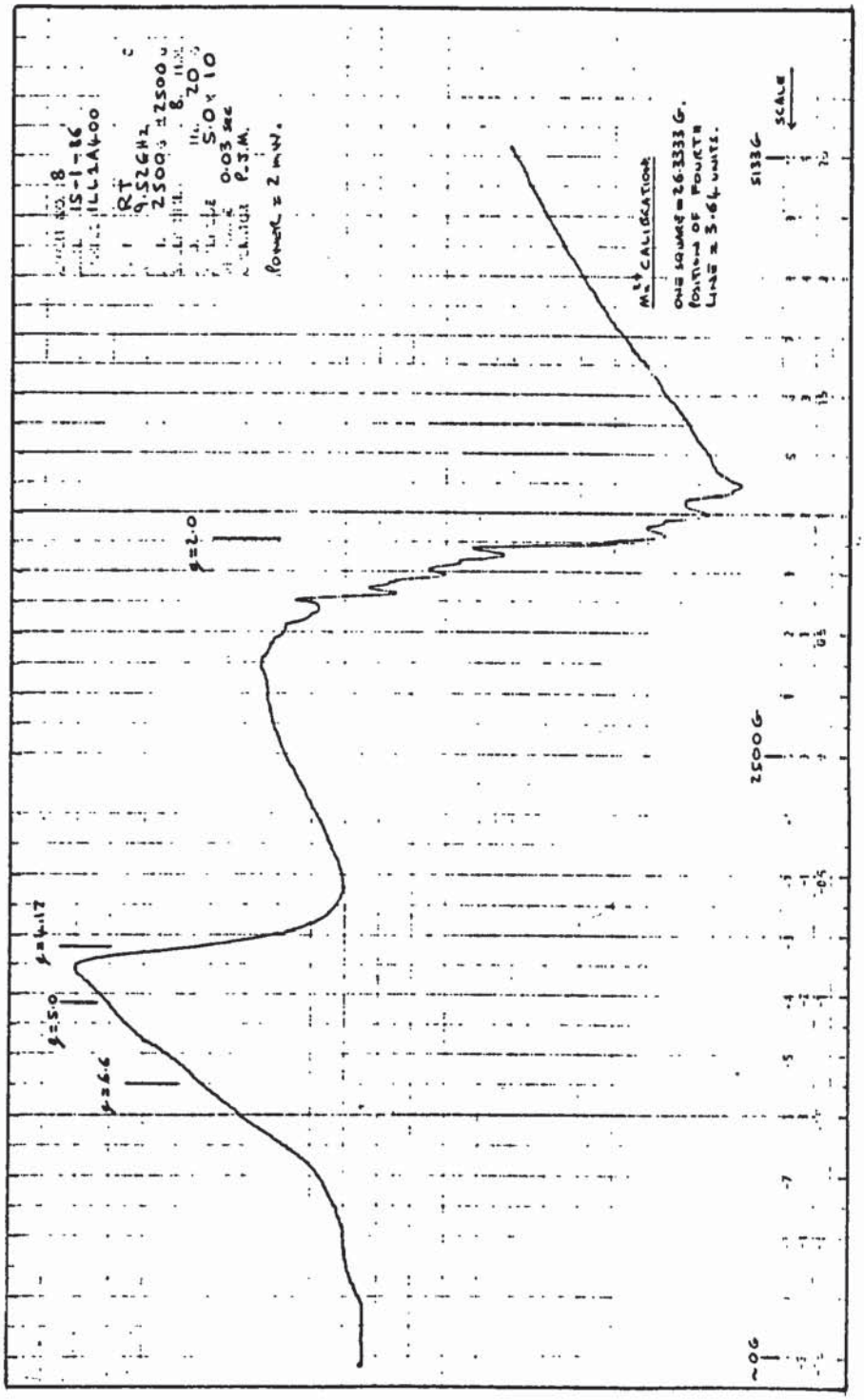

FIG. 51. E.S.R. spectrum of ILL1A500.

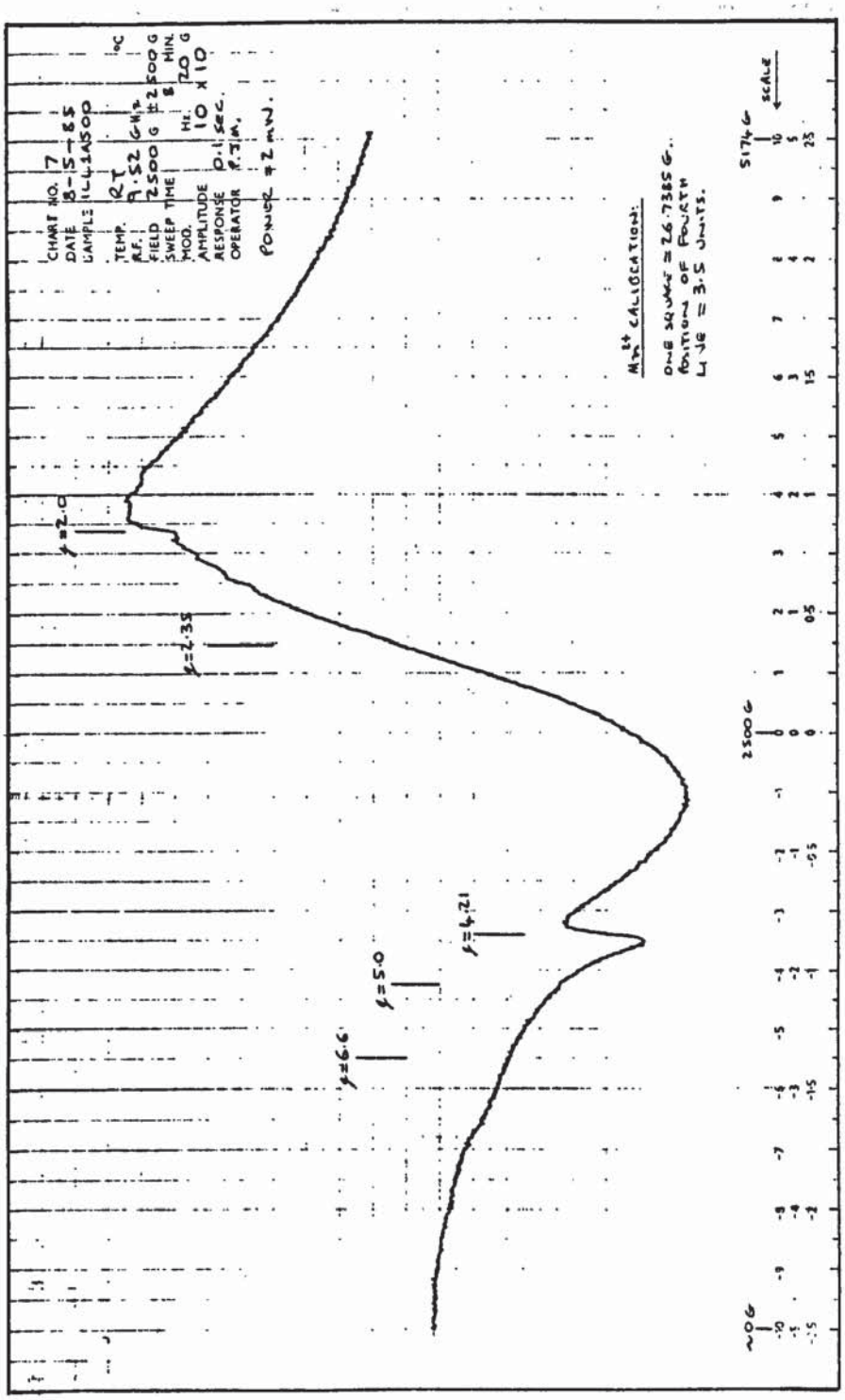

FIG. 52. E.S.R. spectrum of ILL1A600.

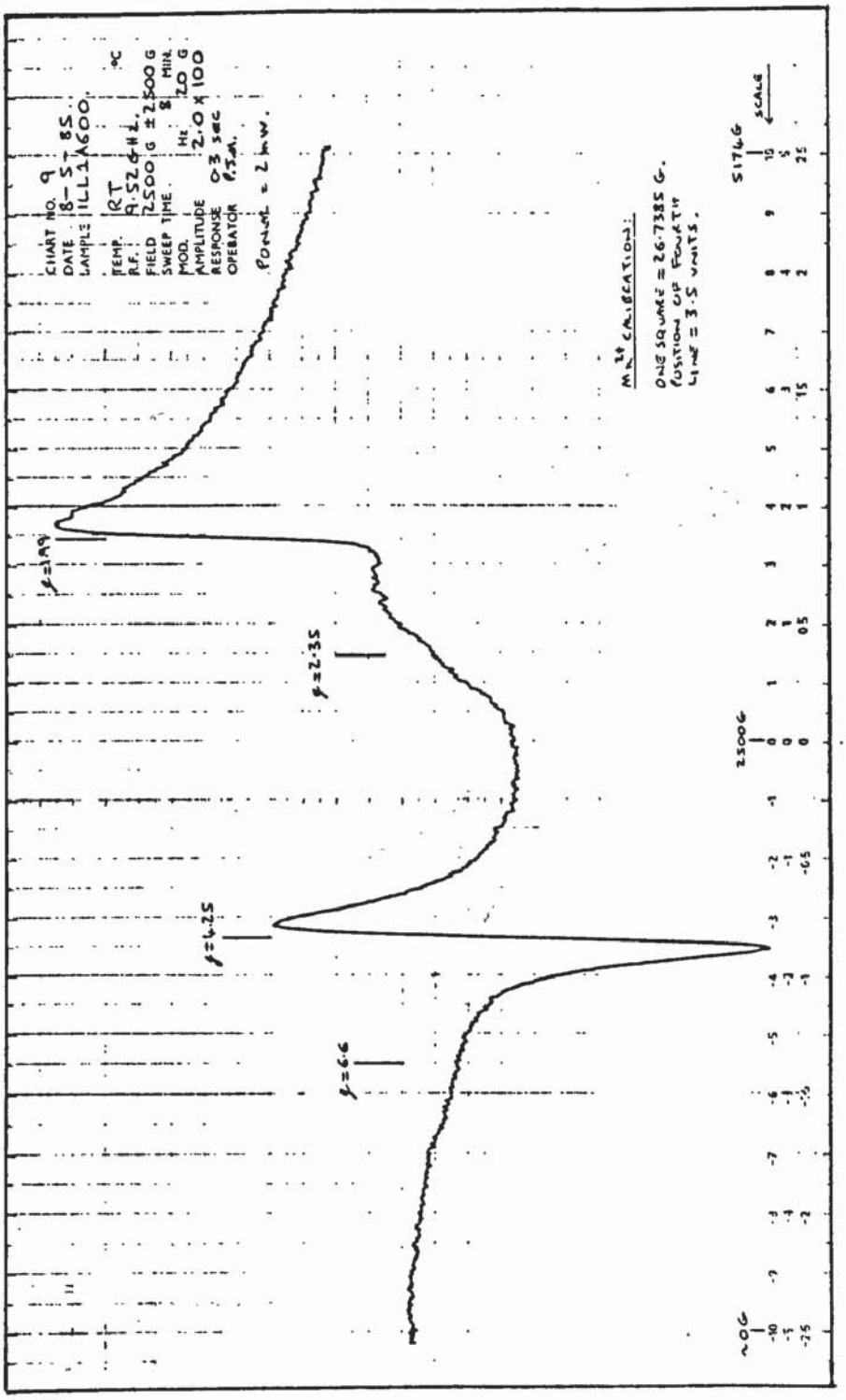

FIG. 53. E.S.R. spectrum of ILL1A700.

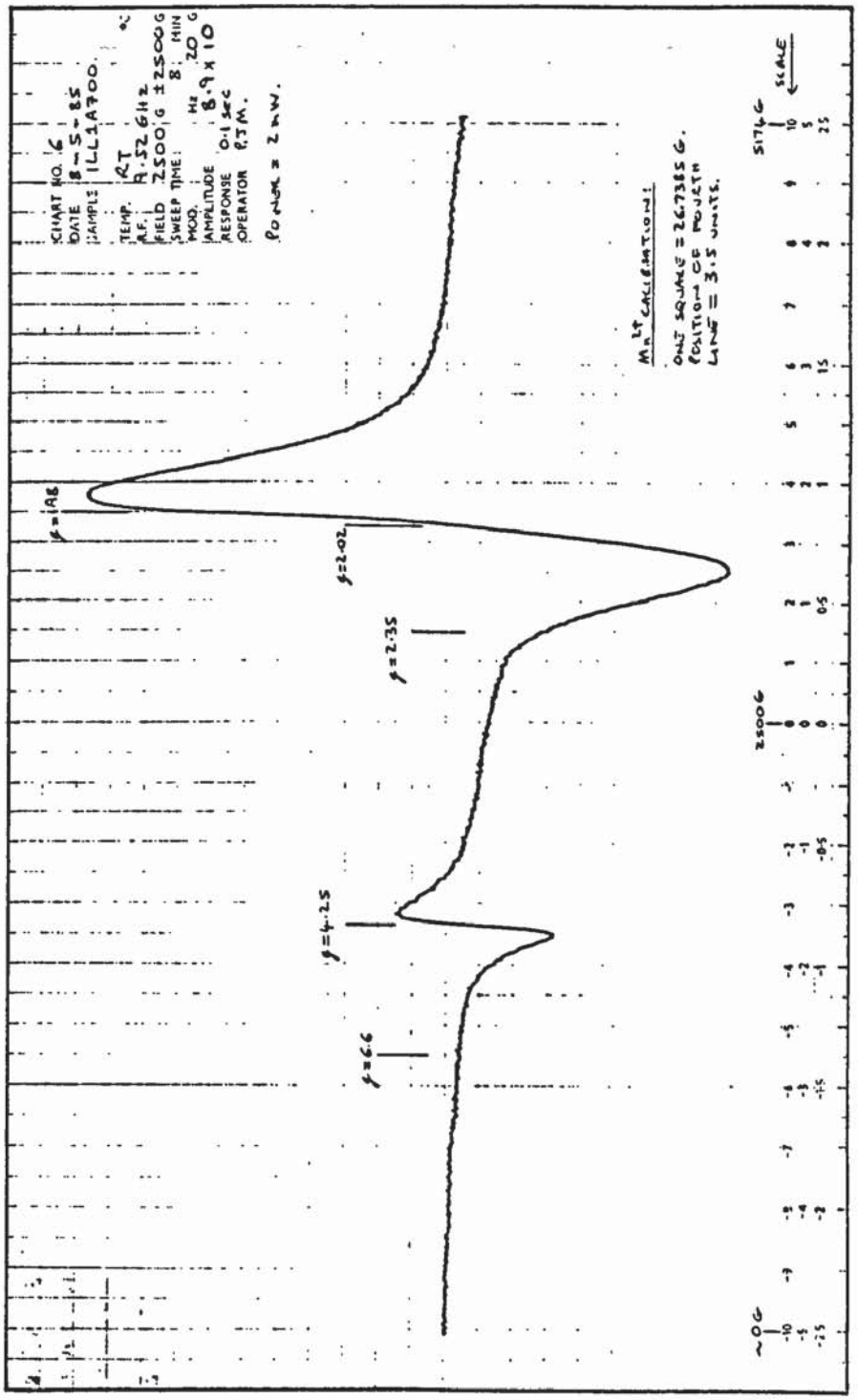

FIG. 54. E.S.R. spectrum of ILL1A800.

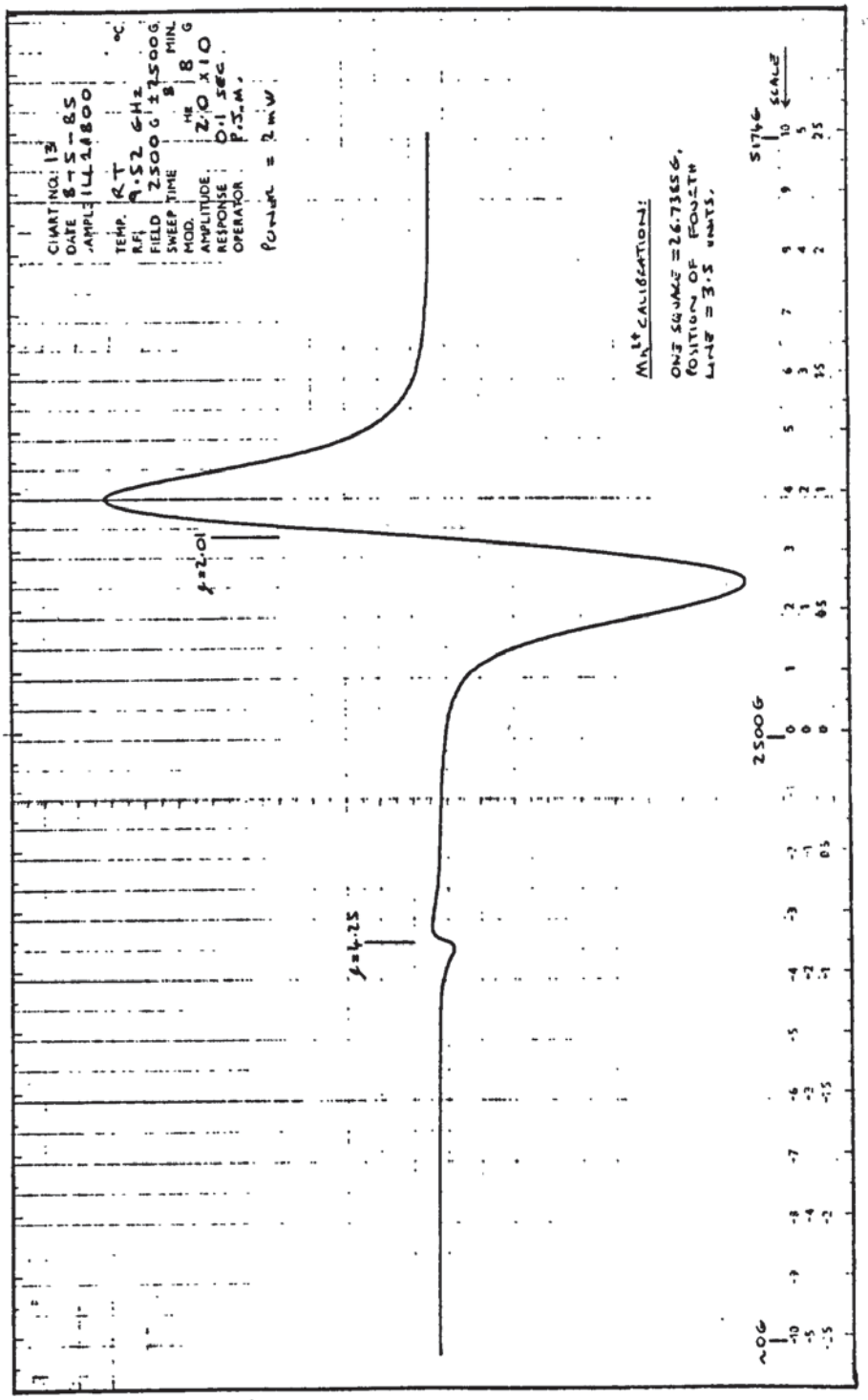

FIG. 55. E.S.R. spectrum of ILL1A1000.

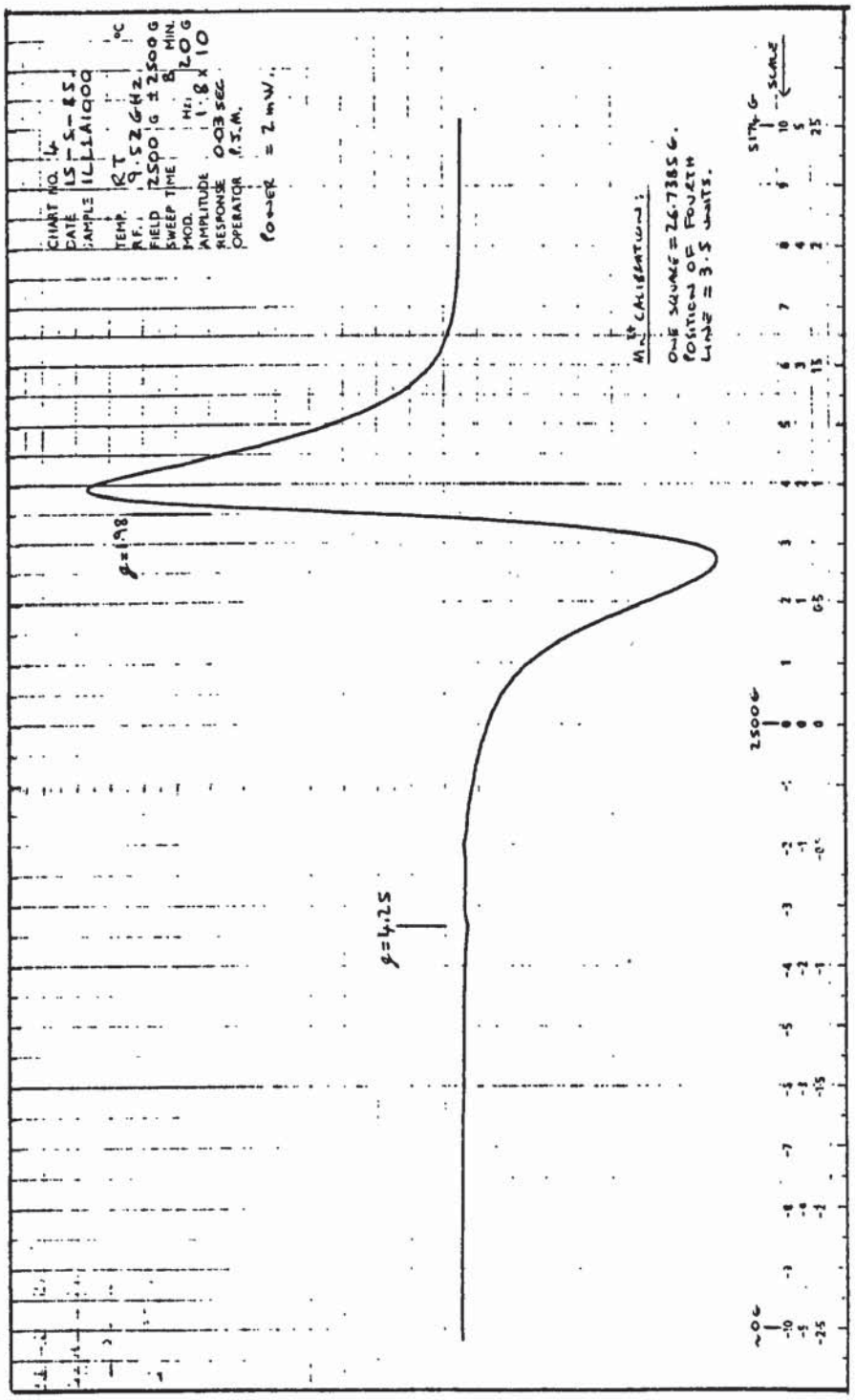

FIG. 56. E.S.R. spectrum of ILL1A1200.

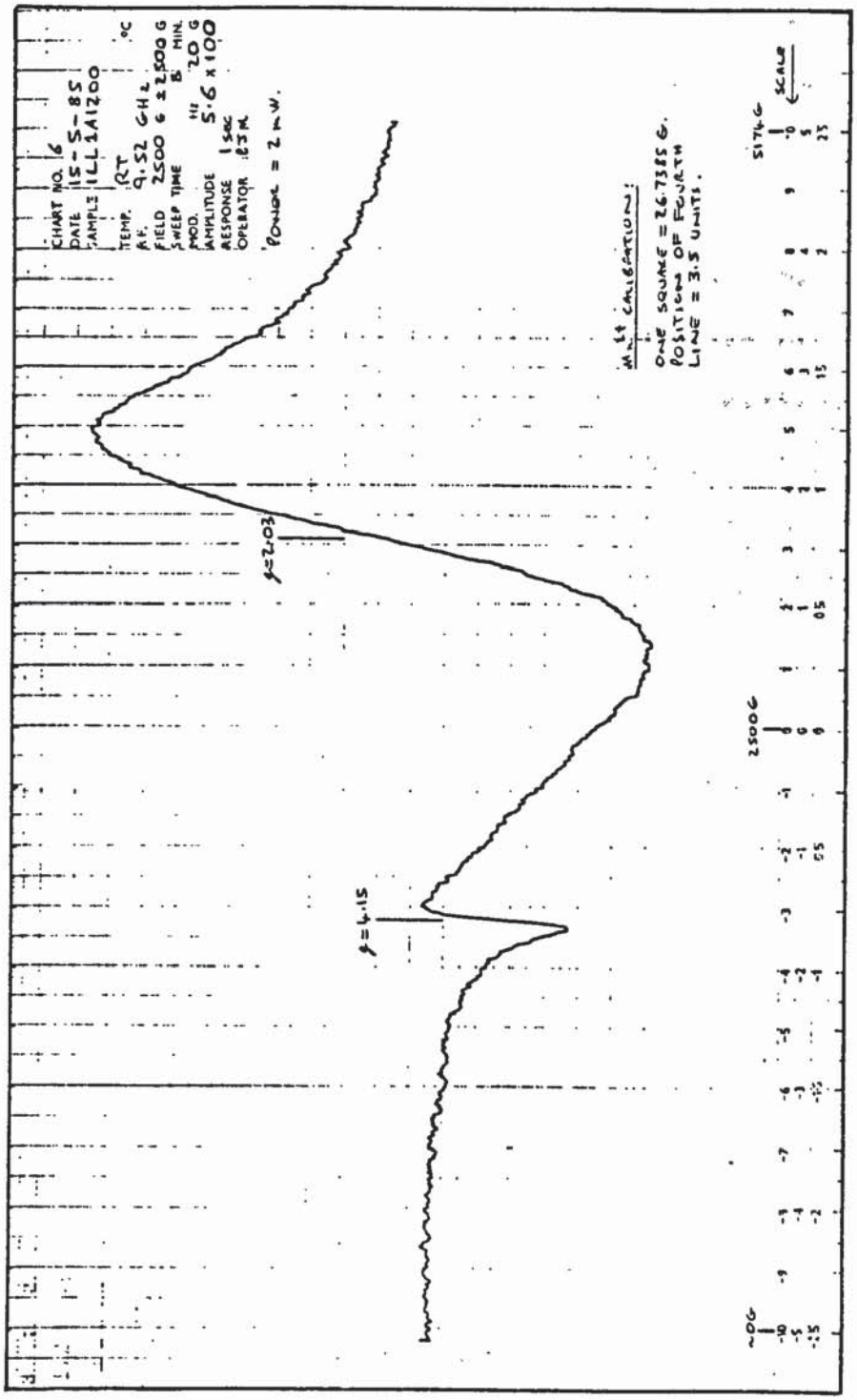

6.2.4. DISCUSSION AND SUMMARY;

The results and spectra of the preceding sections have been discussed and interpreted, on an individual sample/experimental technique basis, alongside their presentation. However, it is intended here to draw together the various components within these sections and give an overall picture of the thermo-chemical changes taking place within the natural clay mineral upon heating.

Results for the major element analysis of the natural illite sample, by X-ray fluorescence, have been presented in TABLE 17. The Mössbauer spectroscopy data, presented individually for the natural illite and each thermally treated sample, have been assimilated in TABLE 19, together with a summary of the major conclusions deduced from the X-ray diffraction study. Electron spin resonance data for the various illite samples is summarised in TABLE 20. A graphical representation of the major changes occurring during the thermal treatment of illite are summarised in FIG. 57.

The elemental analysis (XRF) of the natural illite sample used in this study is in close agreement with literature data for natural illites[74],[75]. The slightly higher than expected weight percent of SiO_2, and the presence of a relatively strong XRD trace for α-quartz[131] clearly indicates the presence of a quartz (SiO_2) impurity phase within the sample. Otherwise, the X-ray diffractogram of the natural clay mineral was consistent with that expected for illite[73]. A representative basal spacing [d(001)] of 10.05 Å was observed, but two relatively weaker signals,

TABLE 19. ^{57}Fe Mössbauer data for thermally treated illite: summary of XRD conclusions.

Temperature (°C)	$\delta(\pm 0.05)^a$ (mm s^{-1})	$\Delta(\pm 0.05)^a$ (mm s^{-1})	$\Gamma_{1/2}(\pm 0.05)^a$ (mm s^{-1})	XRD conclusions
Ambient	1.21	2.88	0.39	
	1.48	2.84	0.62	
	0.38	0.67	0.60	
400	1.18	2.90[b]	0.69	
	0.30	1.10	0.91	
500	0.36	1.53	0.71	Little change, SiO_2 impurity.
	0.36	0.95	0.59	
600	0.32	1.73[b]	0.66	
	0.37	1.11	0.54	
700	0.34	1.76	0.68	
	0.36	1.14	0.50	
800	0.37	1.42	0.79	
900	0.33	1.36	0.75	Loss of illite structure, growth of spinel
	0.28	0.78	0.43	
	(Hint of magnetic phase)			
1000	0.27	0.88	0.60	Spinel + α-Fe_2O_3 (quartz decreasing)
	0.42[b]	−0.08[b]	(H = 513 kG)[d]	
1100	0.33	0.83	0.54	
	0.40	−0.15	(H = 516 kG)[d]	
1200	0.32	0.77	0.55	Mullite + spinel loss of α-Fe_2O_3 Glass
	0.83[c]	2.15[c]	0.68[c]	
1300	0.85	2.59	0.67	
	0.41	1.13	0.77	

[a] Maximum error
[b] Error, > ±0.05 mm s^{-1}
[c] Error, > ±0.10 mm s^{-1}
[d] Error, ≤ ±4 kG

TABLE 20. Summary of ESR data for specimens of illite heated to the indicated temperatures. Resonances are classified by the g-value.

TEMPERATURE (°C)	Mn^{2+}	IRON(III) FEATURES	ORGANIC
Ambient	~2.0[a]	2.0,4.15,4.9,6.6	2.010
400	~2.0[a]	2.0,4.17,5.0,6.6	Trace
500	Trace	2.35(br),4.21,5.0,6.6	Trace(?)
600	Trace(~2.0)	2.35(br),1.99,4.25,6.6(w)	X
700	Not observed	2.35(w),1.98,2.02(s)4.25(m), 6.6(w)	X
800	Not observed	2.01(s),4.25(w)	X
900	Not observed	2.01(s),4.25(w)	X
1000	Not observed	1.98(s),4.25(w)	X
1100	Not observed	1.98(s),4.21(w)	X
1200	Not observed	2.03(br),4.15(m)	X
1300	Not observed	2.04(br),4.07(m)	X

(a) = Complex six-line spectrum; (br) = broad(width in excess of 1000 G); (s) = strong resonance
(m) = moderate resonance; (w) = weak resonance.

FIG. 57: Summary of XRD, Mössbauer and ESR results for illite. ($\bar{\delta}$ and $\bar{\Delta}$ represent average chemical isomer shift and quadrupole splitting, respectively).

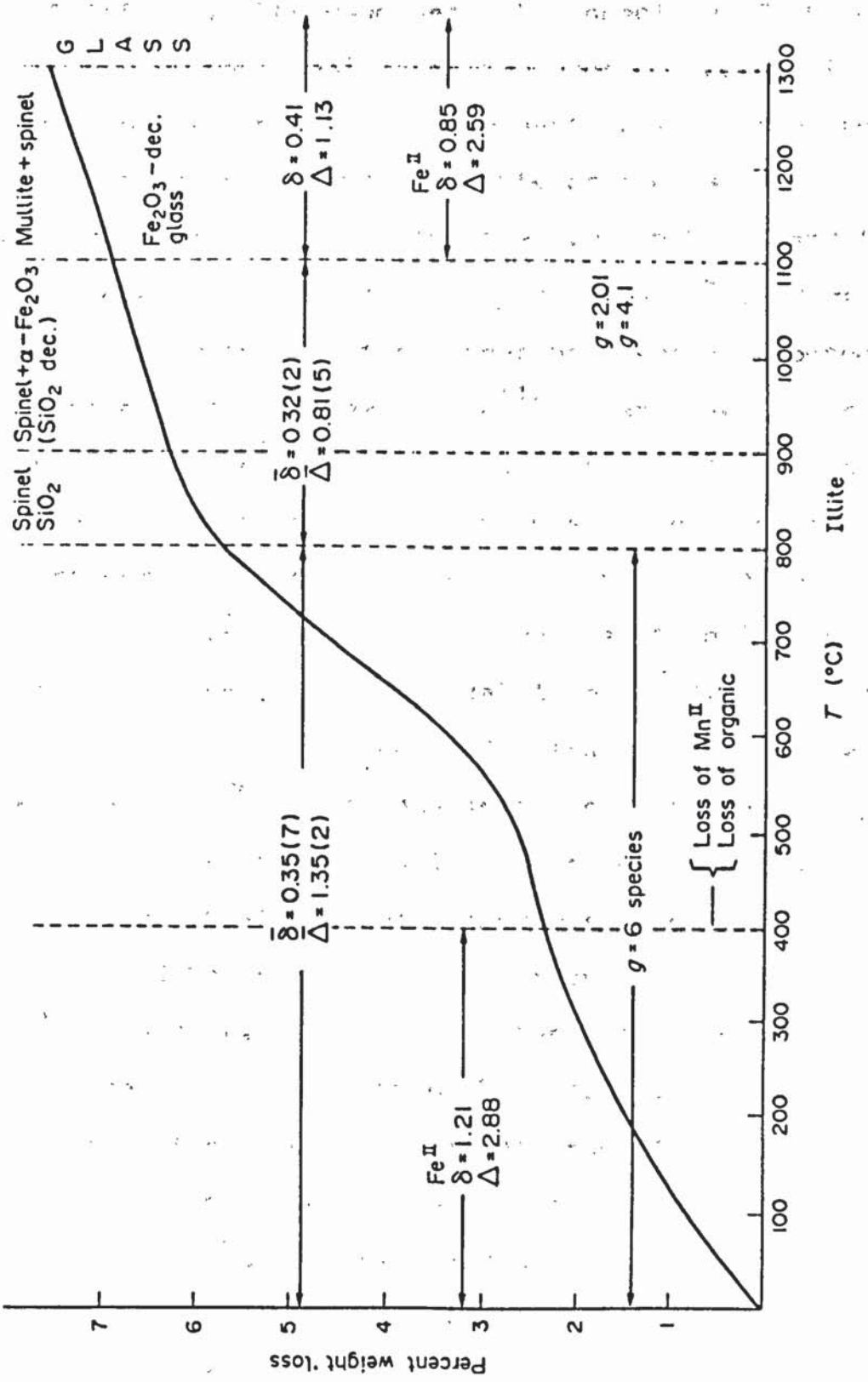

d-spacings = 7.25 and 13.10 Å, imply the presence of some chlorite and mixed-layer illite-montmorillonite. The elemental analysis also indicates that a trace of manganese is present within the sample, and this is borne out by the ESR data (TABLE 20). The manganese (II) spectrum (FIGS. 48 and 49) is complex and consists of two overlapping six line spectra superimposed on a broad component arising from iron (III). These resonances have been interpreted as Mn^{2+} contained within calcite impurity ($g \approx 2.0; A \approx 81$ G) and the illite structure ($g \approx 2; A \approx 94$ G) respectively[134]. However, a similar resonance type to the former has been attributed to Mn^{2+} in exchange sites for hectorite[120], and the latter to another impurity phase[117],[135]. The interpretation is not clear-cut, and the apparent overlapping six line spectra may simply represent a single six line spectrum showing some evidence of forbidden electronic and nuclear transitions giving weaker signals between the individual lines (FIG. 49). Such a spectrum would imply the presence of a trace of calcite with a manganese impurity[136]. If this were the case, following a calcite-to-aragonite phase transition, the carbonate should decompose between 700-800°C when, from past experience[136], the signal should be lost on the formation of silicate phases above 800°C. However, in this study the resonance due to Mn^{2+} decreases in relative intensity on heating from 400 to 600°C, the signal being lost under a dominant iron (III) contribution. No signal corresponding to Mn^{2+} was observed in the illite sample heated to 700°C. Calcite was not detectable by XRD, indicating that if calcite is present within the natural illite sample, it is so, only as a very minor constituent.

This would tend to indicate that an alternative explanation is required for the Mn^{2+} signal. In section 6.2.3.1 it was suggested that the Mn^{2+} resonance attributed to calcite may in fact be due to Mn^{2+} present in exchange sites on the clay mineral[120].

If the observed Mn^{2+} signal is attributed to Mn^{2+} intimately associated with the illite, either as an exchange ion within the interlayers or as a structural component, then dehydration of the clay mineral would remove the Mn^{2+} resonance for exchanged ions and dehydroxylation would remove the resonance due to structural Mn^{2+}. Both these changes would produce a modified Mn^{2+} environment such that no Mn^{2+} spectrum could be obtained[136]. Comparison of the above scenario with the observed data indicates that the manganese (II) is in fact substitutional in the illite, which upon dehydroxylation results in a diminishing ESR signal from 400 to 600°C. At 700°C dehydroxylation is in effect complete and no Mn(II) ESR signal is observed.

The Mössbauer spectrum of the natural illite (FIG.37) has been fitted with two quadrupole doublets and interpreted as containing iron (III) and iron (II) in cis-octahedral coordination[145],[146], with the possible contribution of some iron (III) in trans-coordination[106]. This is in agreement with that reported by Ericsson, T. et al.[106] for the spectrum of a similar illite (No. 36) to which they have fitted two iron (III) doublets (δ = 0.32, Δ = 0.58 mm/s; δ = 0.41, Δ = 1.07 mm/s) and one iron (II) doublet (δ = 1.18, Δ = 2.88 mm/s). The two iron (III) doublets were assigned to cis- and trans-octahedral coordination (M(2) and M(1) sites)

respectively, the former being the most intense of the two doublets and therefore the 'preferred' location for iron (III). In a dioctahedral clay mineral the ions in the octahedral layer may occupy sites with either cis- or trans-environments, and from simple electrostatic reasoning [88] the quadrupole splitting (Δ) of the trans-site should be twice that of the cis-site; thus giving rise to the above interpretation of the iron (III) being predominantly located in the cis-M(2) sites. However, Johnston, J.H. and Cardile, C.M.[142] have indicated that iron (III) within a montmorillonite is mainly contained within the trans-M(1) sites. This is based on a careful electron diffraction study by Tsipursky, S.I. and Drits, V.A. [144]. It has since been suggested by Cardile, C.M. and Johnston, J.H.[133] that the actual "best fit" of a Mössbauer spectrum of montmorillonite is often an artefact of the fitting procedure and that in reality the iron (III) ions, located in essentially M(1) sites, are subjected to differing degrees of distortion in these sites and hence are subject to a spectrum of electric field gradients at the nuclei. This would result in a complex Mössbauer spectrum of multiple, unresolvable iron (III) quadrupole doublets with very similar parameters. The half-width of the spectral lines will give some measure of the range of field gradients operating, whereas the quadrupole splitting will simply represent an average value for broad doublets. It is hypothesised that this is also the case for illite, and that the interpretation put forward for iron (III) by Ericsson, T. et al.[106] is simplistic. Likewise, the interpretation of the natural illite within this work, as containing iron (III) in cis-M(2) sites with a possible contribution from trans-M(1) sites, is also thought to

be simplistic. The single doublet fit (TABLE 19) for iron (III) is therefore considered to be the most appropriate, and to represent the average iron (III) environment within the illite structure (δ = 0.38, Δ = 0.67 mm/s). The inadequacy of the M(1), M(2) site assignment is further indicated by the XRD data which suggests the natural illite sample may not be monophasic. In a similar fashion, the iron (II) spectrum has only been fitted with a single quadrupole doublet. However, a small asymmetry in the high velocity line of the iron (II) doublet resulted in the fitting of a third doublet to the overall spectrum. Ericsson, T. et al.[106] interpreted this asymmetry as being due to iron (II) in trans-M(1) sites as opposed to cis-M(2) sites for the major iron (II) component. It was found that this third doublet (δ = 1.48, Δ = 2.48 mm/s) could be removed by washing the illite in 0.5M acetic acid, thus suggesting that it arises from one of the hydrates, $FeSO_4.nH_2O$[5],[6], e.g. szomolnokite (n = 1), rozenite (n = 4) or melanerite (n = 7). A trace of sulphur was detected by XRF analysis of illite (TABLE 17), but the quantity was too small to make this assignment anything but tentative.

The ESR spectrum of the natural illite (FIG. 48) is complex, although it agrees well with that presented previously in a study of illite containing shales[134]. The sharp isotropic resonance (g = 2.010) which vanishes on heating the illite to above 500°C is attributed to organic radicals which are oxidised upon heating. The manganese (II) components have already been discussed, and there are five observable iron (III) components to the spectrum. A broad resonance centred on g $\approx$ 6 (presumably with a counterpart

at g = 2.0 hidden under the major broad feature of the spectrum) can be interpreted as arising from iron (III) in an axially distorted environment[121],[136],[137]. The broad resonance at $g \approx 2$ can be assigned with reasonable certainty to transitions within the super-exchange multiplet resulting from the coupling of two $S = {}^{5}/_{2}$ ions in adjacent cation sites, i.e. Fe-O-Fe pairs either within the clay lattice or in an impurity phase[117],[121],[135]. The most probable impurity phase would be Fe_2O_3 or perhaps FeO(OH) — no magnetic spectrum was observed in the Mössbauer study, but if the particle size were small superparamagnetic behaviour is possible. Since no specific iron oxide impurity phase was observed in the XRD trace, the balance of probability is that this ESR feature arises from adjacent iron (III) ions in structural cation sites. However, the resonance pattern designated 'type E' in section 6.2.3.1. and represented by a general signal drift across the whole spectrum, has been interpreted as due to iron oxide impurities, probably Fe_2O_3. Therefore, the presence of iron oxide impurities cannot be ruled out. The $g \approx 4$ resonances in clay minerals have been given many interpretations in the literature[117],[135],[138]; in the present case the g = 4.15 resonance is considered to arise from iron (III) sites of complete orthorhombic symmetry within the clay mineral structure[121],[134]. The $g \approx 4.9$ resonance has been interpreted as iron (III) occupying sites of 'partial' orthorhombic symmetry[117]. These two resonances, representing two non-equivalent octahedrally disposed iron (III) sites, may perhaps indicate a distinction between cis- and trans-$FeO_4(OH)_2$ arrangements within the illite

structure[121]. Thus the ESR data for the natural illite sample confirms that a variety of iron (III) sites and environments exist within the illite structure. This is parallelled by the observed iron (III) Mössbauer data, justifying the interpretation of the broad quadrupole doublets as representing a range of similar iron (III) environments.

The loss of absorbed water from illite is in effect complete by 400°C and the structural water is lost between 400 and 800°C (FIGS. 36 and 57). XRD revealed no appreciable changes within the illite structure on heating to 800°C, indicating that the X-ray crystallinity of illite is not lost as a result of dehydroxylation[130]. The local environments of the iron ions will obviously change due to dehydroxylation, this is seen in the Mössbauer data for illite heated to 400°C which shows a more distorted range of iron (III) sites as indicated by the larger value of Δ and $\Gamma_{\frac{1}{2}}$ (TABLE 19). Another change is the oxidation of iron (II) to iron (III), which is in effect complete on heating to 500°C. The illite samples heated to 500, 600 and 700°C show two clear doublets, one with parameters comparable to the 400°C spectrum and a new doublet with a greater quadrupole splitting. At 800°C, when the illite structure is about to undergo irreversible breakdown, restructuring of the silicate lattice and possible migration of the iron (III) ions has produced a range of similar less distorted octahedral sites. This is reflected in the single doublet fit at 800°C and the reduction of Δ from 1.76 mm/s for one of the doublets at 700°C to 1.42 mm/s. The changes occurring in the Mössbauer data between 400 and 700°C can be interpreted on the basis of there being two

iron (III) ligand environments, i.e. FeO_6 and $FeO_{6-x}(OH)_x$ ($2 > x > 0$); a range of site micro-symmetries existing in each of these ligand environments. At 400°C the $FeO_{6-x}(OH)_x$ sites (representing fully hydroxylated and partially dehydroxylated sites) would be expected to dominate, the doublet with δ = 0.30-0.36 and Δ = 0.95-1.14 mm/s being assigned to these environments. This would imply that the second doublet at 500, 600 and 700°C with the larger Δ (1.53-1.76 mm/s) corresponds to the FeO_6 sites (representing fully dehydroxylated sites) which are, by implication, more distorted. The ESR spectra show a significant increase in the broad $g \approx 2.0$ resonance and a more complex $g \approx 4.0$ resonance on heating to 400°C. The $g \approx 6.0$ resonance is also present. An increase in the relative intensity of the $g \approx 5.0$ resonance with respect to the g = 4.17 resonance may possibly be related to the oxidation of iron (II), the iron (II) ions originally occupying different environmental sites to those occupied by iron (III) ions. Samples heated to 500, 600, 700 and 800°C show a progression to two broad isotropic resonances at 800°C. A resonance feature at g = 2.35 is apparent at 500 and 600°C which could well be the $g \approx 2.0$ component expected with the $g \approx 6$ component for iron (III). These resonances are gradually lost on heating to 800°C. At 800°C, the dominant feature of the spectrum is a very broad isotropic resonance centred on $g \approx 2.01$, which together with a weak feature at g = 4.25 can now, following the Mössbauer deductions, be ascribed to the fully dehydroxylated environmental sites, FeO_6. A contribution to the $g \approx 2.0$ resonance from Fe-O-Fe pair interactions due to restructuring of the illite and the

possible migration of the iron (III) ions to form clusters cannot be ruled out. Similarly, the $g \approx 6$ and $g = 2.35$ features can be tentatively assigned to the partially dehydroxylated environmental sites, $FeO_{6-x}(OH)_x$. The broad $g \approx 2.0$ resonance at 700°C appears to consist of two components (FIG. 53); a $g = 2.02$ and $g = 1.98$ resonance. The $g = 1.98$ resonance can be related to $g = 1.99$ at 600°C and $g = 2.0$ at 500°C which have been assigned to FeO_6 environments. The relatively broader $g = 2.02$ component, which appears as the $g = 2.01$ resonance at 800°C, therefore probably represents the increasing Fe-O-Fe pair interactions due to restructuring or iron (III) ion migration. From the above it can be clearly be seen that the Mössbauer data and ESR data compliment each other to a satisfying degree of self consistency.

Further heating of the illite beyond 800°C results in the irreversible breakdown of the silicate structure and the crystallisation of new phases. Heating to 900°C and above produced initially a spinel phase and then hematite (α-Fe_2O_3) at 1000°C. The decrease in the XRD trace for the SiO_2 impurity above 1000°C indicated the partial melting of the sample. Reactions between spinel and the silicate melt resulted in the formation of mullite ($3Al_2O_3.2SiO_2$) at 1200°C (130). Heating to 1300°C resulted in the formation of an amorphous silicate glass.

The ESR spectra show no significant changes above 800°C, being dominated by a very broad isotropic resonance centred on $g \approx 2.01$-2.04. This resonance may be attributed to species with Fe-O-Fe groupings; the weak resonance at $g = 4.25$ (800-1000°C) becomes a little more intense at higher temperatures

and drifts to g = 4.07 at 1300°C. This resonance may be attributed to iron (III) in a low-symmetry rhombically-distorted phase, and the drift to g = 4.07 at 1300°C may represent the gradual incorporation of iron (III) ions into distorted tetrahedral environments within the silicate glass [136],[137]. The ESR data corresponds well with the Mössbauer observations that the iron (III) is distributed between two phases above 900°C. The quadrupole doublet corresponding to δ = 0.33, Δ = 1.36 mm/s at 900°C can be attributed to FeO_6 present within the relic illite structure as indicated for the data at 800°C. The second doublet (δ = 0.28, Δ = 0.78 mm/s) may represent iron (III) associated with the spinel phase identified by XRD at this temperature. However, Simopoulos, A. et al.[163] have hypothesised that this paramagnetic component could be due to very small oxide particles exhibiting superparamagnetic behaviour. It is interesting to note that a very weak absorption due to hematite (α-Fe_2O_3) was observed within the spectrum of the illite heated to 900°C, but not within the XRD data. Heating of the clay to 1000°C resulted in the total collapse and recrystallisation of the illite structure giving rise to the increased presence of spinel and the appearance of hematite, as recognised by XRD. The production of α-Fe_2O_3 as a decomposition product of illite at this temperature is clearly supported by the Mössbauer data, and correlates well with the broad g $\simeq$ 2.0 resonance of the ESR data attributed to Fe-O-Fe groupings. The Mössbauer doublet corresponding to FeO_6 environments within the illite structure is lost at 1000°C, indicating the total collapse of the illite structure as observed in the XRD data. The

remaining iron (III) paramagnetic doublet (δ = 0.27, Δ = 0.88 mm/s) may now, with reasonable certainty, be attributed to iron (III) associated with the spinel phase. By 1200°C the α-Fe_2O_3 phase is not clearly discernable from the Mössbauer spectrum, nor is it detectable by XRD. This would indicate that the α-Fe_2O_3 has dissolved in the silicate melt. The presence of mullite within the XRD trace at 1200°C, and a change in the Mössbauer parameters for the iron (III) doublet (δ = 0.33, Δ = 0.77 mm/s) at 1100°C, may indicate the selective dissolution of iron (III) containing spinel in the silicate melt to form mullite [130] at 1100°C. The Mössbauer parameters would therefore represent iron (III) isomorphously substituted for Al^{3+} in the octahedral sites of mullite[10], [130]. Most interestingly, a new iron phase is detectable by Mössbauer spectroscopy at 1200°C — one containing iron (II), and at 1300°C the iron (II) signal is about a third the intensity of the iron (III) signal. The origin of the iron (II) is problematic and must be an artefact of the experimental conditions. The furnace used to heat the samples was lined with silicon carbide and at temperatures beyond 1200°C the furnace atmosphere may be somewhat reducing (it is well known to Craft Potters that the addition of SiC to a glaze will give "reduced" effects in electric kilns[165]).

Fusion of the clay sample occurs upon heating the illite to 1300°C, as indicated by its morphology (TABLE 18) and the XRD trace typical of an amorphous glass. ESR and Mössbauer data suggest that a spectrum of iron (III) sites occur in the glass. Small clusters of Fe-O-Fe species (superparamagnetic) give rise to the very broad g = 2.04 resonance, while other

iron (II) and (III) ions locate in appropriate holes within the glassy silicate structure to give the g = 4.07 ESR signal and the broad Mössbauer spectrum.

6.3. THE THERMAL TREATMENT OF MONTMORILLONITE:

The chemical composition of the natural montmorillonite sample, as given by X-ray fluorescence analysis and corrected for H_2O content, is detailed in TABLE 17. The results are in close agreement with those of other natural montmorillonite samples cited in the literature[74],[75]. The weight percent of SiO_2, however, is slightly higher than expected relative to that of Al_2O_3, indicating the presence of quartz impurity within the sample. Also, the weight percent Fe_2O_3 is very high, probably indicating the presence of iron oxyhydroxides.

Portions of the natural montmorillonite sample were heated at various temperatures up to a maximum of 1300°C. The thermal products were investigated in 100°C steps from a starting point of 400°C; MONT3A400 to MONT3A1300. The percent weight loss and change in morphology of the clay upon heating are outlined in TABLE 21, and a graphical representation of the weight loss is shown in FIG. 58.

It can be seen that the percent weight loss increases gradually until about 400°C, representing the loss of adsorbed interstitial water, whereupon it increases rapidly to about 700/750°C, representing the temperature range over which dehydroxylation is occurring[74],[127]. The graph levels out at about 800°C, the weight loss increasing only slightly up to 1300°C, representing the loss of residual hydroxyl ions.

TABLE 21. Weight loss and change in morphology of montmorillonite upon heating.

TEMP., °C.	% WT. LOSS.*	MORPHOLOGY.
20	-	Light brown-yellow powder.
100	13.36	Light brown-yellow powder.
200	13.80	Light brown powder.
300	14.85	Light brown powder.
400	14.95	Light brown powder.
500	16.50	Medium brown powder.
600	17.51	Medium brown powder.
700	18.03	Medium brown powder.
800	18.68	Medium brown powder.
900	17.56	Dark brown powder.
1000	18.26	Dark brown, very soft and porous briquette. Powdered easily.
1100	18.36	Dark brown, firm but brittle, porous briquette. Powdered easily.
1200	18.31	Dark purple, hard but brittle, porous briquette. Powdered easily.
1300	18.50	Dark steel-grey, very hard but brittle, solid briquette. Slightly vesicular, glassy texture. Clay has collapsed - melting. Powdered easily to a steel-grey powder.

* = Average result of two samples.

FIG. 58. Graph of the weight loss of montmorillonite with respect to temperature.

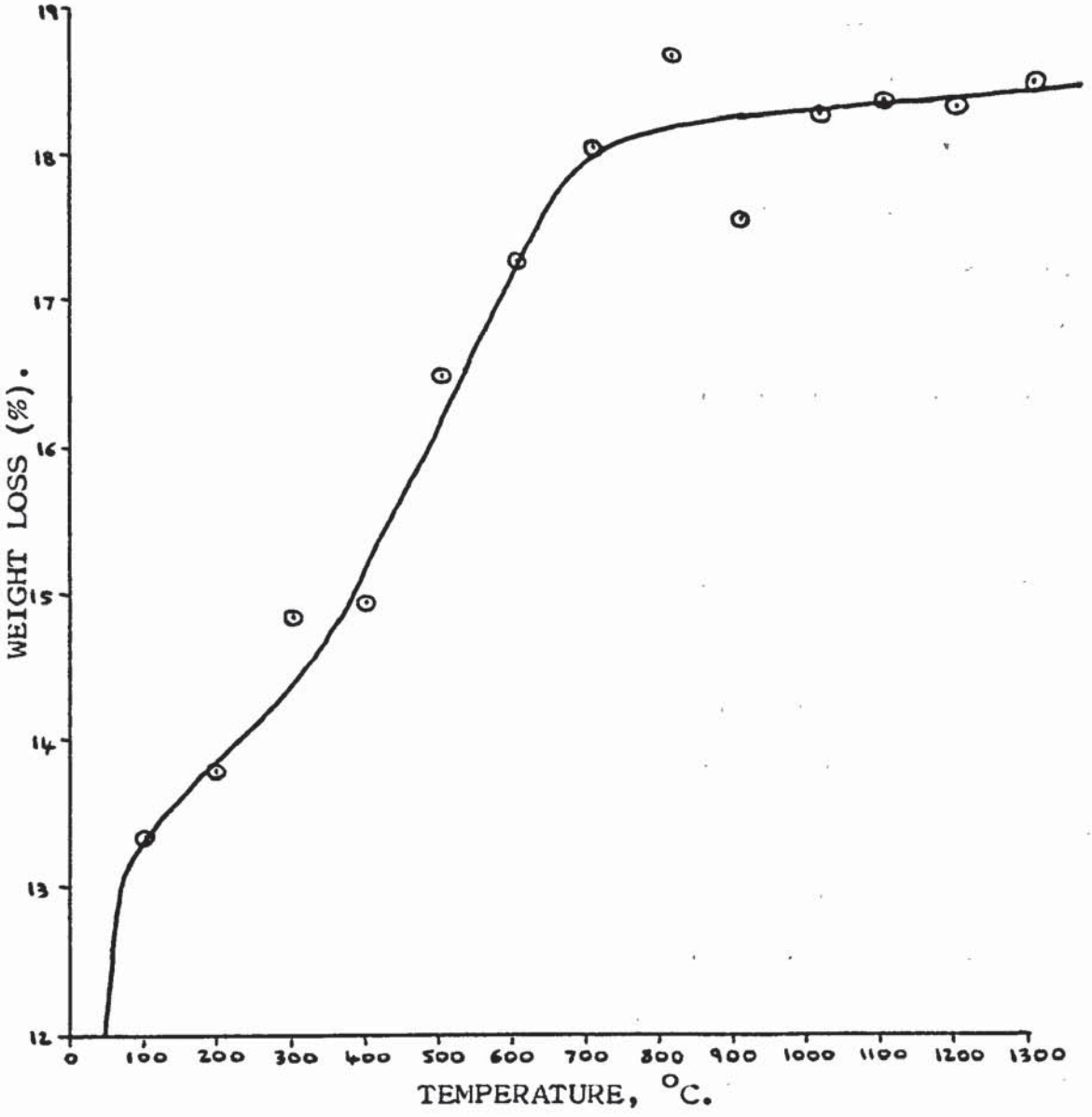

6.3.1. X-RAY DIFFRACTION DATA:

The X-ray diffraction trace of the natural montmorillonite sample revealed the characteristic trace expected for montmorillonite[73], together with a relatively strong trace for α-quartz and other weak traces indicating the presence of iron oxyhydroxide minerals[131]. The intensity of the trace for the montmorillonite is relatively low and the background rather high, indicating the poorly crystalline character of this clay mineral sample. Investigation of the basal spacing of the clay gave a d-spacing of 15.24 Å, typical of montmorillonite[75].

The X-ray diffraction traces of the thermal products showed no appreciable change from 400 to 700°C. At 800°C the trace for montmorillonite was greatly reduced in intensity and had completely disappeared by 900°C. This indicates that the X-ray crystallinity of montmorillonite is not lost as a result of dehydroxylation[127],[130]. Between 800 and 900°C a rapid consolidation of the montmorillonite structure occurred, representing a collapse of the crystalline lattice. At 900°C relatively low intensity peaks within the X-ray diffraction trace indicate the onset of reactions taking place within the relic octahedral sheets of the montmorillonite lattice, resulting in the formation of spinel ($MgAl_2O_4$), hematite (α-Fe_2O_3) and enstatite ($MgSiO_3$).

The crystallinity of the sample, as indicated by the X-ray diffraction trace, had increased significantly at 1000°C. A relatively strong intensity trace for cristobalite (SiO_2) is apparent, indicating recrystallisation within the relic

tetrahedral lattices of the clay. Other traces indicate the increasing presence of spinel ($MgAl_2O_4$), enstatite ($MgSiO_3$), hematite (α-Fe_2O_3), and possibly anorthite ($CaAl_2Si_2O_8$). At 1100°C the diffraction trace is dominated by the high intensity trace of cristobalite. There is also a general increase in relative intensity of all the phases present at 1000°C, indicating the increasing recrystallisation of the former clay mineral at 1100°C.

Several changes are apparent within the X-ray diffraction trace at 1200°C when compared to that at 1100°C. The traces for spinel and enstatite have decreased greatly in relative intensity, whereas that of hematite (α-Fe_2O_3) has increased. The relative intensity of cristobalite appears to be only slightly reduced, but the presence of mullite ($3Al_2O_3.2SiO_2$) is clearly indicated in the diffraction trace. It would appear from this that spinel, enstatite and a portion of the cristobalite have melted or reacted in the solid state, resulting in the formation of mullite and a liquid phase at 1200°C(130). The low level of alkali oxides within the original montmorillonite sample is probably responsible for the apparent refractory nature of the sample at this temperature. This is further highlighted by an increase in the relative intensity of the trace for hematite and the continuing presence of the α-quartz impurity phase, both of which would normally dissolve in an alkali oxide silicate melt at this temperature. The increase in intensity of the hematite phase is probably due to the migration of Fe^{3+} ions resulting in the formation of Fe_2O_3 clusters, and the expulsion of Fe^{3+} previously contained within the structure

of spinel. At 1300°C the only phases present within the sample are cristobalite, hematite and mullite. The X-ray diffraction trace for cristobalite is greatly reduced in relative intensity, as are the traces for hematite and mullite. This would indicate further melting of cristobalite, forming a silicate melt into which the hematite and mullite have partially dissolved[130].

6.3.2. MÖSSBAUER SPECTROSCOPY DATA:

The Mössbauer spectra for the natural illite sample and its thermal decomposition products are shown in FIGS. 59 to 69. The interpretation of each individual spectrum together with the Mössbauer parameters are given in the following sub-sub-sections.

6.3.2.1. NATURAL MONTMORILLONITE:

The Mössbauer spectrum of the natural montmorillonite sample consists of a single quadrupole doublet, FIG. 59. The parameters are as follows:

Isomer shift	= 0.36 ($\pm$0.01) mm/s.
Quadrupole splitting	= 0.54 ($\pm$0.01) mm/s.
Half-Width	= 0.66 ($\pm$0.01) mm/s.
Relative intensities	= 68554 ($\pm$2003).
	67448 ($\pm$2009).

These parameters are characteristic of an Fe^{3+} containing montmorillonite where the Fe^{3+} ions are in cis-octahedrally coordinated environmental sites [133],[141]. The half-width is rather broad, indicating a considerable degree of structural disorder or slightly differing environments around the respective Fe^{3+} ions within the clay structure. However, Cardile, C.M. and Johnston, J.H.[133] have argued, in the light of an electron diffraction study by Tsipursky, S.I. and Drits, V.A.[144], that the Fe^{3+} ions appear to be located

essentially in the trans-octahedral sites, and that a two doublet computer fit to a broad Mössbauer spectrum for montmorillonite probably only represents the mean extremes of a continuum of slightly different Fe^{3+} signals arising from the variable nature of the environment surrounding these sites. This would tend to indicate that the broad single doublet fit presented here represents the mean of the range of slightly different Fe^{3+} sites, and that its assignment to specific cis-octahedral sites is incorrect.

The spectrum may be further complicated by the presence of iron oxyhydroxides as impurity phases within the sample. These phases tend to give isomer shift values $\approx$ 0.40 mm/s, and quadrupole splitting values $\approx$ 0.65 mm/s[106].

6.3.2.2. MONT3A400:

The Mössbauer spectrum of MONT3A400 consists of two quadrupole doublets, spectrum lines (1)+(4) and (2)+(3) respectively, FIG. 60. The parameters are as follows:

Lines (1)+(4):

Isomer shift	= 0.38 ($\pm$0.04) mm/s.
Quadrupole splitting	= 1.27 ($\pm$0.08) mm/s.
Half-Width	= 0.58 ($\pm$0.10) mm/s.
Relative intensity	= 3417 ($\pm$1514).

Lines (2)+(3):

Isomer shift	= 0.33 ($\pm$0.01) mm/s.
Quadrupole splitting	= 0.52 ($\pm$0.03) mm/s.
Half-Width	= 0.69 ($\pm$0.04) mm/s.
Relative intensity	= 17432 ($\pm$1640).

The general broadening of the overall Mössbauer spectrum with respect to the natural montmorillonite sample has made it possible to computer fit an outer quadrupole doublet. The parameters for lines (2)+(3) are very similar to those for the single doublet fit of the natural montmorillonite, and the interpretation of this doublet is regarded to be the same. However, the parameters for lines (1)+(4) are indicative of a more highly distorted octahedral Fe^{3+} site (Δ = 1.27 mm/s) [145],[146]. Removal of the adsorbed water by heating to 400°C is unlikely to have affected the structural iron, but the

onset of dehydroxylation would create a range of new environments with similar Mössbauer parameters[132]. Lines (1)+(4) may therefore be interpreted as representing the more highly distorted Fe^{3+} sites of a combination of partially and fully dehydroxylated environments, whereas lines (2)+(3) represent their less distorted fully hydroxylated equivalents.

6.3.2.3. MONT3A500:

The Mössbauer spectrum of MONT3A500 consists of two quadrupole doublets, spectrum lines (1)+(4) and (2)+(3) respectively, FIG. 61. The parameters are as follows:

Lines (1)+(4):

Isomer shift	= 0.38 ($\pm$0.02) mm/s.
Quadrupole splitting	= 1.73 ($\pm$0.05) mm/s.
Half-Width	= 0.57 ($\pm$0.06) mm/s.
Relative intensity	= 8405 ($\pm$1722).

Lines (2)+(3):

Isomer shift	= 0.43 ($\pm$0.03) mm/s.
Quadrupole splitting	= 0.89 ($\pm$0.05) mm/s.
Half-Width	= 0.72 ($\pm$0.06) mm/s.
Relative intensities	= 17528 ($\pm$2232).
	12885 ($\pm$1630).

These parameters can be interpreted as a progression of the situation observed for MONT3A400, lines (1)+(4) increasing in relative intensity with respect to lines (2)+(3) as dehydroxylation of the Fe^{3+} environments increases. The two quadrupole doublets, together with their parameters, represent the best fit possible for the range of Fe^{3+} environments from fully hydroxylated to fully dehydroxylated sites.

6.3.2.4. MONT3A600:

The Mössbauer spectrum of MONT3A600 consists of a single quadrupole doublet, FIG. 62. The parameters are as follows:

Isomer shift	= 0.36 ($\pm$0.01) mm/s.
Quadrupole splitting	= 1.26 ($\pm$0.01) mm/s.
Half-Width	= 0.91 ($\pm$0.02) mm/s.
Relative intensities	= 36188 ($\pm$634).
	34616 ($\pm$611).

The spectrum of MONT3A600 has been computer-fitted with a single doublet, however, the very broad half-width would tend to indicate the presence of other unresolved doublets. At this temperature (600°C) it is unlikely that a high proportion of fully hydroxylated Fe^{3+} sites remain. This quadrupole doublet therefore represents a combination of environments produced by partially and fully dehydroxylated Fe^{3+} sites, which correspond to lines (1)+(4) for MONT3A400 and MONT3A500.

6.3.2.5. MONT3A700:

The Mössbauer spectrum of MONT3A700 consists of a single quadrupole doublet, FIG. 63. The parameters are as follows:

Isomer shift	= 0.34 ($\pm$0.01) mm/s.
Quadrupole splitting	= 1.43 ($\pm$0.01) mm/s.
Half-Width	= 0.76 ($\pm$0.01) mm/s.
Relative intensity	= 43804 ($\pm$313).

These parameters can be interpreted in a similar way to those for MONT3A600. At 700°C dehydroxylation is nearing completion, and hence the wide range of Fe^{3+} environmental sites is reduced, resulting in a reduction of half-width with respect to MONT3A600. However, the half-width is still relatively broad, indicating a range of unresolved doublets resulting from similar environmental sites.

Within the spectrum there is also a hint of the presence of the outer four lines of a magnetic hyperfine sextet (upward pointing arrows in FIG. 63), indicating the formation of a small quantity of hematite (α-Fe_2O_3). This is probably being produced by the dehydroxylation of iron oxyhydroxide impurities.

6.3.2.6. MONT3A800:

The Mössbauer spectrum of MONT3A800 consists of two quadrupole doublets, spectrum lines (1)+(4) and (2)+(3) respectively, FIG. 64. The parameters are as follows:

Lines (1)+(4):

Isomer shift	= 0.35 ($\pm$0.02) mm/s.
Quadrupole splitting	= 1.46 ($\pm$0.03) mm/s.
Half-Width	= 0.70 ($\pm$0.03) mm/s.
Relative intensities	= 27709 ($\pm$2597). 27464 ($\pm$2671).

Lines (2)+(3):

Isomer shift	= 0.31 ($\pm$0.01) mm/s.
Quadrupole splitting	= 0.86 ($\pm$0.03) mm/s.
Half-Width	= 0.52 ($\pm$0.03) mm/s.
Relative intensity	= 15288 ($\pm$2397).

The parameters for the outer doublet (lines (1)+(4)) are very similar to those of the doublet observed for MONT3A700, and can therefore be interpreted as representing a range of similar fully dehydroxylated Fe^{3+} environments. However, the parameters for the inner doublet (lines (2)+(3)) indicate the formation of a new paramagnetic Fe^{3+} containing phase(6), resulting from the onset of the irreversible breakdown and recrystallisation of the relic montmorillonite structure. From the parameters, the new Fe^{3+} environments would appear to be octahedral in character and less distorted

(Δ = 0.86 mm/s) than the environments represented by lines (1)+(4), possibly with a narrower range of site variability ($\Gamma_{\frac{1}{2}}$ = 0.52 mm/s).

The increasing presence of hematite (α-Fe_2O_3) is indicated by the unresolved outer four lines of the magnetic hyperfine sextet (FIG. 64). The increase in intensity relative to the inner doublet is representative of the further dehydroxylation of iron oxyhydroxide impurities and the structural collapse of the iron containing clay lattice.

6.3.2.7. MONT3A900:

The Mössbauer spectrum of MONT3A900 consists of a quadrupole doublet (lines (3)+(4)) and the outer four lines of a six peak magnetic hyperfine spectrum (lines (1),(2),(5) and (6)), FIG. 65. The parameters are as follows:

Quadrupole Doublet:

Isomer shift	= 0.32 (±0.01) mm/s.
Quadrupole splitting	= 0.89 (±0.01) mm/s.
Half-Width	= 0.67 (±0.01) mm/s.
Relative intensities	= 43570 (±747).
	40981 (±713).

Magnetic Hyperfine Spectrum:

Isomer shift	= 0.36 (±0.03) mm/s.
Quadrupole splitting	= -0.10 (±0.03) mm/s.
Magnetic hyperfine field	= 504 (±2) kG.
	50.4 (±0.2) T.
Half-Widths	= 0.45 (±0.09) mm/s.
	0.56 (±0.10) mm/s.
Relative intensities	= 2470 (±381).
	3088 (±444).

The parameters for the quadrupole doublet can be interpreted in the same way as the explanation given for the inner doublet (lines (2)+(3)) of MONT3A800. The loss of the outer doublet (lines (1)+(4)) observed for MONT3A800 would tend to indicate the total collapse of the relic montmorillonite lattice and the further formation of

the new Fe^{3+} phase, represented here by the central quadrupole doublet. The increase in intensity of the magnetic hyperfine sextet relative to the central doublet has made it possible to computer-fit the outer four lines of the sextet. The resulting parameters are in close agreement with those expected for hematite (α-Fe_2O_3), and the increase in relative intensity is probably due to the migration of Fe^{3+} ions forming iron oxide clusters.

6.3.2.8. MONT3A1000:

The Mössbauer spectrum of MONT3A1000 consists of a quadrupole doublet (lines (4)+(5)) and a six peak magnetic hyperfine spectrum (lines (1)-(3) and (6)-(8)), FIG. 66. The parameters are as follows:

Quadrupole doublet:

Isomer shift	= 0.31 ($\pm$0.01) mm/s.
Quadrupole splitting	= 0.79 ($\pm$0.01) mm/s.
Half-Width	= 0.77 ($\pm$0.02) mm/s.
Relative intensity	= 24524 ($\pm$389).

Magnetic Hyperfine Spectrum:

Isomer shift	= 0.40 ($\pm$0.02) mm/s.
Quadrupole splitting	= -0.06 ($\pm$0.02) mm/s.
Magnetic hyperfine field	= 511 ($\pm$1) kG.
	51.1 ($\pm$0.1) T.
Half-Widths	= 0.62 ($\pm$0.05) mm/s.
	0.65 ($\pm$0.07) mm/s.
	0.31 ($\pm$0.09) mm/s.
Relative intensities	= 6763 ($\pm$434).
	5590 ($\pm$415).
	1015 ($\pm$260).

The parameters for MONT3A1000 are very similar to those of MONT3A900. The interpretation of the spectrum is therefore considered to be the same. It is now possible to fit all six lines to the magnetic hyperfine sextet of hematite, due to its increase in relative intensity with respect to the

central quadrupole doublet. This increase in intensity is due to the further recrystallisation of the breakdown products of the montmorillonite structure, and the migration of Fe^{3+} ions forming iron oxide clusters.

6.3.2.9. MONT3A1100:

The Mössbauer spectrum of MONT3A1100 consists of a quadrupole doublet (lines (4)+(5)) and a six peak magnetic hyperfine spectrum (lines (1)-(3) and (6)-(8)), FIG. 67. The parameters are as follows:

Quadrupole Doublet:

Isomer shift	= 0.32 ($\pm$0.01) mm/s.
Quadrupole splitting	= 0.79 ($\pm$0.01) mm/s.
Half-Width	= 0.55 ($\pm$0.02) mm/s.
Relative intensities	= 14062 ($\pm$492).
	13981 ($\pm$464).

Magnetic Hyperfine Spectrum:

Isomer shift	= 0.39 ($\pm$0.01) mm/s.
Quadrupole splitting	= -0.08 ($\pm$0.01) mm/s.
Magnetic hyperfine field	= 513 ($\pm$1) kG.
	51.3 ($\pm$0.1) T.
Half-Widths	= 0.58 ($\pm$0.03) mm/s.
	0.45 ($\pm$0.03) mm/s.
	0.42 ($\pm$0.05) mm/s.
Relative intensities	= 7730 ($\pm$375).
	4923 ($\pm$287).
	2620 ($\pm$280).

The parameters for the components of the Mössbauer spectrum of MONT3A1100 are very similar to those of MONT3A1000. The interpretation of the spectrum is therefore considered to be the same.

6.3.2.10. MONT3A1200:

The Mössbauer spectrum of MONT3A1200 consists of a quadrupole doublet (lines (4)+(5)) and a six peak magnetic hyperfine spectrum (lines (1)-(3) and (6)-(8)), FIG. 68. The parameters are as follows:

Quadrupole Doublet:

Isomer shift	= 0.32 ($\pm$0.02) mm/s.
Quadrupole splitting	= 0.95 ($\pm$0.04) mm/s.
Half-Width	= 0.70 ($\pm$0.05) mm/s.
Relative intensity	= 6504 ($\pm$323).

Magnetic Hyperfine Spectrum:

Isomer shift	= 0.39 ($\pm$0.01) mm/s.
Quadrupole splitting	= -0.09 ($\pm$0.01) mm/s.
Magnetic hyperfine field	= 509 ($\pm$1) kG. 50.9 ($\pm$0.1) T.
Half-Widths	= 0.60 ($\pm$0.01) mm/s. 0.45 ($\pm$0.02) mm/s. 0.34 ($\pm$0.02) mm/s.
Relative intensities	= 19381 ($\pm$382). 11612 ($\pm$296). 5314 ($\pm$267).

The parameters for the magnetic hyperfine sextet indicate the presence of hematite, which dominates the spectrum of MONT3A1200. The greatly reduced relative intensity of the central quadrupole doublet indicates the onset of melting of the silicate phases present at 1100°C. The parameters for

the quadrupole doublet indicate that the Fe^{3+} ions are in an octahedral environment, but the high quadrupole splitting value points to a higher degree of distortion. This quadrupole doublet could possibly represent Fe^{3+} ions present within the octahedral sites of mullite ($3Al_2O_3.2SiO_2$)[10], [147], or alternatively contained within tetrahedral sites of a silicate glass[148].

6.3.2.11. MONT3A1300:

The Mössbauer spectrum of MONT3A1300 consists of two quadrupole doublets (lines (4)+(8) and (5)+(6)) and a six peak magnetic hyperfine spectrum (lines (1)-(3) and (7),(9)+(10)), FIG. 69. The parameters are as follows:

Doublet, lines (4)+(8):

Isomer shift	= 0.90 (±0.07) mm/s.
Quadrupole splitting	= 1.90 (±0.15) mm/s.
Half-Width	= 0.72 (±0.09) mm/s.
Relative intensity	= 6258 (±825).

Doublet, lines (5)+(6):

Isomer shift	= 0.35 (±0.06) mm/s.
Quadrupole splitting	= 0.80 (±0.12) mm/s.
Half-Width	= 0.89 (±0.07) mm/s.
Relative intensity -	= 11097 (±713).

Magnetic Hyperfine Spectrum:

Isomer shift	= 0.36 (±0.01) mm/s.
Quadrupole splitting	= -0.10 (±0.01) mm/s.
Magnetic hyperfine field	= 487 (±1) kG. 48.7 (±0.1) T.
Half-Widths	= 0.71 (±0.03) mm/s. 0.51 (±0.03) mm/s. 0.33 (±0.03) mm/s.
Relative intensities	= 13925 (±401). 8391 (±319). 3192 (±398).

The outer four lines of the magnetic hyperfine sextet are rather asymmetrical indicating the presence of one or more unresolved overlapping magnetic hyperfine spectra. This is highlighted by the rather broad half-widths of the outer lines and the low magnetic hyperfine field value, indicating a possible combination of the spectra resulting from hematite (α-Fe_2O_3), maghemite (γ-Fe_2O_3) and magnesioferrite ($Mg_xFe_{3-x}O_4$, $x<1$). The presence of magnetite (Fe_3O_4) cannot be ruled out. The decrease in relative intensity with respect to the central quadrupole doublet would correspond to assimilation of a quantity of the iron oxide phases within the silicate melt.

The central region of the Mössbauer spectrum consists of two broad quadrupole doublets, one representing Fe^{2+} (lines (4)+(8)) and the other Fe^{3+} (lines (5)+(6)) within a silicate glass[6],[10],[148]. The doublet for Fe^{3+} may alternatively represent Fe^{3+} contained within mullite ($3Al_2O_3.2SiO_2$)[10]. The broad half-widths indicate a wide range of local environments for the Fe^{3+} and Fe^{2+} ions. Virgo, D. and Mysen, B.O.[148] have indicated that in oxidised glasses the majority of Fe^{3+} ions are in tetrahedral coordination. The parameters for the two doublets are similar to those presented by Virgo, D. and Mysen, B.O., indicating comparative assignments of the doublets.

FIG. 59. Mössbauer spectrum of the natural montmorillonite sample.

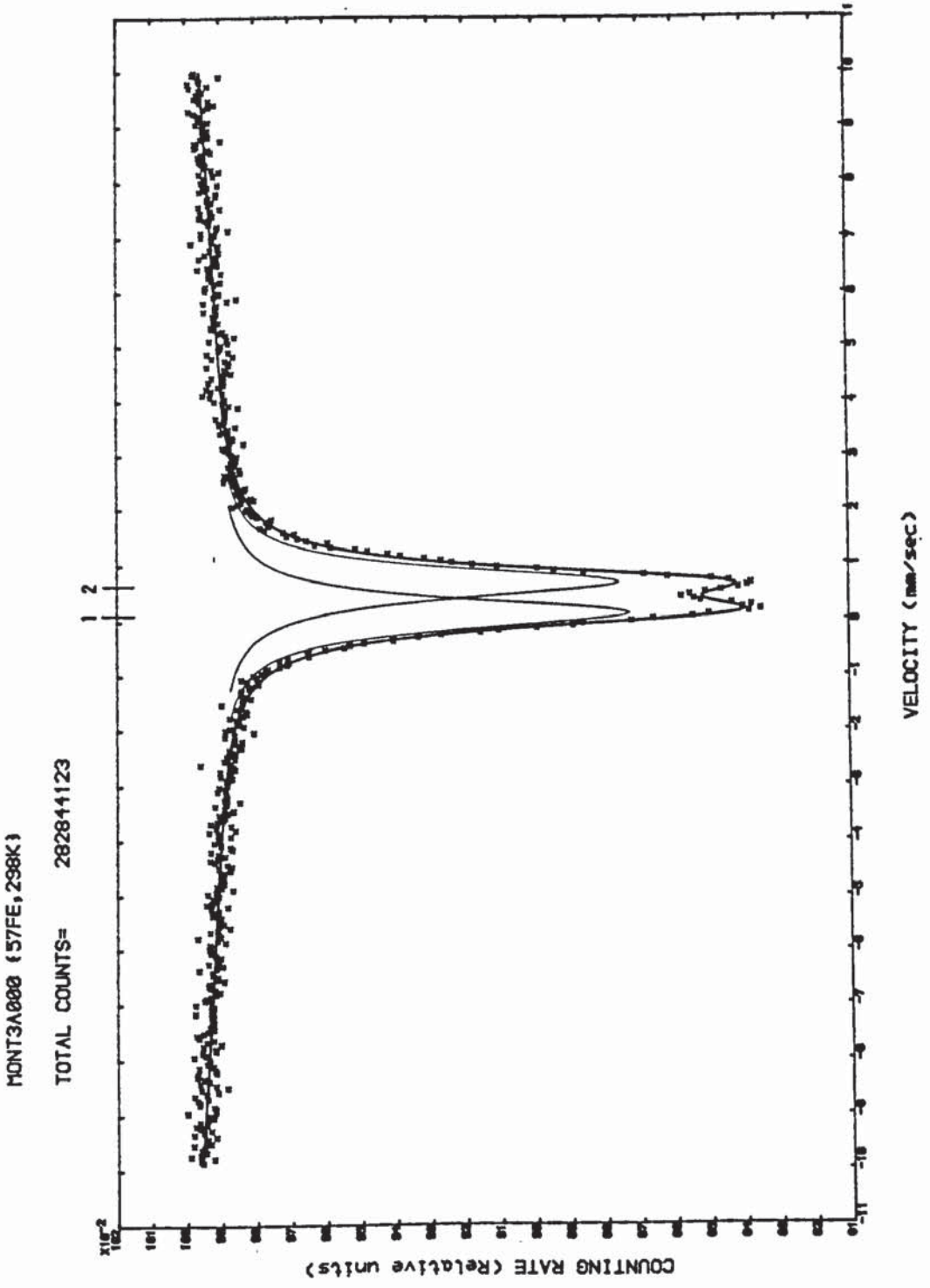

FIG. 60. Mössbauer spectrum of MONT3A400.

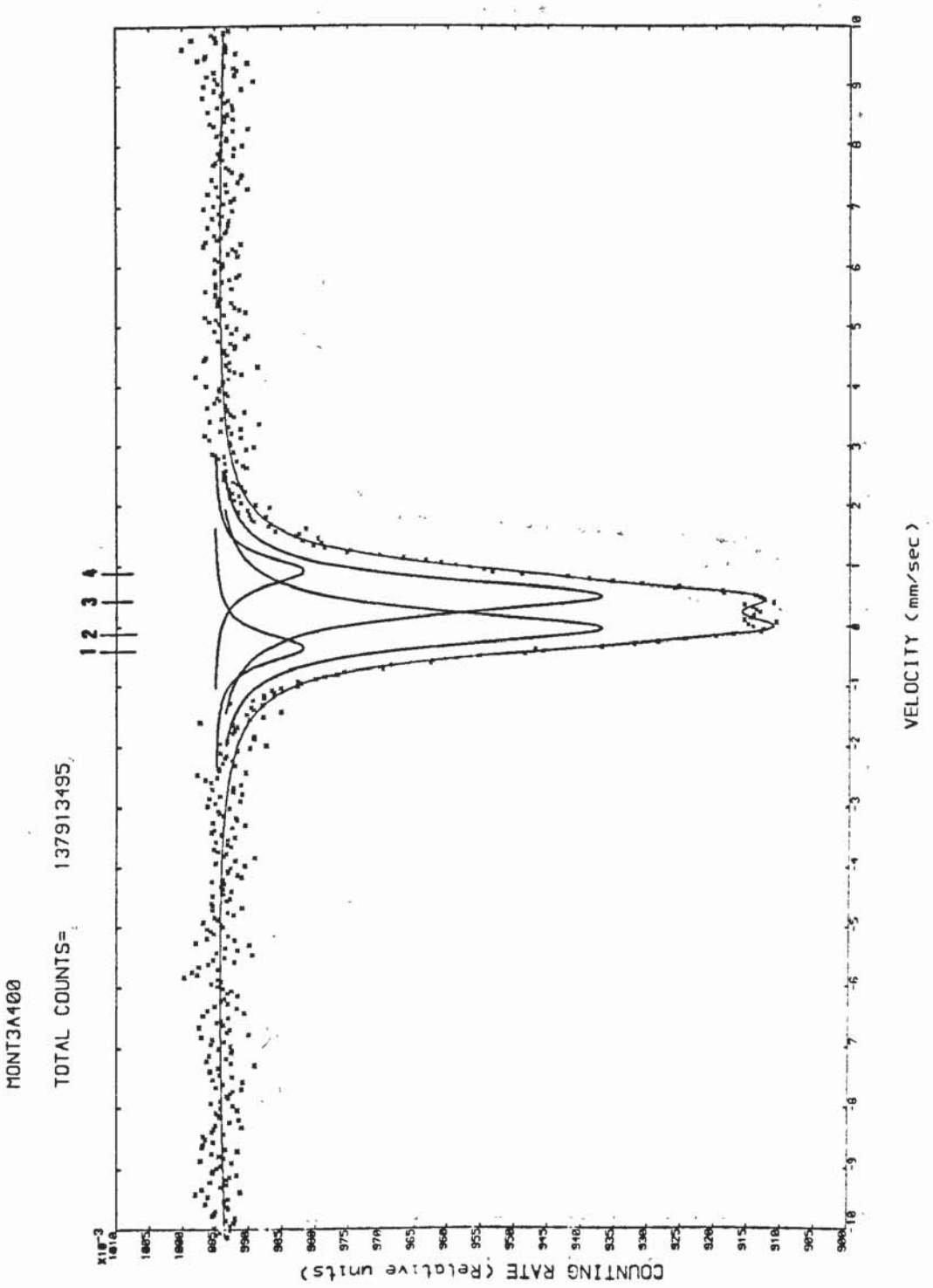

FIG. 61. Mössbauer spectrum of MONT3A500.

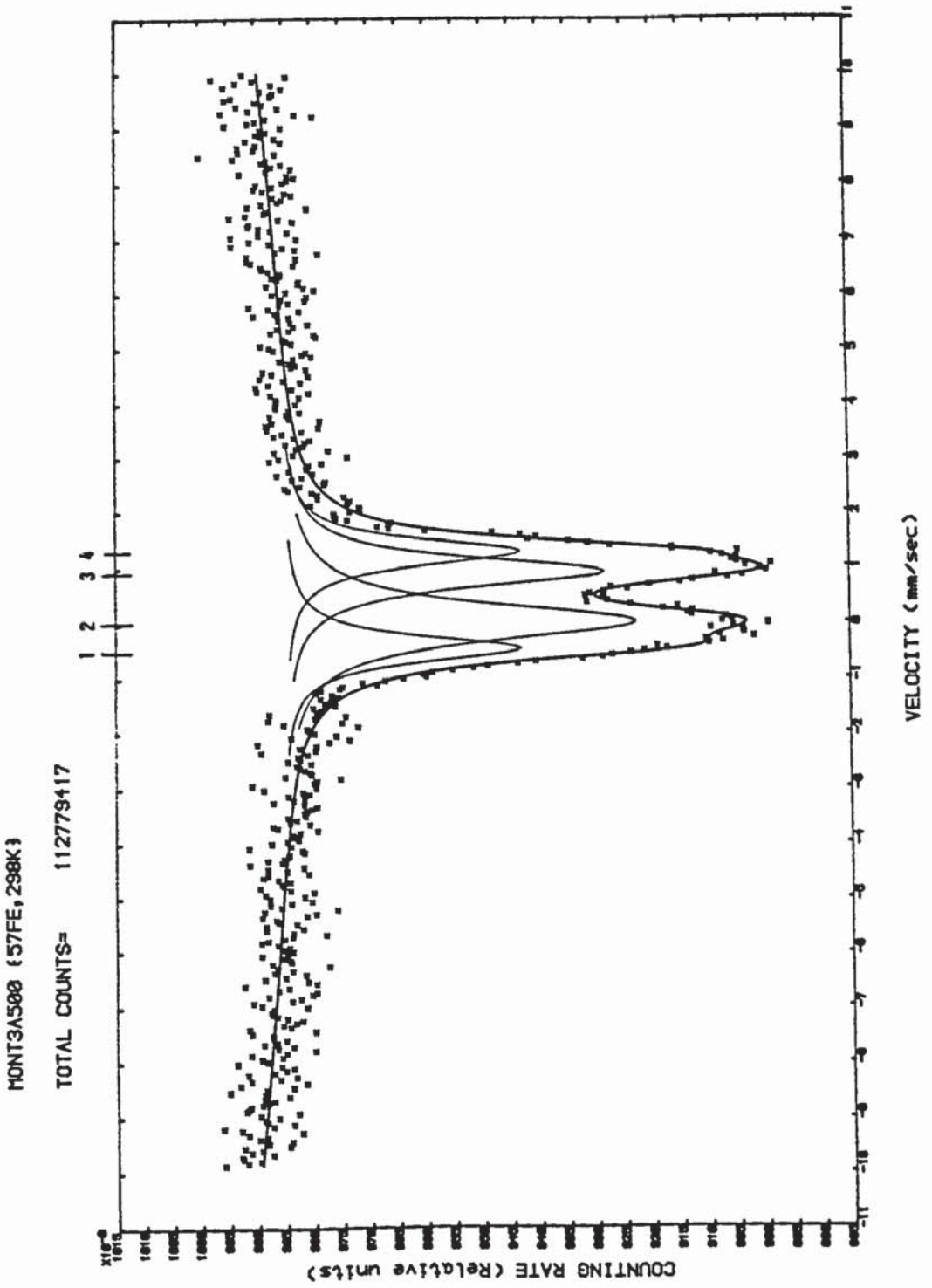

FIG. 62. Mössbauer spectrum of MONT3A600.

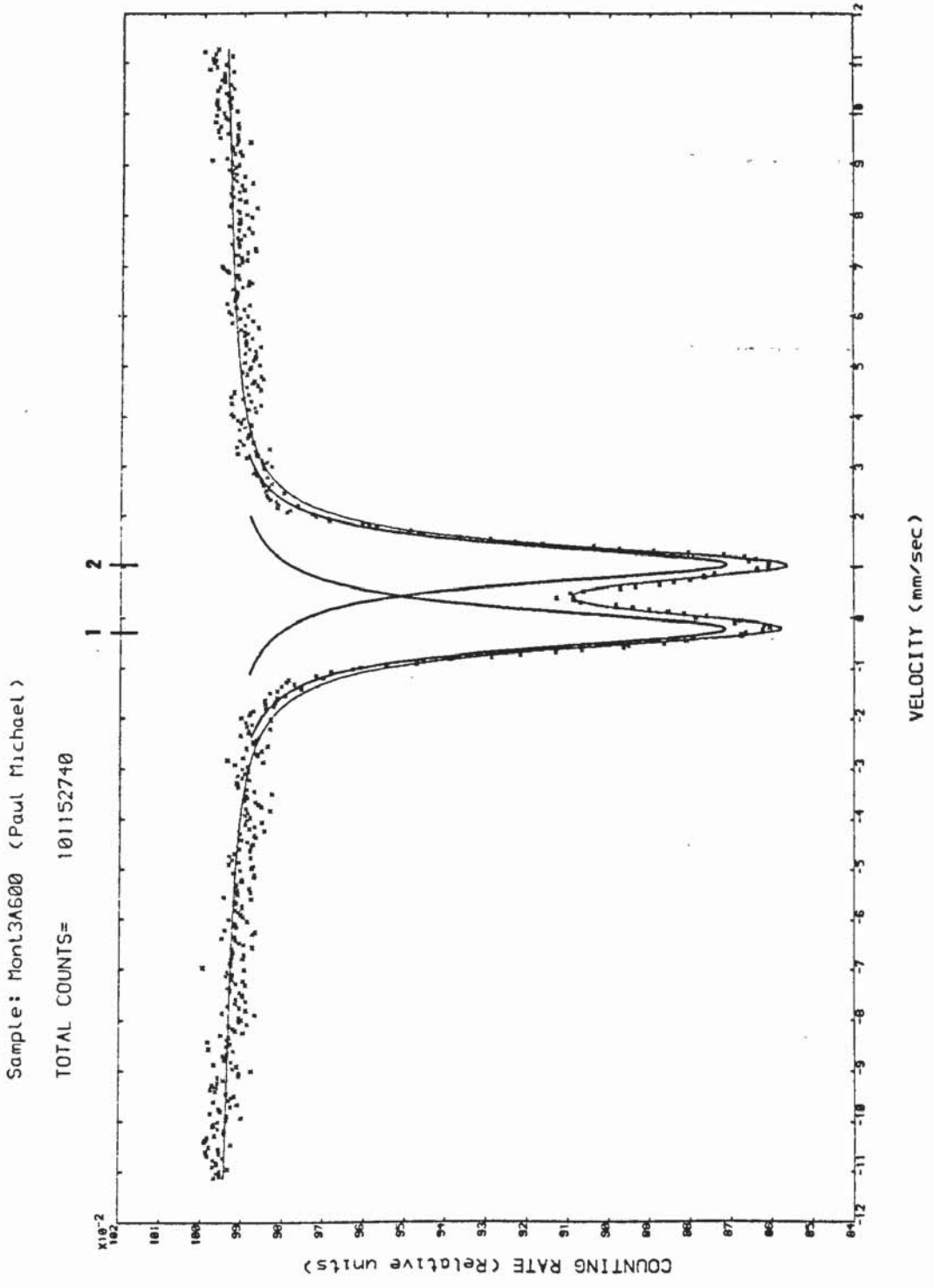

FIG. 63. Mössbauer spectrum of MONT3A700.

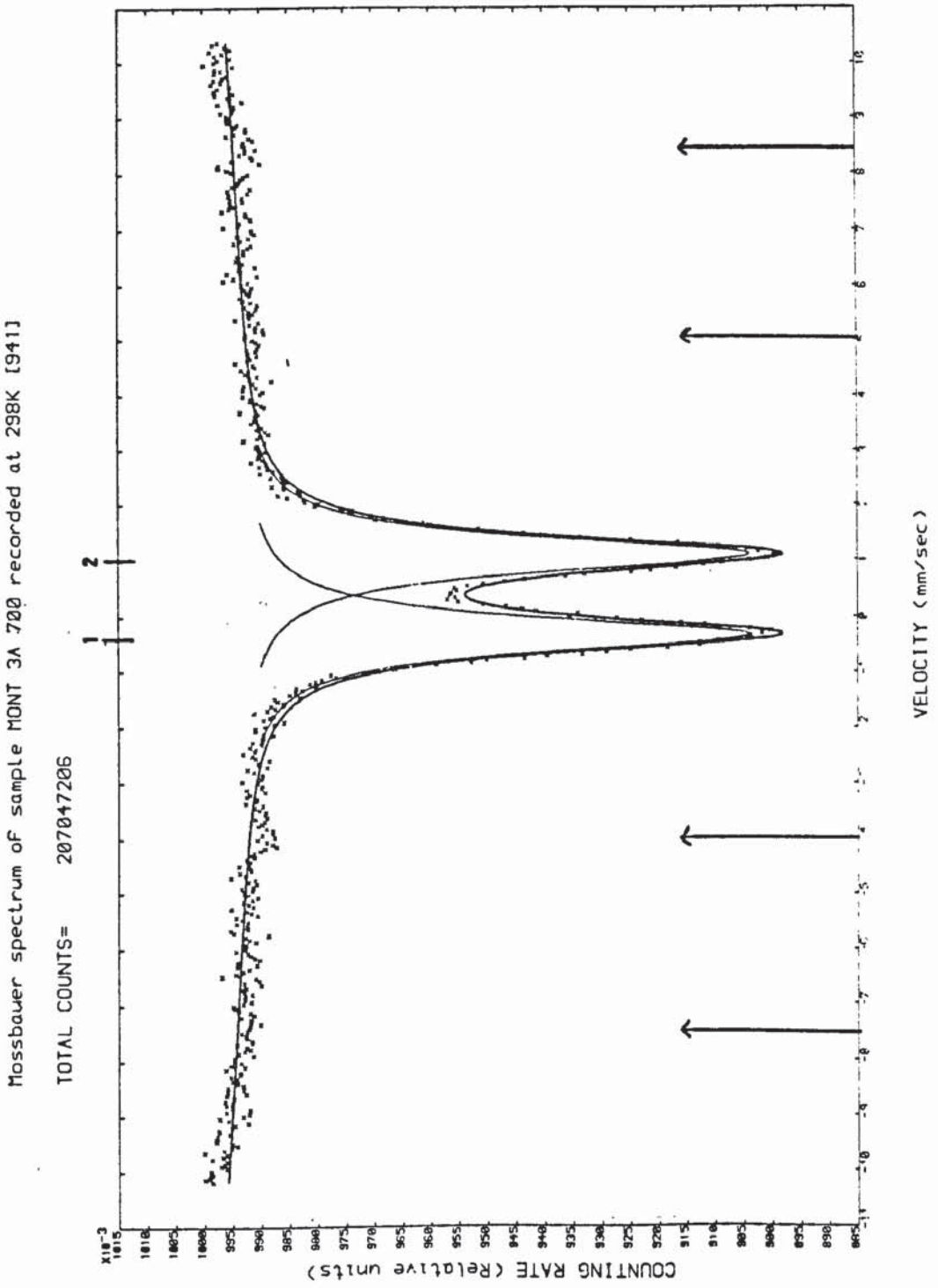

FIG. 64. Mössbauer spectrum of MONT3A800.

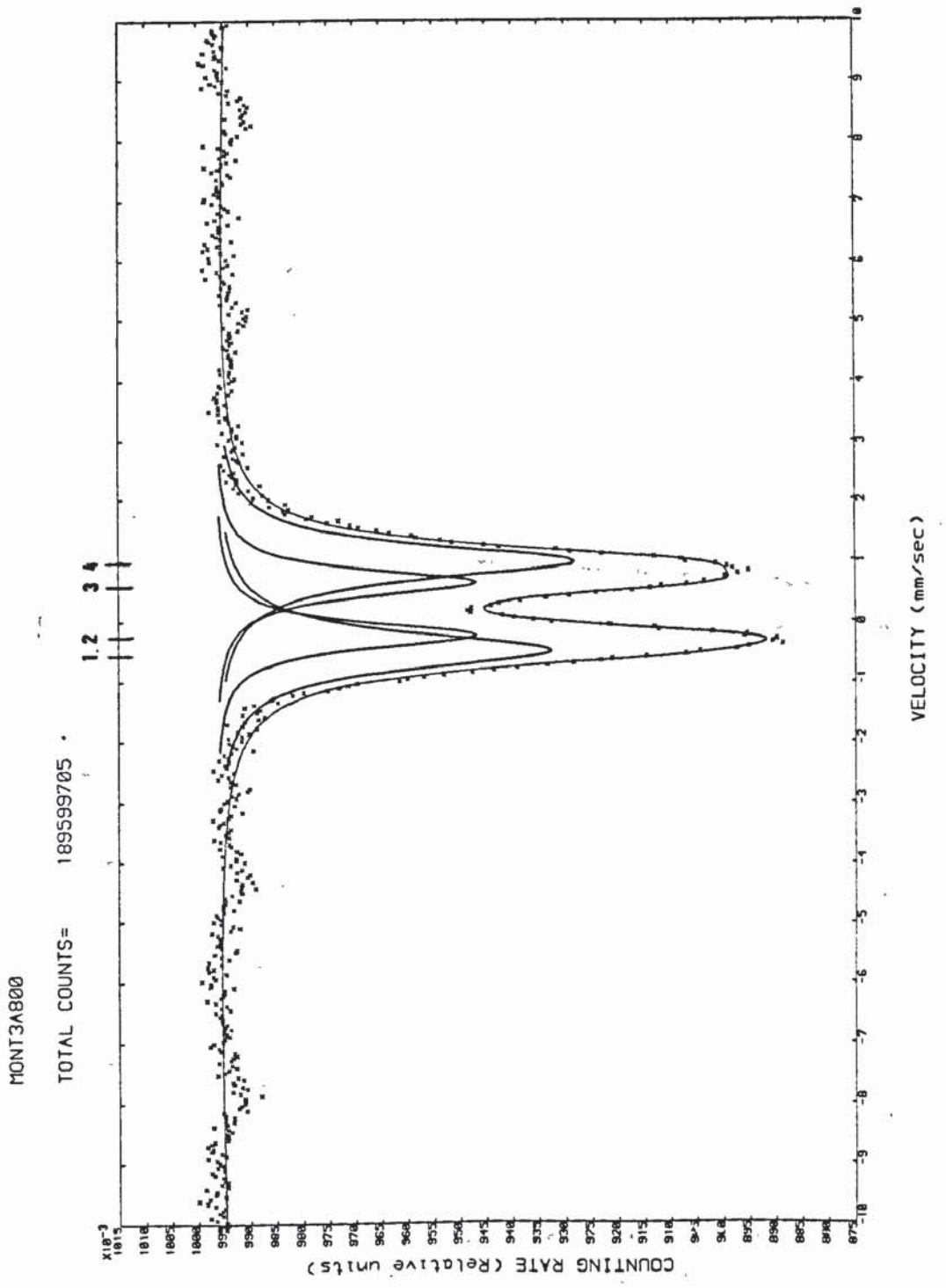

FIG. 65. Mössbauer spectrum of MONT3A900.

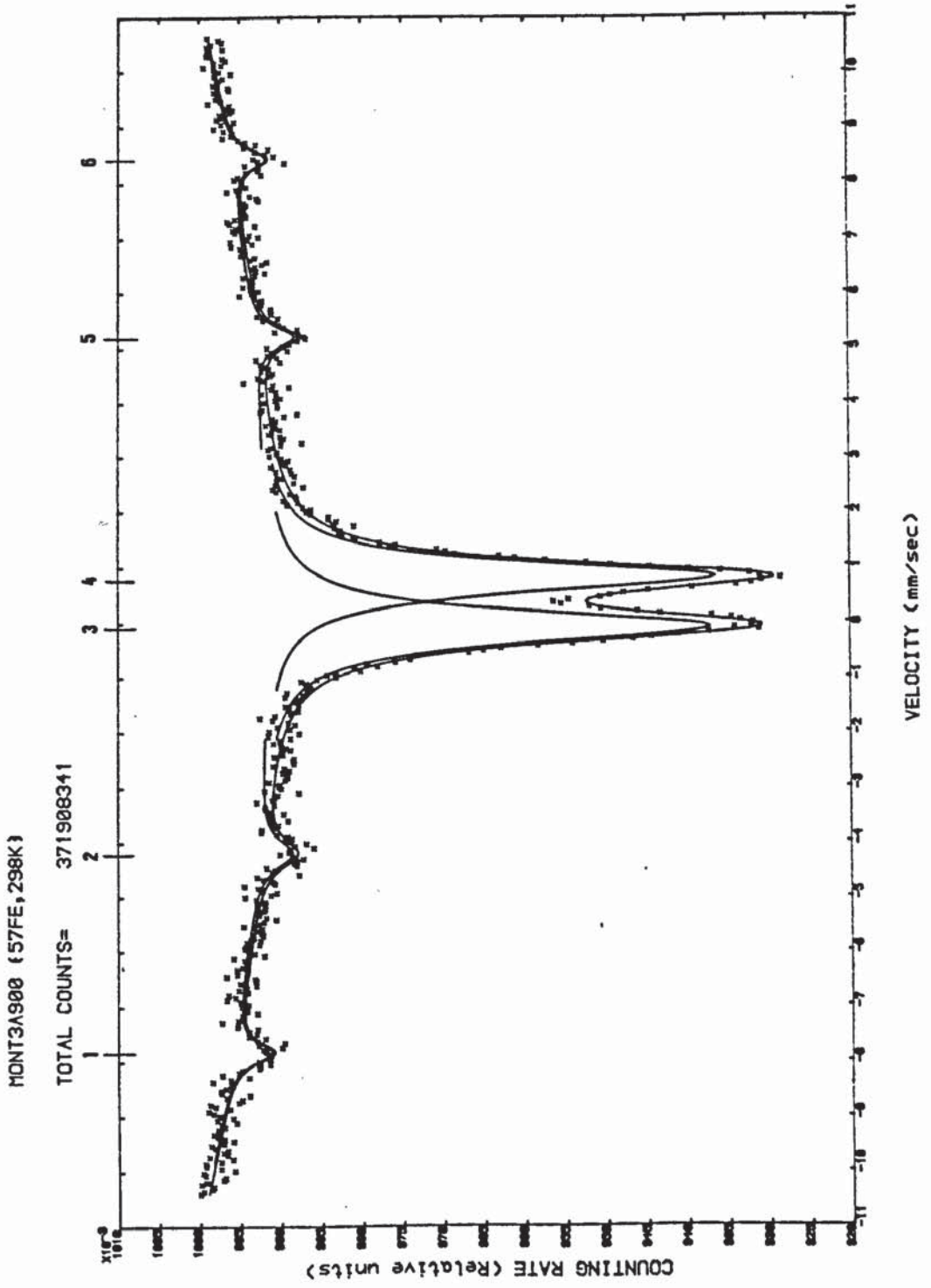

FIG. 66. Mössbauer spectrum of MONT3A1000.

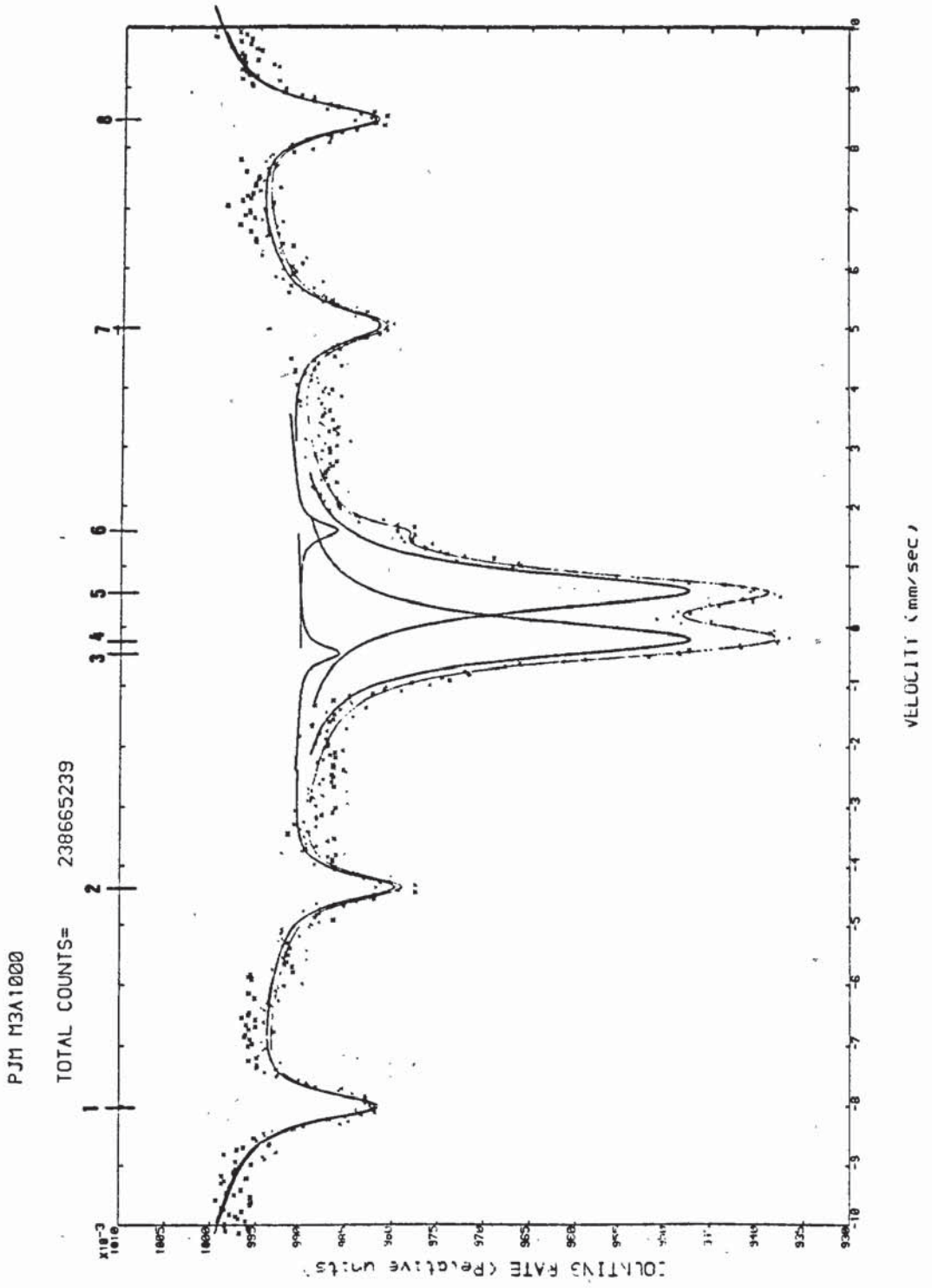

FIG. 67. Mössbauer spectrum of MONT3A1100.

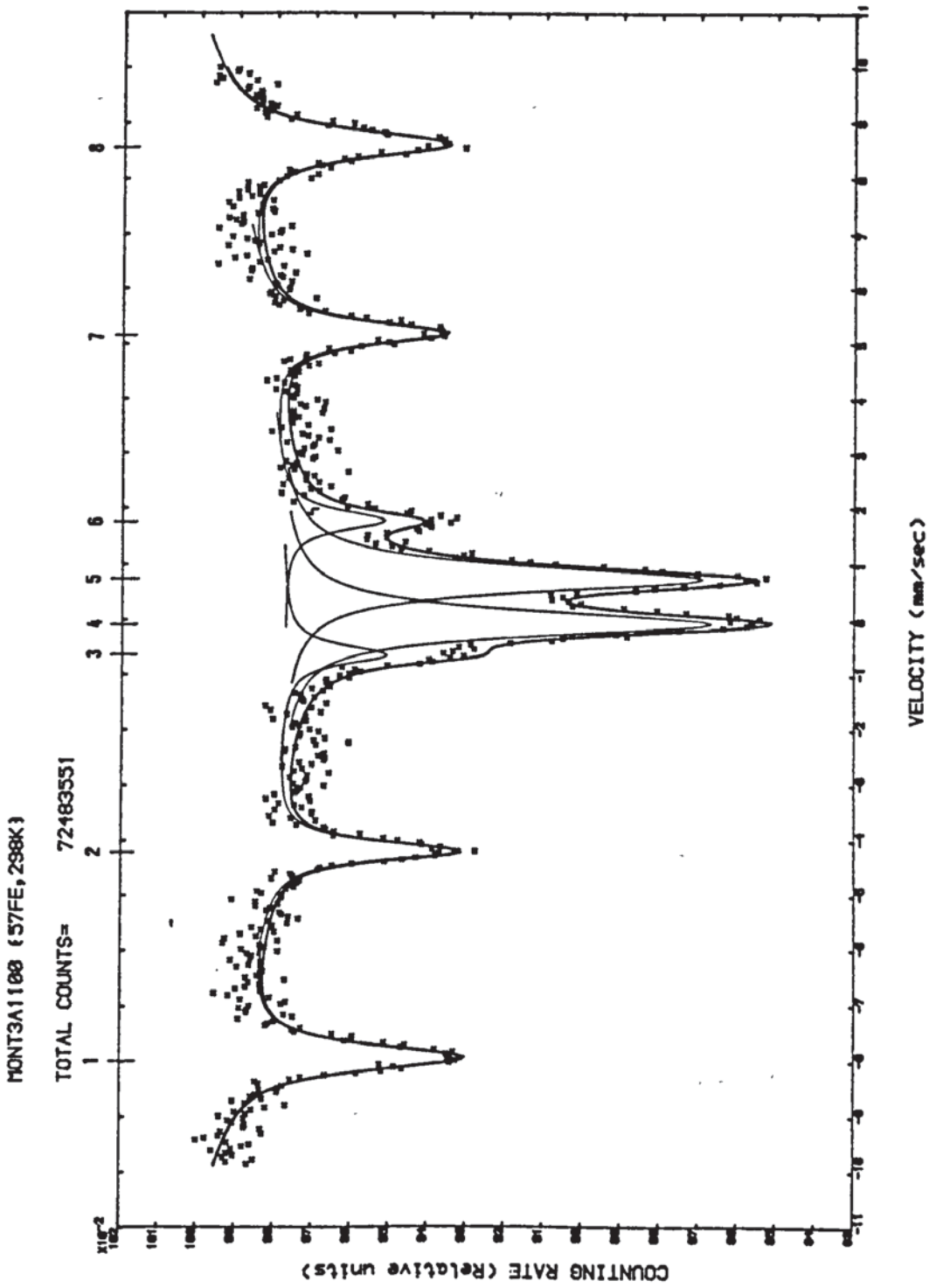

FIG. 68. Mössbauer spectrum of MONT3A1200.

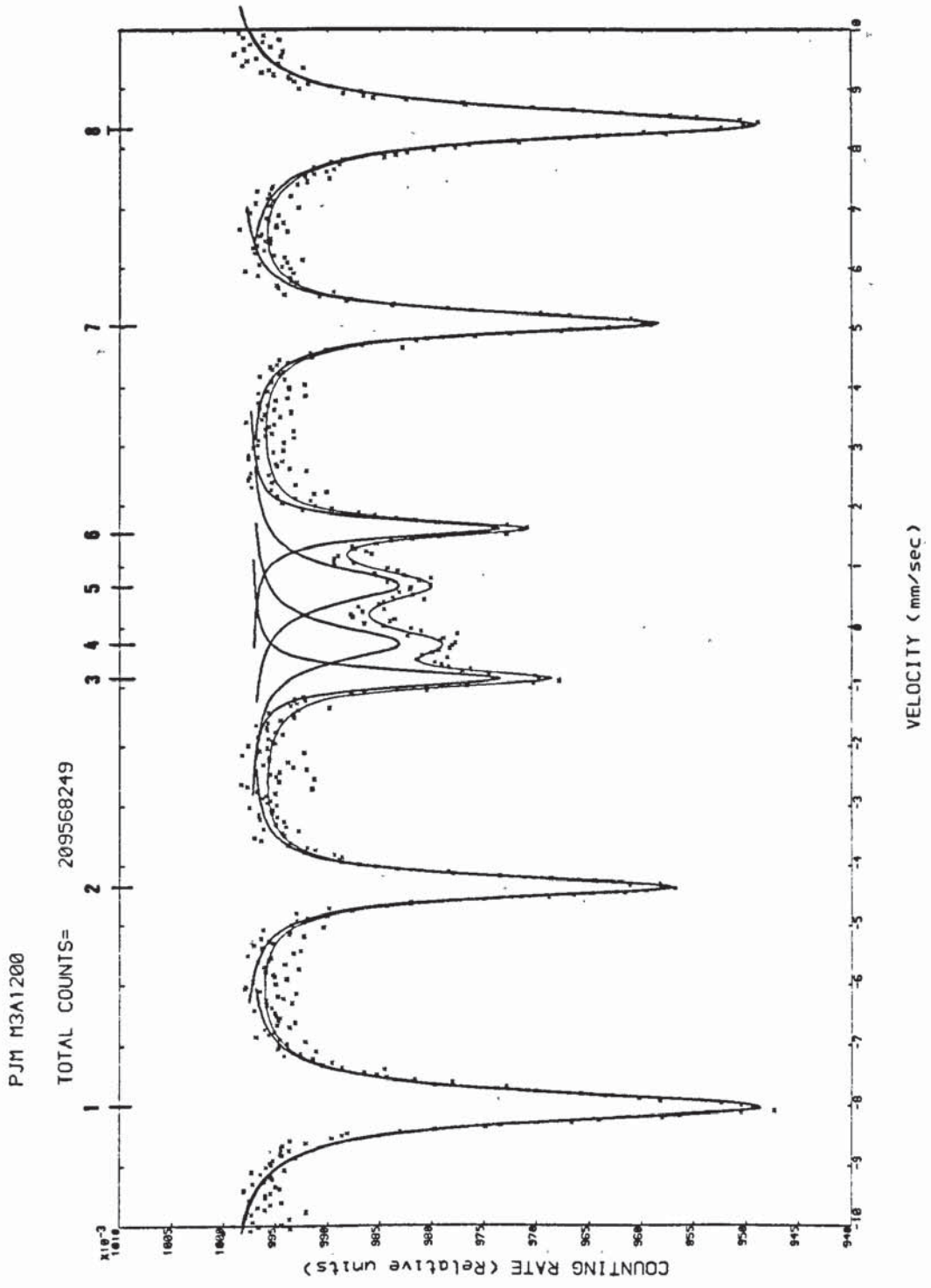

FIG. 69. Mössbauer spectrum of MONT3A1300.

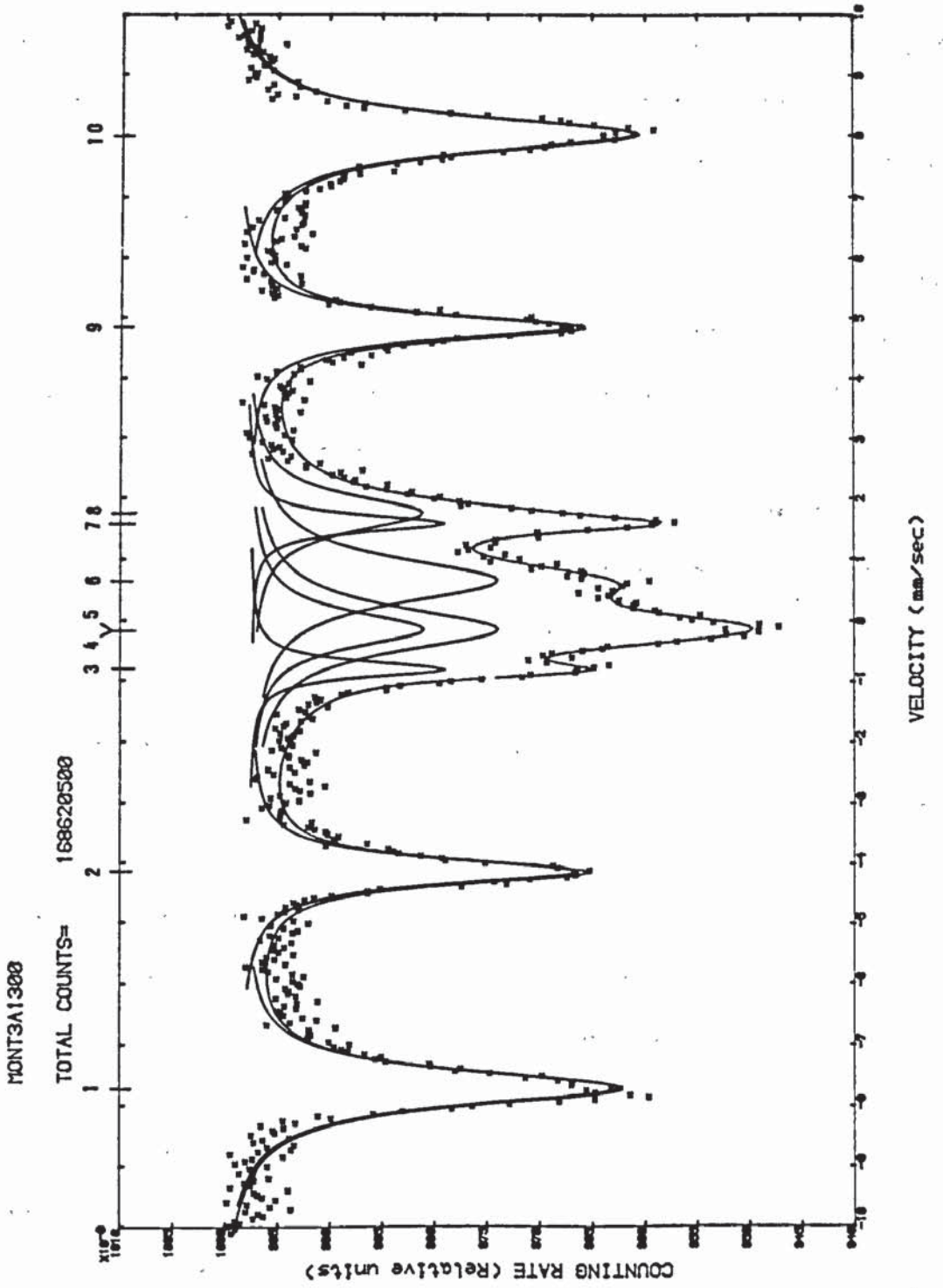

6.3.3. ELECTRON SPIN RESONANCE DATA:

The E.S.R. spectrum of the natural montmorillonite is typical of a poorly crystalline iron-rich clay sample[139]. Resonance features occur at g = 2.06 ($\pm$0.04), line width $\approx$ 1330 G; and g = 4.26 ($\pm$0.02), line width $\approx$ 55 G. The spectrum is dominated by a very broad resonance centred on g = 2.06, which reflects the iron-rich character of this montmorillonite sample. This resonance is due to Fe-O-Fe pair interactions, either within the clay mineral lattice or impurity phases such as iron oxyhydroxides[117],[121],[135]. It is similar to the type B resonance observed for the natural illite sample, section 6.2.3.1. Crăciun, C. and Meghea, A.[139] investigated similar iron-rich montmorillonites and found that the g $\approx$ 2.0 resonance was due to Fe^{3+} clusters present in the form of iron-rich oxyhydroxide phases, either as discrete particles or as coatings on the surface of the montmorillonite particles. However, they did speculate that a portion of this resonance could be attributed to an Fe^{3+} structural component. The resonance centred on g = 4.26 can be attributed to isolated Fe^{3+} ions occupying distorted octahedral sites within the montmorillonite structure[139]. This resonance is the same as the type D resonance observed for the natural illite sample and a full explanation of the resonance is given in section 6.2.3.1.

There are no significant changes in the E.S.R. spectrum of the montmorillonite sample upon heating to a temperature of 500°C, other than a drift of the g $\approx$ 2 resonance from g = 2.06 to g = 2.24. The E.S.R. spectrum of MONT3A600 is similar to

the lower temperature samples, except for the appearance of a relatively sharp resonance centred on g = 2.00 ($\pm$0.02), line width $\approx$ 30 G, FIG. 70. Other resonances occur at g = 2.24 ($\pm$0.04), line width $\approx$ 1100 G; and g = 4.26 ($\pm$0.02), line width $\approx$ 60 G. The drift in g-value of the broad g $\approx$ 2 resonance up to 500°C may be attributed to the effect of dehydration and/or dehydroxylation upon the iron oxyhydroxide impurity phases and Fe^{3+} structural components. The appearance of the resonance centred on g = 2.00 for MONT3A600 could possibly be attributed to a change in the local symmetry of Fe^{3+} ions from octahedral to distorted six-coordinate configurations as the result of dehydroxylation of $FeO_4(OH)_2$ environmental sites.

Heating the montmorillonite sample further to 1100°C resulted in little change of the spectrum observed for MONT3A600. There is a general broadening of the g $\approx$ 2 resonance with increasing temperature, indicating the increasing formation of hematite and Fe^{3+} clusters. The relatively sharp resonance at g = 2.00 increases in intensity and broadens out to 400 G at 1100°C. The increase in intensity of this resonance up to 800°C can be attributed to the increasing number of dehydroxylated Fe^{3+} structural sites, whereas the increasing line width from 800 to 1100°C may be attributed to the formation of new crystalline phases above 800°C and the migration of Fe^{3+} ions causing an increase in Fe-O-Fe pair interactions. A decrease in the g-value of the g = 4.26 resonance to g = 4.21 ($\pm$0.02) at 1000°C can also be attributed to recrystallisation of the relic montmorillonite structure and the incorporation of Fe^{3+} in the distorted octahedral sites of a new crystalline phase.

The E.S.R. spectrum of MONT3A1200 is shown in FIG. 71, and consists of a very broad resonance centred on $g \approx 2$ together with resonances centred on g = 2.00 ($\pm$0.02), line width $\approx$ 350 G; and g = 4.18 ($\pm$0.02), line width $\approx$ 75 G. The very broad $g \approx 2$ resonance represents the presence of hematite, and the decrease in relative intensity of the g = 2.00 resonance is indicative of the Fe^{3+} containing relic montmorillonite structure partially dissolving in the silicate melt. The increase in relative intensity and drift of the g = 4.18 resonance from g = 4.21 for MONT3A1100 indicates that this resonance is due to Fe^{3+} ions contained within the distorted octahedral or tetrahedral environments of a glassy phase[136],[137],[148].

The E.S.R. spectrum of MONT3A1300 is relatively featureless and dominated by an extremely broad resonance centred on $g \approx 2$, line width $\approx$ 1700 G. This is indicative of the presence of hematite within the sample, and of a high degree of Fe-O-Fe pair interactions within a glassy phase. A relatively weak resonance centred on g = 4.07 ($\pm$0.02), line width $\approx$ 75 G, probably indicates the presence of isolated Fe^{3+} ions contained within the distorted tetrahedral environments of a silicate glass[136],[137],[148].

FIG. 70. E.S.R. spectrum of MONT3A600.

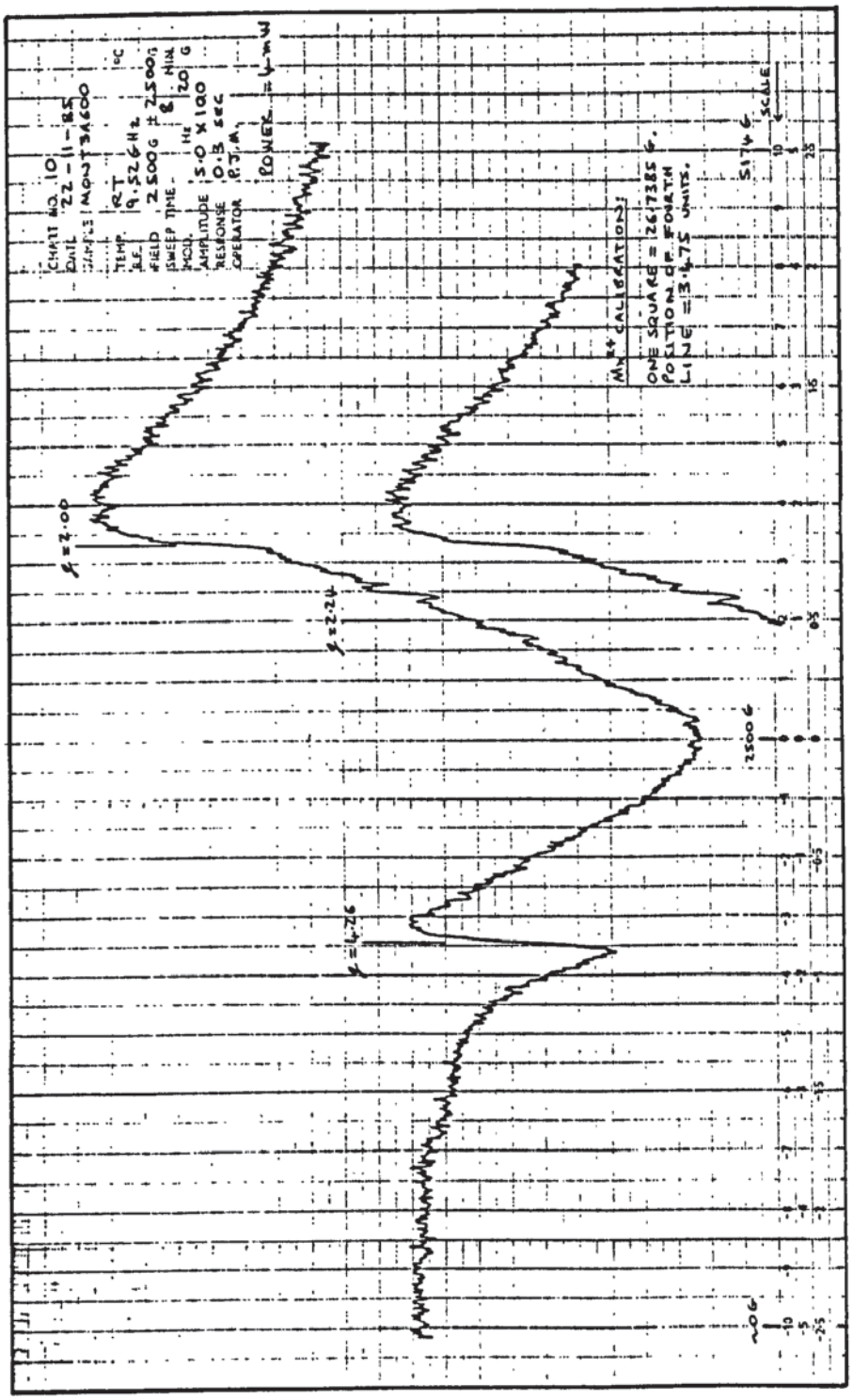

FIG. 71. E.S.R. spectrum of MONT3A1200.

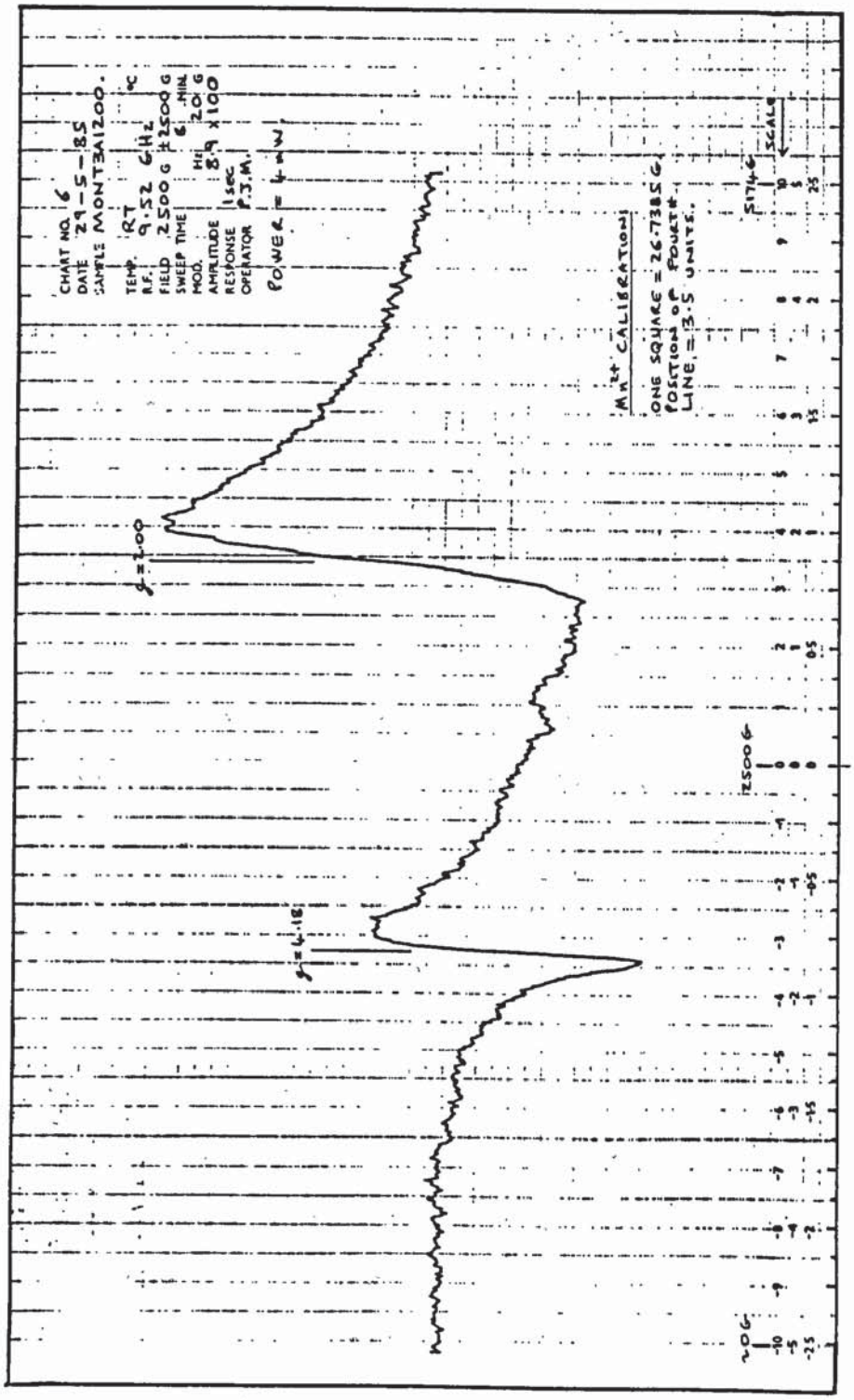

6.3.4. DISCUSSION AND SUMMARY:

The results and spectra of the preceding sections have been discussed and interpreted, on an individual sample/experimental technique basis, alongside their presentation. However, it is intended here to draw together the various components within these sections and give an overall picture of the thermo-chemical changes taking place within the natural clay mineral upon heating. Many of the ideas developed in the discussion of the illite data are directly applicable to the data for montmorillonite, thus the results for montmorillonite may be dealt with more briefly.

Results for the major element analysis of the natural montmorillonite sample, by X-ray fluorescence, have been presented in TABLE 17. The Mössbauer spectroscopy data, presented individually for the natural montmorillonite and each thermally treated sample, have been assimilated in TABLE 22, together with a summary of the major conclusions deduced from the X-ray diffraction study. Electron spin resonance data for the various montmorillonite samples is summarised in TABLE 23. A graphical representation of the major changes occurring during the thermal treatment of montmorillonite are summarised in FIG. 72.

The elemental analysis (XRF) of the natural montmorillonite sample used in this study is in close agreement with the literature data for natural montmorillonites [74],[75]. The SiO_2:Al_2O_3 ratio is slightly higher than expected indicating an α-quartz (SiO_2) impurity, as confirmed by the XRD data. The weight percent Fe_2O_3 is very high

TABLE 22. ^{57}Fe Mössbauer data for thermally treated montmorillonite: summary of XRD conclusions.

Temperature (°C)	$\delta(\pm 0.05)^a$ ($mm\ s^{-1}$)	$\Delta(\pm 0.05)^a$ ($mm\ s^{-1}$)	$\Gamma_{1/2}(\pm 0.05)^a$ ($mm\ s^{-1}$)	XRD conclusions
Ambient	0.36	0.54	0.66	Little change, SiO_2 impurity
400	0.38	1.27[d]	0.58[d]	Trace of FeO(OH)?
	0.33	0.52	0.69	
500	0.38	1.73	0.57[d]	
	0.43	0.89	0.72[d]	
600	0.36	1.26	0.91	
700	0.34	1.43	0.76	Breakdown of montmorillonite structure
	(Trace of magnetic spectrum)			
800	0.35	1.46	0.70	
	0.31	0.86	0.52	
	(Trace of magnetic spectrum)			
900	0.32	0.89	0.67	Spinel, α-Fe_2O_3, $MgSiO_3$
	0.36	−0.10	$H^b = 504$ kG	
1000	0.31	0.79	0.77	Spinel, α-Fe_2O_3, $MgSiO_3$, Cristobalite
	0.40	−0.06	$H^b = 511$ kG	
1100	0.32	0.79	0.55	
	0.39	−0.08	$H^b = 513$ kG	
1200	0.32	0.95	0.70	Spinel and $MgSiO_3$ decrease, α-Fe_2O_3 increases
	0.39	−0.09	$H^b = 509$ kG	
1300	0.90[d]	1.90[e]	0.72[d]	Mullite, cristobalite, α-Fe_2O_3
	0.35[d]	0.80[e]	0.89[d]	
	0.36	−1.10	$H^b = 487$[c]	

[a] Maximum errors.
[b] ±4 kG.
[c] $\Gamma_{\frac{1}{2}} = 0.71, 0.51, 0.33$ mm s^{-1}
[d] Error, $> \pm 0.05$ mm s^{-1}
[e] Error, $> \pm 0.10$ mm s^{-1}

TABLE 23. Summary of ESR data for specimens of montmorillonite heated to the indicated temperatures. Resonances are classified by the g-value.

TEMPERATURE (°C)	IRON(III) FEATURES
Ambient	2.06(br),4.26
400	2.14(br),4.26
500	2.24(br),4.26
600	2.24(br),4.26(narrow feature at g = 2?)
700	2.09(br),4.26(narrow feature at g = 2?)
800	2.00(s),2.06(br),4.26
900	2.00(s),2.06(br),4.26
1000	2.00(overlap)(br),4.21
1100	~2.00(br),4.21
1200	~2.00,4.18(very broad resonance as background)
1300	~2(extremely broad),4.07(w)

(br) = broad(width in excess of 1000 G); (s) = strong resonance; (w) = weak resonance.

FIG. 72. Summary of XRD, Mössbauer and ESR results for montmorillonite.

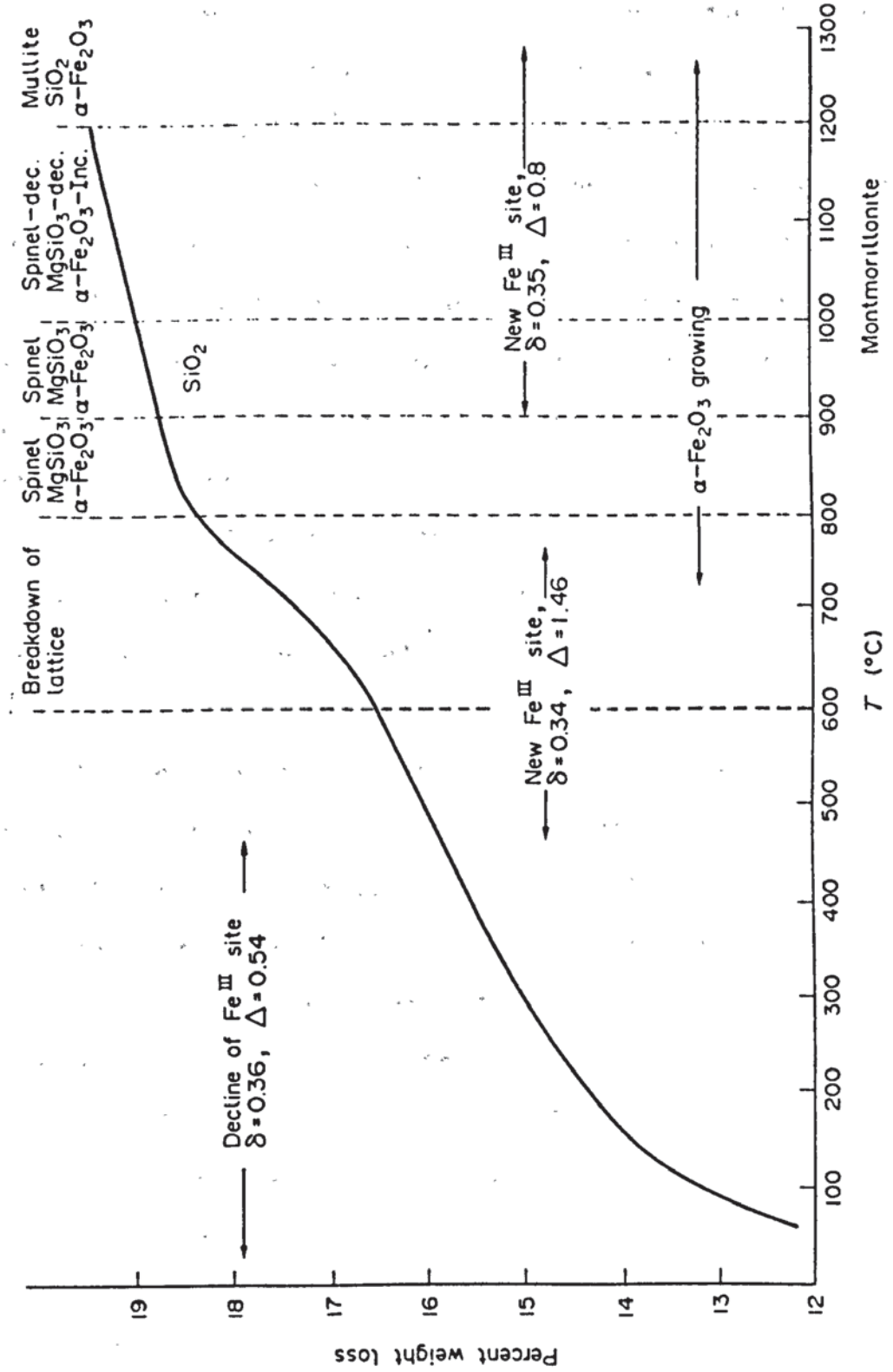

relative to a pure montmorillonite indicating the presence of iron oxyhydroxide impurity phases, as confirmed again by the XRD data[131]. The XRD trace of the natural montmorillonite sample had a high background and a low intensity trace that was typical of a montmorillonite[73]. This indicated the poorly crystalline character of the clay mineral sample, but a basal spacing d(001) of 15.24 Å was observed, typical of montmorillonite[75]. On heating the montmorillonite sample, the XRD trace for the clay showed little change until 700°C, but by 900°C it had been lost totally. The major weight loss due to dehydration and dehydroxylation is complete by 700/750°C (FIGS. 58 and 72), therefore indicating that the X-ray crystallinity is not lost as a result of dehydroxylation[127], [130]. At 900°C, low intensity reflections indicate the onset of recrystallisation of the relic montmorillonite structure to new phases, e.g. spinel ($MgAl_2O_4$), hematite (α-Fe_2O_3) and enstatite ($MgSiO_3$). A significant amount of the hematite may, however, derive from the dehydroxylation of the iron oxyhydroxide impurity phases known to exist in the clay. The crystallinity of the sample increases on heating to 1000°C, when a strong cristobalite (SiO_2) component is apparent and the spinel, enstatite and hematite components have grown. At 1200°C the spinel and enstatite phases have decreased, as has cristobalite slightly, and mullite ($3Al_2O_3.2SiO_2$) has crystallised. This would indicate that these phases have undergone solid state reactions with cristobalite to form mullite[130]. The quantity of hematite increased at 1200°C, and by 1300°C the only crystalline phases discernable are mullite, cristobalite and hematite. The drastic reduction in

cristobalite at 1300°C and the morphology of the cooled material (TABLE 21) indicated a considerable degree of melting to form a glass, but not to the same extent as observed for illite, a fact explained by the considerably smaller quantities of alkali metal oxides associated with montmorillonite than illite (TABLE 17).

The Mössbauer spectrum of the unheated montmorillonite sample has been fitted with a broad quadrupole doublet, which has been interpreted as representing a range of similar iron (III) sites within the clay structure[133], possibly including some contribution from the iron oxyhydroxide phases identified by XRD. The E.S.R. spectrum is typical of that of an iron-rich poorly crystalline clay[139]. It consists of two features: a broad resonance at g = 2.06 and a sharper signal at 4.26. The broad resonance indicates Fe-O-Fe groupings, either within the clay structure or impurity phases such as the iron oxyhydroxides identified by XRD[117],[121],[135],[139]. The g = 4.26 resonance has been attributed to isolated iron (III) ions occupying distorted octahedral sites within the montmorillonite structure[139].

Upon heating the clay sample to 700°C and complete dehydroxylation, a new iron (III) environment was established. The Mössbauer data of the natural clay revealed a quadrupole doublet with δ = 0.36, Δ = 0.54 mm/s which was gradually replaced, with increasing temperature, by a doublet with δ = 0.34, Δ = 1.43 mm/s at 700°C. This follows almost exactly the data observed for illite, whereby the initial quadrupole doublet represents $FeO_{6-x}(OH)_x$ ($2 \geqslant x > 0$) sites and the latter quadrupole doublet (Δ = 1.43 mm/s) represents

the more highly distorted octahedral environments of fully dehydroxylated FeO_6 sites. The E.S.R. data remains relatively invariant on heating to 600°C, apart from a drift of the g = 2.06 signal to g = 2.24 and the appearance of a narrow feature centred on g = 2.00 at 600°C. The drift of the $g \approx 2$ signal can be attributed to the change in the iron oxyhydroxide impurity phases and iron (III) structural clay sites upon dehydroxylation, e.g. $FeO_4(OH)_2$ g = 2.06 $\longrightarrow$ $FeO_{6-x}(OH)_x$ g = 2.24. The further drift of this broad feature back to 2.06 at 800°C may well represent the overwhelming contribution of Fe_2O_3 to the spectrum upon full dehydroxylation of the iron impurity phases and breakdown of the clay structure. The narrow g = 2.00 resonance at 600°C may be attributable to the FeO_6 sites observed for illite above 600°C. This resonance becomes more established by 800-900°C, but no corresponding component at g = 6 is seen, possibly being too weak for detection. The Mössbauer data at 700°C revealed the appearance of α-Fe_2O_3 which grows in relative intensity up to 1200°C, and is detectable by XRD above 800°C. The origin of the hematite will be a combination of the initial dehydroxylation of iron oxyhydroxide impurity phases (700-800°C), structural iron from the collapse of the clay lattice (700-900°C), and the later migration of iron (III) at higher temperatures. From the above, it can be seen that there is a satisfying degree of self consistency between the Mössbauer, E.S.R. and XRD data.

Major recrystallisation of the relic montmorillonite structure occurs above 800°C, XRD indicating the presence of spinel, hematite and enstatite at 900°C, and cristobalite by

1000°C. The Mössbauer spectrum at 800°C (FIG. 64) consists of two quadrupole doublets (δ = 0.35, Δ = 1.46 mm/s and δ = 0.31, Δ = 0.86 mm/s), the doublet with the larger quadrupole splitting corresponds to the FeO_6 environments seen at 700°C whereas the second doublet represents a new iron (III) paramagnetic phase. In the light of the XRD data this doublet may be attributed to iron (III) contained within the spinel phase. By 900°C the doublet corresponding to the FeO_6 environments has been lost due to the total collapse of the montmorillonite structure, the doublet corresponding to the iron (III) in the spinel phase dominates the spectrum. The intensity of this doublet remains strong until 1200°C, whereupon it decreases greatly and the quadrupole splitting increases to Δ = 0.95 mm/s. This is reflected within the XRD data, the trace for spinel increased from 900 to 1100°C and then suddenly decreased at 1200°C. A reduction in the intensity of cristobalite and the appearance of mullite at this temperature indicated a solid state reaction between spinel and cristobalite to form mullite. The quadrupole doublet at 1200°C (δ = 0.32, Δ = 0.95 mm/s) may therefore represent iron (III) contained within mullite[10],[147], or alternatively a silicate glass[148]. There is little change in the E.S.R. data on further heating the clay to 1100°C, other than a general broadening of the $g \approx 2$ resonance due to the increasing quantity of hematite in the sample, an increase in the relatively sharp g = 2.00 resonance, and a decrease in the g-value of the g = 4.26 resonance to g = 4.21. At 1200°C, the g = 2.00 resonance decreases in relative intensity and the g = 4.21 resonance drifts to g = 4.18 and increases in

intensity. The increase in intensity of the g = 2.00 resonance with increasing temperature and then its reduction at 1200°C matches the behaviour of spinel, as expressed in the XRD data, and the changes observed in the Mössbauer data. This resonance may therefore reasonably be assigned to iron (III) contained within the spinel phase. Its initial appearance as a very weak resonance at 600/700°C (FIG. 70) may indicate that 'spinel-like' micro-environments are produced within the clay structure during dehydroxylation, which then fully recrystallise to spinel on the collapse of the clay structure at 800°C. The g = 4.26 resonance is an enigma, remaining unchanged until 1000°C and then decreasing to g = 4.18 at 1200°C. The only change of any note at 1000°C is the appearance of cristobalite within the XRD trace, indicating recrystallisation within the relic tetrahedral lattices of the clay. It may therefore be tentatively speculated that the g = 4.26 resonance is perhaps attributable to isolated iron (III) ions contained within the distorted tetrahedral sites of the clay[137]. A very weak g = 4.07 resonance at 1300°C may be attributed to isolated iron (III) ions contained within the distorted tetrahedral environments of a silicate glass[136],[137],[148]. Otherwise, the spectrum is dominated by a very broad resonance due to the 'magnetic' iron phase.

The Mössbauer data for the montmorillonite heated to 1300°C provides definitive evidence for the presence of iron (II), as seen in FIG. 69. As was the case for illite, its presence is considered to be an artefact of the experimental procedure. In this instance, a further complication occurs. The six line spectrum is well resolved and the hyperfine field

may be quite accurately determined at 487 kG, a figure which is not in good agreement with that expected for α-Fe_2O_3(516 kG [88]) but which is in better agreement with one of the components identified for Fe_3O_4, magnetite, (496 kG[88]). However, clear resolution of the iron (II) and (III) components, particularly to negative velocity, would have been expected. The situation is complicated further by the XRD evidence for α-Fe_2O_3. The outer four lines of the magnetic hyperfine sextet are, however, rather asymmetrical, indicating the presence of one or more overlapping spectra. It can therefore be speculated that the spectrum results from a combination of some or all of the following: hematite (α-Fe_2O_3), maghemite (γ-Fe_2O_3), magnesioferrite ($Mg_xFe_{3-x}O_4$, $x<1$) and magnetite (Fe_3O_4). The central region of the Mössbauer spectrum consists of two broad quadrupole doublets which correspond to iron (II) and (III) contained within a silicate glass[6],[10],[148].

6.4. THE THERMAL TREATMENT OF HECTORITE:

The chemical composition of the natural hectorite sample (HEC1A), as given by X-ray fluorescence analysis and corrected for H_2O content, is detailed in TABLE 17. The results are in close agreement with other analyses of hectorite cited in the literature[74],[75]. However, the weight percent of Fe_2O_3 is slightly higher than would be expected, probably indicating the presence of iron oxyhydroxide impurity phases. The analysis of a second sample of natural hectorite (HEC2A) indicated that this sample was very impure, TABLE 17. The weight percent CaO was given as 25.43%, as compared to 0.42% for HEC1A. This would indicate a large proportion of calcite ($CaCO_3$) impurity within the sample, which is further confirmed by the value for H_2O+ (1100°C) = 30.05% caused by the release of CO_2 on the decomposition of calcite at approximately 700°C. The weight percent Al_2O_3 and Fe_2O_3 are also significantly higher than those for HEC1A, indicating the presence of iron-aluminium oxyhydroxide phases.

Portions of HEC1A and HEC2A were heated at various temperatures up to a maximum of 1300°C. The thermal products were investigated in 100°C steps from a starting point of 400°C, HEC1A/2A400 to HEC1A/2A1300. The percent weight loss and change in morphology of HEC1A and HEC2A upon heating are outlined in TABLES 24 and 25, respectively. From TABLE 24 it can be seen that the percent weight loss of HEC1A increases gradually until about 500°C, representing the loss of adsorbed interstitial water, whereupon it increases rapidly to about 900°C, representing the temperature range over which

TABLE 24. Weight loss and change in morphology of hectorite (HEC1A) upon heating.

TEMP., °C.	% WT. LOSS.*	MORPHOLOGY.
20	-	Pure white powder.
100	3.16	Pure white powder.
200	3.13	Off-white powder.
300	3.60	Off-white powder.
400	3.20	Off-white powder.
500	3.40	Off-white powder.
600	3.70	Off-white powder.
700	4.70	Off-white powder.
800	6.05	White powder.
900	7.10	White, compact but very soft briquette. Powdered easily.
1000	8.00	Pure white, compact but soft briquette. Powdered easily.
1100	7.80	Pure white, firm but brittle porous briquette. Powdered easily.
1200	7.90	Pure white, very hard but brittle briquette. High degree of sintering. Hard to powder.
1300	8.00	Pure white, very hard but brittle briquette. High degree of sintering, but no evidence of melting. Hard to powder.

* = Average result of two samples.

TABLE 25. Weight loss and change in morphology of hectorite (HEC2A) upon heating.

TEMP., °C.	% WT. LOSS.*	MORPHOLOGY.
20	-	Pale cream powder.
100	2.96	Creamy-white powder.
200	2.81	Creamy-white powder.
300	3.03	Creamy-white powder.
400	2.90	Pale cream powder.
500	3.90	Pale cream powder.
600	5.95	Pale cream powder.
700	30.45	Off-white/cream powder.
800	35.00	Off-white/cream powder.
900	33.15	Pale cream, compact but very soft briquette. Powdered easily.
1000	32.90	Off-white/cream, compact but soft briquette. Powdered easily.
1100	32.45	Light yellow-green, compact but soft briquette. Powdered easily.
1200	33.60	Light yellow-green, compact but soft briquette. Powdered easily.
1300	34.00	Pale green glass.

* = Average result of two samples.

dehydroxylation is occurring. The slight increase in percent weight loss from 900 to 1300°C represents the loss of residual hydroxyl ions[130]. The percent weight loss of HEC2A (TABLE 25) stays fairly constant between 100 and 400°C, and then increases rapidly between ≈ 450 and 600°C. This rapid increase is representative of the onset of dehydroxylation of the clay mineral and iron-aluminium oxyhydroxides. At 700°C the percent weight loss increases five-fold to 30.5%, indicating the decomposition of calcite impurity within the clay sample. The percent weight loss only increases slightly between 700 and 1300°C, representing further dehydroxylation of the clay mineral.

6.4.1. X-RAY DIFFRACTION DATA:

6.4.1.1. HEC1A:

The X-ray diffraction trace of HEC1A revealed the characteristic trace expected for hectorite[73]. No other traces were apparent within the diffractogram other than a very weak signal corresponding to the strongest intensity peak observed for calcite[131]. Investigation of the basal spacing gave a relatively strong signal corresponding to a d-spacing of 12.83 Å, typical of a smectite[73]. Washing the clay with 0.5 M acetic acid removed the weak signal corresponding to calcite.

The X-ray diffraction traces of the thermal products showed no appreciable change from 400 to 600°C. At 700°C there was a slight decrease in the relative intensity of the hectorite trace, and the appearance of very weak signals corresponding to enstatite ($MgSiO_3$). This would indicate the onset of reactions or restructuring taking place within the hectorite structure, producing enstatite as a result. The X-ray diffraction trace of HEC1A800 indicated the continuing formation of enstatite at the expense of hectorite, the trace for hectorite decreasing greatly in relative intensity. At 900°C the presence of hectorite was no longer detectable within the diffraction trace, indicating a rapid consolidation of the hectorite structure between 800 and 900°C. The diffraction trace of HEC1A900 consists of several relatively intense traces corresponding to enstatite ($MgSiO_3$) and an equally intense signal for α-quartz. The plethora of traces within the diffractogram of HEC1A1000, as with HEC1A900,

indicate the high degree of recrystallisation that has taken place within the sample between 800 and 1000°C. Several different crystalline phases of enstatite (Powder diffraction file No's.: 3-523, 18-778, 19-769 and 11-273)[149] are present within the diffractogram of HEC1A1000, together with a relatively strong intensity trace indicating the presence of cristobalite.

The X-ray diffraction traces of HEC1A1000, -1100, -1200 and -1300 are essentially the same in that they all indicate the presence of enstatite and cristobalite in approximately the same relative proportions. The samples on the whole, with regard to their diffractograms, are highly crystalline in character, and the continuing undiminished presence of cristobalite up to 1300°C indicates that the system is saturated with respect to SiO_2.

6.4.1.2. HEC2A:

The X-ray diffraction trace of HEC2A revealed the characteristic trace expected for hectorite[73], together with high intensity patterns indicating the presence of calcite ($CaCO_3$) and dolomite ($Mg,Ca(CO_3)_2$) impurities within the clay sample[131]. Washing the clay with 0.5 M acetic acid removed the patterns corresponding to these impurities.

The X-ray diffraction traces of the thermal products showed no appreciable change from 400 to 600°C. At 700°C there was a complete change within the diffractogram, various patterns indicating the continuing presence of calcite and the formation of lime (CaO), periclase (MgO) and hematite (α-Fe_2O_3) as a result of the thermal decomposition of calcite, dolomite and iron oxyhydroxides. The presence of hectorite was no longer indicated within the diffractogram, indicating consolidation of the clay mineral structure, recrystallisation and/or reaction with the other components within the sample. Other patterns within the diffraction trace indicated the presence of enstatite ($MgSiO_3$) and possibly wollastonite ($CaSiO_3$). The X-ray diffraction trace of HEC2A800 indicated the presence of enstatite, lime, periclase and hematite within the sample. At 900°C solid state reactions had started to take place within the sample, resulting in the presence of patterns within the X-ray diffraction trace for lime, periclase, enstatite, wollastonite, larnite (Ca_2SiO_4) and forsterite (Mg_2SiO_4). The presence of larnite, forsterite, lime and periclase at this temperature indicates that the system is unsaturated with respect to SiO_2. The X-ray diffraction

traces of HEC2A1000, -1100 and -1200 indicate that the samples are highly crystalline in character. Patterns within the diffractogram indicate the presence of enstatite, wollastonite, diopside ($CaMg(SiO_3)_2$), larnite (calci-olivine), forsterite and possibly monticellite ($CaMgSiO_4$) and merwinite ($Ca_3Mg(SiO_4)_2$). The X-ray diffraction trace of HEC2A1300 is typical of an amorphous glass, indicating that the sample had melted.

6.4.2. MÖSSBAUER SPECTROSCOPY DATA:

It was not possible to obtain a Mössbauer spectrum for the natural hectorite sample, HEC1A, due to its very low Fe_2O_3 content. However, it was possible to obtain a very weak absorbtion for HEC2A at liquid nitrogen temperature. The parameters are given below:

Isomer shift	= 0.19 ($\pm$0.07) mm/s.
Quadrupole splitting	= 0.40 ($\pm$0.14) mm/s.
Half-Widths	= 0.92 ($\pm$0.14) mm/s.
	0.67 ($\pm$0.25) mm/s.
Relative intensity	= 3468 ($\pm$350).

These parameters indicate the presence of structural Fe^{3+} ions, most probably in octahedral coordination[106]. The thermal products of HEC1A and HEC2A were not investigated by Mössbauer spectroscopy due to their low iron content.

6.4.3. ELECTRON SPIN RESONANCE DATA:

The E.S.R. spectrum of the natural hectorite sample, HEC1A, is shown in FIG. 73. Resonance features occur at g = 4.28 ($\pm$0.02), line width $\approx$ 100 G; and g $\approx$ 2.2, line width $\approx$ 1000 G. The broad resonance centred on g $\approx$ 2.2 is due to Fe-O-Fe pair interactions, either as clusters of Fe^{3+} ions within the clay mineral lattice or impurity phases such as iron oxyhydroxides. The relatively strong resonance centred on g = 4.28 can be attributed to isolated Fe^{3+} ions occupying octahedral sites within the hectorite structure. The thermal products of HEC1A were not investigated by E.S.R. spectroscopy.

The E.S.R. spectrum of the natural hectorite sample, HEC2A, is shown in FIG. 74. The spectrum consists of a relatively weak resonance at g = 4.28 ($\pm$0.02), line width $\approx$ 75 G; a very broad resonance centred on g $\approx$ 2.2, line width $\approx$ 800 G; and a complex hyperfine spectrum centred on g = 1.99 ($\pm$0.01), A $\approx$ 94 G. The resonances centred on g = 4.28 and g $\approx$ 2.2 can be interpreted in the same way as the resonances observed for the natural hectorite sample, HEC1A, given above. However, the complex spectrum centred on g = 1.99 can only be interpreted as being due to the presence of Mn^{2+} ions contained within calcite or dolomite impurity phases. The complexity of the hyperfine spectrum is due to g-anisotropy and spin forbidden transitions[121],[136]. There is no significant change in the E.S.R. spectra of HEC2A between 400 and 600°C. However, at 700°C the complex hyperfine signal due to g-anisotropy and spin forbidden transitions of Mn^{2+} is partially lost, being replaced by a single isotropic

six line pattern. At 800°C only the single isotropic pattern remains. This change is illustrated in the spectra of HEC2A600 and HEC2A800, FIGS. 75 and 76 respectively, and can be interpreted as indicating the decomposition of rhombohedral calcite to cubic calcium oxide[121],[136]. The isotropic six line resonance of Mn^{2+} contained within cubic calcium oxide, observed in the spectrum of HEC2A800, is centred on g = 1.99 ($\pm$0.01), A $\approx$ 83 G. The only other change that occurs between 600 and 800°C is a narrowing in line width and increase in relative intensity of the g = 2.2 resonance, which has now drifted to g = 2.05 ($\pm$0.04), line width $\approx$ 560 G. The line shape of this resonance is very asymmetrical, indicating the presence of two overlapping resonances. These changes are probably due to the formation of hematite (α-Fe_2O_3) at 700°C, formed by the dehydroxylation of iron oxyhydroxides and consolidation of the hectorite structure, and its subsequent reaction with and assimilation in the new phases being produced by the reaction of MgO and CaO with the relic silicate structure of hectorite. The MgO and CaO are produced by the decomposition of dolomite and calcite at approximately 700°C. The above reactions would have the effect of 'diluting' the Fe^{3+} ions previously contained within hematite and iron oxy-hydroxides. This would in turn reduce the number of Fe-O-Fe pair interactions, resulting in a narrower g $\approx$ 2 resonance for Fe^{3+} ions contained within structural sites of the newly formed silicate phases. The g $\approx$ 2 resonance can therefore be considered to consist of a broad resonance due to the remaining hematite, and a narrower resonance due to Fe^{3+} in structural sites.

Changes in the E.S.R. spectra of HEC2A heated between 800 and 1200°C, include the loss of the isotropic six line hyperfine resonance (due to Mn^{2+} in calcium oxide) at 1000°C and a further narrowing and increase in relative intensity of the $g \approx 2$ resonance to $g = 2.01 (\pm 0.01)$, line width $\approx$ 150 G at 1200°C. The loss of the Mn^{2+} resonance at 1000°C is due to the complete consumption of CaO and MgO in reactions with the silicate phases present between 900 and 1000°C. The new Mn^{2+} environmental sites are modified in such a way that no E.S.R. spectrum can be obtained[136]. Changes in the $g \approx 2$ resonance can be interpreted as a continuation of the 'dilution' process of Fe^{3+} ions described above.

The E.S.R. spectrum of HEC2A1300 is shown in FIG. 77. The spectrum consists of a very weak and broad resonance centred on $g \approx 2$, line width $\approx$ 400 G; and a high relative intensity resonance centred on $g = 4.23 (\pm 0.01)$, line width $\approx$ 65 G. The intense resonance at $g = 4.23$ may well be due to isolated Fe^{3+} ions contained within the distorted tetrahedral environments of a silicate glass[136],[137],[148], indicating that the sample had melted. The loss of the $g = 2.01$ resonance observed in the E.S.R. spectrum of HEC2A1200 is due to the melting of the sample and subsequent destruction of the Fe^{3+} environmental sites responsible for this resonance. The broad resonance that remains at $g \approx 2$ is due to a small degree of Fe-O-Fe pair interactions at sites of high Fe^{3+} ion concentration within the glass.

FIG. 73. E.S.R. spectrum of natural hectorite (HEC1A).

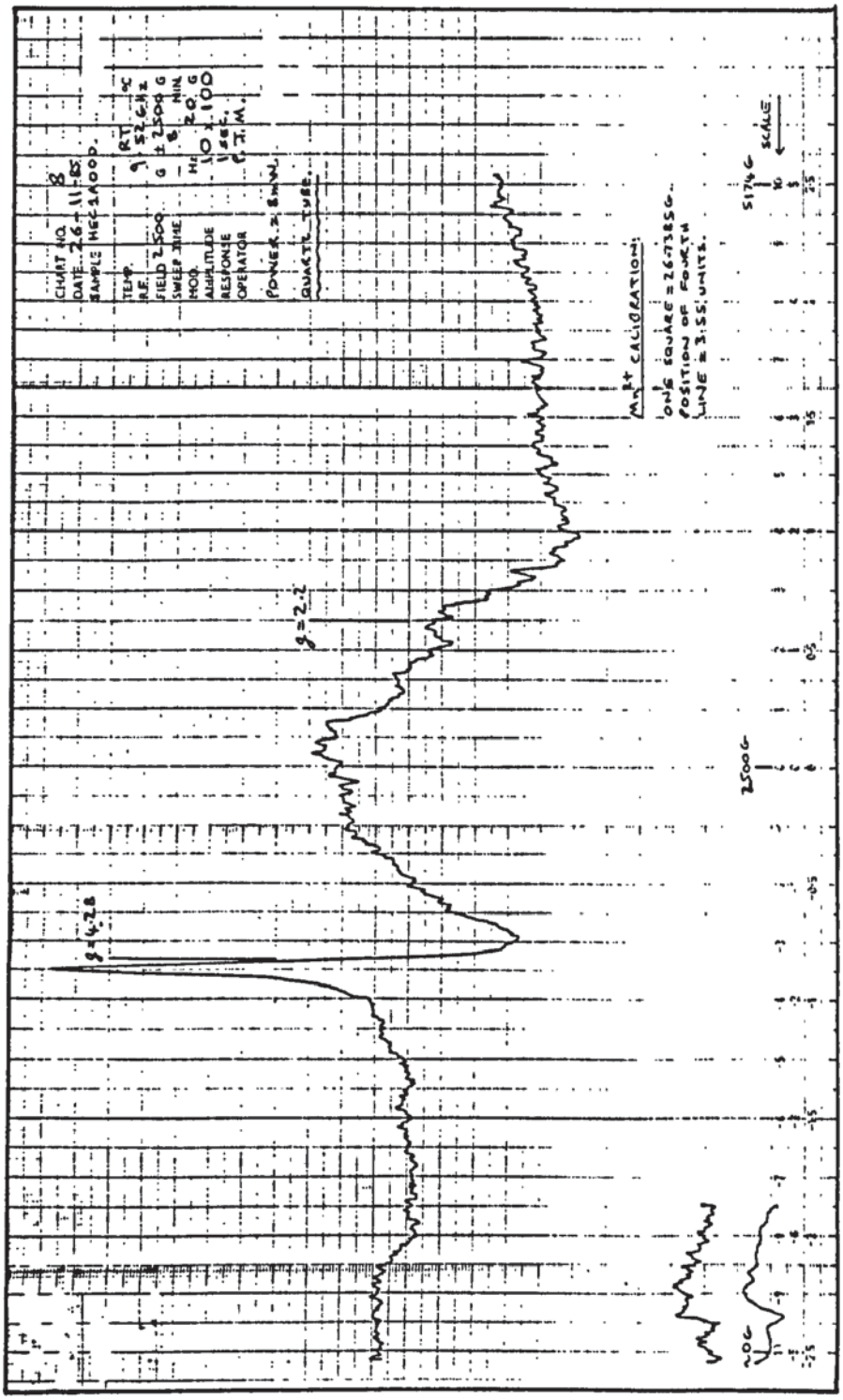

FIG. 74. E.S.R. spectrum of natural hectorite (HEC2A).

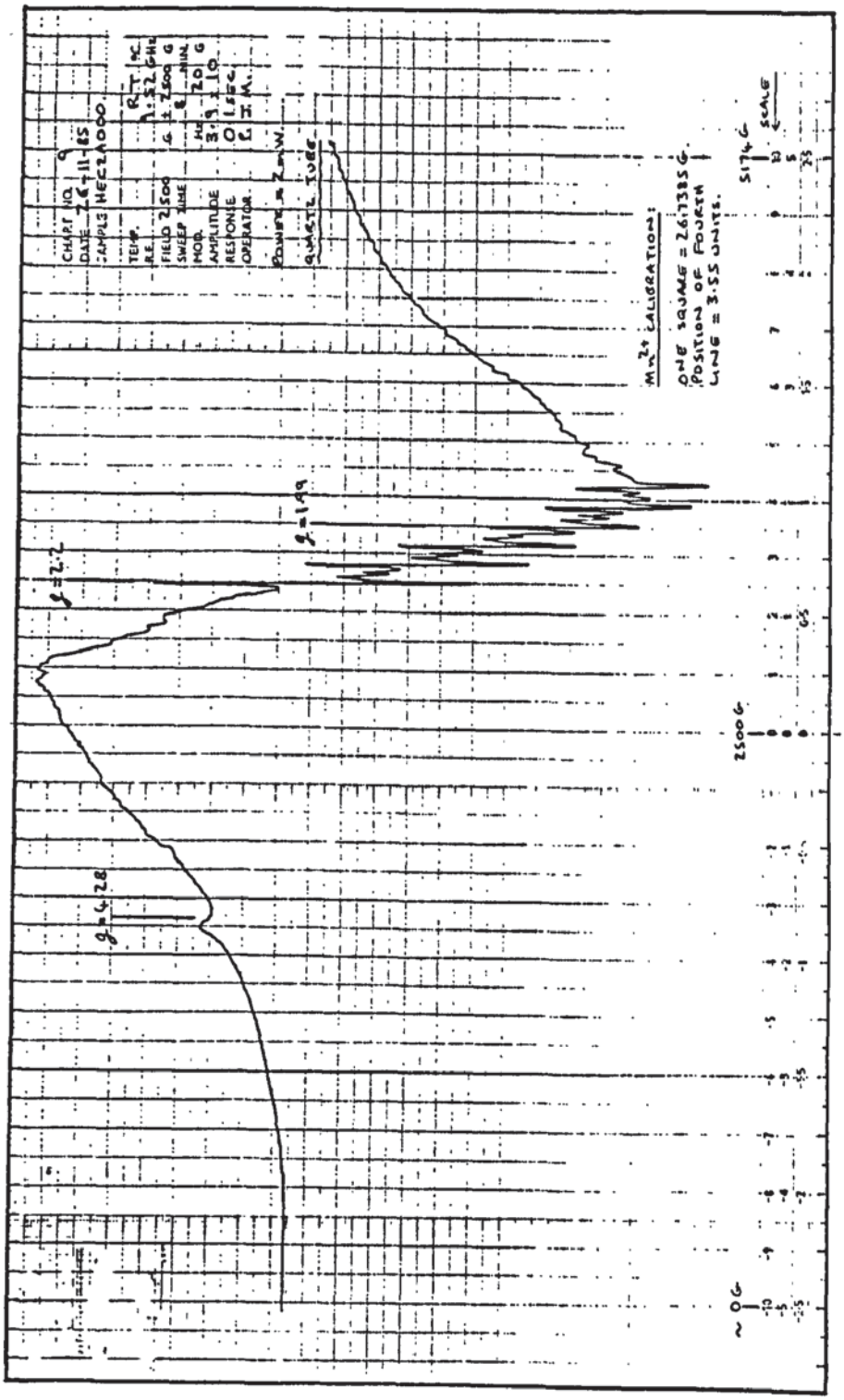

FIG. 75. E.S.R. spectrum of HEC2A600.

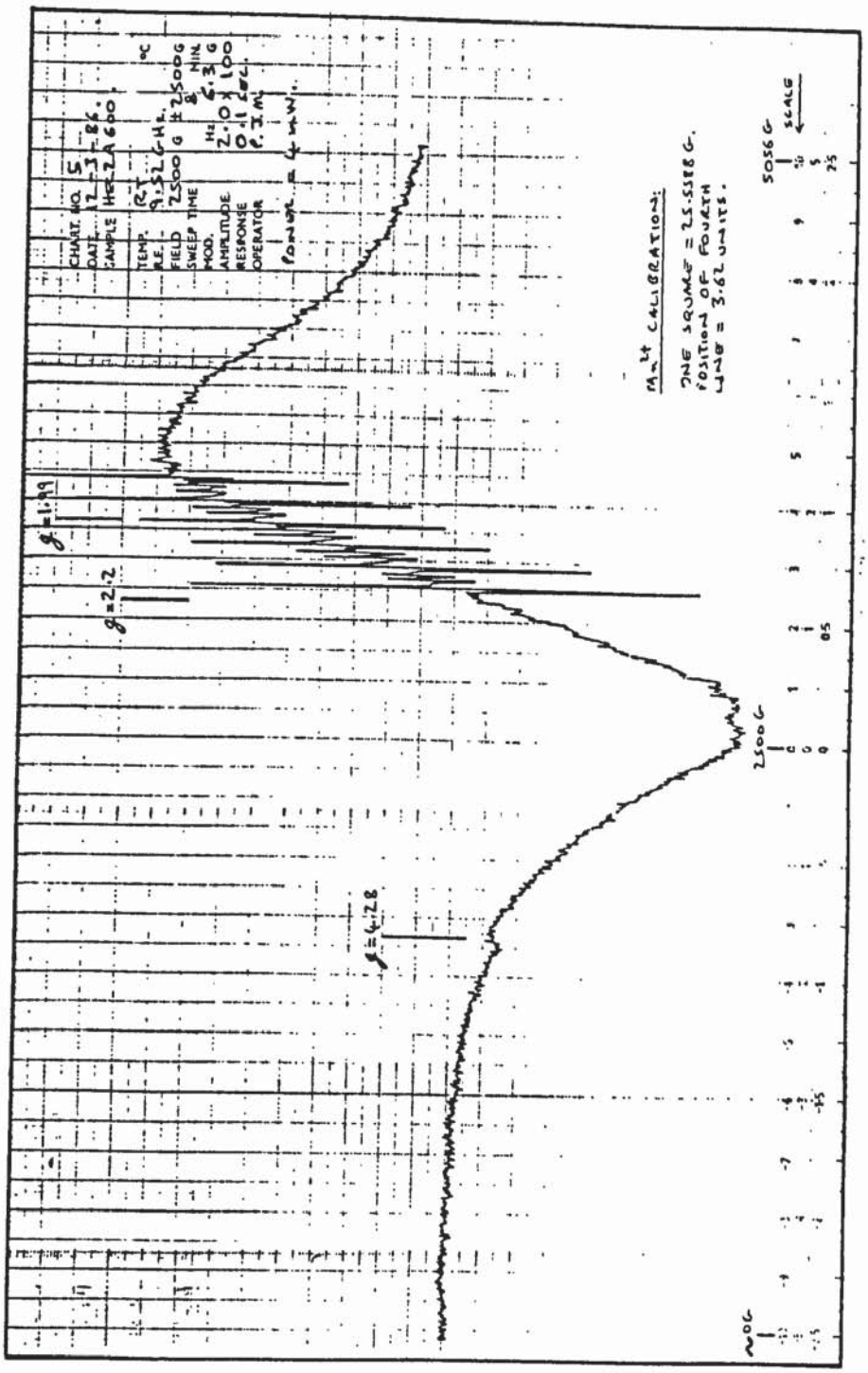

FIG. 76. E.S.R. spectrum of HEC2A800.

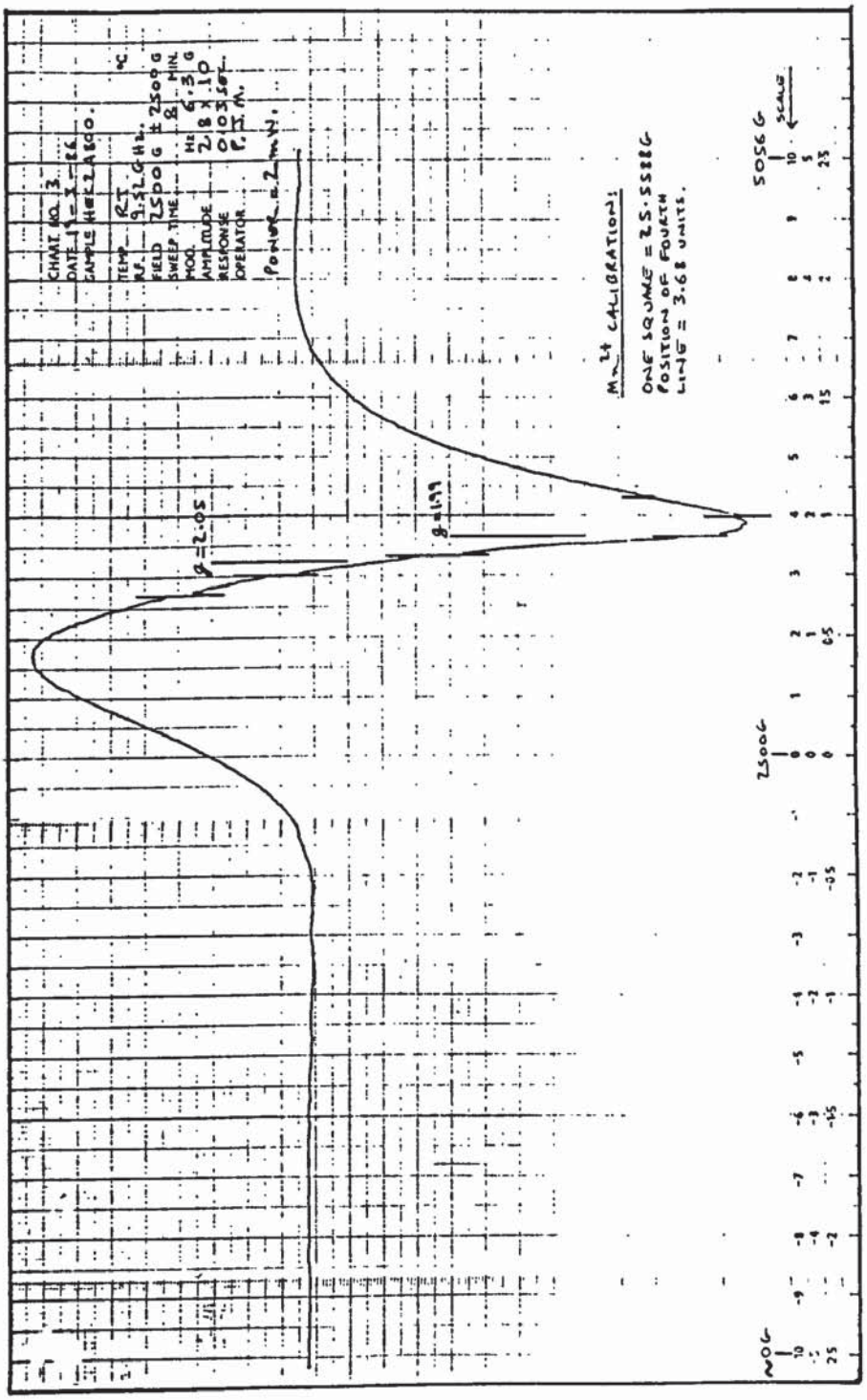

FIG. 77. E.S.R. spectrum of HEC2A1300.

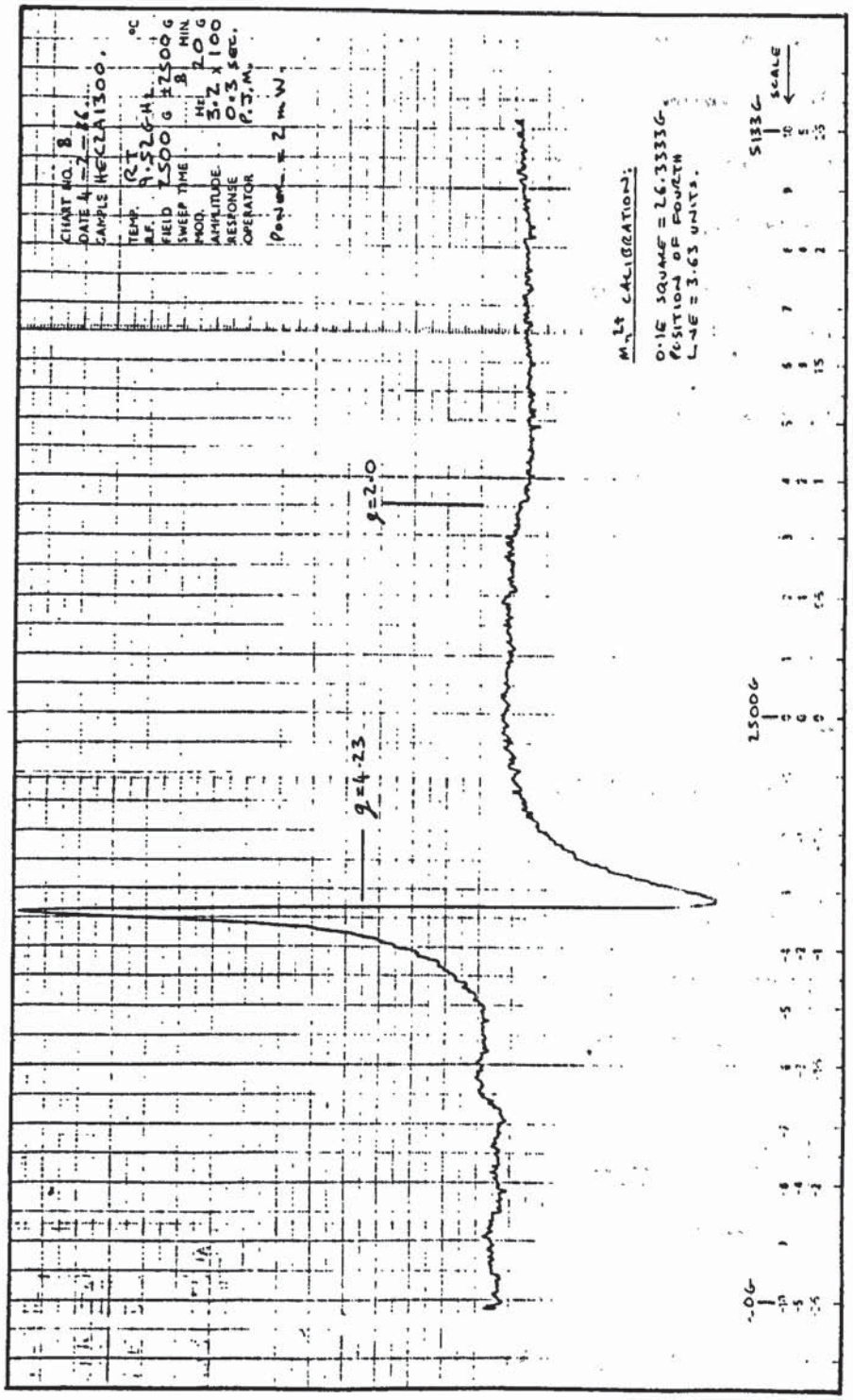

6.4.4. DISCUSSION AND SUMMARY:

The results and spectra of the preceding sections have been discussed and partially interpreted, on an individual sample/experimental technique basis, alongside their presentation. However, it is intended here to draw together the various components within these sections and give an overall picture of the thermo-chemical changes taking place within the natural clay mineral samples upon heating.

Results for the major element analysis of the natural hectorite samples (HEC1A and HEC2A), by X-ray fluorescence, have been presented in TABLE 17. The ESR data for HEC2A has been assimilated in TABLE 26, together with a summary of the major conclusions deduced from the XRD study.

6.4.4.1. HEC1A:

The natural hectorite sample HEC1A and its thermal decomposition products have only been investigated by X-ray diffraction. A study by ^{29}Si MAS-NMR has been carried out and is discussed in section 6.5. It was possible to obtain an ESR spectrum for the natural clay sample, but the very low iron content (TABLE 17) made it impossible to obtain any Mössbauer spectra. Due to the lack of ESR-monitors (Mn(II) and Fe(III)), the thermal decomposition products were not analysed by ESR. The ESR data for the natural clay, HEC1A, merely distinguished between isolated iron (III) ions occupying distorted octahedral sites within the hectorite structure ($g = 4.28$), and Fe-O-Fe pair interactions due to iron (III) ions contained within

TABLE 26. Summary of ESR and XRD data for specimens of thermally treated hectorite(HEC2A). Resonances are classified by the g-value.

TEMPERATURE (°C)	Mn^{2+}	IRON(III) FEATURES	XRD CONCLUSIONS
Ambient	Complex[a], (1.99).	2.2(br),4.28(w)	Hectorite. $CaCO_3$, $MgCa(CO_3)_2$ impurities.
400	Complex[a].	2.2(br),4.28(w)	
500	Complex[a].	2.2(br),4.28(w)	
600	Complex[a].	2.2(br),4.28(w)	
700	Complex[a], (Isotropic).	2.0(br),4.28(w)	Breakdown of hectorite structure. Decomposition of carbonates. $CaCO_3$,CaO, MgO, α-Fe_2O_3,$MgSiO_3$,$CaSiO_3$(?).
800	Isotropic[b].	2.05(overlap)(br)	Growth of: CaO,MgO,$MgSiO_3$, α-Fe_2O_3.
900	Isotropic[b](w).	2.05(m)	Solid state reactions. CaO,MgO,$MgSiO_3$, $CaSiO_3$,Ca_2SiO_4,Mg_2SiO_4.
1000	X	2.03(s)	Solid state reactions. $MgSiO_3$,$CaSiO_3$, $CaMg(SiO_3)_2$,Ca_2SiO_4,Mg_2SiO_4.
1100	X	2.03(s)	As above.
1200	X	2.01(s)	As above.
1300	X	~2.0(w),4.23(s)	Glass.

(a) = Six-line spectrum with doublets between hyperfine lines arising from simultaneous electronic and nuclear transitions — typical of Mn(II) with zero-field splitting. Evidence of g-anisotropy;
(b) = Six-line isotropic spectrum; (br) = broad(width in excess of 500 G); (s)= strong resonance;
(m) = moderate resonance; (w) = weak resonance.

either the clay mineral structure or iron oxyhydroxide impurity phases ($g \simeq 2.0$,broad).

The elemental analysis (XRF) of HEC1A is in close agreement with the literature data for natural hectorites[74], [75]. However, the weight percent of Fe_2O_3 is slightly higher than expected, which in conjunction with the ESR data would indicate the presence of an iron oxyhydroxide impurity phase.

The XRD trace of HEC1A was characteristic of that expected for hectorite[73]. The basal spacing of 12.83 Å is typical of a smectite[73]. A very weak signal corresponding to calcite was observed[131], which was removed by washing the clay with 0.5 M acetic acid. Dehydroxylation of the clay is not complete until about 900°C (TABLE 24). However, XRD reveals that the clay structure has completely collapsed by this temperature with restructuring and recrystallisation to enstatite ($MgSiO_3$) occurring as low as 700°C. Therefore, dehydroxylation and the breakdown of the clay structure appear to be proceeding at the same time. Green, J.M., et al.[164] postulated an inhomogeneous reaction mechanism, similar to talc, for the dehydroxylation of synthetic hectorite to enstatite, in which acceptor regions lose eight protons compensated by a gain of four Mg^{2+} ions. The donor regions, from which water is lost, become silica-rich. A schematic representation of this mechanism is shown in FIG. 78.

Large scale recrystallisation of the clay sample occurs between 800 and 1000°C, enstatite being the major product. Cristobalite (SiO_2) appears within the XRD trace at 1000°C marking the collapse of the relic tetrahedral lattice of the clay. Above 1000°C the XRD data remains essentially the same

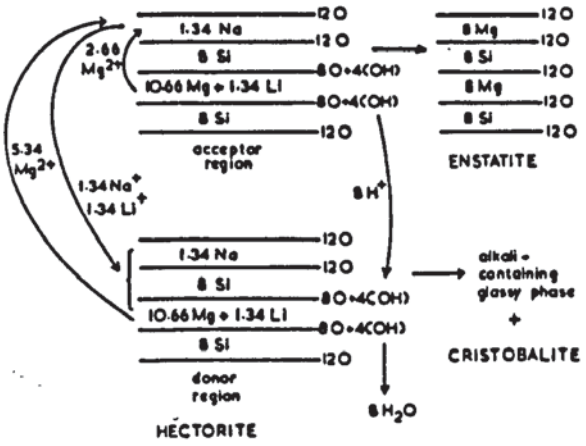

FIG. 78. Schematic diagram of the inhomogeneous reaction mechanism for synthetic hectorite. (After Green, J.M. et al.[164])

right up to 1300°C. The continuing undiminished presence of cristobalite above 1000°C indicates that the sample is saturated with respect to SiO_2, and that the high temperature thermochemistry is therefore based on the polymorphic changes of enstatite.

Enstatite is present within all of the samples heated to a temperature greater than 700°C, but the crystalline form of the enstatite does change with increasing temperature. At 800 and 900°C, ORTHO-enstatite (file No's.: 7-216 and 19-768) is the only crystalline phase present. For samples heated to 1000°C the dominant crystalline phase is PROTO-enstatite (file No's.: 11-273 and 3-523), with minor quantities of CLINO-enstatite (19-769 and 18-778). But for samples heated between 1100 and 1300°C the situation reverses, with CLINO-enstatite (19-769) being the dominant phase for samples heated at 1200 and 1300°C. These changes are consistent with the known thermal chemistry of enstatite[153], FIG. 79.

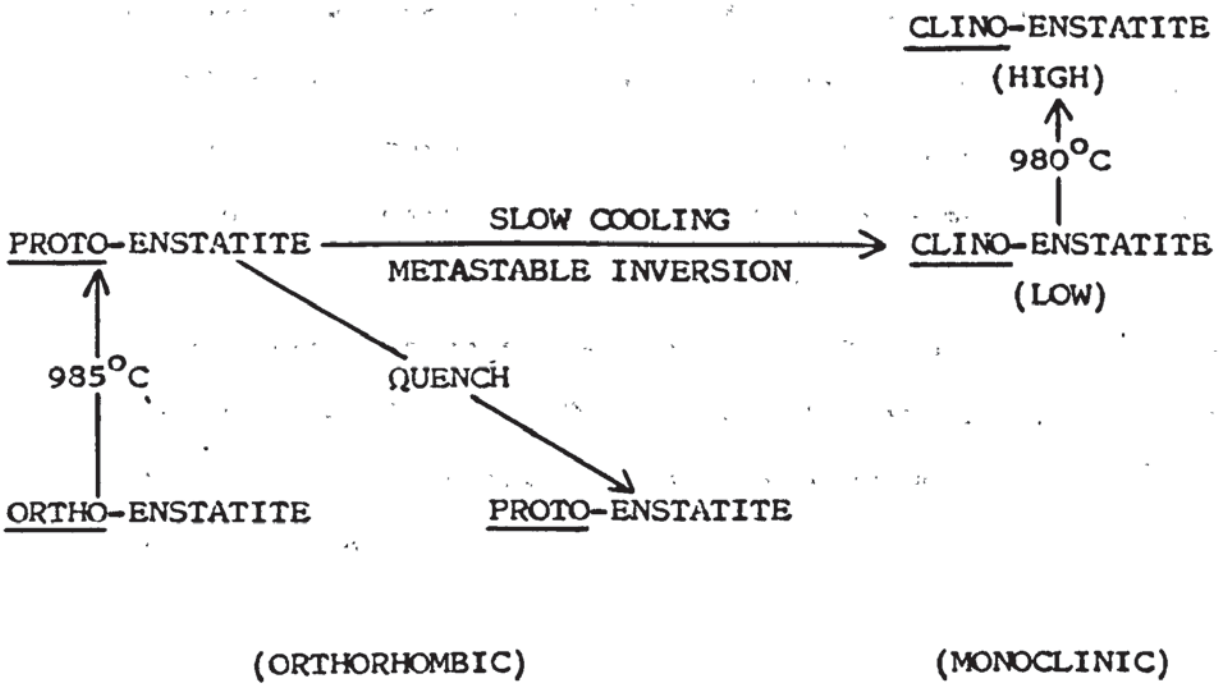

FIG. 79. Schematic representation of the polymorphs of enstatite ($MgSiO_3$).

At temperatures less than 985°C the stable polymorph of $MgSiO_3$ is ORTHO-enstatite, and between 985 and 1385°C PROTO-enstatite is the stable polymorph. However, if the sample is not quenched rapidly PROTO-enstatite will undergo a metastable inversion to CLINO-enstatite. The samples investigated in this work were not quench cooled, therefore the higher the thermal treatment temperature the longer time it took for the sample to cool. This would result in a higher concentration of CLINO-enstatite within samples progressively heated to higher temperatures.

One other unusual observation, was the apparent presence of 'α-quartz' within the XRD data for the sample heated to 900°C, which was replaced by cristobalite at 1000°C. Since α-quartz should normally invert to β-quartz at 573°C, it is possible that β-quartz, which can exist in a metastable form above 870°C and has a similar XRD trace to α-quartz, is in fact being seen. Perhaps then, when the hectorite structure collapses between 800 and 900°C, a quartz-like phase is formed initially which then recrystallises between 900 and 1000°C to form cristobalite.

6.4.4.2. HEC2A:

The natural hectorite sample HEC2A and its thermal decomposition products have been investigated by X-ray diffraction and ESR spectroscopy. Unlike HEC1A, it was possible to obtain a very weak Mössbauer spectrum for the natural clay (HEC2A) at liquid nitrogen temperature. The parameters of the observed doublet tend to indicate the presence of iron (III) contained within structural octahedral sites within the clay. Since the absorption doublet was very weak no attempt was made to obtain spectra of the thermally treated samples.

The elemental analysis (XRF) of HEC2A indicated that the sample was very impure compared to HEC1A (TABLE 17). It contained 25 wt% CaO and significantly higher levels of Al_2O_3 and Fe_2O_3 (indicating the presence of iron-aluminium oxyhydroxide phases). The weight loss on heating HEC2A (TABLE 25) follows that observed for HEC1A until 700°C, whereupon it jumps from 5.95% at 600°C to 30.45%. This clearly indicates

a high level of carbonate impurity in the sample, which on the basis of the CaO wt% appears to be mainly calcite ($CaCO_3$). Decomposition of the carbonate phase is complete by 800°C (wt. loss = 35%), and is confirmed by the XRD data.

The XRD trace of HEC2A revealed the characteristic trace expected for hectorite[73], together with high intensity patterns for calcite ($CaCO_3$) and dolomite ($MgCa(CO_3)_2$)[131]. Washing the clay with 0.5 M acetic acid removed these impurity phases. The XRD data follows that of HEC1A until 700°C, whereupon the thermochemistry of HEC2A is dominated by reactions of the decomposing carbonate phases with the clay mineral. At 700°C lime (CaO), periclase (MgO) and hematite (α-Fe_2O_3) are produced from the decomposition of the impurity phases calcite, dolomite and iron oxyhydroxides. Enstatite ($MgSiO_3$) results from the decomposition of the clay and reaction of MgO with structural (SiO_4) units; similarly, wallastonite ($CaSiO_3$) may be being formed from CaO. These reactions result in the total breakdown of the clay structure. By 900°C the chemical components of the clay have been completely consumed by the large excess of CaO and MgO, the continuing presence of these two phases and the appearance of larnite (Ca_2SiO_4) and forsterite (Mg_2SiO_4) within the XRD data indicates that the system is unsaturated with respect to SiO_2 [130]. Thus, CaO and MgO are reacting with $CaSiO_3$ and $MgSiO_3$ as the only sources of SiO_2. These reactions proceed until all of the CaO and MgO has reacted, and by 1000°C the sample consists mainly of $MgSiO_3$, $CaSiO_3$, Mg_2SiO_4, Ca_2SiO_4 and their solid-solutions. This situation remains during heating to 1200°C, indicating that equilibrium within the system has been

reached. At 1300°C the sample melted to a glass.

The ESR data for HEC2A can be divided into two sets; Mn (II) resonances acting as a monitor for the carbonate and oxide phases, and Fe (III) resonances acting as a monitor for the clay structure and silicate phases. The close agreement between the ESR and XRD data is illustrated in TABLE 26. The Mn (II) resonance for the unheated clay consists of a complex hyperfine spectrum due to g-anisotropy and spin forbidden transitions[121],[136]. This resonance pattern is typical of Mn (II) ions contained within calcite[136], and persists within the ESR data for samples heated to 700°C. At this temperature the resonance is partially lost, and by 800°C only a single isotropic six line pattern remains. This is due to the decomposition of rhombohedral calcite to cubic calcium oxide [121],[136], and correlates well with the decomposition of the carbonate phases between 600 and 800°C observed within the XRD data. The isotropic resonance pattern for Mn (II) in CaO eventually disappears at 1000°C when no more CaO remains, as indicated by XRD, and the new Mn (II) environmental sites are modified in such a way that no ESR spectrum can be obtained [136].

The Fe (III) resonances change little over the temperature range of the heat treated clay samples, and it would appear that the ESR data does little more than differentiate between Fe-O-Fe groupings ($g \simeq 2$) and isolated iron (III) sites ($g = 4.2$). In general the ESR data for the HEC2A samples follows very closely that already observed for the other smectite clay mineral, montmorillonite (TABLE 23). The $g = 4.28$ resonance present for samples heated to 700°C can be attributed

to isolated iron (III) ions within the clay structure which are lost on decomposition of the clay above 700°C, as indicated by XRD. Its reappearance as g = 4.23 at 1300°C indicates the renewed formation of isolated iron (III) environments within the silicate glass, probably tetrahedral in character[136], [137],[148]. The broad g = 2.2 resonance remains constant until 600°C, and then becomes narrower, increases in intensity and drifts to g = 2.05 at 800/900°C. The resonance is now very asymmetrical, indicating the presence of two overlapping resonances. It would appear that the g = 2.2 signal can be attributed to iron (III) contained within either iron oxyhydroxide phases or the clay mineral structure. At 700°C, these phases decompose to give hematite (g = 2.0), which then reacts between 700 and 900°C with the other mineral phases present. This has the effect of 'diluting' the iron (III) ions, previously concentrated within the hematite and iron oxyhydroxide, in structural sites within the new crystalline phases; thus reducing the Fe-O-Fe pair interactions leading to a stronger and narrower resonance (g = 2.05). This process continues until 1200°C, iron (III) being isomorphously substituted within the various crystalline phases present. At 1300°C the clay sample melts and the iron (III) ions become widely dispersed within the resulting glass (g = 4.23) with minor iron-clusters giving some Fe-O-Fe pair interactions ($g \simeq 2$).

6.5. THE THERMAL TREATMENT OF ION-EXCHANGED HECTORITE:

Sub-Samples of the natural hectorite sample, HEC1A, were ion-exchanged with a range of transition metal cations, and then thermally treated at 1200°C for three hours. The quantity of transition metal cations exchanged onto the hectorite samples, together with the p.H. of the resulting exchange solutions are given in TABLE 27. Samples of hectorite exchanged in a 0.1 M solution of the cation are designated by A, 0.075 M = B, 0.05 M = C, 0.025 M = D, and 0.01 M = E. All cation exchanged samples lie approximately within the maximum exchange capacity of hectorite for that particular cation. However, HEC1ACrA has exceeded its maximum exchange capacity for Cr^{3+} by a factor of three. This may well be due to hydrolysis of the $(Cr(H_2O)_6)^{3+}$ ion on the clay mineral surface.

The use of Scanning Electron Microscopy, in conjunction with the EDAX-system, was investigated as an alternative method to atomic absorbtion spectrophotometry in the measurement of the quantity of the cation exchanged onto the clay. It was envisaged that the percent elemental composition of the clay particles, given by the EDAX-system, could be converted to percent oxide composition by the available software. However, this attempt was not successful, due mainly to the very low level of the various cations exchanged onto the clay. The percent elemental composition of cations at the maximum exchange level of the clay was only just above the level of sensitivity of the instrumentation. Therefore, small changes in the exchanged cation concentration could not

TABLE 27. Quantity of transition metal cations exchanged onto hectorite samples.

CATION	SAMPLE No.	pH OF EXCHANGE SOLUTION.	AMOUNT OF EXCHANGED CATION, mg/g of clay.
Cu^{2+}	HEC1ACuA	5.3	17.2
	HEC1ACuB	5.5	19.3
	HEC1ACuC	5.6	18.4
	HEC1ACuD	5.9	11.2
	HEC1ACuE	6.2	10.5
Ni^{2+}	HEC1ANiA	6.7	17.1
	HEC1ANiB	6.6	16.9
	HEC1ANiC	6.8	16.3
	HEC1ANiD	7.2	11.9
	HEC1ANiE	7.5	9.8
Mn^{2+}	HEC1AMnA	6.5	17.6
	HEC1AMnE	7.2	9.1
Co^{2+}	HEC1ACoA	5.9	16.9
	HEC1ACoE	6.6	9.7
Cr^{3+}	HEC1ACrA	3.18	26.7
	HEC1ACrE	7.0	8.1
Zn^{2+}	HEC1AZnA	5.88	18.7
Fe^{3+}	HEC1AFeE	3.02	10.9

be detected. The situation was further complicated by the variation of exchanged cation content from particle to particle of the same sample. This would indicate adsorption of the exchanged cation onto the clay particle surfaces, and perhaps even clustering, as well as the usual interlayer exchange. The amount of cation taken up by the clay was therefore determined from atomic absorption measurements of the cation concentration within the supernatent liquid following exchange.

6.5.1. X-RAY DIFFRACTION DATA:

The X-ray diffraction traces of all the transition metal exchanged samples of HEC1A were identical to that observed for the natural unexchanged hectorite sample.

The X-ray diffraction traces of the cation exchanged samples that had been heated to 1200°C were all very similar. Patterns within the diffraction traces indicated the presence of enstatite and cristobalite, however, no patterns were detected for phases specifically attributable to the presence of the cation exchanged element within the sample. This would indicate that the exchanged cations are isomorphously substituted within the phases produced as a result of the thermal decomposition and recrystallisation of the natural hectorite sample. Although the exchanged cations are not present at a high enough concentration to produce their own silicate phases at 1200°C, they do appear to have significantly affected the crystallisation of enstatite. The X-ray diffraction trace of HEC1A1200 indicated clino-enstatite (file no. 19-769) as the dominant crystalline phase of enstatite within the sample. However, the dominant crystalline phase present within the cation exchanged hectorite samples heated to 1200°C is proto-enstatite (file no. 11-273). This would indicate that the exchanged cations have in some way stabilised the proto-enstatite crystalline structure so that it does not invert metastabily to clino-enstatite during cooling. On closer inspection of the X-ray diffraction traces of the thermally treated cation exchange samples, it was noticed that for the series of samples

HEC1ANiA1200 to HEC1ANiE1200 the content of proto-enstatite decreased, whereas that of clino-enstatite increased, as the quantity of exchanged cation decreased. This change was not, however, indicated within the X-ray diffraction traces of the Cu^{2+} exchanged samples. Nevertheless, the results for the Ni^{2+} exchanged samples do indicate that as the exchanged transition metal concentration at 1200°C is reduced, the stability of proto-enstatite with respect to clino-enstatite is also reduced. The above observations may be related to the ionic radii of the various exchange cations compared to that of Mg^{2+}. The ionic radii of Cu^{2+}, Ni^{2+}, Cr^{3+}, Mn^{2+}, Co^{2+}, and Zn^{2+} are larger than that of Mg^{2+} and could well explain the stabilisation of proto-enstatite. However, the ionic radius of Fe^{3+} is almost the same as that of Mg^{2+}, yet the same effect is observed. This discrepancy could be explained if some of the iron within the sample at 1200°C was in fact present as Fe^{2+}. The ionic radii of the various cations are given below[150]:

CATION	Å
Cr^{3+}	0.069
Mn^{2+}	0.080
Fe^{2+}	0.076
Fe^{3+}	0.064
Co^{2+}	0.078
Ni^{2+}	0.078
Cu^{2+}	0.069
Zn^{2+}	0.074
Mg^{2+}	0.065

6.5.2. MÖSSBAUER SPECTROSCOPY DATA:

Samples of HEC1A were exchanged in a 0.01 M solution of $FeCl_3$ to produce Fe^{3+} exchanged samples of hectorite (HEC1AFeE) containing approximately 11 $mg(Fe)g^{-1}$. These samples were then thermally treated in 200°C steps from 400 to 1200°C, HEC1AFeE400 to HEC1AFeE1200. It was not possible to obtain a Mössbauer spectrum of the exchanged sample (HEC1AFeE) at room temperature. This would indicate that the exchanged Fe^{3+} ions are present within environmental sites that give rise to a very low recoil-free fraction(151). It was, however, possible to obtain spectra for the thermally treated samples.

An attempt was also made to exchange a sample of HEC1A with a 1.4×10^{-6} M solution of $^{57}Fe^{3+}$. Atomic absorbtion spectrophotometry of the post-exchange solution indicated that the majority of $^{57}Fe^{3+}$ ions had been taken up by the clay as expected. However, it was not possible to obtain room temperature spectra of this sample even after the clay had been thermally treated at 1200°C. This would indicate that either the level of ^{57}Fe exchanged onto the clay sample was still too low to obtain Mössbauer spectra, or that a quantity of the ^{57}Fe had been lost during the thermal treatment due to the volatilisation of the $FeCl_3$. The latter condition would indicate that a proportion of the exchanged iron was present on the unheated clay as ferric chloride complexes, e.g. $FeCl^{2+}_{aq.}$ (151).

The Mössbauer spectra of HEC1AFeE400,-800, -1000 and -1200 are presented in FIGS. 80 to 83, and the Mössbauer

parameters are summarised in TABLE 28. From the Mössbauer data it can be seen for the samples heated to 400 and 600°C that the Fe^{3+} ions are present within distorted octahedral sites. Dehydration of the hectorite sample would effectively sandwich exchanged Fe^{3+} ions between the tetrahedral layers of the opposing structural sheets of the clay. This would create a wide range of slightly different Fe^{3+} environmental sites, and this is reflected in the broad half-width of the spectral lines. At 800°C there is a significant decrease in the quadrupole splitting from Δ = 1.13 mm/s at 600°C to Δ = 0.85 mm/s. This change indicates an increase in the symmetry of the Fe^{3+} octahedral environments, due to either the breakdown of the hectorite structure or crystallisation of new phases containing isomorphously substituted Fe^{3+} ions. The very broad half-width of the quadrupole doublet indicates, again, a range of similar environmental sites. This correlates well with the XRD data for unexchanged hectorite, whereby the clay structure breaks down above 700°C to form enstatite.

The Mössbauer data for samples heated to 1000°C revealed the presence of two quadrupole doublets: a high intensity doublet corresponding to Fe^{3+} ions contained within the relatively undistorted octahedral sites of a crystalline phase (δ = 0.37, Δ = 0.49 mm/s), and a weak, poorly resolved broad doublet attributable to Fe^{2+} ions (δ = 0.60, Δ = 2.47 mm/s) contained within the octahedral sites of enstatite[5],[152]. The data for samples heated to 1200°C may be further resolved into three quadrupole doublets. The high intensity doublet (δ = 0.38, Δ = 0.42 mm/s) attributed to Fe^{3+} ions can be interpreted as for the 1000°C sample, and the Fe^{2+} doublet

(δ = 1.14, Δ = 2.33 mm/s) likewise. However, the third doublet which is weak, poorly resolved and very broad must be assigned to Fe^{3+} ions contained within highly distorted environments of an amorphous or glassy phase[148]. The narrow half-width of the Fe^{2+} and Fe^{3+} spectral lines indicates that they are both contained within specific environmental sites of a highly crystalline phase. This would also suggest that the broad doublet assigned to Fe^{2+} for the 1000°C sample is in fact a combination of the very broad Fe^{3+} doublet observed at 1200°C and a weak Fe^{2+} doublet.

The formation of Fe^{2+} at above 1000°C is again considered to be an artefact of the experimental procedure, as indicated for illite and montmorillonite.

TABLE 28. ^{57}Fe Mössbauer data for iron (III) exchanged, thermally treated hectorite.

TEMPERATURE (°C)	δ ($\pm$0.03)[a] (mm/s)	Δ ($\pm$0.06)[a] (mm/s)	$\Gamma_{\frac{1}{2}}$ ($\pm$0.08)[a] (mm/s)
Ambient	-	-	-
400	0.34	1.03	0.66
600	0.33	1.13	0.65
800	0.33	0.85	1.00
1000	0.37	0.49	0.67
	0.60[b]	2.47[b]	1.54[b]
1200	0.38	0.42	0.46
	0.30[b]	1.42[b]	1.35[b]
	1.14	2.33	0.03

(a) = Maximum error.

(b) = Error > $\pm$0.10 mm/s.

FIG. 80. Mössbauer spectrum of HEC1AFeE400.

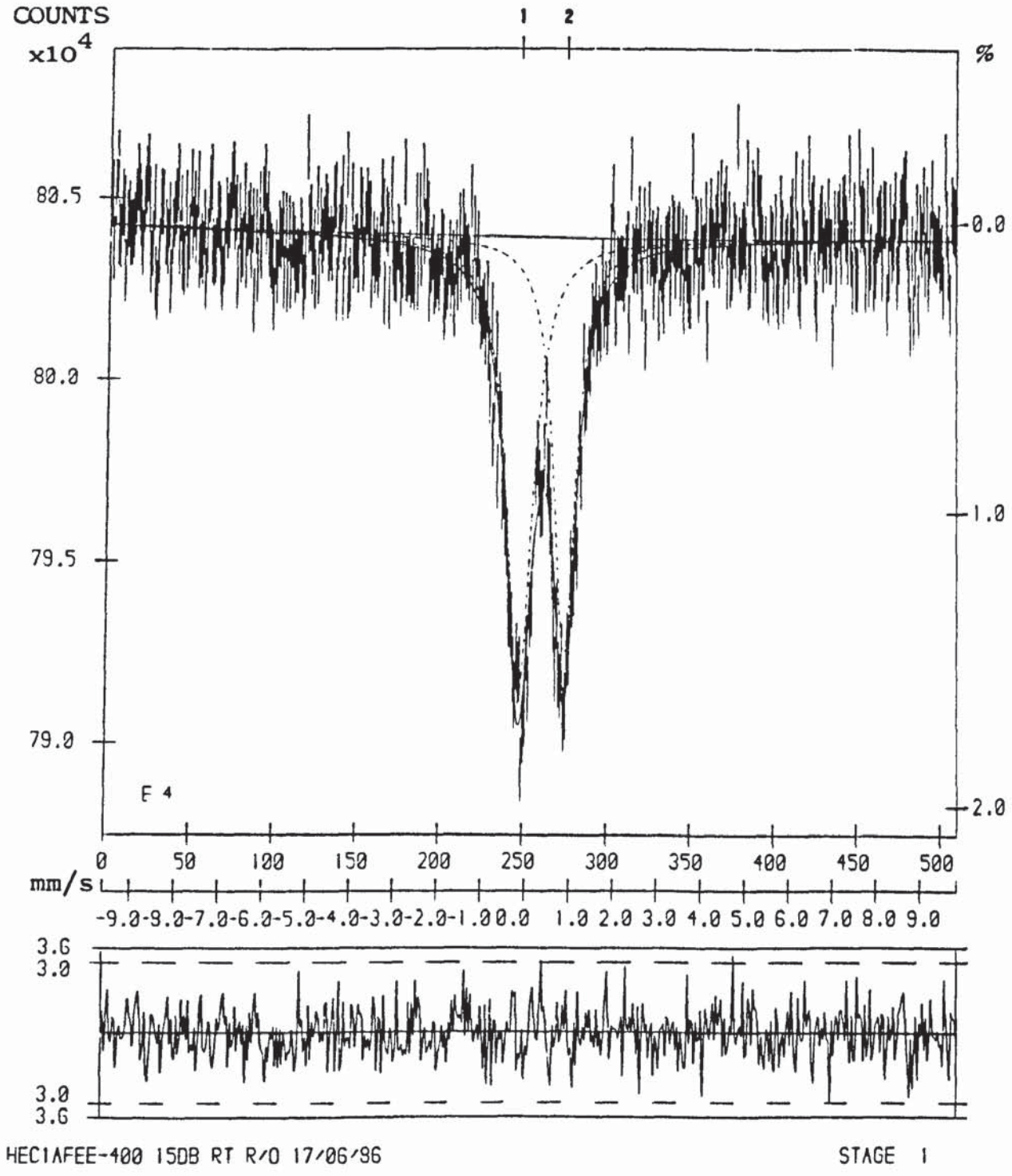

FIG. 81. Mössbauer spectrum of HEC1AFeE800.

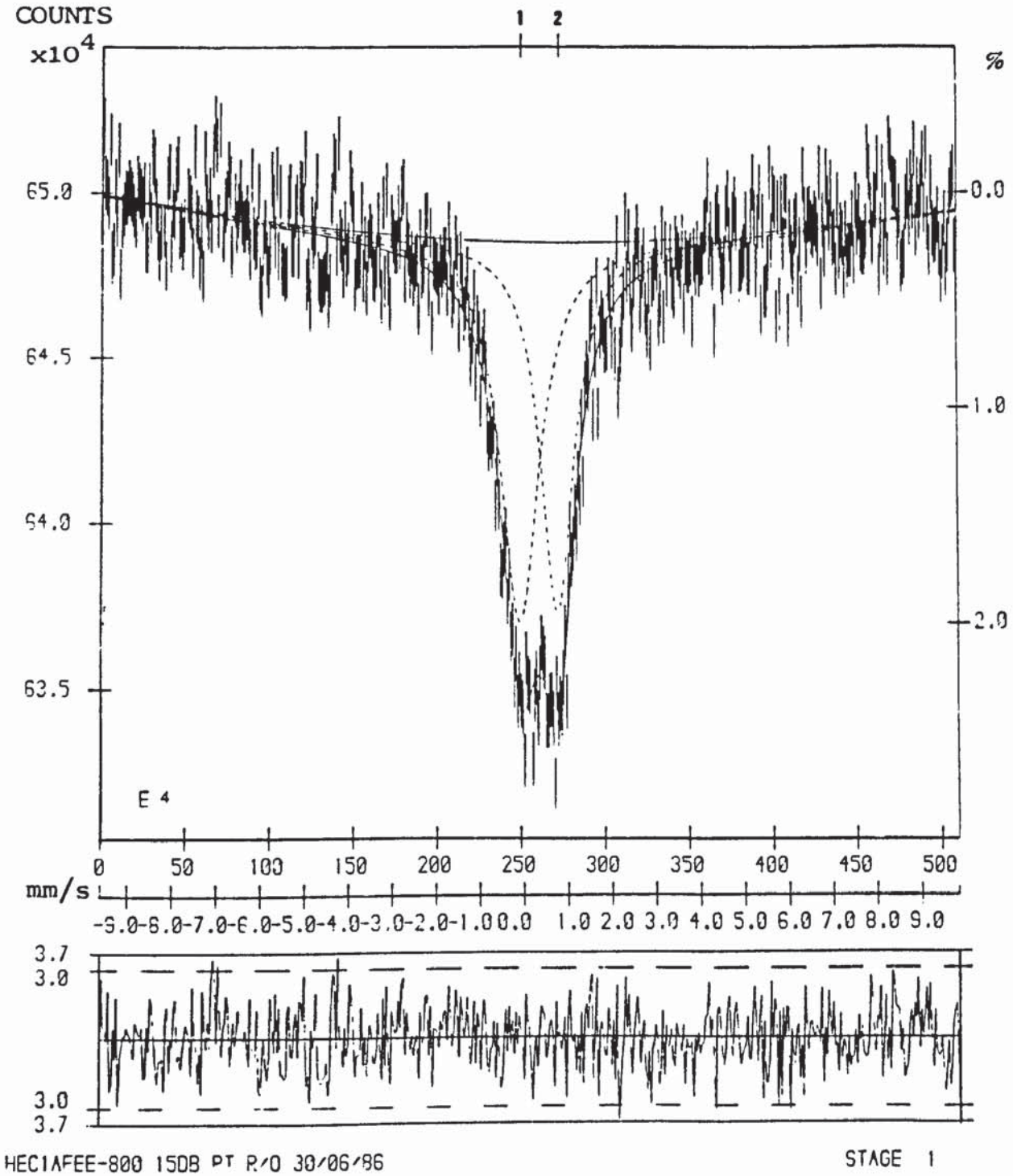

FIG. 82. Mössbauer spectrum of HEC1AFeE1000.

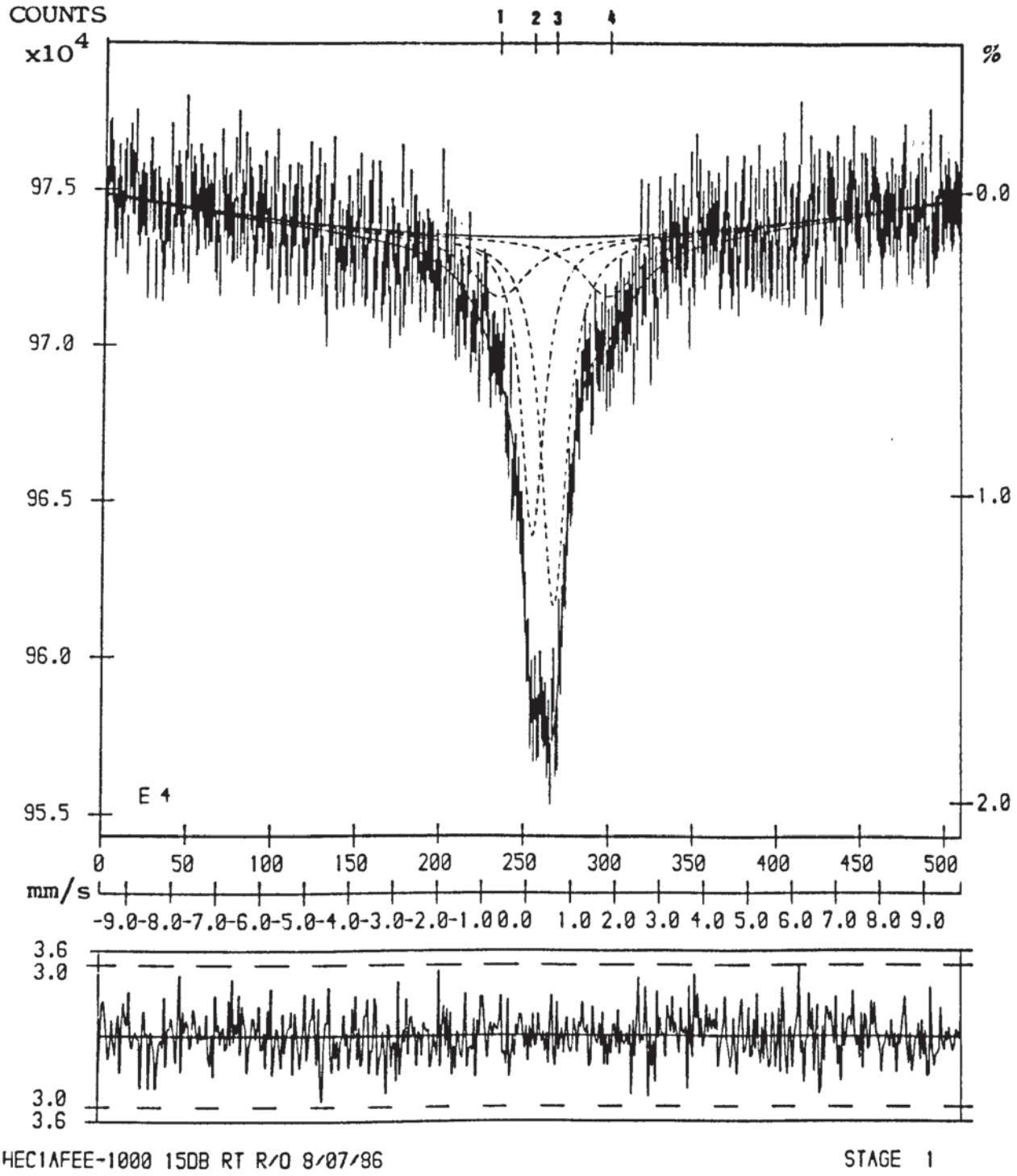

FIG. 83. Mössbauer spectrum of HEC1AFeE1200.

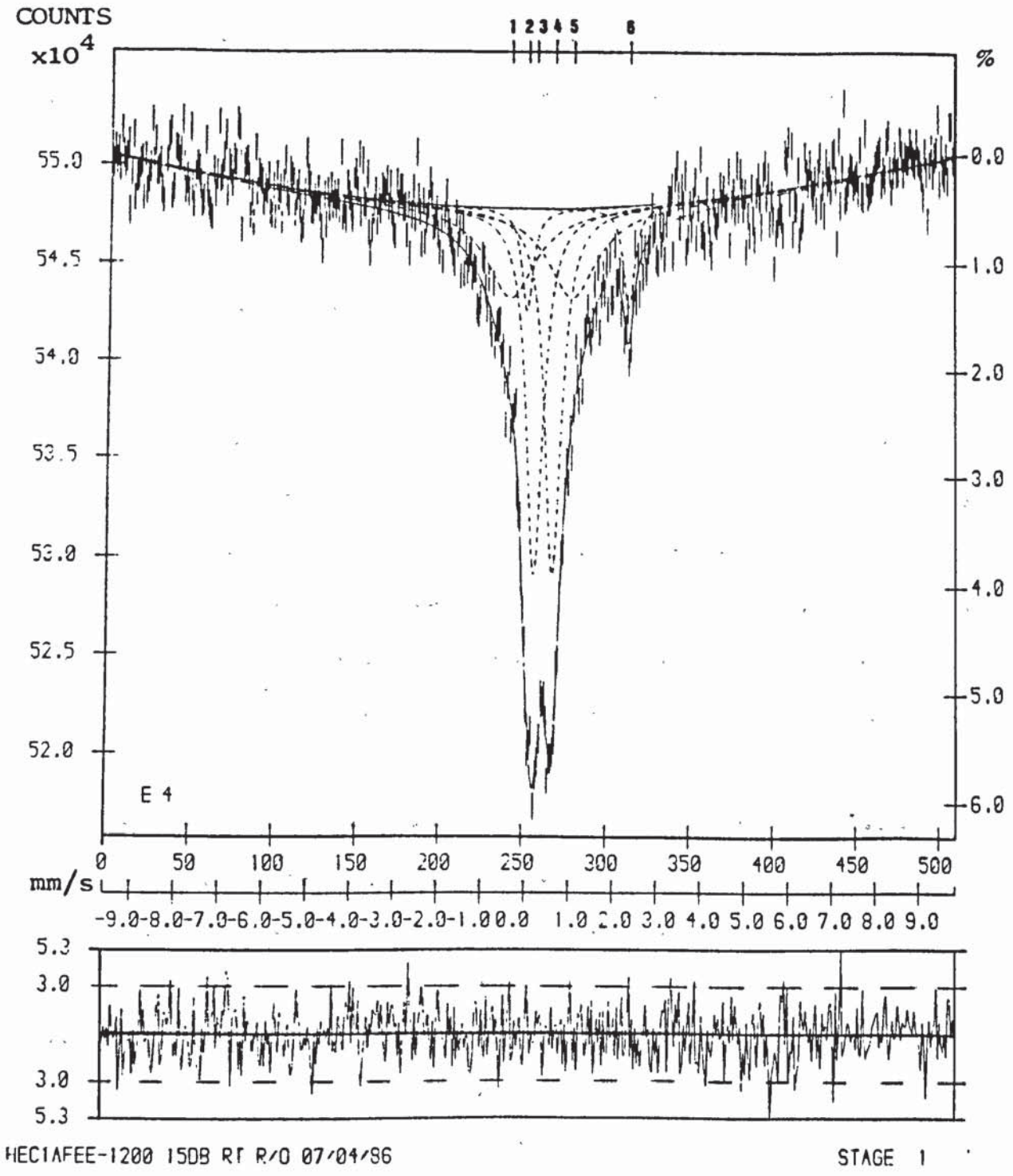

6.5.3. ELECTRON SPIN RESONANCE DATA:

6.5.3.1. COPPER (II) EXCHANGED HECTORITE:

The E.S.R. spectra of all the copper exchanged hectorite samples (HEC1ACuA to -CuE) were similar, giving $g_{//}$ and $g_{\perp}$ components as expected for Cu^{2+} exchanged clay minerals[120], [121], [154]-[157]. The E.S.R. spectrum of HEC1ACuB is shown in FIG. 84, and the g-values for the anisotropic resonance are given below:

$$g_{//} = 2.336\ (\pm 0.005);\ A_{//} = 147\ (\pm 5)\ G.$$

$$g_{\perp} = 2.082\ (\pm 0.005).$$

The $g_{//}$ component is clearly split into four components due to the spin (I = 3/2) of ^{63}Cu and ^{65}Cu. The above results are consistent with a single molecular layer of water occupying the hectorite interlayers[120]. This would imply that the Cu^{2+} ions are coordinated to four water molecules in the xy-plane and to surface oxygen of the silicate lattice along the z-axis[154].

The E.S.R. spectra of two of the thermally treated Cu^{2+} exchanged hectorite samples are shown in FIGS. 85 and 86. From these spectra, and others in the series, it can be seen that an increase in the quantity of Cu^{2+} contained within the sample on going from HEC1ACuE1200 to HEC1ACuA1200 leads to a significant broadening of the resonance lines. The cause of this broadening may be due to Cu^{2+}-Cu^{2+} dipolar interactions similar to that observed for Mn^{2+}[156]. Within the E.S.R. spectrum of HEC1ACuE1200, (FIG. 86), there are three observable

g-values:

$g_1 = 2.005\ (\pm 0.005)$, $A_1 = 154\ (\pm 5)$ G.

$g_2 = 2.197\ (\pm 0.005)$.

$g_3 = 2.335\ (\pm 0.005)$.

Unlike the unheated Cu^{2+} exchanged samples, where $g_{//}$ (equivalent to g_3) is split indicating that the ion has a $d_{x^2-y^2}$ ground state[121], HEC1ACuE1200 and -CuA1200 have g_1 split and also a g_2 is present ($g_1 + g_2$ are equivalent to $g_\perp$ for the unheated sample). This situation has been interpreted as Cu^{2+} having a d_{z^2} ground state, which could arise from a rhombic distortion superimposed on a compressed tetragonal environment. This is consistent with the Cu^{2+} ions being located in the structure of an orthorhombic polymorph of enstatite.

FIG. 84. E.S.R. spectrum of HEC1ACuB.

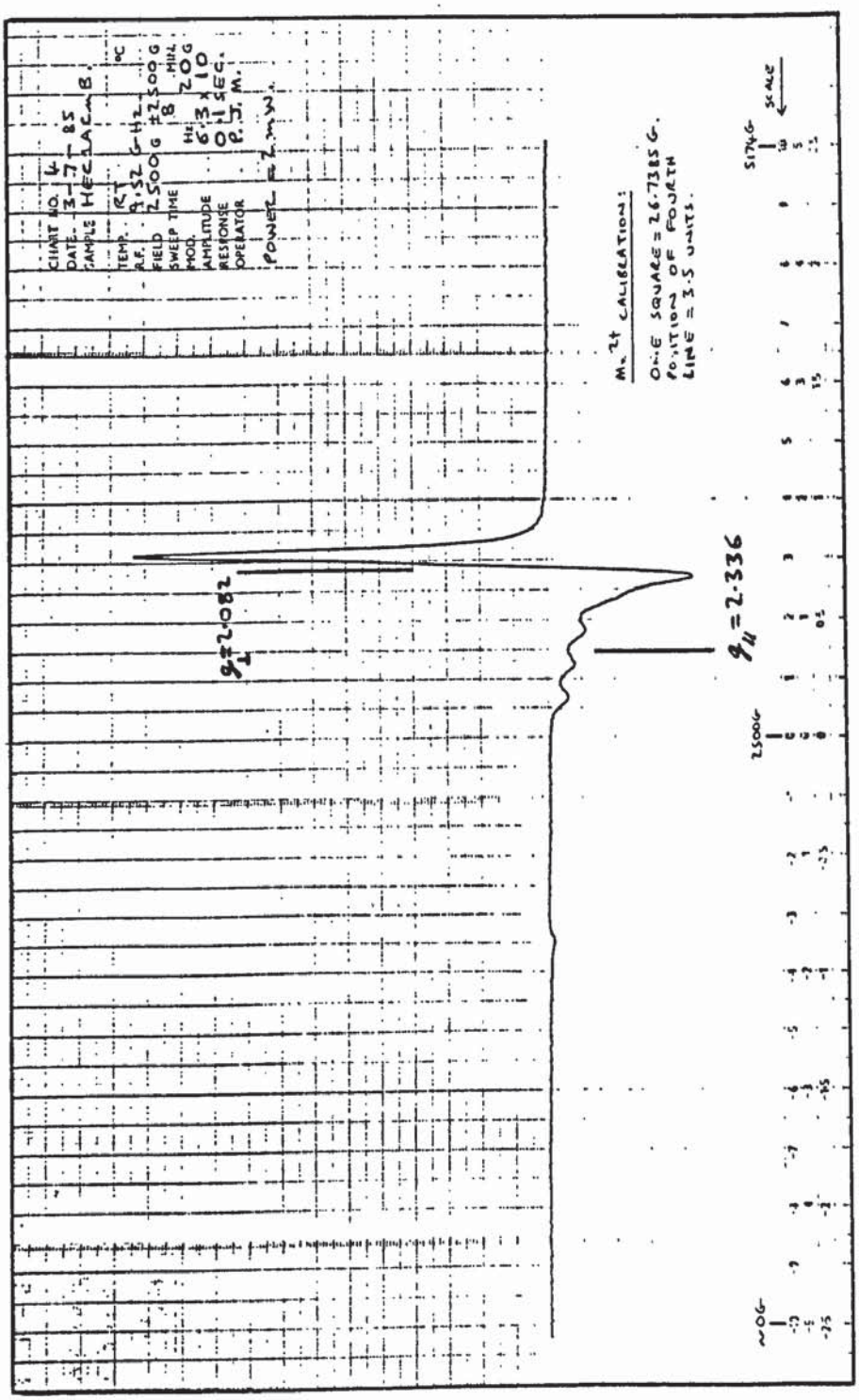

FIG. 85. E.S.R. spectrum of HEC1ACuA1200.

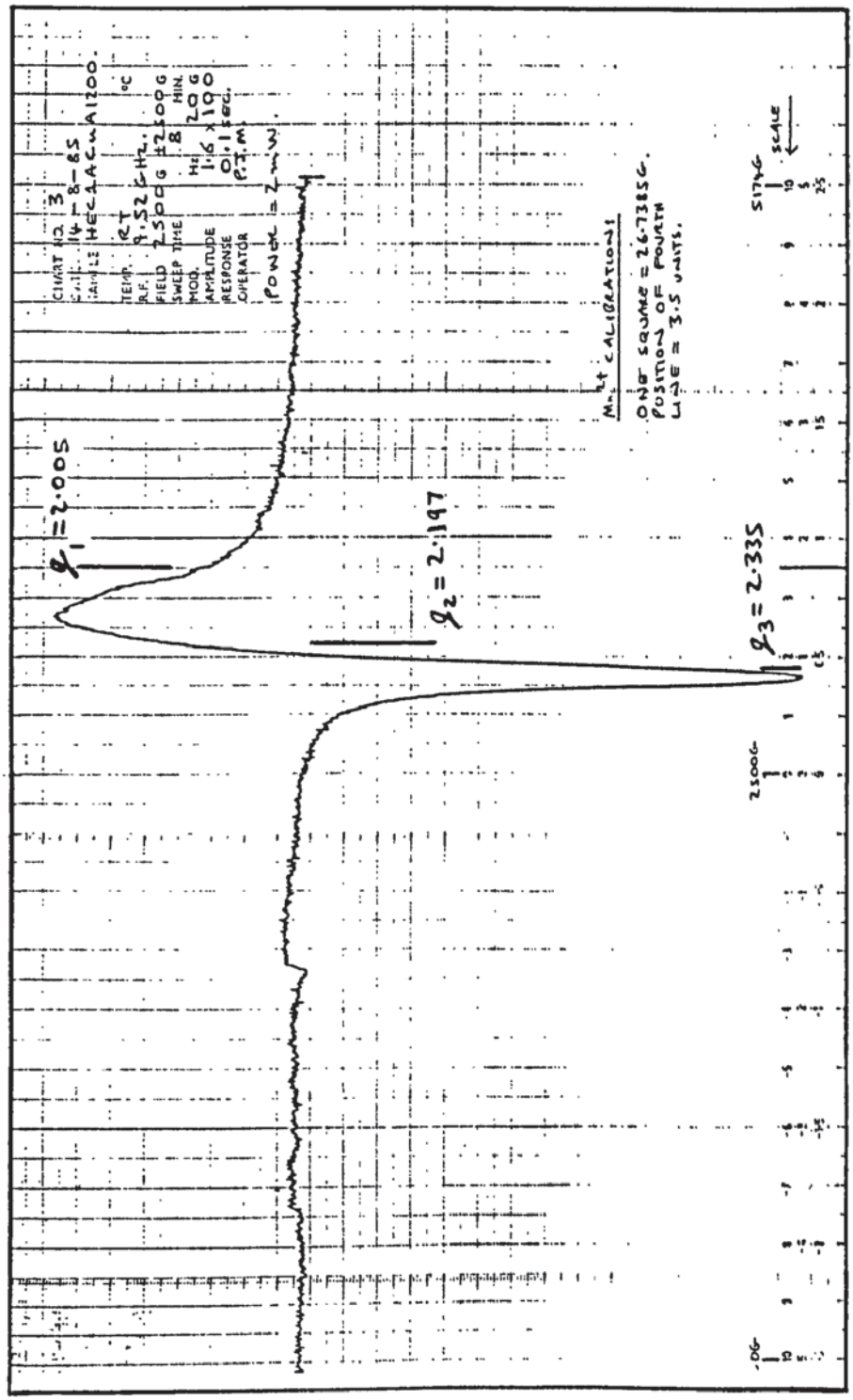

FIG. 86. E.S.R. spectrum of HEC1ACuE1200.

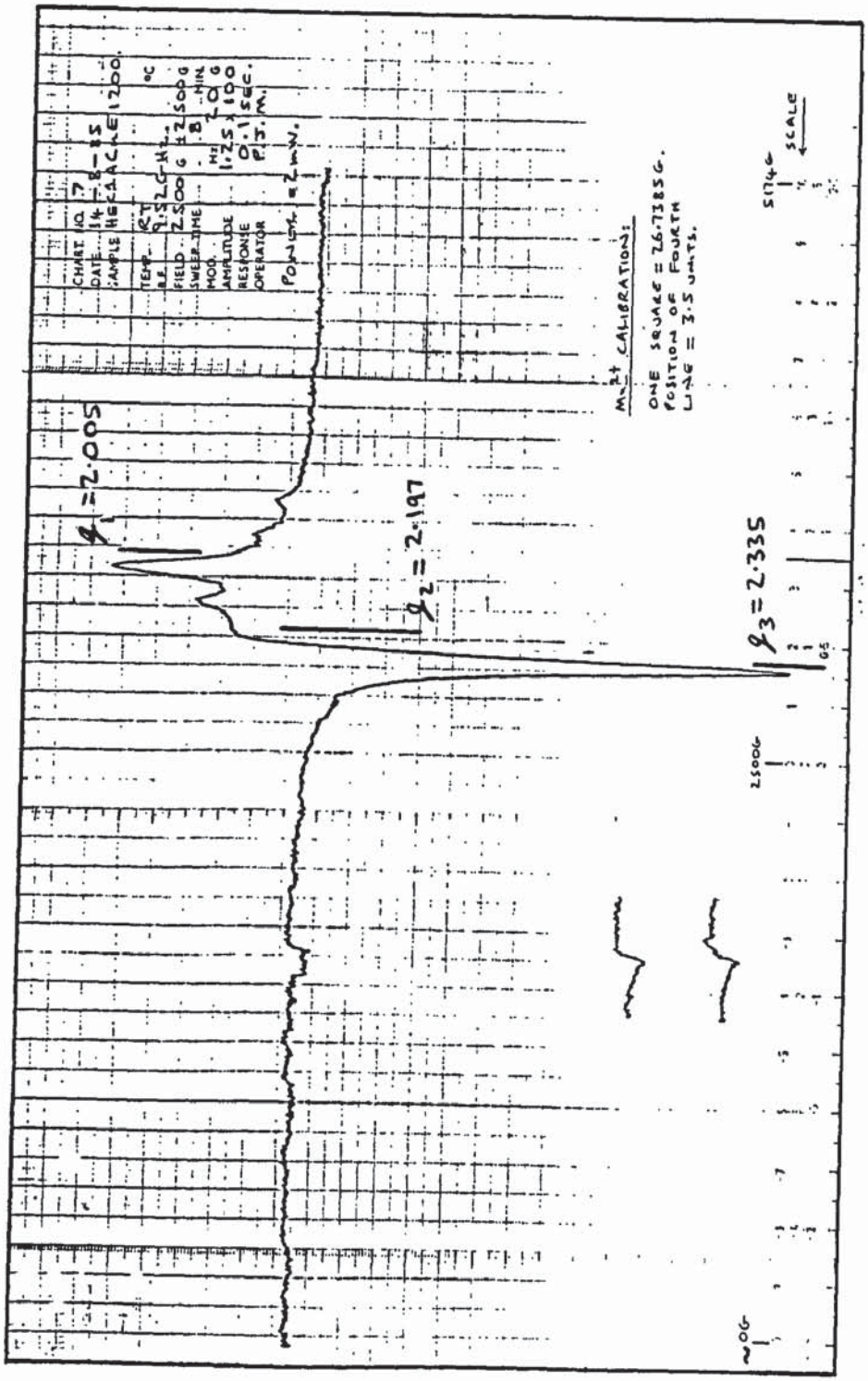

6.5.3.2. MANGANESE (II) EXCHANGED HECTORITE:

The E.S.R.spectra of HEC1AMnA1200 and HEC1AMnE1200 are essentially the same. Both consist of a broad, apparently isotropic resonance centred on g = 2.00 ($\pm$0.01), line width $\approx$ 600 G. The spectrum of HEC1AMnA1200 is shown in FIG. 87. This resonance is typical of Mn^{2+} ions in a non-dilute environment, Mn^{2+}- Mn^{2+} dipolar relaxation mechanisms greatly broadening the line widths of the hyperfine sextet to produce a broad 'isotropic' resonance[156],[157]. No great detail can be obtained from this resonance other than that the Mn^{2+} ions are present either within an Mn (II) oxide phase or the octahedral coordination sites of proto-enstatite.

The E.S.R. spectrum of the unheated hectorite sample HEC1AMnE shows a broadened Mn^{2+} hyperfine sextet centred on g = 1.98 ($\pm$0.01), A = 100 ($\pm$5) G and line width $\approx$ 48 G; FIG. 88. This resonance is typical of partially dehydrated Mn^{2+} ions contained within the interlayers of hectorite, with a decrease in relaxation processes due to ion-water molecule collisions giving rise to the broad line widths[121],[157].

FIG. 87. E.S.R. spectrum of HEC1AMnA1200.

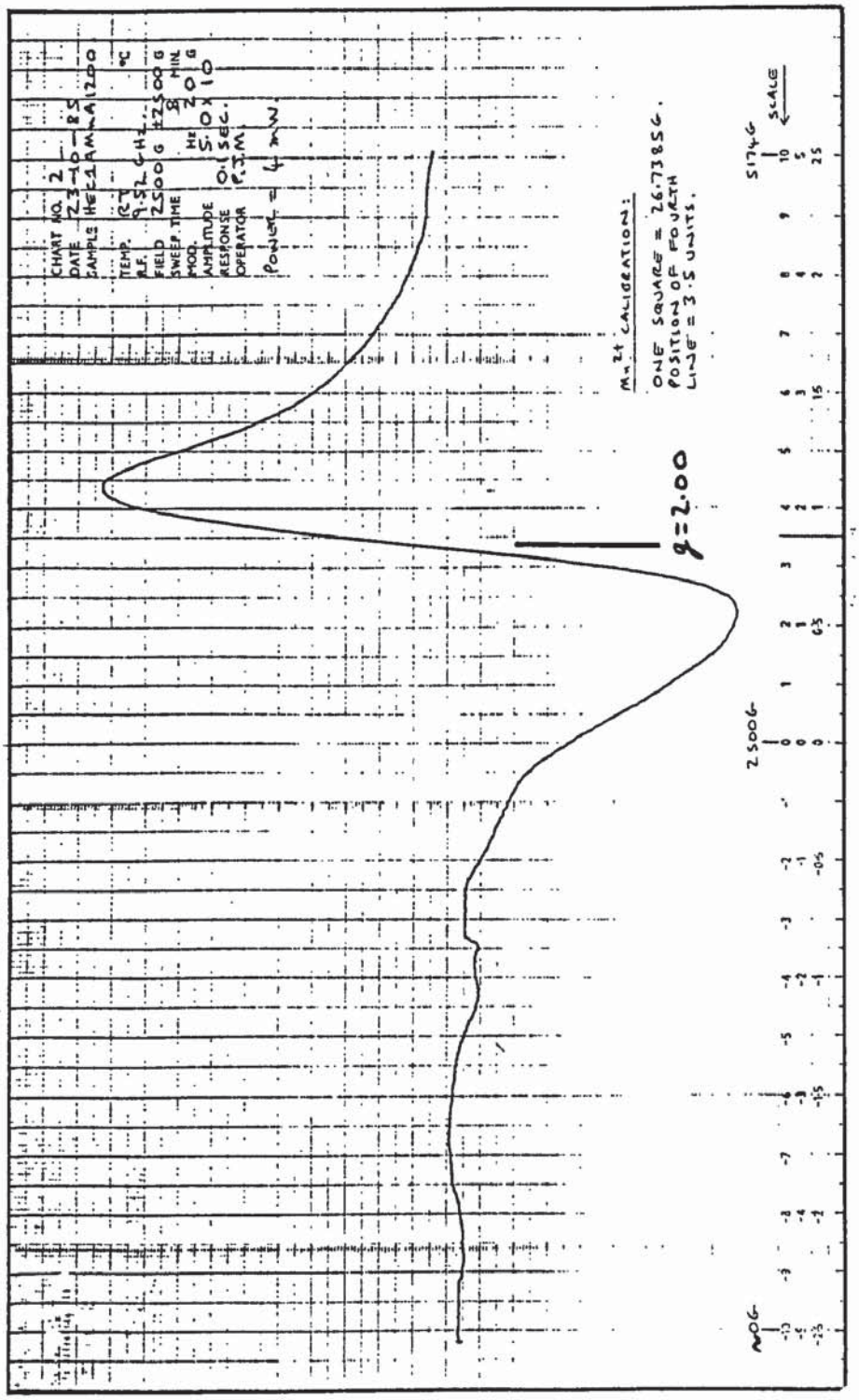

FIG. 88. E.S.R. spectrum of HEC1AMnE.

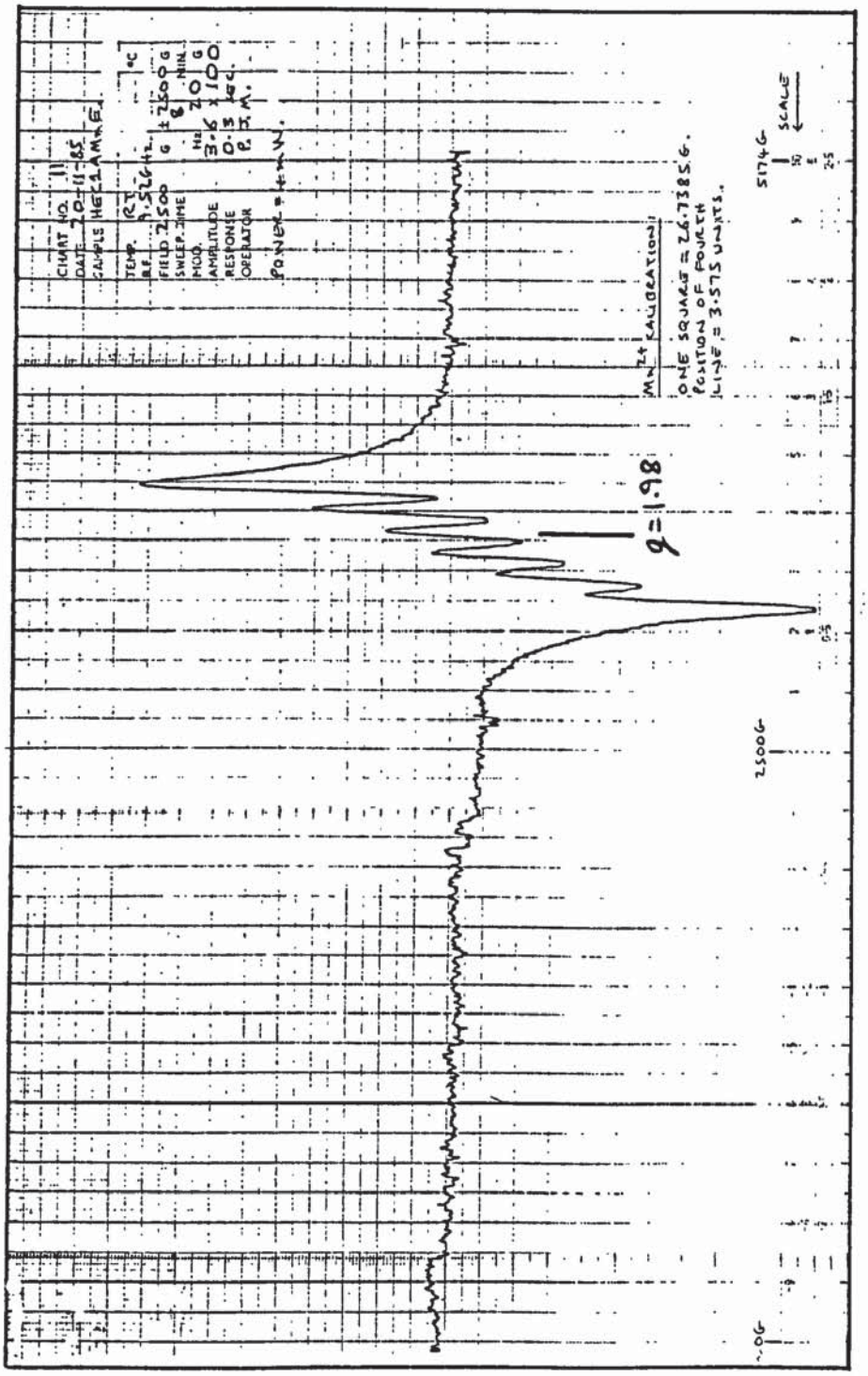

6.5.3.3. CHROMIUM (III) EXCHANGED HECTORITE:

The E.S.R. spectra of HEC1ACrA and HEC1ACrE are essentially the same. Both consist of a broad, isotropic resonance centred on g = 1.98 ($\pm$0.01), line width $\approx$ 420 G, FIG. 89. A g-value of 1.976 has been reported for the $(Cr(H_2O)_6)^{3+}_{aq.}$ species, and the environment of the Cr^{3+} ions on the clay surface is considered to be similar[158]. The isotropic signal may indicate a solution-like environment on the clay, but the broadness of the line suggests that the chromium ions are not well separated.

The E.S.R. spectrum of HEC1ACrA1200 is very similar to that of HEC1ACrA; g = 1.99 ($\pm$0.02), line width $\approx$ 640 G. This would indicate that the Cr^{3+} ions are contained within the octahedral sites of enstatite, however, the broad line width points to Cr^{3+}- Cr^{3+} interactions.

The above samples were also subjected to diffuse reflectance ultra violet spectroscopic analysis. HEC1ACrA1200 and HEC1ACrE1200 gave two broad, low intensity bands at 23,220 cm^{-1} and 17,720 cm^{-1}. These bands are indicative of octahedrally coordinated Cr^{3+} ions, most probably contained within the silicate structure of enstatite. The unheated hectorite sample (HEC1ACrE) gave bands at 24,290 cm^{-1} and 18,150 cm^{-1}, indicating Cr^{3+} in a $(Cr(H_2O)_6)^{3+}_{aq.}$ environment within the clay interlayers.

FIG. 89. E.S.R. spectrum of HEC1ACrE.

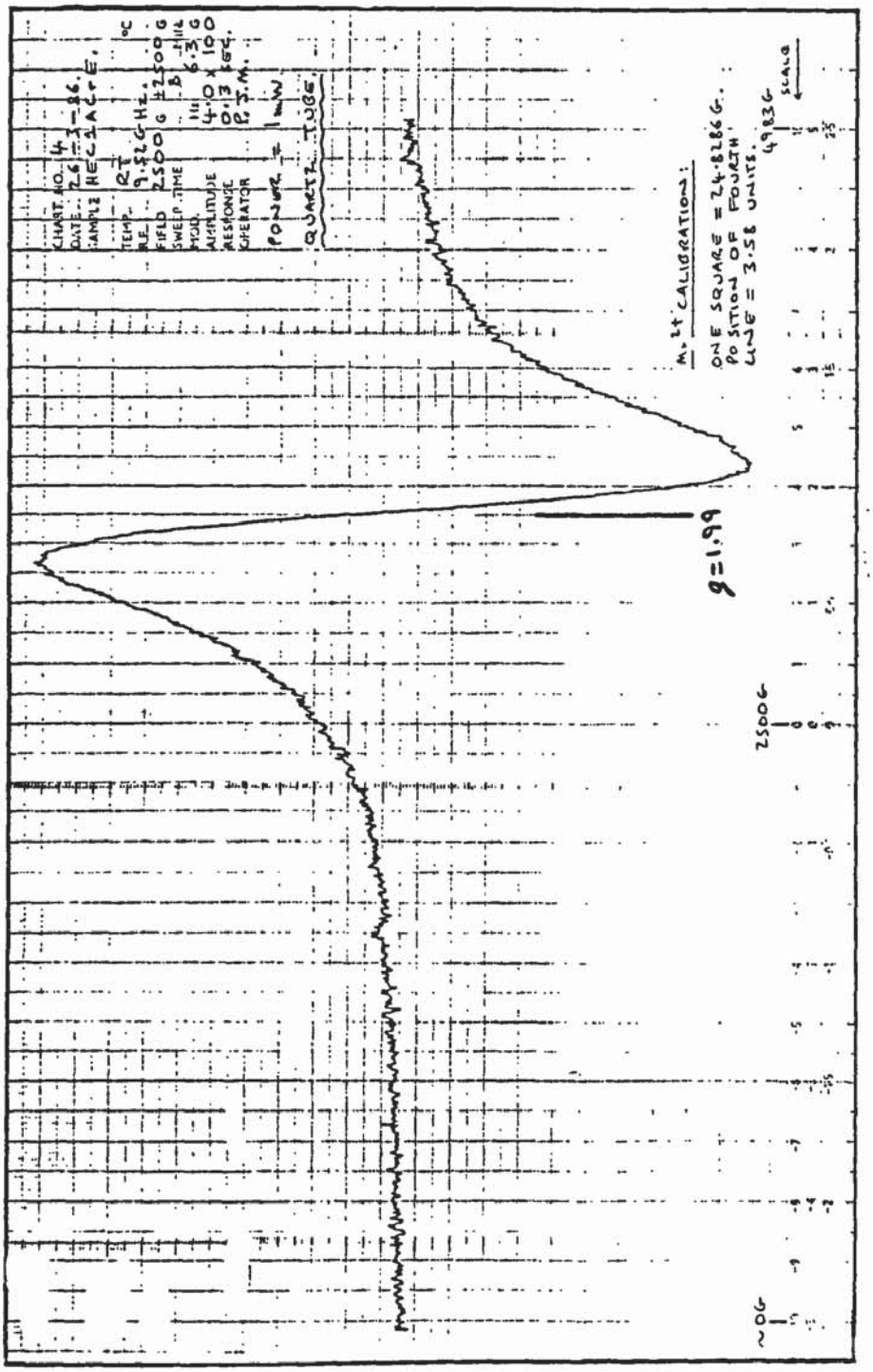

6.5.4. NUCLEAR MAGNETIC RESONANCE DATA:

The ^{29}Si N.M.R. spectra of the thermally treated natural hectorite sample (HEC1A) are shown in FIG. 90. Spectra obtained for some of the cation exchanged hectorite samples are shown in FIGS. 91 to 95.

The spectrum of the natural hectorite sample (HEC1A) heated to 560°C, FIG. 90, shows a broad resonance centred on -96 ppm. The broad line width is typical of the spectra observed for poorly crystalline, hydrated clay minerals[56], [121]. Although the hectorite sample will have undergone partial dehydroxylation at this temperature, a considerable number of -OH groups will remain. The chemical shift value of -96 ppm correlates well with that given for hectorite samples in the literature[159], and represents the silicate(Q^3) lattice. Upon heating the sample to 1300°C one can observe several phase changes within the ^{29}Si N.M.R. spectra. Between 560 and 840°C the hectorite structure has collapsed and recrystallisation has led to the formation of a new highly crystalline silicate phase (note the narrow line width). A remnant of the dehydroxylated and consolidated hectorite structure still remains at 840°C. However, this gradually decreases in intensity upon further recrystallisation of the sample up to 1300°C. The resonance corresponding to this remnant drifts gradually to a chemical shift of -91 ppm at 960°C, and this may well be due to structural changes within the poorly crystalline remnant as a result of reactions taking place within the sample. The remnant could well represent an amorphous glassy phase at higher temperatures[57].

The resonance representing the new crystalline phase at 840°C gradually increases in relative intensity up to 1300°C. This represents further crystallisation of this phase within the the sample. At 960°C another resonance has appeared, -84.8 ppm, which also increases in intensity at 1300°C. The resonances contained within the spectrum of HEC1A1300 occur at -80.39, -83.1, -84.8, -108.6, and possibly -111.8 ppm. The first three represent Q^2 silicon environments, and the latter two Q^4 environments. Similar resonances occur within the spectra of the cation exchanged clay samples.

FIG. 90. N.M.R. spectra of the thermally treated natural hectorite (HEC1A).

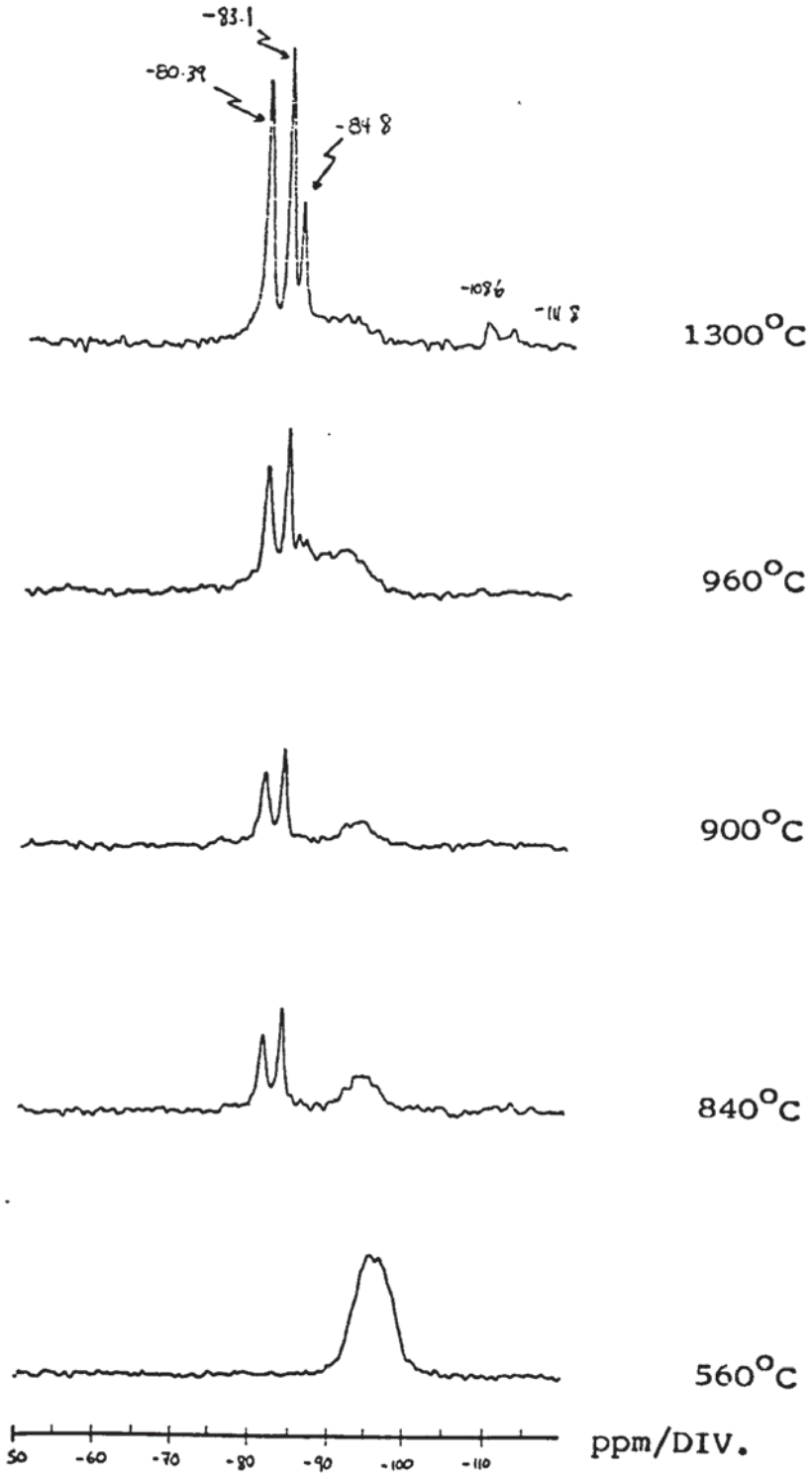

FIG. 91. N.M.R. spectrum of HEC1A1200.

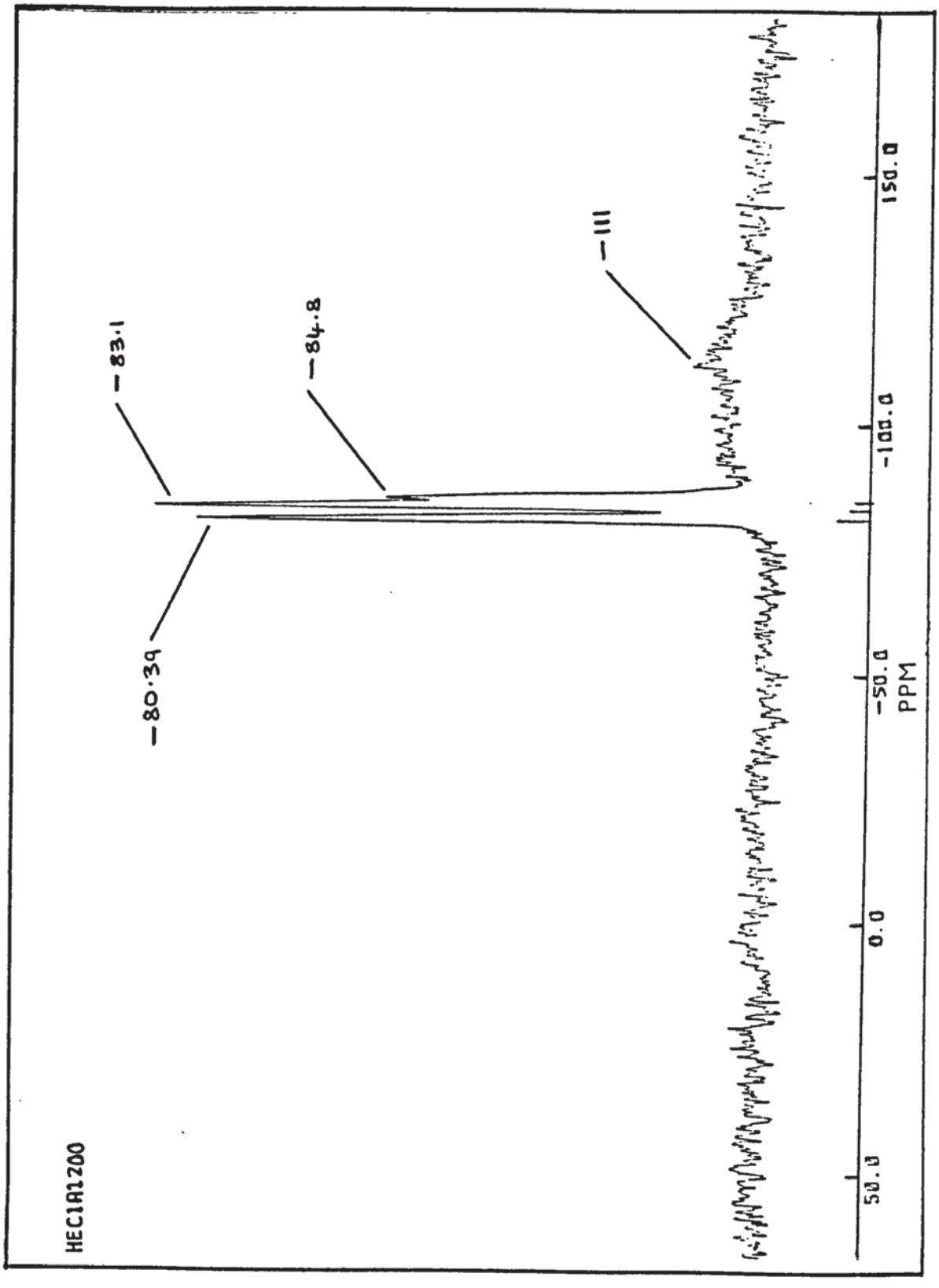

FIG. 92. N.M.R. spectrum of HEC1AZnA1200.

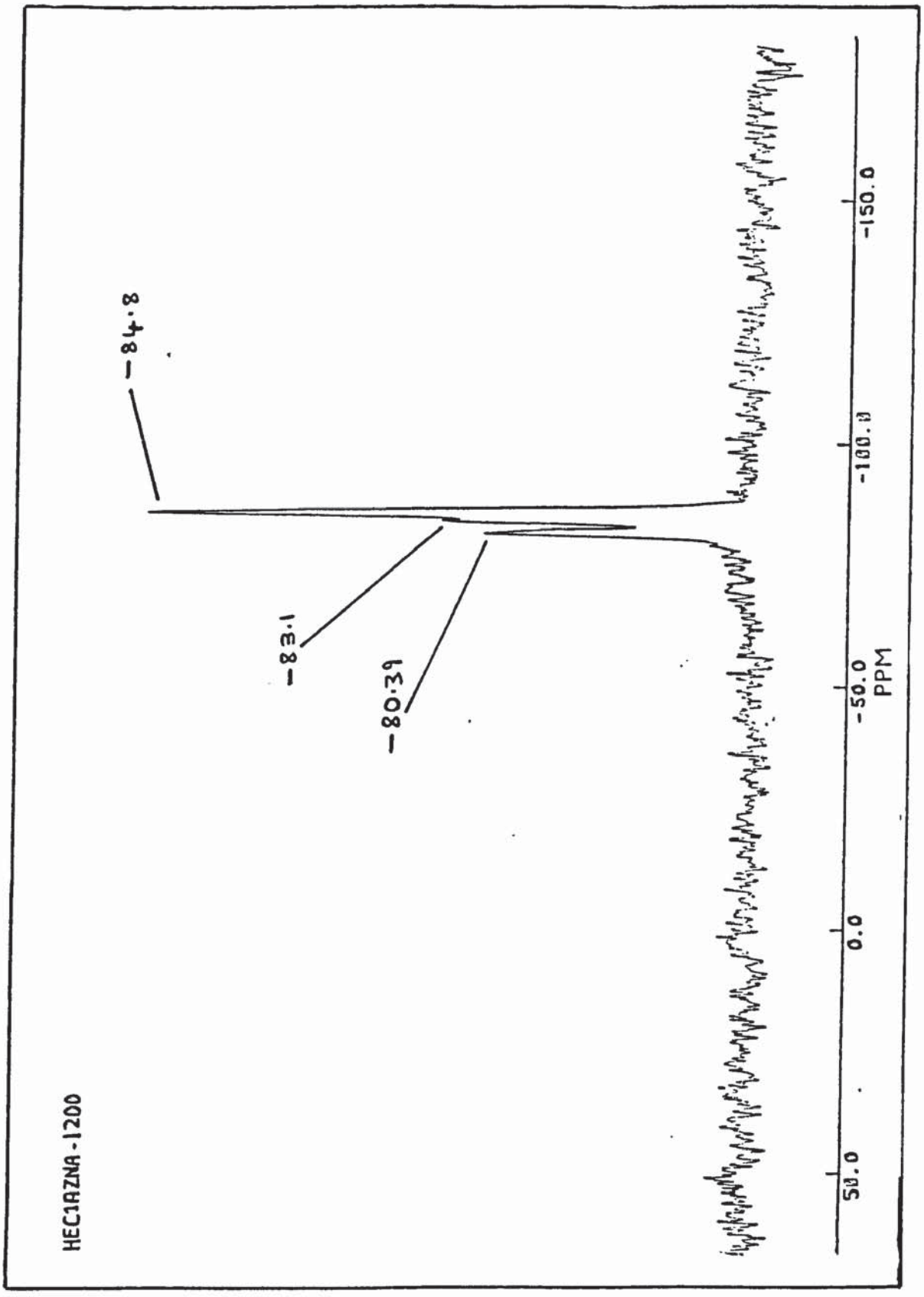

FIG. 93. N.M.R. spectrum of HEC1ACuB1200.

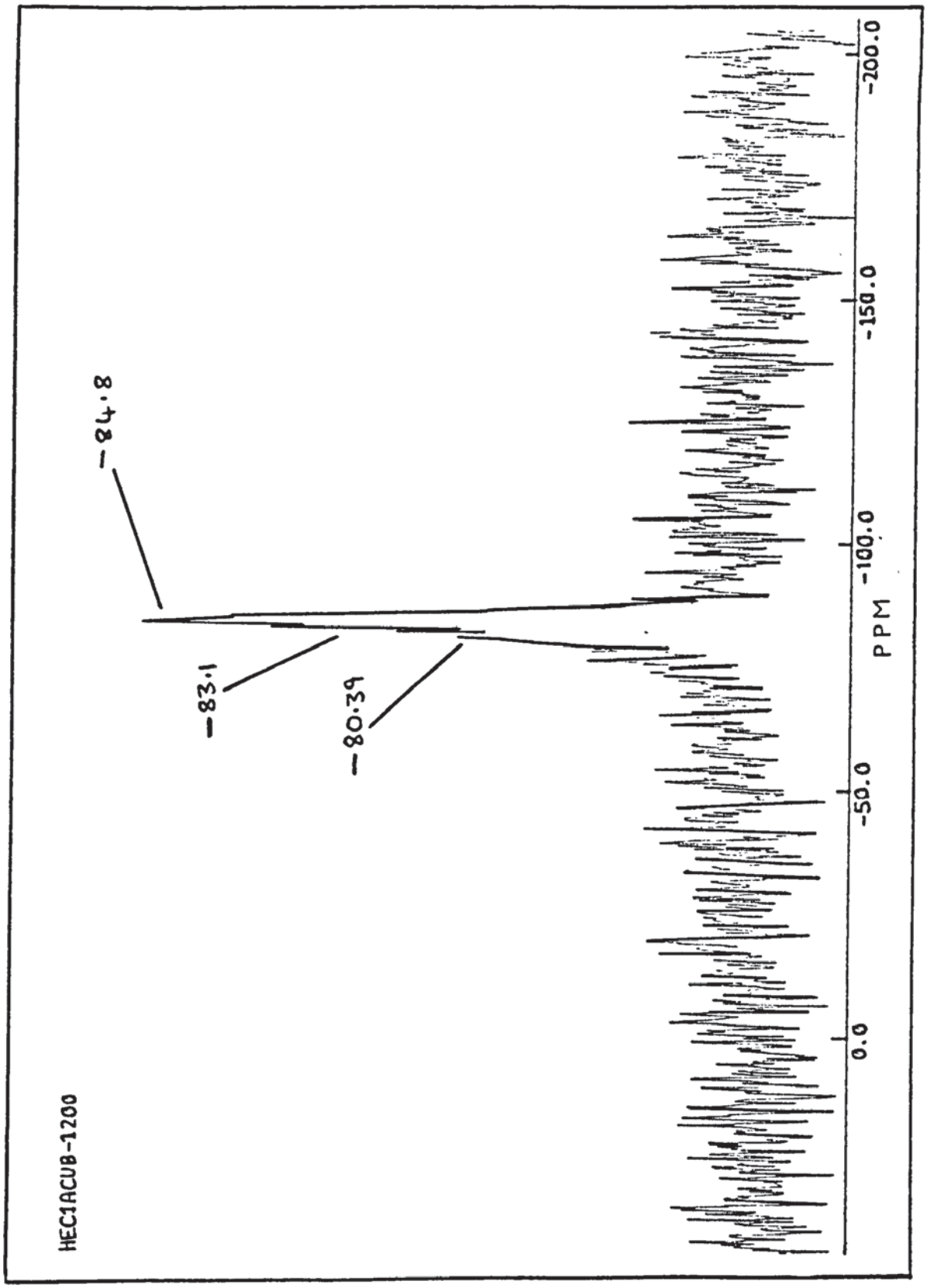

FIG. 94. N.M.R. spectrum of HEC1ACuD1200.

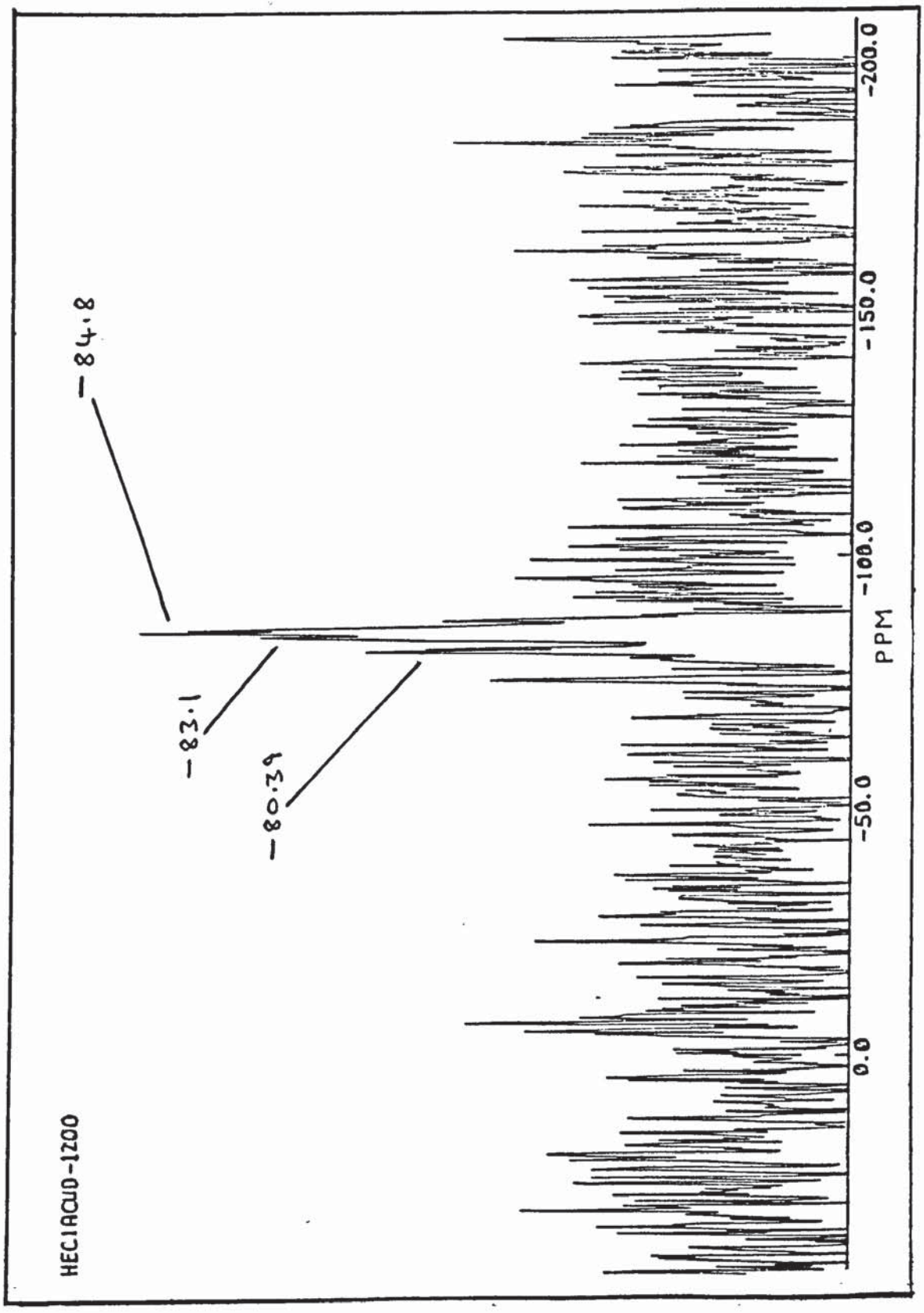

FIG. 95. N.M.R. spectrum of HEC1ANiA1200.

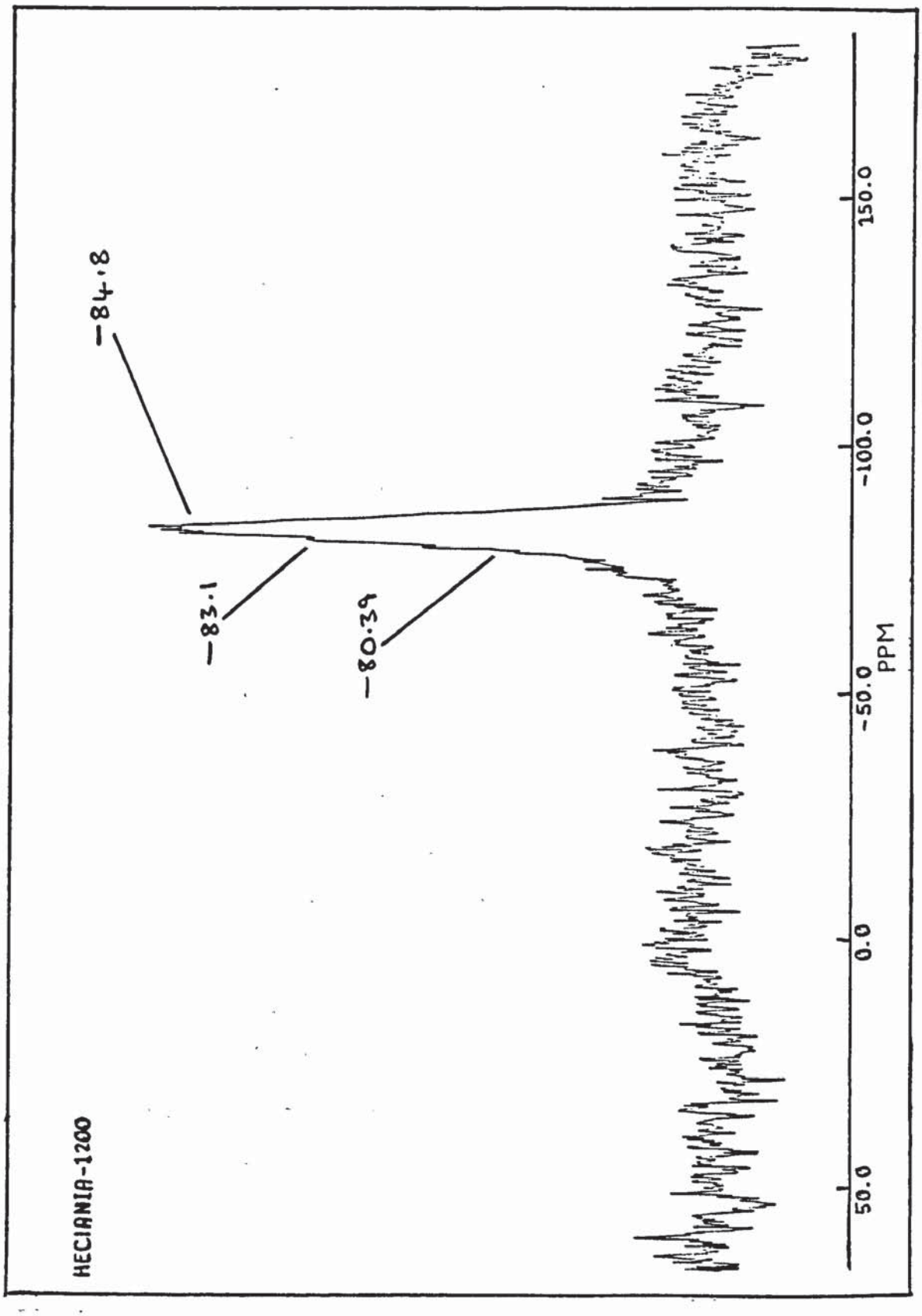

6.5.5. DISCUSSION AND SUMMARY:

The results and spectra of the preceding sections have been discussed and partially interpreted, on an individual sample/experimental technique basis, alongside their presentation. It is intended here to draw together various components within these sections and give an overall picture of the thermo-chemistry of cation-exchanged hectorite.

The XRD data for the cation exchanged hectorite samples that had been heated to 1200°C were all very similar. Diffractograms revealed the presence of enstatite and cristobalite as seen for the unexchanged clay, however, no patterns were detected for phases directly attributable to the presence of the cation exchanged element within the sample. This would indicate that the exchanged cations are isomorphously substituted within the existing silicate phases. The Mössbauer data for the iron (III) -exchanged clay, HEC1AFeE (TABLES 27 and 28), has been used to trace the fate of a typical exchanged cation upon thermolysis. The formation of iron (II) at 1200°C, an artefact of the experimental technique, is advantageous in this case as it reveals the behaviour of a typical dipositive ion. The exchanged iron (III) does not appear to participate in thermo-chemical reactions below approximately 700°C, i.e. before the clay structure starts to collapse and form enstatite ($MgSiO_3$). At 800°C the iron (III) ions are located in more highly symmetrical octahedral environments (Δ = 0.85 mm/s), and by 1200°C the iron (III) doublet has a quadrupole splitting, Δ = 0.42 mm/s, indicating a highly symmetrical octahedral environment. Iron (II),

present at 1200°C, appears to be located in relatively less symmetrical octahedral environments (δ = 1.14, Δ =2.33 mm/s) [88]. From the XRD data, both iron (II) and (III) can be considered to be isomorphously substituted in enstatite. Within pyroxenes there are normally two crystallographically distinct cation positions, labelled M_1 and M_2 [88]. The cations in the smaller M_1 positions are coordinated to six oxygen atoms in a nearly regular octahedron, while the cations in the larger M_2 positions are coordinated to a varying number of oxygens in a very distorted environment. The M_2 position is normally occupied by Ca(II), Mg(II), Fe(II), Mn(II) or Na(I), while the M_1 position is preferentially occupied by Mg(II), Mn(II), Al(III) or Fe(III). It would therefore appear that the iron (III) ions are contained within the M_1 sites, and the iron (II) ions within the M_2 sites of enstatite.

The ESR data for the Mn (II) and Cr (III) exchanged, thermally treated hectorite reveals little, other than that they are contained within octahedrally coordinated environments. However, the data for Cu (II) clearly indicates that the Cu (II) ions are located within the highly distorted octahedral environments of an orthorhombic polymorph of enstatite. The Cu (II) ions may therefore be assigned to the M_2 positions of orthorhombic proto-enstatite, as indicated by XRD.

One interesting observation from the XRD data is that the presence of the exchanged cations increases the proportion of proto-enstatite in the samples heated to 1200°C. Unexchanged hectorite heated to 1200°C resulted in the presence of mainly clino-enstatite. This would indicate that the exchanged cations have in some way stabilised proto-enstatite such that

it does not invert metastably to clino-enstatite during cooling. The M_1 and M_2 crystallographic sites of clino-enstatite are similar and both exhibit six-fold nearly octahedral coordination. However, proto-enstatite has M_2 larger than M_1, with M_2 exhibiting a very distorted environment[153]. It would appear from the ESR and Mössbauer data that the Cu (II) and Fe (II) ions are located within the larger and more distorted M_2 sites contained in proto-enstatite. The transformation of these sites to smaller 'M_1-like' sites on the metastable inversion to clino-enstatite, may thus be prevented by the actual size of the cation. Cu (II) and Fe (II) cations have noticably larger ionic radii than Mg (II) [150]. Fe (III) has a similar ionic radius to Mg (II) and is known to preferentially locate itself within M_1 sites[88], indicating that proto-enstatite should not be stabilised for iron (III) exchanged hectorite. However, XRD indicates that it does. This discrepancy may well be due to the presence of a quantity of Fe (II) within the sample, as indicated by the Mössbauer data. The stabilisation of proto-enstatite with respect to clino-enstatite, therefore appears to be directly related to the size of the exchanged cation within the thermally treated clay.

The ^{29}Si MAS-NMR data for the thermally treated natural hectorite sample (HEC1A) and the cation exchange samples all contained the following three major resonances: -80.39, -83.1 and 84.8 ppm. However, the natural hectorite sample did show two other minor resonances: one centred on -108.6 ppm, which is typical of Si^{4+} ions in a Q^4 environment[121], and is assigned to cristobalite (SiO_2)[57],[121],[162]; and the

second centred on -111.8 ppm, which is tentatively assigned to β_2-tridymite (SiO_2)[153],[162]. The -80.39 and -83.1 ppm resonances are consistent with the two crystalline environments of Si^{4+} within clino-enstatite ($MgSiO_3$)[52],[53],[57],[153],[160]. Clino-enstatite consists of (SiO_3) chains, each SiO_4-unit sharing two oxygens with adjacent units (Q^2). Neighbouring (SiO_3) chains are non-equivalent, giving rise to the two Si^{4+} environments. The resonance at -84.8 ppm was initially thought to be due to ortho-enstatite, but as this polymorph of enstatite is unstable above 985°C (inverting to proto-enstatite) and the chemical shift of ortho-enstatite is -82 ppm[161], another assignment was required. Diopside ($CaMgSi_2O_6$) has a single Si^{4+} environment and a chemical shift of -84.7 ppm, however, diopside was not present within the X-ray diffraction trace of HEC1A1300 and the CaO content of the hectorite sample was only 0.42%. This resonance is therefore unlikely to be due to diopside. It is therefore necessary to identify a silicate phase with a single Si^{4+} environment that is structurally very similar to diopside. A small proportion of proto-enstatite is indicated in the X-ray diffraction trace of HEC1A1300, having survived the inversion to clino-enstatite on cooling. Since the -84.8 ppm resonance does not appear within the NMR spectra until $\gtrsim$ 960°C, and proto-enstatite has crystallographically equivalent (SiO_3) chains similar to diopside, it is suggested that this resonance is due to ^{29}Si contained within proto-enstatite.

Work carried out by Dr. P. Gillespie, at the University of Durham, into the correlation between the magnetic susceptibility of a sample and the ability to obtain a ^{29}Si NMR spectrum for that sample, has identified the following observations(166):

(1) If χ_g is less than 1.4×10^{-6} cgs units/g, a signal is always obtained.

(2) If χ_g is between $1.4 - 2.2 \times 10^{-6}$ cgs units/g, a signal is sometimes and sometimes not obtained. This is sort of a 'grey area'.

(3) If χ_g is greater than 2.2×10^{-6} cgs units/g, a signal is never obtained.

Several cation exchanged samples of hectorite were sent to Durham University for ^{29}Si NMR analysis. They are listed in TABLE 29, together with their magnetic susceptibilities and cation exchange loading.

It is hoped that this data and the corresponding NMR spectra (FIGS. 90 to 95) will give some idea as to the paramagnetic cation loading that can be exchanged on to a clay mineral, such as hectorite, before paramagnetic broadening effects lead to a significant loss of spectral resolution. One very interesting point to note, as observed in the NMR spectra of the cation exchanged samples as compared to the spectrum of HEC1A1200, is the drastic reduction in intensity of the -80.39 and -83.1 ppm resonances with respect to that of the -84.8 ppm resonance for the cation exchanged samples. This is best seen by comparing HEC1AZnA1200 (FIG. 92) with HEC1A1200 (FIG. 91). According to the assignment of the

TABLE 29. Magnetic susceptibilities and cation exchange loading of thermally treated hectorite samples.

SAMPLE	χ_g cgs units/g $x10^6$.	CATION LOADING mg/g.	^{29}Si SPECTRUM
HEC1A1200	-	-	Good signal.
HEC1AMnA1200	6.401	17.6	Not tried.
HEC1AMnE1200	3.209	9.1	No signal.
HEC1ACoA1200	4.796	16.9	Not tried.
HEC1ACoE1200	1.998	9.7	No signal.
HEC1ANiA1200	-	17.1	Broad signal.
HEC1ANiE1200	0.579	9.8	No signal(?).
HEC1ACuB1200	-	19.3	Broad signal.
HEC1ACuD1200	2.100	11.2	Poor signal.
HEC1AZnA1200	-	18.7	Good signal.

-80.39 and -83.1 ppm resonances to clino-enstatite and the -84.8 ppm resonance to proto-enstatite, this matches exactly what was observed within the XRD data. The NMR data therefore provides further proof that the exchanged cations are in some way preventing the inversion of proto-enstatite metastably to clino-enstatite on cooling from 1200°C. Conversely, this confirms the assignment of the -84.8 ppm resonance to proto-enstatite.

As can be seen from the above discussion, there is again a satisfying degree of self consistency between the XRD, ESR, ^{29}Si-NMR and ^{57}Fe Mössbauer data. This clearly indicates the value of employing several complimentary experimental techniques in the elucidation of the thermo-chemistry of clay minerals and their ion exchanged derivatives.

7. REFERENCES.

(1) Francis, W., "Coal: Its formation and composition." 1st. Ed. (1954); 2nd Ed. (1961). Edward Arnold Ltd.

(2) Bouška, V., "Geochemistry of coal." Elsevier. (1981).

(3) Vrtal, V., Světové zásoby uhlí. Uhlí, 26 No. 4, 169. SNTL, Praha. (1978).

(4) Hoogendoorn, J.C. and Salomon, J.M., Sasol: Worlds largest oil from coal plant. Brit. Chem. Eng., 2, 238;308;368;418, (1957).

(5) Huffman, G.P. and Huggins, F.E., Mössbauer studies of coal and coke: Quantative phase identification and direct determination of pyritic and iron sulphide sulphur content. Fuel, 57, 592, (1978).

(6) Huggins, F.E. and Huffman, G.P., Mössbauer analysis of iron-bearing phases in coal, coke and ash. In: "Analytical methods for coal and coal products." Vol. III, Chap. 50. Academic, N.Y. (1980).

(7) Horsfield, B. and Douglas, A.G., The influence of minerals on the pyrolysis of kerogens. Geochim. Cosmochim. Acta., 44, 1119, (1980).

(8) Espitalié, J.; Makadi, S. and Trichet, J., Role of the mineral matrix during kerogen pyrolysis. Org. Geochem., 6, 365, (1984).

(9) Gray, D., Inherent mineral matter in coal and its effects upon hydrogenation. Fuel, 57, 213, (1978).

(10) Hinkley, C.C.; Smith, G.V.; Twardowska, H; Saporoschenko, M.; Shiley, R.H. and Griffen, R.A., Mössbauer studies of iron in Lurgi gasification ashes and power plant fly and bottom ash. Fuel, 59, 161, (1980).

(11) Herman, R.G.; Simmons, G.W.; Cole, D.A.; Kuzmicz, V. and Klier, K., Catalytic action of minerals in the low temperature oxidation of coal. Fuel, 63, 673, (1984).

(12) Attar, A., Chemistry, thermodynamics and kinetics of reactions of sulphur in coal-gas reactions: A review. Fuel, 57, 201, (1978).

(13) Given, P.H.; Spackman, W.; Davis, A and Jenkins, R.G., In: "Coal liquefaction fundamentals." Ed. D.D. Whitehurst. ACS Symposium Series, 139, Chap. 1, (1980).

(14) Given, P.H.; Cronauer, D.C.; Spackman, W.; Lovell, H.L.; Davis, A. and Biswas, B., Dependence of coal liquefaction behaviour on coal characteristics. Fuel, 54, 34, (1975).

(15) Anderson, R.R. and Bockrath, B.C., Effect of sulphur on coal liquefaction in the presence of dispersed iron or molybdenem catalysts. Fuel, 63, 329, (1984).

(16) Montano, P.A., Application of Mössbauer spectroscopy to coal characterization and utilization. In: "Mössbauer spectroscopy and its chemical applications." Chap. 7. ACS Washington, D.C.. (1981).

(17) Nakao, Y.; Yokoyama, S.; Maekawa, Y. and Kaeriyama, K., Coal liquefaction by colloidal iron sulphide catalyst. Fuel, 63, 721, (1984).

(18) Mukherjee, D.K. and Mitra, J.R., Catalytic roles of iron and hydrogen sulphides on hydrogenation of coal. Fuel, 63, 722. (1984).

(19) Montano, P.A.; Shah, V.; Reddy, S. and Bommannavar, A.S., Mössbauer study of the transformation of iron minerals during coal conversion. In: "New approaches in coal chemistry." ACS Symposium Series, 169, Chap. 21, (1981).

(20) Montano, P.A. and Granoff, B., Stoichiometry of iron sulphides in liquefaction residues and correlation with conversion. Fuel, 59, 214, (1980).

(21) Lambert, J.M., Alternative interpretation of coal liquefaction catalysis by pyrite. Fuel, 61, 777, (1982).

(22) Aitchison, D.W.; Clark, P.D.; Fitzpatrick, E.; Hawkins, R.W. and Lee, T.L.K., The liquefaction of Alberta sub-bituminous coals with iron-sulphur catalyst systems. Fuel, 65, 603, (1986).

(23) Johns, W.D. and Shimoyama, A., Clay minerals and petroleum forming reactions during burial and diagenesis. Am. Assoc. Petroleum Geologists Bull., 56, 2160, (1972).

(24) Johns, W.D., Clay mineral catalysis and petroleum generation. Ann. Rev. Earth Planet Sci., 7, 183, (1979).

(25) Mackowsky, M.T.. In: "Coal and Coal-bearing Strata." Eds. Murchison, D. and Westall, T.S.. Oliver and Boyd, Edinburgh and London. (1968).

(26) Brindley, G.W. and Nakahira, M., The kaolinite-mullite reaction series. J. Amer. Cer. Soc., 42 No 7, 311, (1959).

(27) Bulens, M.; Leonard, A. and Delmon, B., Spectroscopic investigations of the kaolinite-mullite reaction sequence. J. Amer. Cer. Soc., 61 No. 1-2, 81, (1978).

(28) Chakraborty, A.K. and Ghosh, D.K.. Comment on: Interpretation of the kaolinite-mullite reaction sequence from Infrared absortion spectra. J. Amer. Cer. Soc., 61 No. 1-2, 90, (1978).

(29) Chakraborty, A.K. and Ghosh, D.K., Re-examination of the kaolinite to mullite reaction series. J. Amer. Cer. Soc., 61 No. 3-4, 170, (1978).

(30) Moya, J.S.; Serna, C.J. and Iglesias, J.E., On the formation of mullite from kandites. J. Mat. Sci., 20, 32, (1985).

(31) MacKenzie, K.J.D., A Mössbauer study of the role of iron impurities in the high temperature reactions of kaolinite minerals. Clay Minerals, 8, 151, (1969).

(32) Cuttler, A.H., The behaviour of a synthetic ^{57}Fe-doped kaolin: Mössbauer and Electron Paramagnetic Resonance studies.
Clay Minerals, 15, 429, (1980).

(33) Komusiński, J. and Stoch, L., Dehydroxylation of kaolinite group minerals: An E.S.R. study.
J. Thermal. Anal., 29, 1033, (1984).

(34) Meinhold, R.H.; MacKenzie, K.J.D. and Brown, I.W.M., Thermal reactions of kaolinite studied by solid state ^{27}Al and ^{29}Si N.M.R..
J. Mat. Sci. Letters, 4, 163, (1985).

(35) MacKenzie, K.J.D.; Brown, I.W.M.; Meinhold, R.H. and Bowden, M.E., Outstanding problems in the kaolinite-mullite reaction sequence investigated by ^{29}Si and ^{27}Al solid state N.M.R.: I, Metakaolinite.
J. Amer. Cer. Soc., 68 No. 6, 293, (1985).

(36) Taneja, S.P. and Jones, C.H.W., Mössbauer studies of iron-bearing minerals in coal and coal ash.
Fuel, 63, 695, (1984).

(37) Smith, G.V.; Liu, J.H.; Saporoschenko, M. and Shiley, R., Mössbauer spectroscopic investigation of iron species in coal.
Fuel, 57, 41, (1978).

(38) Russell, S.J. and Rimmer, S.M., Analysis of mineral matter in coal, coal gasification ash, and coal liquefaction residues by Scanning Electron Microscopy and X-ray diffraction.
In: "Analytical methods for coal and coal products."
Vol. III, Chap. 42. Academic, N.Y.. (1980).

(39) Hubbard, F.H.; McGill, R.J.; Dhir, R.K. and Ellis, M.S., Clay and pyrite transformations during ignition of pulverised coal.
Min. Mag., 48, 251, (1984).

(40) Thomas, J.M.. Sheet silicate intercalations: New agents for unusual chemical conversions.
In: "Intercalation Chemistry." Eds. Whittingham, M.S. and Jacobson, A.J.. Academic Press, N.Y.. (1982).

(41) Theng, B.K.G., Organic reactions catalysed by clay minerals. In: "The chemistry of clay-organic reactions." Chap.7. Adam Hilger, London. (1974).

(42) Stille, J.T., "Industrial organic chemistry." Prentice-Hall, Englewood Cliffs, N.J.. (1969).

(43) Rabo, J.A., "Zeolite chemistry and catalysis." ACS, Monogr. 171, (1976).

(44) Imelik, B., "Catalysis by zeolites." Elsevier, Amsterdam, (1980).

(45) Townsend, R.P., "The properties and applications of zeolites." Special publication No. 33. The Chemical Society, London. (1980).

(46) Highfield, R., Common clay detoxifies dioxin. New Scientist, 1473, 29, (1985).

(47) Farrar, T.C. and Becker, E.D., "Pulse and Fourier Transform N.M.R.: Introduction to theory and methods." Academic Press, N.Y.. (1971).

(48) Andrew, E.R.. Narrowing of N.M.R. spectra of solids by high speed specimen rotation and the resolution of chemical shift and spin multiplet structures for solids. Progress in N.M.R. Spectroscopy, 8, 1, (1971).

(49) Fyfe, C.A.; Gobbi, G.C.; Hartman, J.S.; Lenkinski, R.E. and O'Brien, J.H., High-Resolution solid state M.A.S. spectra of ^{29}Si, ^{27}Al, ^{11}B, and other nuclei in inorganic systems using a narrow-bore 400 MHz high-resolution N.M.R. spectrometer. J. Mag. Reson., 47, 168, (1982).

(50) Lippmaa, E.; Mägi, M.; Samoson, A.; Engelhardt, G. and Grimmer, A.R., Structural studies of silicates by solid state high-resolution ^{29}Si N.M.R.. J. Amer. Chem. Soc., 102 No. 15, 4889, (1980).

(51) Fyfe, C.A.; Thomas, J.M.; Klinowski, J. and Gobbi, G.C., Magic-Angle-Spinning N.M.R. spectroscopy and the structure of zeolites. Angewandte Chemie, 22 No. 4, 259, (1983).

(52) Smith, K.A.; Kirkpatrick, R.J.; Oldfield, E. and Henderson, D.M., High-Resolution ^{29}Si N.M.R. spectroscopic study of rock-forming silicates.
Amer. Mineral., 68, 1206, (1983).

(53) Oldfield, E. and Kirkpatrick, R.J., High-Resolution N.M.R. of inorganic solids.
Science, 227 No. 4694, 1537, (1985).

(54) Fyfe, C.A., "Solid state N.M.R. for chemists."
C.F.C. Press, (1983).

(55) Stone, W.E.E. and Sanz, J., Distribution of ions in the octahedral sheet of micas.
In: "Advanced chemical methods for soil and clay minerals research." Eds. Stucki, J.W. and Banwart, W.L.. Riedel, Dordrecht, (1980).

(56) Stone, W.E.E., The use of N.M.R. in the study of clay minerals.
In: "Advanced techniques for clay mineral analysis."
Ed. Fripiat, J.J.. Elsevier, Amsterdam, (1982).

(57) Murdoch, J.B.; Stebbins, J.F. and Carmichael, I.S.E., High-Resolution ^{29}Si N.M.R. study of silicate alumino-silicate glasses: The effect of network-modifying cations.
Amer. Mineral., 70, 332, (1985).

(58) Thompson, J.G., ^{29}Si and ^{27}Al N.M.R. spectroscopy of 2:1 clay minerals.
Clay Minerals, 19, 229, (1984).

(59) Oldfield, E.; Kinsey, R.A.; Smith, K.A.; Nichols, J.A. and Kirkpatrick, R.J., High-Resolution N.M.R. of inorganic solids. Influence of magnetic centers on Magic-Angle Sample-Spinning lineshapes in some natural aluminosilicates.
J. Mag. Reson., 51, 325, (1983).

(60) Bone, W.A. and Himus, G.W., "Coal: Its constitution and uses." Longmans, Green and Co., London. (1936).

(61) Hickling, H.G.A., The geological history of coal.
Proc. S.W. Inst. Eng., 46, 6, (1931).

(62) Fuchs, W., "Die chemie der kohle." Berlin. (1931).

(63) Manskaya, S.M. and Kodina, L.A., "Geochemistry of Lignin (Geokhimiya Lignina)" Idz. Nauka, Moscow, USSR. (1975).

(64) White, D.. The role of water conditions in the formation and differentiation of common (banded) coals. Econ. Geol., 28, 556, (1933).
(65) Maddock, A.G., In: "Chemical bonding and spectroscopy in mineral chemistry." Eds. Berry, F.J. and Vaughan, D.J.. Chapman and Hall, London. (1985).
(66) Pigulewskaja, L.V. and Rakowski, V.G.. Tr. Inst. Torf. Akad. Beloruss. S.S.R., 6, 12, (1963).
(67) Hubáček, J. In: "Tuhá Paliva Československé Republiky." Nákladen Matice Hornicko-Hutnické, Praha., (1948).
(68) Colombo, V.. In: "Advances in organic geochemistry." (1970).
(69) Lessing, R.,
- The study of mineral matter in coal. Fuel, 1, 6, (1922).
- Coal ash and clean coal. Fuel, 5, 17,65 and 177, (1926).
(70) Svoboda, J.V. and Beneš, K.. Petrografie Uhlí. N.Č.S.A.V., Praha. (1956).
(71) Mackowsky, M.T.. Bergbau-Arshiv, No. 5/6, (1947).
(72) Nelson, J.B.. BCURA Mon. Bull., 17 No. 2 , 41, (1953).
(73) Brindley, G.W. and Brown, G., "Crystal structures of clay minerals and their X-ray identification." Mineralogical Society, Monogragh No. 5, (1951).
(74) Grim, R.E., "Clay Mineralogy." McGraw Hill, N.Y.. (1953).
(75) Deer, W.A.; Howie, R.A. and Zussman, J., "Rock-Forming Minerals." Vol. 3., Sheet Silicates. Longman. (1962).
(76) Millot, G., "Geology of Clays." Chapman and Hall. (1970).
(77) Gruner, J.W., The crystal structure of kaolinite. Z. Krist., 83, 75, (1932).
(78) Hofmann, U.. Z. Krist., 86, 340, (1933).
(79) Marshall, C.E.. Layer lattices and the base-exchange clays. Z. Krist., 91, 433, (1935).

(80) Hendricks, S.B.. Lattice structure of clay minerals and some properties of clays.
J. Geol., 50, 276, (1942).

(81) Ross, C.S. and Hendricks, S.B., Minerals of the montmorillonite group.
U.S. Geol. Surv., Prof. Paper 205B. (1945).

(82) McMurchy, R.C., The crystal structure of the chlorite minerals.
Z. Krist., 88, 420, (1934).

(83) Karl, R.E. and Zuckerman, J.J., Qualitative and quantitative analysis of iron-bearing minerals in fossil fuels and petroleum source rock by ^{57}Fe Mössbauer spectroscopy.
In: "Mössbauer spectroscopy and its chemical applications." Chap. 10, 221. ACS, Washington, D.C.. (1981).

(84) Ingram, G.R. and Rimstidt, J.D., Natural weathering of coal.
Fuel, 63, 292, (1984).

(85) Bullock, P. and Loveland, P.J., Mineralogical analyses.
In: "Soil survey laboratory methods, Technical Monograph No. 6." Eds. Avery, B.W. and Bascomb, C.L.. Harpenden, (1974).

(86) Mehra. O.P. and Jackson, M.L., Iron oxide removal from soils and clays by a dithionite-citrate system buffered with sodium bicarbonate.
Clays Clay Miner., 5, 317, (1960).

(87) Vaughan, D.J. and Linskill, M., "Computer fitting of Mössbauer spectra." University of Aston in Birmingham, (1979).

(88) Bancroft, G.M., "Mössbauer spectroscopy: An introduction for inorganic chemists and geochemists." McGraw-Hill, London. (1973).

(89) Wertheim, G.K., "Mössbauer effect: Principles and applications." Academic Press, New York. (1964).

(90) Greenwood, N.N. and Gibb, T.C., "Mössbauer spectroscopy." Chapman and Hall Ltd., London. (1971).

(91) Gibb, T.C., "Principles of Mössbauer spectroscopy." Chapman and Hall Ltd., London. (1976).

(92) Stach, E., " Stach's textbook of coal petrology." Gebrüder Borntraeger, Berlin. (1982).

(93) Montano, P.A. and Seehra, M.S., Magnetism of iron pyrite (FeS_2) - A Mössbauer study in an external magnetic field. Solid State Comm., 20, 897, (1976).

(94) Morice, J.A.; Rees, L.V.C. and Rickard, D.T., Mössbauer studies of iron sulphides. J. Inorg. Nucl. Chem., 31, 3797, (1969).

(95) Lefelhocz, J.F.; Friedel, R.A. and Kohman, T.P., Mössbauer spectroscopy of iron in coal. Geochim. Cosmochim. Acta, 31, 2261, (1967).

(96) Temperley, A.A and Lefevre, H.W., The Mössbauer effect in marcasite-structure iron compounds. J. Phys. Chem. Solids, 27, 85, (1966).

(97) Montano, P.A., Mössbauer spectroscopy of iron compounds found in West Virginia coals. Fuel, 56, 397, (1977).

(98) Montano, P.A., Characterization of iron bearing minerals in coal. ACS Preprints, 24 No. 1, (1979).

(99) Vertes, A. and Zsoldos, B., Thermal decomposition studies of the iron (II) salt hydrates by Mössbauer spectroscopy. Acta. Chim. Acad. Sci. Hung., 65, 261, (1970).

(100) Hrynkiewiez, A.Z.; Kubisz, J. and Kulgawczuk, D.S., Quadrupole splitting of the 14.4 keV γ line of ^{57}Fe in iron sulfates of the jarosite group. J. Inorg. Nucl. Chem., 27, 2513, (1965).

(101) Daniels,J.M. and Rosencwaig, A., Mössbauer spectroscopy of stoichiometric and non-stoichiometric magnetite. J. Phys. Chem. Solids, 30, 1561, (1969).

(102) Govaert, A.; Dauwe, C.; Plinke, P; DeGrove, E. and DeSitter, J., A classification of geothite minerals based on the Mössbauer behaviour. J. Phys. (Paris), Colloq., 37(C-6), 825, (1976).

(103) Williamson, D.L.; Guettinger, T.W. and Dickerhoof, D.W., Quantitative investigations of pyrite and coal. In: "Mössbauer spectroscopy and its chemical applications." Chap. 8, 177, ACS, Washington, D.C.. (1981).

(104) Montano, P.A.; Vaishnava, P.P.; King, J.A. and Eisentrout, E.N., Mössbauer study of decomposition of pyrite in hydrogen. Fuel, 60, 712, (1981).

(105) Russell, P.E. and Montano, P.A., Magnetic hyperfine parameters of iron-containing minerals in coals. J. Appl. Phys., 49 No. 3, 1573 (4615), (1978).

(106) Ericsson, T.; Wäppling, R. and Punakivi, K., Mössbauer spectroscopy applied to clay and related minerals. Geologiska Föreningens I Stockholm Förhandlinger, 99 No. 3, 229, (1977).

(107) Goodman, B.A., Mössbauer spectroscopy (In the study of clay minerals). In: "Advanced techniques for clay mineral analysis." Ed. Fripiat, J.J.. Chap. 5, 113. Elsevier, Amsterdam. (1982).

(108) Bowen, L.H.; Weed, S.B. and Stenvens, J.G., Mössbauer study of micas and their potassium depleted products. Amer. Mineral., 54, 72, (1969).

(109) Malden, P.J. and Meads, R.E., The Solid State. Substitution by iron in kaolinite. Nature, 215, 844, (1967).

(110) Jefferson, D.A.; Tricker, M.J. and Winterbottom, A.P., Electron-Microscopic and Mössbauer spectroscopic studies of iron-stained kaolinite minerals. Clays Clay Miner., 23, 355, (1975).

(111) Wertz, J.E. and Bolton, J.R., "Electron Spin Resonance- Elementary theory and practical applications." Chapman and Hall Ltd., London. (1986)

(112) Atherton, N.M., "Electron Spin Resonance." Halstead Press, (1973).

(113) McLauchlan, K.A., "Magnetic Resonance." Oxford University Press. (1972).

(114) Tsai, S.C., "Fundamentals of coal beneficiation and utilization." Elsevier. (1982).

(115) Dack, S.W.; Hobday, M.D.; Smith, T.D. and Pilbrow, J.R., Free radical involvement in the drying and oxidation of Victorian brown coal.
Fuel, 63, 39, (1984).

(116) Dack, S.W.; Hobday, M.D.; Smith, T.D. and Pilbrow, J.R., E.P.R. study of paramagnetic metal ions in Victorian brown coal.
Fuel, 64, 222, (1985).

(117) Hall, P.L., The application of E.S.R. spectroscopy to studies of clay minerals.
Clay Minerals, 15, 321 and 337, (1980).

(118) McBride, M.B., Application of spin probes to E.S.R. studies of organic-clay systems.
In: "Advanced chemical methods for soil and clay mineral research." Eds. Stucki, J.W. and Banwart, W.L.. Chap. 9 (1980).

(119) Pinnavaia, T.J., Application of E.S.R. spectroscopy to inorganic-clay systems.
In: "Advanced chemical methods for soil and clay mineral research." Eds. Stucki, J.W. and Banwart, W.L.. Chap. 5. (1980).

(120) Pinnavaia, T.J., Electron Spin Resonance studies of clay minerals.
In: "Advanced techniques for clay mineral analysis." Ed. Fripiat, J.J.. Chap. 6, 139. Elsevier, Amsterdam. (1982).

(121) McWhinnie, W.R., Electron Spin Resonance and Nuclear Magnetic Resonance applied to minerals.
In: "Chemical bonding and spectroscopy in mineral chemistry chemistry." Eds. Berry, F.J. and Vaughan, D.J., 141. Chapman and Hall, London. (1984).

(122) Abragam, A. and Bleaney, B., "Electron Paramagnetic Resonance of transition metal ions." Oxford University Press. (1970).

(123) Barnes, J.R.; Clague, A.D.H.; Clayden, N.J.; Dobson, C.M. and Jones, R.B., The application of ^{29}Si and ^{27}Al solid state N.M.R. spectroscopy to characterising minerals in coals.
Fuel, 65, 437, (1986).

(124) Montgomery, W.J., Standard laboratory test methods for coal and coke.
In: "Analytical methods for coal and coal products." Vol. 1, Chap. 6, (1978).

(125) Rees, O.W., Moisture characteristics of banded ingredients in coal and their influence on preparation of analysis samples.
Talanta, 13 No. 7, 1027, (1966).

(126) Gluskoter, H.J., Electronic low-temperature ashing of bituminous coal.
Fuel, 44, 285, (1965).

(127) Mackenzie, R.C., "The differential thermal investigation of clays." Mineralogical Society (Clay Minerals Group), London. (1957).

(128) Taichi Ogawa; Stenberg, V.I. and Montano, P.A., Hydrocracking of diphenylmethane. (Roles of H_2S pyrrhotite and pyrite.)
Fuel, 63, 1660, (1984).

(129) Rebick, C., Hydrogen transfer catalysis in hydrocarbon pyrolysis.
In: "Frontiers of free radical chemistry." Ed. Pryor, W.A. Academic, N.Y.. (1980).

(130) Brownell, W.E., "Structural clay products." Applied Mineralogy 9. Springer-Verlag. (1976).

(131) Berry, L.G. and Thompson, R.M., "X-ray powder data for ore minerals." The Geological Society of America, (1962).

(132) Saporoschenko, M.; Twardowska, H.; Smith, G.V.; Hinckley, C.C.; Shiley, R.H. and White, W.A., Mössbauer studies of illites and heat-treated illite as related to coal conversion processes.
Fuel, 59, 767, (1980).

(133) Cardile, C.M. and Johnston, J.H., ^{57}Fe Mössbauer spectroscopy of Montmorillonites: A new interpretation. Clays Clay Miner., 34 No. 3, 307, (1986).

(134) Inazumi, A.; Isobe, T. and Tarutani, T., Electron spin resonance and distribution of some elements in shales. Geochemical Journal, 15, 325, (1981).

(135) Meads, R.E. and Malden, P.J., Electron spin resonance in natural kaolinites containing Fe^{3+} and other transition metal ions.
Clay Minerals, 10, 313, (1975).

(136) Gillespie, P.A., Ph.D. Thesis. University of Aston in Birmingham. (1979).

(137) Castner, T; Newell, G.S.; Holton, W.C. and Slichter, C.P., Note on the paramagnetic resonances of iron in glass.
J. Chem. Phys., 32, 668, (1960).

(138) Jones, J.P.E.; Angel, B.R. and Hall, P.L., Electron spin resonance studies of doped synthetic kaolinites II.
Clay Minerals, 10, 257, (1974).

(139) Crăciun, C. and Meghea, A., Electron spin resonance studies of Montmorillonites.
Clay Minerals, 20, 281, (1985).

(140) Chaikum, N. and Carr, R.M., Electron spin resonance studies of halloysites.
Clay Minerals, 22, 287, (1987).

(141) Rozenson, I. and Heller-Kallai, L., Mössbauer spectra of dioctahedral smectites.
Clays Clay Miner., 25, 94, (1977).

(142) Johnston, J.H. and Cardile, C.M., Iron substitution in montmorillonite, illite and glauconite by ^{57}Fe Mössbauer spectroscopy.
Clays Clay Miner., 35 No. 3, 170, (1987).

(143) Cardile, C.M., Structural studies of montmorillonites by ^{57}Fe Mössbauer spectroscopy.
Clay Minerals, 22, 387, (1987).

(144) Tsipursky, S.I. and Drits, V.A., The distribution of octahedral cations in the 2:1 layers of dioctahedral smectites studied by oblique-texture electron diffraction.
Clay Minerals, 19, 177, (1984).

(145) Heller-Kallai, L. and Rozenson, I., The use of Mössbauer spectroscopy of iron in clay mineralogy.
Phys. Chem. Minerals., 7, 223, (1981).

(146) Heller-Kallai, L. and Rozenson, I., Dehydroxylation of dioctahedral phyllosilicates.
Clays Clay Miner,, 28 No. 5, 355, (1980).

(147) Cameron, W.E., Nonstoichiometry in sillimanite: Mullite compositions with sillimanite-type superstructures.
Phys. Chem. Minerals., 1, 265, (1977).

(148) Virgo, D. and Mysen, B.O., The structural state of iron in oxidised vs. reduced glasses at 1 atm.: A ^{57}Fe Mössbauer study.
Phys. Chem. Minerals., 12, 65, (1985).

(149) "Inorganic index to the powder diffraction file."
Joint committee on powder diffraction standards, Pennsylvania. (1971).

(150) Stark, J.G. and Wallace, H.G., "Chemistry data book."
John Murray (Publishers) Ltd., London. (1980).

(151) Helsen J.A. and Goodman, B.A., Characterisation of iron (II)- and iron (III)-exchanged montmorillonite and hectorite using the Mössbauer effect.
Clay Minerals, 18, 117, (1983).

(152) Bancroft, G.M.; Burns, R.G. and Stone, A.J., Applications of the Mössbauer effect to silicate mineralogy - II.
Geochim. Cosmochim. Acta., 32, 547, (1968).

(153) Deer, W.A.; Howie, R.A. and Zussman, J., "An introduction to the rock-forming minerals." Longman, London. (1978).

(154) Clementz, D.M.; Pinnavaia, T.J. and Mortland, M.M., Stereochemistry of hydrated copper (II) ions on the interlamellar surfaces of layer silicates. An E.S.R. study.
J. Phys. Chem., 77 No. 2, 196, (1973).

(155) McBride, M.B., Hydrolysis and dehydration reactions of exchangeable Cu^{2+} on hectorite.
Clays Clay Miner., 30 No. 3, 200, (1982).

(156) McBride, M.B.; Pinnavaia, T.J. and Mortland, M.M., Electron spin resonance studies of cation orientation in restricted water layers on phyllosilicate (smectite) surfaces.
J. Phys. Chem., 79 No. 22, 2430, (1975).

(157) Hall, P.L., The application of E.S.R. spectroscopy to studies of clay minerals - II.
Clay Minerals, 15, 337, (1980).

(158) Monsef-Mirzai, P. and McWhinnie, W.R., Spectroscopic studies of metal ion sorbed on to kaolinite.
Inorganica Chimica Acta, 58, 143, (1982).

(159) Kinsey, R.A.; Kirkpatrick, R.J.; Howie, J.; Smith, K.A. and Oldfield, E., High resolution Al-27 and Si-29 N.M.R. spectroscopic study of layer silicates, including clay minerals.
Amer. Miner., 70, 537, (1985).

(160) Janes, N. and Oldfield, E., Prediction of Si-29 N.M.R. chemical shifts using a group electronegativity approach; Applications to silicate and aluminosilicate structures.
J. Am. Chem. Soc., 107, 6769, (1985).

(161) Mägi, M.; Lippmaa, E.; Samoson, A.; Engelhardt, G. and Grimmer, A.R., Solid-state high-resolution ^{29}Si chemical shifts in silicates.
J. Phys. Chem., 88 No. 8, 1518, (1984).

(162) Smith, J.V. and Scott Blackwell, C., Nuclear magnetic resonance of silica polymorphs.
Nature, 303, 223, (1983).

(163) Simopoulos, A.; Kostikas, A. and Sigalas, I., Mössbauer study of transformations induced in clay by firing.
Clays Clay Miner., 23, 393, (1975).

(164) Green, J.M.; MacKenzie, K.J.D. and Sharp, J.H., Thermal reactions of synthetic hectorite.
Clays Clay Miner., 18, 339, (1970).

(165) Cooper, E., "Electric kiln pottery." Batsford Ltd., London. (1980).

(166) Gillespie, P.A., The University of Durham.
Personal communication. (1985).